The background of the cover is a photograph of a magnifying glass held over a small, square, black antenna array. The array is mounted on a dark, textured surface. The magnifying glass is positioned in the upper half of the frame, with its lens focused on the antenna array. The text is overlaid on the magnifying glass's lens area.

Design of a Wideband Phased Patch Antenna Array

J.P. Bout

Design of a Wideband Phased Patch Antenna Array

by

J.P. Bout

to obtain the degree of Master of Science
at the Delft University of Technology,
to be defended publicly on Thursday April 22, 2021 at 09.00 a.m.

Student number: 4277643
Project duration: May 1, 2020 – April 22, 2021
Thesis committee: Prof. Dsc. A. Yarovoy, TU Delft, supervisor
Dr. A. Endo, TU Delft
R. van der Meer M.Sc., Robin Radar Systems
Dr. J. Puskely, TU Delft

This thesis is confidential and cannot be made public until April 22, 2023.

An electronic version of this thesis is available at <http://repository.tudelft.nl/>.

Preface

It is with great pleasure, that I type these last words of my thesis. One could say my thesis went like a rollercoaster. From a quick start, through some rough months in my small student room and a large delay in the delivery of the created prototype, I was cheerful when it finally arrived and this project could be brought to an end. I would like to thank Robin Radar Systems, and especially my supervisor Rob van der Meer and my university supervisor Prof. dr. Alexander Yarovoy, for giving me this opportunity. To put all of my knowledge learned in almost 8 years of university together into a project. It was quite challenging at first. But, ended in lots of interesting discussions about this topic and I'm proud of the work I finally delivered.

In the end, I would like to give a special word of appreciation towards my mom Marijke and her partner Richard, for their endless support in the years I was studying. To my girlfriend Lotte, for her advice and support. And to all friends, for their emotional support over the last months.

Enjoy!

*J.P. Bout
Delft, April 2021*

Abstract

The increasing number of drones forms a more significant problem every year. Negative impact becomes more apparent during daily life as, for example, airport operations are shut down due to unauthorized users of drones. This report focuses on designing a new wideband antenna array as part of an integrated radar system to detect small objects, such as drones or birds. The design is done by studying generic array design assuming uncoupled antenna elements with omnidirectional radiation patterns. A comparative study of possible antenna element types has been conducted, concluded with selecting the best candidate. An antenna array has been designed with the embedded antenna elements and is verified using a prototype. Finally, an additional enhancement using meta-materials is done in an attempt to improve the antenna's performance further.

A wideband patch antenna array is proposed, which achieves a verified impedance bandwidth of 0.90 GHz with a scanning capability of ± 30 degrees in azimuth and ± 15 degrees in elevation. The measurements verify what the simulations have shown at broadside. Also, simulations have shown that the impedance could be increased to 2.96 GHz if a smaller feeding pin is used. It is also demonstrated that an AMC ground plane doesn't improve the antenna's performance and is, therefore, not implemented.

Contents

1	Introduction	1
1.1	Background	1
1.2	Research Problem	1
1.2.1	Requirements	2
1.3	State-of-the-art Research	2
1.3.1	Wideband Antenna Arrays	2
1.3.2	Artificial magnetic conducting ground plane.	11
1.4	Challenges and outline	14
1.5	Outline of thesis	15
2	Phased Array Analysis	17
2.1	Spherical domain	17
2.2	Substrate material	18
2.3	Element size	18
2.4	Feeding techniques	19
2.5	Maximum scanning angle and element spacing	20
2.6	Gain and number of elements	21
2.7	Amplitude tapering	21
2.8	Topology	22
2.9	Array feeding structures	22
2.10	Cooling structures	23
2.11	Summary	23
3	Comparative Study on Wideband Patch Antennas	25
3.1	Radiation requirements	25
3.1.1	Test patch antenna model	25
3.1.2	Return loss	26
3.1.3	Radiation pattern - gain	27
3.1.4	Radiation pattern - polarimetric properties	28
3.1.5	Signal fidelity	29
3.1.6	Group delay.	30
3.1.7	Manufacturability	32
3.2	Design considerations	32
3.2.1	Probe fed stacked patch with multi-layer substrate	33
3.2.2	Proximity fed patch with a multi-layer substrate.	36
3.2.3	Probe fed double stacked patch in a multi-layer substrate	40
3.2.4	Probe fed patch in a multi-layer substrate.	44
3.3	Trade-off	47
3.4	Conclusion	48
4	Patch Antenna Array	49
4.1	The Model	49
4.2	Simulation Results	51
4.2.1	Return Loss.	51
4.2.2	Radiation Pattern.	54
4.2.3	Signal Fidelity.	61
4.2.4	Manufacturability	61
4.3	Comparison with the infinite array	64
4.4	Conclusion	66

5	Results and Verification	67
5.1	The Prototype	67
5.2	Measurement Setup	68
5.3	Measurements & Verification	70
5.3.1	Return Loss	70
5.3.2	Radiation Pattern	71
5.4	Conclusion	77
6	AMC Ground Plane	79
6.1	AMC element selection	79
6.1.1	Horizontal strips	80
6.1.2	Horizontally polarised grill	82
6.1.3	Diamond with a horizontal strip	83
6.1.4	Two split ring resonators	85
6.1.5	Summary	87
6.2	Location of ground plane	87
6.2.1	Regular location with a thinner substrate	88
6.2.2	Atop substrate 2 next to the feeding strip	88
6.2.3	Between substrate 1 and 2 next to the feeding strip	90
6.2.4	Summary	93
6.3	Conclusion	93
7	Conclusions and Recommendations	95
7.1	Recommendations	96
A	Matlab scripts	97
A.1	Code to plot the active S-parameters	97
A.2	Function to calculate the active S-parameters	100
A.3	Code to plot the measured radiation pattern	100
B	Extra array material	103
B.1	Phase excitation	103
B.2	Electric field antenna array	104
C	Extra results material	105
C.1	Antenna Array Simulations	105
C.1.1	Return loss at negative elevation	105
C.1.2	6x6 array	106
C.2	Verification results	107
C.2.1	Active S-parameters	107
C.2.2	Radiation Patterns	109
	Bibliography	115

Introduction

This chapter introduces this thesis project. First, it provides some background information about the problem. Then, it discusses the research problem and the goals for this project are determined. Subsequently, the requirements and design constraints set by Robin Radar Systems are discussed, followed by the state-of-the-art research done on wideband patch antenna arrays. State-of-the-art research on artificial magnetic conducting (AMC) ground planes is also discussed. The challenges and design approach for this project are established. Finally, the outline of the rest of this thesis is provided.

1.1. Background

Small flying objects, such as drones and birds, are forming an increasing problem. Wind farms are shut down during bird migration, and drones are disturbing airport operations. To prevent collisions between all these 'users' of airspace, radars are used to monitor movements and locations. Mostly, larger objects, such as airplanes, are easily detected due to their large radar cross section. However, smaller objects have a much smaller radar cross section and are, therefore, much harder to detect.

Robin Radar Systems specialises in detecting and classifying these small objects. Their goal is to provide a safer and secure environment for both humans and birds by building specialised radars. After the releases of IRIS® and MAX®, it is time for the next generation radar for tracking of small objects.

1.2. Research Problem

Robin Radar Systems requires their next generation radar to be made fully solid state. In other words, to be made without a mechanical drive. Therefore, printed antennas are preferred. Research on printed antennas goes back a long way. The first time a printed antenna was mentioned, was by Grieg and Engelmann in 1952 [1]. However, research on printed antennas originally started in the 1970's, with the uprising of printed circuit board (PCB) technology [2]. Patch antennas have many advantages, such as: low-profile, simple to manufacture, mechanically robust and easy integration with integrated circuits (IC). On the other hand, they have a low efficiency, a low power handling capacity, an extremely small bandwidth and a relatively low gain [3]. To overcome these disadvantages, such as a low bandwidth of 1-3%, adjustments can be made to the patch. An increase in operational bandwidth is desirable, as antennas can be operational at different frequencies, without changing the antenna layout and structure. Range resolution could also be increased by using a larger bandwidth.

Ultimately, the main objective, addressed in this study, is the design of a wideband phased patch antenna array. Within this design, the two major goals are 1) to obtain a large impedance bandwidth of at least 1 GHz, and 2) to suffice the scanning capabilities of 30° in azimuth and 15° in elevation. Additionally, the design has to fulfill the requirements specified by Robin Radar Systems, shown in table 1.1. Also, the subgoal of this project is, if the performance of the antenna array can be improved by means of implementing an artificial magnetic conducting ground structure.

1.2.1. Requirements

In this section, the requirements set by Robin Radar Systems are elaborated upon. Robin Radar Systems has pre-determined the following requirements:

- The design frequency of the antenna will be in the 15-16 GHz band with a center frequency in the range of 15.4-15.7 GHz. As the new radar will work in the vicinity of other products produced by Robin Radar Systems, this new operational frequency band is chosen to prevent interference with the other radars.
- First detection of the small objects should be at a distance of 10000 m. From 6000 m, the radar should be able to classify small objects, such as drones or birds. Earlier research conducted by Robin Radar Systems shows that these targets have a radar cross section (RCS) of -25 dBm^2 , and are best detected by horizontal linear polarisation. The cross polarisation level is desired to be -25 dB compared to the main lobe of the antenna array.
- To transmit and receive properly, both transmitting and receiving antenna arrays should have a gain of at least 34 dBi.
- The object must be detected in an area of 60° in azimuth and 30° in elevation, and at the classification distance the objects must also be detected within an accuracy of 50 m.

The requirements are summarized in table 1.1.

Table 1.1: Design requirements set by Robin Radar Systems

Parameter	Value
Center frequency	15.4-15.7 GHz
Transmitting antenna gain	34 dBi
Receiving antenna gain	34 dBi
Transmitting power	51.8 dBm
Classification range	6000 m
Detection range	10000 m
RCS target	-25 dBm^2
Azimuth steering capabilities	$\pm 30^\circ$
Elevation steering capabilities	$\pm 15^\circ$
Polarisation	horizontal linear
Max. cross polarisation level	-25 dB

1.3. State-of-the-art Research

As discussed earlier, patch antennas are commonly used, but lack a large impedance bandwidth [3]. As Robin Radar Systems intends to explore the opportunities of a wideband antenna array; sufficient scanning capabilities and a large bandwidth are the main requirements for this design. Section 1.3.1 reviews attempts to increase the impedance bandwidth of patch antennas, and section 1.3.2 reviews attempts to increase performance by implementing an artificial magnetic ground.

1.3.1. Wideband Antenna Arrays

This section will review attempts to increase bandwidth of patch antenna arrays. The following approaches are considered to increase the bandwidth:

- Usage of thick (multi-layer) substrate;
- Modifying the patch shape;
- Adding additional slots;
- Using stacked patches

In addition, wideband feeding constructions will be discussed.

Thick (multi-layer) substrate

In the early research done on patch antennas, research has been conducted in increasing bandwidth by enlarging the substrate thickness. This section compares different approaches trying to improve the relative impedance bandwidth by increasing the substrate thickness or by using multiple substrates [4–6]. The effect of increasing substrate and dielectric permittivity is studied by Verma and Nasimuddin [4]. They propose to increase the thickness in terms of the resonant wavelength, and thus, that the impedance bandwidth increases up to 5-10% for an increasing thickness up to 0.3λ .

In another study by Hasan et al., a multi-layer material substrate patch antenna is designed and compared to a single layer substrate patch antenna [5]. The study focuses on designing the second/top layer of the multi-layer substrate. It is made from yttrium iron garnet nanopowders and exhibits a permittivity around 4.29, a dissipation factor of 0.05, which is slightly higher than a typical FR4 substrate and the permeability is 0.868. All in all, adding the extra layer to the substrate increases the impedance bandwidth from 4.48% to 7.16%.

Subsequently, a multi-layer substrate is proposed by Aslan and Yarovoy for closely spaced elements [6]. It shows that the use of an optimized 4 layer substrate, improves the operational bandwidth while scanning. In a 3x1 X-band array is improved from 3.8% to 9.29% at broadside and from 5.72% to 8.65% at a scanning angle of 25° . The four layers exist out of a very high dielectric layer with permittivity 10.2, followed by a layer with permittivity 2.2, third layer is air (permittivity = 1) and finally, a dielectric substrate with permittivity 2.2. This method focuses on reducing the mutual coupling between closely spaced elements. By reducing the mutual coupling, bandwidth improves as well.

Ultimately, it is apparent that a thick or multi-layer substrate reduces the mutual coupling, and therefore, the operational bandwidth. These attempts are summarized in table 1.2. The best performance is achieved by the multi-layer substrate proposed by Aslan and Yarovoy [6]. The relative bandwidth is improved with 5.5% at broadside, even while scanning.

Table 1.2: A comparison of attempts to increase the operational bandwidth by implementing a thick or multi-layer substrate.

Reference	Relative impedance bandwidth [%]
Thick [4]	5-10
Multi-layer [5]	7.16
Multi-layer[6]	9.29

Modifying the patch shape

The most common microstrip antennas are square, rectangular, or circular antennas, due to the ease of analysis and fabrication [3]. However, these shapes don't provide a large impedance bandwidth. Reshaping the element to any other configuration, has proven to achieve higher impedance bandwidth [7–13]. First, a comparison is made between C-shape, double-C shape, E-shape and a U-slot antenna by Bhardwaj and Rahmat-Samii [7]. The comparison is shown in table 1.3. The different antennas are compared on cross polarisation level, directivity and impedance bandwidth. The cross polarisation level should be minimized, to optimize the received power level.

Table 1.3: A comparison between different shapes of and slots in an antenna. This table compares on cross polarisation level, directivity and relative impedance bandwidth [7].

Shape/Slot	Cross polarisation level (E-plane/H-plane) [dBi]	Directivity [dBi]	Relative impedance bandwidth [%]
C-shape	-14/-19	8.0	0.8
Double C-shape	-24/-18	8.1	1.26
E-shape	-55/-12	7.6	27
U-slot	-55/-12	7.6	24

An octagonal antenna shape is proposed by Abbaspour and Hassani [8]. On three of the antenna's sides are placed slot inlets to change the current distribution on the patch, resulting in a higher bandwidth. The antenna is fed capacitively. i.e. the antenna has a proximity feeding. This also results in an increase in impedance bandwidth [3]. The proposed antenna achieves a relative impedance bandwidth

of 50%, and a gain with peak value of 7.35 dBi

Dalvi and Dessai made an analysis of a staircase shaped antenna [9]. It is compared on 4 different substrates: RT/Duroid 5880, FR4, Bakelite and Ceramic. On all these substrates a relative bandwidth of approximately 13% is achieved. The antenna with RT/Duroid substrate, the antenna works most efficient and achieves the highest gain of 4.85 dBi.

Guo et al. propose to print a two-port antenna with crescent moon-shape on a dielectric substrate [10]. The two patches are fed with 180° phase reversal (i.e. differential feeding), which leads to broad-side radiation. The crescent moon-shape is shown in figure 1.1. Measurements and simulation have shown that the antenna achieves a relative impedance bandwidth of 87%. The drawback of this configuration is that the antenna is fed by twice the amount of ports, leading to increased complexity.

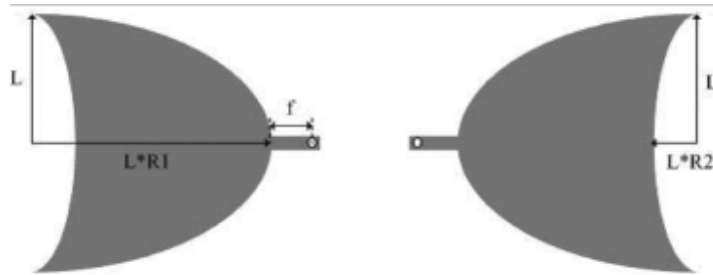


Figure 1.1: The antenna with two opposite crescent moon-shapes fed with a 180° phase shift [10].

Furthermore, an H-shaped patch antenna is placed over a reactive impedance surface (RIS) by Chatterjee et al. [11]. A RIS is a metamaterial structure placed below the antenna to increase the bandwidth. It is comparable to high impedance surface (HIS), explained in chapter 1.3.2. The antenna has an impedance bandwidth of 25.6% without the RIS layer. Nonetheless, it is significantly improved to 44.5% by using the reactive impedance surface. The downside however, is that the antenna is circularly polarized, due to its H-shape. The extra RIS layer also adds more complexity to the antenna.

Two square patches are superimposed to create a octagon-star shape antenna by Shi and Liu [12]. The shape is shown in figure 1.2a. The antenna has a very simple structure and has only a single feed. They proposed to excite the higher order TM modes, by using a slight size difference of the two patch antennas. This creates a conical circular polarized (CP) radiation pattern. But, it gives an impedance bandwidth of 2.4%. In this paper, a truncated-corner antenna is simulated, too. This is displayed in figure 1.2b. It has similar advantages and disadvantages as the octagon-star shape. But, the antenna has a slightly larger impedance bandwidth of 3.5% and provides a unidirectional radiation pattern.

The same truncated corner element is studied in an antenna array by Deng et al. [13]. However, in this case it achieves a much larger impedance bandwidth of 18.7%. In the array, the antennas are excited with three polarisation modes (linear, circular and linear) with sequential phases. All the modes have different resonance frequencies. As one of the modes excites circular polarisation, the linear polarisation is lost.

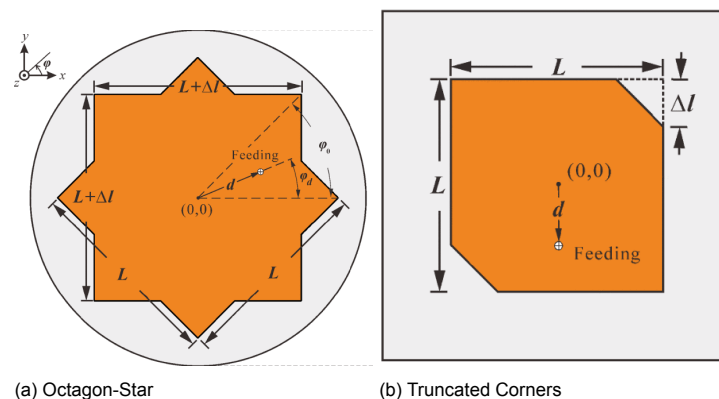


Figure 1.2: The patch antenna elements designed by Shi and Liu [12].

To summarize, the shape of the patch antenna has a large effect on its relative impedance bandwidth. This is shown in table 1.4. The three largest relative impedance bandwidth are the crescent moon, octagonal and E-shape patch antennas. They all have a impedance bandwidth of above 25%. The crescent moon shape has even a bandwidth of 87%. The octagonal shape has three slot inlets to additionally increase the bandwidth, but is an interesting option to consider, just like the E-shape.

Table 1.4: A comparison of attempts to increase relative impedance bandwidth by modifying the shape of the antenna.

Reference	Shape of element	Relative impedance bandwidth [%]
[7]	C	0.8
[7]	Double C	1.26
[7]	E	27
[8]	Octagonal	50
[9]	Stair-Case	13
[10]	Crescent Moon	87
[11]	H	25.6
[12]	Octagon-Star	2.4
[12]	Truncated-Corner	3.5
[13]	Truncated-Corner	18.7

Adding additional slots

Another approach to increase the impedance bandwidth of an antenna, is adding additional slots to the patch antennas [7, 14–22]. A double U-slot is proposed by Valavan and Knott [14]. Both slots are connected to each other. It creates a large relative impedance bandwidth of 35%. But, this approach uses proximity feeding, which has a larger bandwidth than microstrip or coaxial fed antennas [3]. Yoon and Seo suggested a patch with two non-connected U-slots, as shown in figure 1.3a [15]. It achieves a gain of 8.5 dBi for a single antenna and an impedance bandwidth of 13.37%.

A T- or L-slot is proposed by Saini and Agarwal to achieve higher bandwidth [16]. The small slotted patch antenna is of size $3.3 \times 1.7 \text{ mm}^2$. The antenna is shown in figure 1.3b. It achieves a 6.4 dB gain and has a relative impedance bandwidth of 10.5%. Additionally, an antenna proposed by Wei et al. has a double-y slot [17]. It has a huge relative impedance bandwidth of 64.4% and high gain of 8.5 dB. Wei et al. only proposed additional enhancements, such as multiple substrates to widen the bandwidth and a reflector for a uni-directional directivity and gain improvement. Also, an aperture coupled feeding mechanism is used, which like proximity feeding, has a larger bandwidth [3].

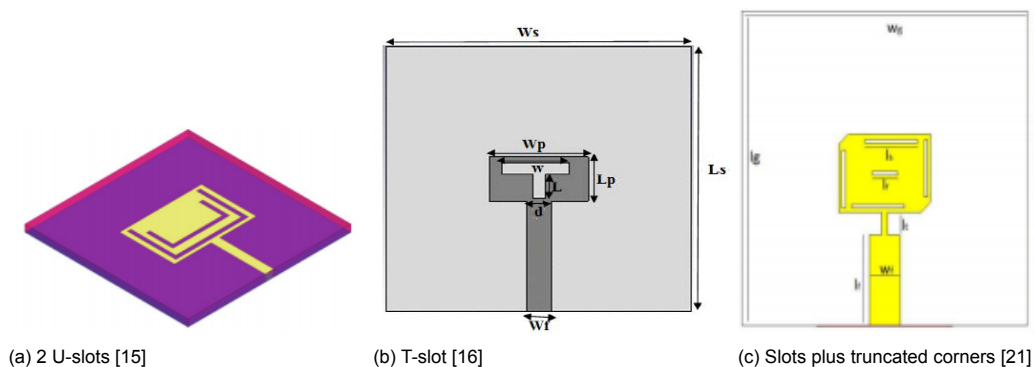


Figure 1.3: Patch antennas with different slots that increase the impedance bandwidth and gain.

A single U-slot antenna is discussed in the comparison of Bhardwaj and Rahmat-Samii [7]. The comparison is shown in table 1.3. The antenna achieves a large impedance bandwidth of 24%. An antenna with a cross slot is proposed by Díaz et al. [18]. The design is improved with multiple enhancements, such as a mirroring technique on array level for cross polarisation reduction and stacking the patch antenna with multiple substrates. Therefore, it has a impedance bandwidth of 370 MHz at a center frequency of 2.9 GHz and has a high scanning performance up to $\pm 60^\circ$.

Liu et al. suggested another approach: an air gap between the two stacked antenna improves the impedance bandwidth of a U-slot and E-shape patch antenna [19]. The antenna is dual band and the impedance bandwidth becomes 26.9% and 6.9%, respectively. Even though the antennas are fed by a coaxial probe. A drawback is that the cross polarisation level is still -13 dB. A modified U-slot antenna is proposed by Costanzo and Costanzo [20]. The arms of the U-slot are open, which reduce the cross polarisation effects, but retains the higher impedance bandwidth. It has a relative impedance bandwidth of 18% at C-band. Within the U-slot, the cross polarisation level is still -13 dBi. El-Sayed et al. suggested to use a rectangular patch antenna with two truncated corners, four narrow slots etched around the etches and one central slot [21]. They intend to enhance the bandwidth and gain. The patch antenna is displayed in figure 1.3c. It has a maximum impedance bandwidth of 845 MHz and a maximum gain of 7.65 dB.

A patch antenna is proposed with a combined T- and U-slot at 3 GHz by Mishra et al. [22]. However, this study focuses on gaining a larger return loss improvement instead of increasing impedance bandwidth. They proposed also to use a kind of artificial ground structure. By cutting three holes in the ground plane, the ground plane works as a polarizer, which converts the linear polarisation outside the 3-dB axial ratio into circular polarisation.

To conclude, the effect on the impedance bandwidth by adding slots to existing patch antennas is summarized in table 1.5. It is illustrated that a U-slot overall achieves a high relative impedance bandwidth. But, this antennas creates a high cross polarisation level. The largest bandwidth is created by the double Y slot. However, this antenna uses additional enhancements to improve the gain. All in all, slots achieve an improvement in impedance bandwidth, but unfortunately, create a lot of cross polarisation due to the variations in current distribution on the surface. All the other approaches achieve quite a high bandwidth of at least 10%, but create a high cross polarisation level as well.

Table 1.5: A Comparison of approaches to increase the impedance bandwidth using different slots in patch antennas.

Reference	Type of slot	Relative impedance bandwidth [%]
[14]	Double U (connected)	35
[15]	Double U (disconnected)	13.37
[16]	T-slot	10.5
[16]	L-slot	13.81
[17]	Double Y	64.4
[7]	U-slot	24
[18]	Cross	12.76
[19]	U-slot combined with E-shape	26.9
[20]	Modified U-slot	15-20
[21]	4 edge and 1 center slot(s)	4.75
[22]	Combined T- and U-slot	9.9

Using stacked patch antennas

Another approach to increase the impedance bandwidth is to stack multiple antennas on top of each other. The antennas can be radiating patches (and be physically connected), or one patch antenna can act as an parasitic patch on top of the radiating patch. In both cases, the antenna uses the radiation properties of both patches to increase the impedance bandwidth [23–29].

First, Klionovski and Shamim suggested a physically connected stacked square patch antennas with circular cutouts in the corners [23]. The setup is shown in figure 1.4. The antenna achieves a relative impedance bandwidth of 100.3% with a constant gain of at least 5 dBi. It achieves such a high bandwidth due to 5 different resonant frequencies. However, this configuration is not discussed in array form, and therefore, it remains unknown how the upper and lower layer patches will influence each other.

A stacked patched antenna array of 4 by 1 elements is proposed by Huang et al. [24]. The patch antennas both have a square shape and the bottom antenna is only fed by a coaxial feed. The array has a relative bandwidth of 21.67%, which is comparable to the single stacked element, that is also discussed in their study.

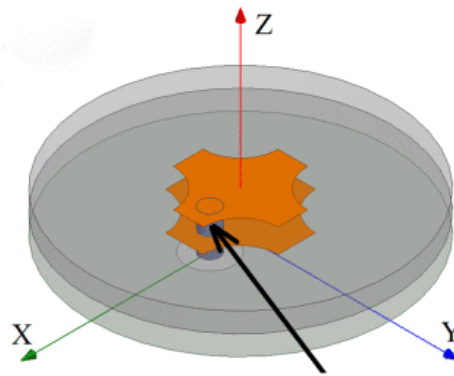


Figure 1.4: The physically connected stacked patch antenna [23]. The arrow points to the physical connection between the patches.

Yan et al. designed a 5 layer substrate stacked patch antenna and its extension into a 2x4 element array [25]. The layers are in the following order (from bottom to top): ground plane, air gap, driven patch, air gap and the stacked patch. The layers on their own increase the impedance bandwidth, already. Additionally, a U-slot is added to the radiating antenna and the patch antenna is fed using proximity feeding. With all the extra enhancements, the fractional impedance bandwidth is 15.83% and the gain is 9.7 dBi for a single antenna. The impedance bandwidth is more or less equal in the antenna array, but the gain increased to 16.2 dBi.

The same antenna structure is used by Yan et al. [26]. Most distinct changes are those of the radiating and parasitic patch. The lay-out is shown in figure 1.5. The antenna is put into a 2x2 array, with a designed feeding network. The array achieves an impedance bandwidth of 20.2%. In addition, a peak gain of 13.8 dBi is achieved. Furthermore, two aperture coupled stacked antenna arrays are

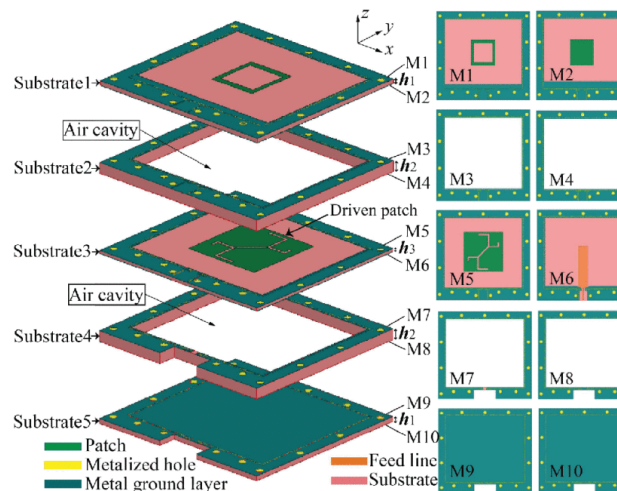


Figure 1.5: The stacked patch antenna configuration proposed by Yan et al. [26]. On the left side view of all 5 layers and on the right top and bottom view of each layer.

discussed by Bondarik and Sjöberg [27]. The radiating array has 2x2 elements. In one configuration, each radiating patch antenna has 3x3 parasitic patch antennas, and the radiating patch antenna is aligned with the center parasitic patch. In the other configuration, each radiating element shares the outer parasitic patches with each other. Therefore, the radiating patches can be placed closer together, and there are less feeding losses. The configurations are shown in figure 1.6. The bandwidth and the gain of the shared array have slightly decreased to 20.8% and 10.8 dBi, while the array has 11 parasitic patches less. On the other hand, the efficiency of the shared antenna array increases over the frequency band.

Subsequently, Hu et al. proposed an 2x2 polarisation reconfigurable stacked microstrip line antenna array [28]. This array has the possibility to radiate with 4 possible polarisations: linear (horizontal

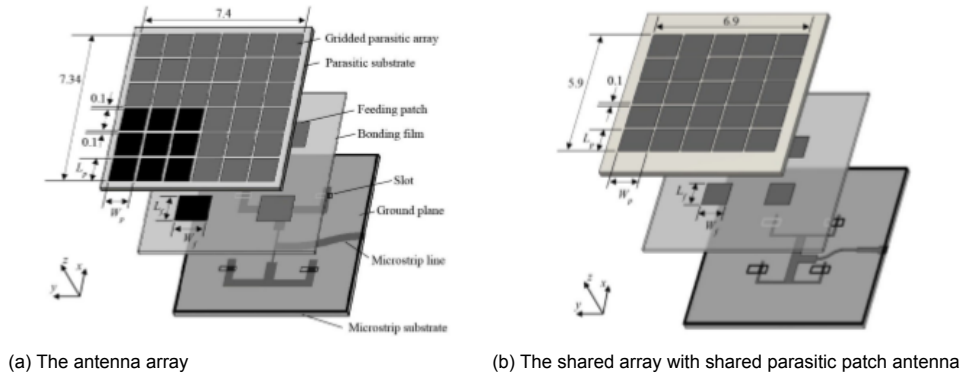


Figure 1.6: The aperture coupled stack microstrip antenna configurations [27].

and vertical) and circular (right-handed and left-handed). Each radiating patch has again 2x2 parasitic patches placed on top. The total size of the 4 parasitic patches is equal to the size of the radiating patch. A horizontal linear polarized antenna is required. In this configuration, the antenna has an impedance bandwidth of 23.4% and a gain of 10.35 dBi. The cross polarisation level is approximately 30 dBi lower than the co-polarisation level. The disadvantage is that this configuration has 4 switches in its feeding method to switch between polarisations. Therefore, the radiation properties could be improved if there was specialised on one polarisation for the radiated wave.

A dual band stacked antenna is proposed by Liu et al. [19]. Both patch antennas are fed by one probe, where the lower patch is an E-shape and the top patch has a U-slot. The impedance bandwidth increases to 26.9%. Unfortunately, the antenna exhibits a high cross polarisation level of just below -13 dBi.

At last, Yang et al. proposed a stacked ultra wideband antenna using the Low Temperature Co-fired Ceramic (LTCC) technology [29]. The radiating antenna is fed using an aperture slot in the ground plane. Conventionally, an aperture slot is fed using a microstrip line. In this configuration, the feed is changed to a parallel-wire transmission line. The differential feeding method excites the aperture slot, which in turn couples the energy to the stacked patch antennas. This creates a large impedance bandwidth of 44% and a maximum broadside gain of 7.2 dBi is achieved. However, the gain varies a lot over impedance bandwidth, therefore, an additional rectangular shielding ring is added. Unfortunately, this setup is not simulated in an array, and it is unknown how the aperture coupled feeding and shielding ring will influence other proximate antennas.

To conclude, the approaches have illustrated that stacked patches create some good approaches for wideband antennas and antenna arrays. The approaches are summarized in table 1.6. The largest bandwidth that is achieved is by the physically connected stacked antenna [23]. It has an impedance bandwidth of 100.3%. Unfortunately, it is unknown how this antenna will radiate in an array. As both antennas are excited, it might induce a lot of mutual coupling. Furthermore, the other approaches that were presented, have all more or less a bandwidth around 20% and one approach has 44% bandwidth.

Table 1.6: A comparison of approaches to increase the impedance bandwidth using stacked patch antennas and antenna arrays

Reference	Element or array	Relative impedance bandwidth [%]
[23]	Element	100.3
[24]	Element	21.67
[25]	Element	15.8
[25]	2x4 Array	15.8
[26]	2x2 Array	20.2
[27]	2x2 Array	25.8
[27]	Shared array	20.8
[28]	2x2 Array	23.4
[19]	Element	26.9
[29]	Element	44

Wideband feeding methods

Next to doing modifications to the patch antenna, its feeding mechanism can be modified to enhance its bandwidth [30–33]. In this section, approaches of wideband feeding methods will be discussed.

First, an antisymmetric L-shape probe is presented by Mak et al. [30]. The probe exists out of a H-shaped feedline ground with 2 antisymmetric L-shape patches on top of it. The probe is placed perpendicular between the patch antenna and the ground plane. This configuration is shown in figure 1.7. As the probe is aligned in one dimension, linear polarisation is achieved. The antenna achieves an impedance bandwidth of 49.3%. Within this frequency band, a measured gain is achieved from 8 to 10 dBi. Unfortunately the probe is 2.4 mm in height, which enlarges the complexity and size of the antenna. Manufacturing of the antenna might be difficult. Also, the feeding probe isn't tested or simulated in array form, therefore, the mutual coupling between the antenna elements is unknown.

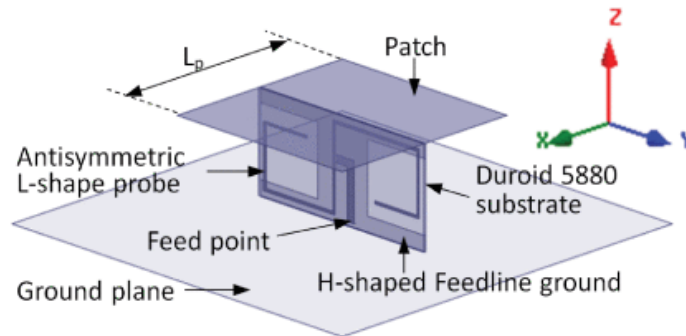


Figure 1.7: The anti-symmetric L-shaped probe in perspective view [30].

Another approach proposed by Haider, uses a blind-via fence to encircle the probe [31]. In this way, the antenna matches more the characteristic impedance $Z_0 = 50 \Omega$ of the feeding line. This increases the operational bandwidth and reduces the mutual coupling between radiating elements. The relative impedance bandwidth is increased to about 20% for a S-band antenna and to even 30% for a C-band microstrip antenna.

Wong et al. proposed to use a meandering probe in multiple layers of substrate [32]. A meandering probe introduces an additional capacitance to reduce the probes inductance, increasing the relative bandwidth. Normally, this feeding technique uses an air-loaded structure, but this paper designed an integrated structure. The linearly polarized patch antenna achieves a measured gain of 7 to 8 dBi and an impedance bandwidth of 33.8%. In addition, cross polarisation levels are reduced to over -20 dB across the operating bandwidth.

A modified L-probe feed with a capacitive matching ring arrangement is proposed by Valavan [33]. The probe exists out of a plate-through-hole cylinder, which results in an inductive reactance, connected with a field-matching ring and a stripline transition. Together this looks like a 'lamppost' and it is shown in figure 1.8. In this configuration, the matching ring and the stripline transition create a capacitive reactance, which balances out together with the inductive reactance. This creates a highly matched feeding mechanism, resulting in mutual coupling reduction. Therefore, a widescan array can be created. The impedance bandwidth is around 6-7%. The proposed patch antenna is dual band, and if the resonances would lie closer together the dual band antenna could act as wideband.

The approaches to use a wideband feeding technique to increase the bandwidth are summarized in table 1.7. It is discernible that most of the wideband feeding techniques give a larger bandwidth than regular patch antennas, with even a largest bandwidth of 49.3%. The downside is that complexity is increased drastically with multiple layers or matched probes.

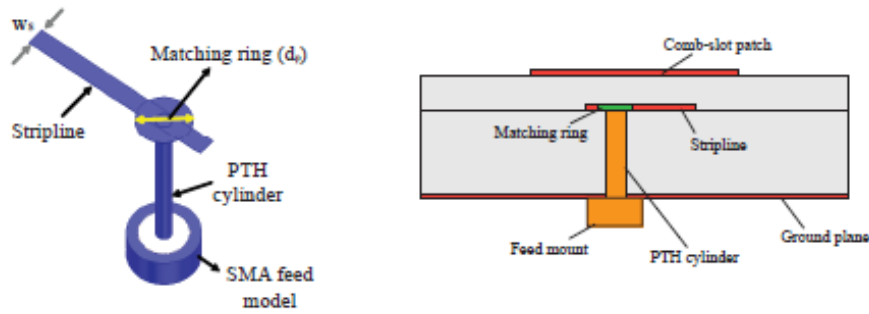


Figure 1.8: The 'Lamppost' feeding mechanism [33].

Table 1.7: A comparison between approaches to increase the impedance bandwidth using wideband feeding methods.

Reference	Method	Relative impedance bandwidth [%]
[30]	Antisymmetric L-shape probe	49.3
[31]	Blind-Via Fence	30
[32]	Meandering Probe	33.8
[33]	'lamppost' apparatus	6-7

Summary

Thick or multi-layer substrates improve the bandwidth slightly, but can be used to reduce mutual coupling between elements, which is beneficial for a large and dense array.

Subsequently, modifying the shape of the patch antenna has a huge impact on the impedance bandwidth. Table 1.4 shows that the crescent moon shape has the best relative bandwidth, however, this one is fed by two ports and might not be a good approach. Nonetheless, the octagonal or E-shape are good alternatives, as they have quite a large impedance bandwidth as well.

Adding slots to the patch antenna creates extra resonant frequencies, which can increase the bandwidth. Furthermore, it is apparent that slots increase the complexity of the antenna. The current distribution is altered, and thus, the cross polarisation level increases.

Stacked patch antennas also increase the relative impedance bandwidth at least over 15%. In the physically connected antenna [23], the best relative impedance bandwidth of 100.3% is achieved. However, the mutual coupling effects of this antenna are unknown.

Finally, wideband feeding methods have been discussed. It is clear that the used feeding mechanism has to match the antenna. Where a normal coaxial probe creates a bandwidth of 2-3%, wideband feeding techniques can achieve a bandwidth up to 49.3%. On the other hand, the complexity of these feeding techniques might be hard to implement. Sometimes the size of the antenna increases, and therefore, wideband feeding techniques are mostly not preferably for low-profile antennas.

To summarize, it is conspicuous that each approach hardly exceeds the required relative impedance bandwidth of 10%. All those to have reached that level, are either combinations of approaches or ones which are hard to realise. Some stacked patches or wideband fed antennas also achieve quite a large bandwidth, but aren't validated in array form and might create a lot of mutual coupling between the elements. Modifying the patch shape or adding additional slots induce high cross polarisation levels. So, a combination of thick or multi-layer substrates, stacked antennas and wideband feeding methods is to be investigated to meet the requirements while maintaining acceptable cross polarisation level and complexity.

1.3.2. Artificial magnetic conducting ground plane

Due to limited space on the PCB, the antenna array will be dense, which causes additional mutual coupling. An approach to enhance the performance and reduce mutual coupling between elements is to implement an artificial magnetic conducting ground plane. This section explains what an AMC ground plane is and why does an AMC ground plane exhibit properties, a perfectly electric conducting (PEC) ground plane does not. Then, different attempts of designing an artificial magnetic conducting ground plane and its properties are reviewed. Finally, it is concluded which ground planes are an interesting approach to implement to a wideband antenna.

What is an artificial magnetic conducting ground plane?

An AMC ground acts as a metamaterial, which does not exist in nature. Nonetheless, an AMC mimics the behaviour of a perfect magnetic conductor (PMC) [34]. Before explaining the basic principles of an AMC ground plane, one must have some knowledge about surface waves.

A property from metals is that they support surface waves. Surface waves are AC currents occurring on any electric conductor and will radiate, if they are scattered by any discontinuities in the surface [35]. Surface waves will also induce more mutual coupling between elements, and therefore, need to be minimized. The magnitude of the surface wave depend on the substrate thickness. If the substrate decreases, the quantity and the magnitude of the surface waves will also decrease.

The operation of a patch antenna in the proximity of a conductor is displayed in figure 1.9. A ground plane works constructively with an antenna, if they are $\lambda/4$ apart from each other. This is due to the phase shift of magnitude π , a good conducting plane gives to the back-radiating wave. Using the phase shift of the ground plane and the distance between the elements, the phase of the reflected back-radiated wave is equal to the phase of the main radiated wave, and therefore, works constructively. This is displayed in figure 1.9b. But to reduce surface waves, the distance between the ground plane and antenna needs to be decreased. Resulting in the conductor is not separated $\lambda/4$ anymore and the back-scattered wave will work destructively due to the phase shift induced by the conductor. This is shown in figure 1.9a. Another approach is to place the antenna in the proximity of an AMC ground plane (also known as high impedance surface (HIS)). The back-scattered wave will not have any phase shift and the distance between the antenna and the ground plane is insignificant, as shown in figure 1.9c. The separation can be of any distance, the back-radiated wave will always work constructively now.

Patch antennas are usually required to have low costs and to be low-profile due to limited available space in their applications. Implementing an AMC ground plane, increases the antenna's dimension and complexity drastically. The relatively small increase in gain on a large antenna array is quite small, and therefore, AMC ground planes are not widely used, yet.

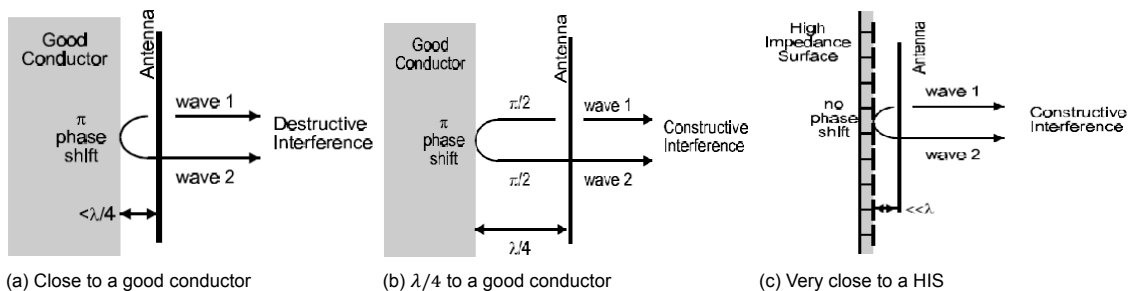


Figure 1.9: A radiating antenna separated on different distances from a good conductor or a high impedance surface [35]. The figures explain that the backwards radiated wave is only working constructively, if the separation between the antenna and good conducting ground plane is $\lambda/4$. Otherwise, the backwards radiated will work destructively. The only exception is, when the the good conducting ground plane is a high impedance surface. In that case the separation is insignificant.

Attempts to design an AMC ground plane

First, an AMC ground plane is designed by Ghosh et al. on the same three resonant frequencies of an antenna [36]. The designed metasurface exists of 4×4 unit cells. Each unit cell is approximately 1.5 by 1 cm, which is smaller than the antenna of ± 2.5 by 1.5 cm. Additionally, each unit cell has a square loop and two stepped impedance resonators, to achieve all three resonant frequencies. The design is shown in figure 1.10. The metasurface combined with the antenna gives a gain improvement of 3.57

dBi. The antenna is a microstrip antenna, backed by a slotted ground plane. A small air gap between the AMC and the antenna of 1.7 mm is set to give a good impedance matching at all three resonant frequencies.

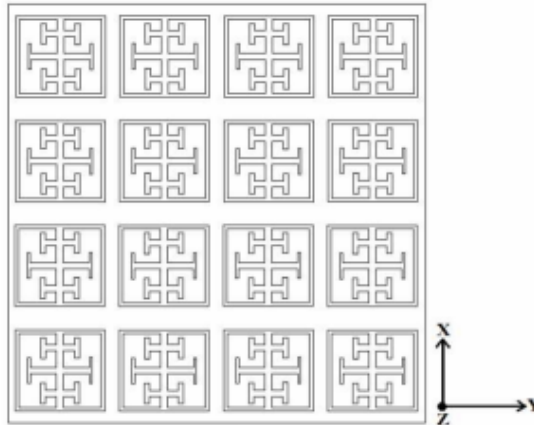


Figure 1.10: The designed AMC metasurface of [36].

Zhong et al. proposed an improvement in bandwidth and gain enhancement by using a fractal wide-band AMC [37]. Their design exists of a printed bow-tie antenna with the dimensions of 57 by 7 mm, combined with a fractal AMC, that exists of 6x9 unit cells. Each cell is circular with a radius of approximately 6 mm. Adding the fractal AMC unit cell improves the gain of the antenna by approximately 4 dBi and improves the relative impedance bandwidth to 16.7%. This configuration is interesting, as it is implemented on a wideband bow-tie antenna[38].

Ameen and Chaudhary suggested to use an AMC-metasurface with a metamaterial antenna [39]. The metasurface exists of 4x4 unit cells. The cells have asymmetric V-shaped slots arranged in a rotated manner, this reduces the size of the unit cell to 10.4 by 9.8 mm. The antenna exists of two perpendicular unit cells, with an inverted L-shaped feed. Therefore, the antenna is 45 mm long and 40 mm wide. It operates at a frequency of 2.5 GHz and combined with the metasurface the gain and the impedance bandwidth are increased with 3.6 dBi and 260 MHz.

Subsequently, a polarisation-independent AMC ground plane is proposed by Lin et al. with a circularly polarized antenna and 1x4 antenna array [40]. Adding the AMC to the antenna (array), the antenna (array) has a realized gain of 6.6 (13) dBi and a high relative bandwidth of 25 (21.7)%. The AMC ground plane has 3x3 unit cells for each antenna. Dimensions of the unit cell are 58x58 mm and the dimensions of a single antenna are about 70 by 70 mm. In the array, the outer unit cells overlap, as shown in the prototype in figure 1.11.

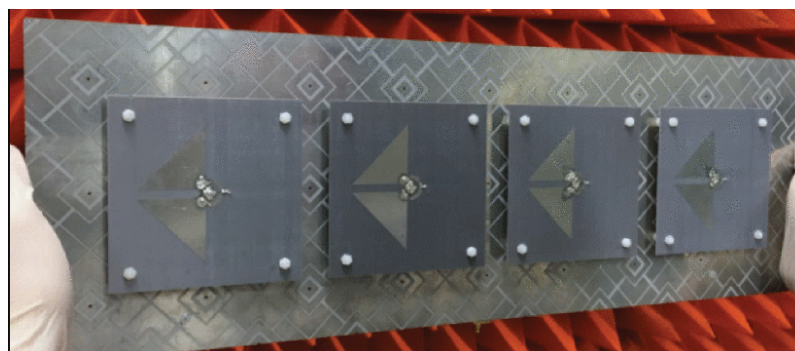


Figure 1.11: A 1x4 antenna array backed by an AMC. The unit cells of the AMC overlap for each antenna [40].

A 4x4 first order fractal unit cells AMC structure is proposed by Manoj et al. [41]. The unit cells exist of two split ring resonators and have a size of 6.1 by 6.1 mm. This gives an overall dimension of 24.1 by 24.1 mm with an antenna of dimensions 20 x 14 mm. When this AMC structure is mounted under

the antenna, it gives a 2.61 dBi gain improvement and the relative impedance bandwidth is increased from 12.18 to 26.51%.

Zhang et al. proposed a coded design of two designed artificial magnetic ground unit cells [42]. The AMC ground plane exists of 4x4 AMC cells, each 45 by 45 mm. Each AMC cell consists of 5x5 smaller unit cells of 9 by 9 mm. The AMC cells are made out of 2 different unit cells, which are placed in a coded design, as shown in figure 1.12. A patch antenna is mounted on every 2x2 AMC cell, with sides of length 27 mm. The metamaterial ground does not influence the polarisation and other radiation properties of the antenna at all, as the AMC and array are designed at different frequencies. The coded design manipulates the antenna's scattering performance, and therefore, is hardly detectable by other antennas.

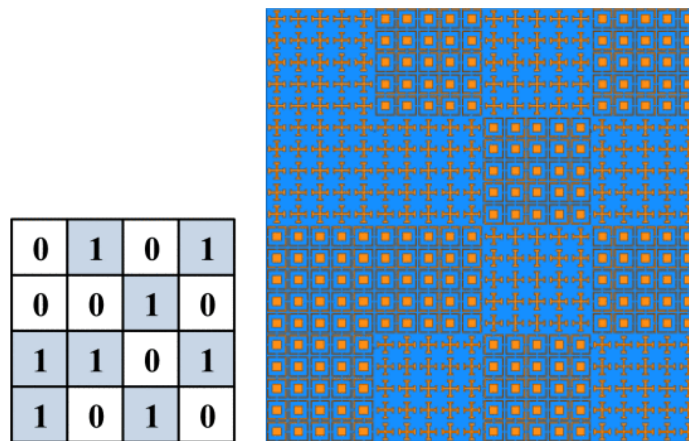


Figure 1.12: The coded design of the AMC [42]. On the left the coded design in 0,1. And on the right the design using the two different unit cells.

Furthermore, two artificial magnetic conductor cells are combined in a chessboard-like metamaterial surface (CLMS) by Zheng et al. [43]. The surface exists of 3x3 AMC cells, which exists of 3x3 elements of 9.0 by 9.0 mm. The center AMC cell is replaced by an antenna of 9.0 by 7.8 mm. The antenna with the CLMS shows a peak gain enhancement of 3.6 dB and it has also a bandwidth of 1.72 GHz at a center frequency of 10.5 GHz. The disadvantage of this configuration is that the surface is an AMC structure instead of the ground plane. Thus, the AMC cannot be used in antenna arrays.

At last, Zhu et al. proposed a wideband multiple-input multiple-output (MIMO) antenna with an AMC ground plane [44]. The combination achieves a high unidirectional gain compared to an antenna with a perfect electric conducting ground plane. The proposed antenna has a 7.1 dBi peak gain and a relative impedance bandwidth of 31.0%. The structure is used on a wideband antenna, which explains partially the high bandwidth. The dipole is of approximate dimension 30 by 30 mm and is combined with a couple of V-shaped patch antennas. The antennas are placed on top- and bottomside of a laminate and are shorted at certain points. Therefore, the current flow in both patches is in the same direction. In the end, this laminate is placed diagonal on a 5x5 square patch AMC, each AMC unit cell has a size of 12 by 12 mm with a gap of 3 mm between the antennas.

Summary

Overall, most of the artificial magnetic ground planes give an adequate performance improvement. This is summarized in table 1.8. The dimensions of the antennas compared to the ground planes are compared in table 1.9. The AMC ground plane must also be applicable to an antenna array, like the polarisation independent AMC [40]. All in all, it is apparent that a designed AMC ground plane could be a useful addition in the antenna design. If the design frequency of the AMC is matched with the resonant frequency of the antenna or antenna array, a gain improvement of 4 dBi could be achieved. Additionally, it is discernible that the relative impedance bandwidth varies between 0.5 and 33%. Therefore, a proper design will work with narrow- as well as wideband antennas, such as the bow-tie dipole. If the AMC ground plane allows to mount multiple antennas on top of it, it could work on an antenna array, as well.

Observing at tables 1.8 and 1.9, solutions for gain enhancement of a wideband antenna array might be the approaches of the fractal wideband AMC cells [37] or the 4x4 first order fractal unit cells [41] as

they both have a high relative impedance bandwidth and a good gain improvement. Another option is the fractal unit cells of [36], if the resonance frequencies are close enough to each other, such that the unit cell has wideband character. An interesting feature to consider is to overlap the unit cells, such as Lin et al. did [40]. Ultimately, these designs show promising features that electrical conductor ground planes don't have.

Table 1.8: Comparison of different variations of AMC's on gain improvement and bandwidth

Reference	Gain without AMC [dBi]	Gain with AMC [dBi]	Gain improvement [dBi]	Relative impedance bandwidth [%]
[36]	1.38, 3.22, 7.58	3.77, 6.29, 11.16	2.39, 3.07, 3.57	0.5-1.5
[37]	2.5	6.5	4	16.7
[39]	1.9	5.92	4.02	33.07
antenna[40]	-	6.6	-	25
1x4 array[40]	-	13	-	21.7
[41]	0.65	3.26	2.61	26.51
2x2 array [42]	14.3	14.3	0	4.83
[43]	6.8	8.1	1.3	16.38
[44]	-	7.1	-	31.0

Table 1.9: Comparison of the dimensions of a single antenna with the dimensions of the AMC ground or surface.

Reference	Antenna dimension [mm ²]	Unit cell dimension [mm ²]	AMC ground plane dimension [mm ²]
[36]	25x20	15x10	65x60
[37]	57x7	12x12	72x108
[39]	45x40	10.4x9.8	45x45
[40]	70x70	58x58	174x174
[41]	20x14	6.1x6.1	24.1x24.1
[42]	27x27	9x9	90x90
[43]	9x7.8	9x9	81x81
[44]	30x30	12x12	75x75

1.4. Challenges and outline

Designing the phased antenna array leads to the following challenges:

- Mutual coupling needs to be minimized to prevent changes in the radiation pattern of the array and changes in the input impedance of the individual elements in the array.
- To prevent radiation in unwanted directions, side lobe level should be at least -25 dBi.
- The cross polarisation level is desired to be in the order of -25 dB compared to the main lobe. As drones are best detected by horizontal linear polarised waves, the vertical component should be small. The cross polarisation level depends on the antenna element, how the wave is excited and the scattering object.
- The -1 dB bandwidth should at least cover the full operational bandwidth. This is to have a constant transmitting gain over the bandwidth and ensure the amount of receiving power keeps being equal.
- The beamwidth of a single patch element should be wide enough to support scanning in an array. As gain and beamwidth are dependent on each other, the gain of a single element can't be too large. Also at the maximum scanning angle, the gain may not be lower than 1 dB in the radiation pattern of the single patch antenna.
- The patch antennas might be integrated with the artificial magnetic conducting ground plane. The patch elements are small, this means the elements of the AMC are even smaller. Creating the right resonances and integrating the AMC with the antenna will be complex.

All these challenges, makes it difficult to start designing the antenna array at array level. Therefore, the following design approach is proposed:

1. First, design multiple single elements with the challenges, discussed above. Each single element is put into an infinite array using the periodic boundary conditions in CST, such that mutual coupling is taken into account. The goal is to find out what the radiation properties, like gain and bandwidth are of each single element with different feeding methods and patch types. And verify all the necessary properties. Finally, choose the best model to suit for the array.
2. Compute a 2-dimensional of 4x4 elements using the element from the infinite array and verify if the array is able to scan properly, has still wide enough bandwidth, and fulfill the rest of the requirements.
3. Create a prototype with the designed phased array and verify the results.
4. Design an artificial magnetic ground plane for the 4x4 array and implement this on the array. Also, verify that mutual coupling has been reduced and gain has been increased on the resonant frequency.

1.5. Outline of thesis

The outline of this thesis is as follows: this chapter gives an introduction to the problem. It defines the research problem as well as the requirements and the design constraints. It also discusses the state of the art topics regarding the subject of wideband phased antenna arrays as well as artificial magnetic ground planes. And the challenges of this project are introduced and a design approach is made.

Chapter 2 gives background information on designing a generic antenna array. It discusses all the properties of a single patch antenna, such as substrate material and element size. But also, properties of the antenna array, such as maximum scanning angle and its feeding network.

There is made a comparative study on different wideband antenna elements in chapter 3. The candidates are analysed and a trade-off between the candidates is made.

Chapter 4 proposes a new wideband antenna array. It gives a detailed design of the antenna element and the antenna array. A full wave analysis of the antenna array has been performed. And compares this to its infinite array simulation.

Subsequently in chapter 5, the creation of a prototype and its results are explained. It is discussed how the prototype is measured and how it compares to the simulated antenna array.

Chapter 6 discusses if an artificial magnetic conductor ground plane could improve the performance of the proposed model from chapter 4.

Ultimately, conclusions and recommendations are given in chapter 7.

2

Phased Array Analysis

In this chapter, a phased patch antenna array is analysed. Properties of a single patch antenna as well as a phased array are discussed. First, the coordinate system for the antenna is explained. Then, for a single patch antenna, the substrate material, element size, and feeding mechanism are analysed. Then, the antenna array is considered. The interelement spacing and number of elements are calculated to fulfill the requirements from section 1.2.1. Furthermore, a non-uniform amplitude distribution is discussed in order to decrease the side lobe level, but also, the topology of the array to minimize mutual coupling. Finally, as the array becomes large, feeding and cooling structures are mentioned, too.

2.1. Spherical domain

Radiation patterns and other properties of an antenna or antenna array are simulated and measured in the spherical domain. The scanning limit requirements are given in azimuth and elevation. As explained in chapter 1.2.1, the requirement on scanning capabilities is that the antenna is able to scan $\pm 30^\circ$ in azimuth, thus in the x-direction, and $\pm 15^\circ$ in elevation, which is in the y-direction of the antenna. However, the antenna is characterized in the spherical domain, so with theta and phi. From this perspective, theta is the angle how far the antenna scans. So by increasing theta, the array scans further away from broadside. Phi in this perspective is the angle towards which direction is scanned. This is graphically shown in figure 2.1.

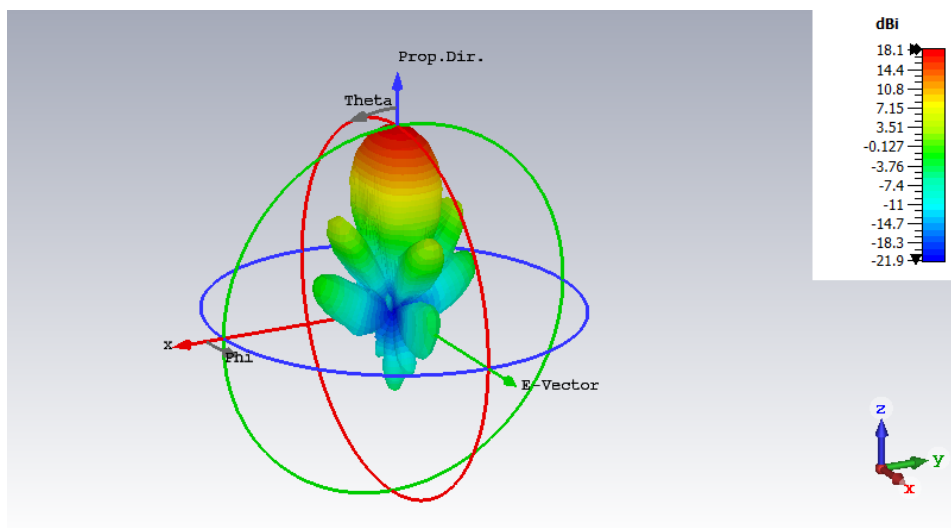


Figure 2.1: A farfield radiation pattern to explain the spherical coordinates compared to scanning in azimuth and elevation.

The antenna is required to be horizontally polarized, such that in the model for $\phi = \pm 90^\circ$ the antenna array scans in the azimuth plane and $\phi = 0^\circ$ or $\phi = 180^\circ$ the array scans in the elevation plane. The maxima of the scanning limits are when the antenna array scans in both directions simultaneously. Using this knowledge the angles for theta and phi can be calculated for the azimuth and elevation by trigonometry. The corresponding angles with the scanning limit are shown in table 2.1. Using these angles, the phase of each element can be calculated using the equations from chapter 2.5.

Table 2.1: The corresponding angles in spherical coordinates for the maximum scanning angles of the antenna array.

Azimuth	Elevation	Theta	Phi
30°	15°	33.5°	116.6°
-30°	15°	33.5°	-116.6°
-30°	-15°	33.5°	-63.4°
30°	-15°	33.5°	63.4°

2.2. Substrate material

The substrate affects some of the most important properties of an antenna. One of these properties is, the size of the patch. For a wideband patch antenna, the substrate is most desirable thick with a low permittivity [3]. A thicker substrate also gives a better efficiency, however, element size will increase to keep the same resonance frequency. For antenna arrays the substrate needs to be as thin as possible to prevent surface waves and decrease the spurious feed radiation for the microstrip feeding line. Some example substrate materials are given in table 2.2. They are compared on dielectric constant and dissipation factor using the Rogers Product Selector Guide [45] and some data given by Balanis [3].

Table 2.2: Some substrate materials compared on dielectric constant and dissipation factor [3, 45].

Material	Dielectric constant ϵ_r	Dissipation factor $\tan \delta$
Rogers RT/Duroid 5880	2.20	0.0009
Rogers RO4350B TM	3.48	0.0037 (10 GHz/23°C)
Rogers RT/Duroid 6035HTC	3.50	0.0013
FR4 Epoxy	≈4.5	0.004
Arlon DiClad 870	2.33	0.0013
Neltec NH9320	3.20	0.0024
Taconic RF-60A	6.15	0.0038

2.3. Element size

The size of a single rectangular patch antenna element is determined by the following parameters:

- Dielectric permittivity of the substrate ϵ_r []
- Height of the substrate h [m]
- Resonant frequency f_r [Hz]

There are four steps to calculate the size of a patch antenna. These are given in equations 2.1-2.4 [3]. First, the width W of the patch antenna is calculated,

$$W = \frac{c}{2f_r} \sqrt{\frac{2}{\epsilon_r + 1}} \quad [\text{m}] \quad (2.1)$$

where c is the free-space velocity of light. Then, the effective dielectric constant can be determined using equation 2.2:

$$\epsilon_{r,\text{eff}} = \frac{\epsilon_r + 1}{2} + \frac{\epsilon_r - 1}{2} \left[1 + 12 \frac{h}{W} \right]^{-1/2} \quad (2.2)$$

The actual electric length of a rectangular patch antenna is extended by $2\Delta L$ due to fringing fields. ΔL is determined by equation 2.3.

$$\Delta L = 0.412h \frac{(\epsilon_{r,\text{eff}} + 0.3) \left(\frac{W}{h} + 0.264\right)}{(\epsilon_{r,\text{eff}} - 0.258) \left(\frac{W}{h} + 0.8\right)} \quad [\text{m}] \quad (2.3)$$

Finally, the actual length of the patch antenna can be calculated by solving equation 2.4.

$$L = \frac{c}{2\sqrt{\epsilon_{r,\text{eff}}}f_r} - 2\Delta L \quad [\text{m}] \quad (2.4)$$

For example, when the resonant frequency is equal to a center frequency 15.6 GHz and the antenna is designed with a RT/Duroid5880 ($\epsilon_r = 2.2$) substrate with a standardised height of $h = 0.254$ mm [45]. The size of the element is equal to the values in table 2.3.

Table 2.3: The calculated parameters of a single patch element to achieve a resonant frequency at 15.6 GHz with a RT/Duroid 5880 substrate of 0.254 mm thickness.

Parameter	Value
Width W	7.602 mm
Effective dielectric constant $\epsilon_{r,\text{eff}}$	2.107
Extended length ΔL	0.134 mm
Length L	6.356 mm

In an array, the elements can easily be placed too dense together, which will increase mutual coupling. One approach to prevent this, is to decrease the element size, while resonant frequency does not change. The element size can be decreased by altering the dielectric permittivity or the height of the substrate. Increasing the dielectric permittivity, decreases both length and width as the permittivity influences the results of equations 2.1 and 2.4. The substrate height influences the effective dielectric permittivity and the extensions of the length ΔL . The width of the patch does not depend on these parameters.

2.4. Feeding techniques

Aside from the wideband feeding techniques discussed in chapter 1.3.1, there are also the four traditional feeding techniques: microstrip, coaxial probe, aperture & proximity [3]. Their advantages and disadvantages are summarized in table 2.4.

Table 2.4: The advantages and disadvantages of the traditional feeding techniques for a patch antenna.

Microstrip	Coaxial probe	Aperture	Proximity
Easy to manufacture (+)	Easy to manufacture (+)	Easy to model (+)	Widest bandwidth (+)
Planar structure (+)	Simple matching (+)	Low interference with circuitry (+)	Easy to model (+)
Simple matching (+)	Low spurious radiation (+)	Relatively large bandwidth (+)	Versatile matching (+)
Narrow bandwidth (-)	Narrow bandwidth (-)	Independent design (+)	Difficult fabrication (-)
Spurious radiation from feed line (-)	Difficult modeling for thick substrates (-)	Minimized spurious radiation (+)	
Asymmetric feeding (-)	Asymmetric feeding (-)	Difficult fabrication (-)	

Due to size constraints, it is preferred to place the phase-shifters and other components are placed on opposite side of the PCB. Thus, the radiating antennas are fed from the other side of the PCB.

Microstrips lines can feed the antennas in this array, if each strip is connected to a coaxial probe. This will take a lot of space on the PCB and the microstrip feeding lines will cause unwanted spurious radiation. Therefore, using a microstrip as feeding technique will not be considered.

Coaxial probes are useful as it connects the radiating patch directly with the relative components. Easy to manufacture, but lack the ability to create a large bandwidth. Nonetheless, coaxial fed patch antennas can still achieve a high bandwidth by using one of the techniques from section 1.3.1. And coaxial probes are still an adequate technique to feed the antennas.

Aperture feeding has a lot of advantages, such as a large bandwidth and low interference with circuitry. But, it is difficult to fabricate and if the gain will be increased by using the artificial magnetic ground plane, the antenna can't be feed with the aperture. As placing the AMC between the aperture slot plane and the patch antenna will reflect all the energy back and the patch won't receive any energy. And placing the AMC below the slot, will create lots of unwanted reflections between the slot plane and the AMC. Therefore, aperture feeding will not be considered as a technique in this project.

Finally, proximity feeding is considered as an option. It has also a large bandwidth capability and is easy to model. And compared to the aperture feeding, proximity feeding can be implemented with an AMC. On the other hand, this feeding method is difficult to fabricate and might be hard to match with the patch antenna.

All in all, proximity and coaxial probe are the most promising methods to implement in this patch antenna array. Proximity feeding has a larger bandwidth, but is harder to fabricate. Coaxial probe has a lower impedance bandwidth, but this can be increased by using one of the methods, discussed in section 1.3.1.

2.5. Maximum scanning angle and element spacing

The antenna should have beam-steering capabilities in azimuth, as well as elevation. An azimuth coverage of 60° is required, which means the antennas azimuth beam must be able to steer 30° in the positive and negative direction. In the elevation plane, the antenna should have a coverage of $\pm 15^\circ$. To prevent grating lobes from occurring, the interelement distance should be sufficient. For a main beam in the direction of (θ_0, ϕ_0) , the principal maximum ($m = n = 0$) and the grating lobes ($m, n \neq 0$) can be located by equations 2.5-2.6 [3],

$$kd_x(\sin \theta \cos \phi - \sin \theta_0 \cos \phi_0) = \pm 2\pi m \quad m = 0, 1, 2, \dots \quad (2.5)$$

$$kd_y(\sin \theta \sin \phi - \sin \theta_0 \sin \phi_0) = \pm 2\pi n \quad n = 0, 1, 2, \dots \quad (2.6)$$

From this, it follows that ϕ is equal to:

$$\phi = \tan^{-1} \left[\frac{\sin \theta_0 \sin \phi_0 \pm n\lambda/d_y}{\sin \theta_0 \cos \phi_0 \pm m\lambda/d_x} \right] \quad m, n = 0, 1, 2, \dots \quad (2.7)$$

and θ is equal to:

$$\theta = \sin^{-1} \left[\frac{\sin \theta_0 \cos \phi_0 \pm m\lambda/d_x}{\cos \phi} \right] = \sin^{-1} \left[\frac{\sin \theta_0 \sin \phi_0 \pm n\lambda/d_y}{\sin \phi} \right] \quad m, n = 0, 1, 2, \dots \quad (2.8)$$

A grating lobe truly exists, if both parts of equation 2.8 give the same θ . If the interelement distance is less or equal than $\lambda/2$, no grating lobes exists [3]. As a guideline the interelement spacing can be used to determine the maximum interelement distance to prevent grating lobes:

$$d_e \leq \lambda_{op}/(1 + \sin \theta_{max}) \quad (2.9)$$

with θ_{max} the maximum scanning angle. For a scanning angle of 30 degrees, an interelement distance of $2\lambda/3$ is required to prevent grating lobes. For example, at a center frequency of 15.6 GHz, the interelement spacing of $d = 12.82$ mm is required. The largest size of the example given in chapter 2.3 is 7.602 mm, which means those elements in the array are very close together. This might create an undesired level of mutual coupling between elements. The spacing, however, is still a guideline, as the array works in two dimensions θ_{max} might be larger due to different scanning angles in the azimuth and elevation plane.

2.6. Gain and number of elements

Robin Radar Systems specified that the transmitting and receiving antenna gain needs to be 34 dBi in order to have a classification range of 6 km. The total array gain G_a can be calculated using equation 2.10 [3],

$$G_a = D_0 + G_e \text{ [dBi]} \quad (2.10)$$

with G_e the element gain and D_0 the array factor directivity, which is equal to array factor gain as the array factor has no losses. Typical element directivity is usually between 5 to 7 dBi [3]. The gain is even less, due to antenna efficiency. Element gain can be increased by modifying the antenna or structure of the antenna with e.g. an artificial magnetic ground plane. For example, if the element gain is 7 dBi. The total array factor gain is equal to 27 dBi, excluding losses, such as amplitude tapering to reduce the side lobe level, discussed in section 2.7. The directivity for a large and dense planar array is equal to the total number of elements in the array N , shown in equation 2.11.

$$D_0 = 10 \log_{10}(N) \text{ [dBi]} \quad (2.11)$$

and the embedded gain G_e of an element is given by equation 2.12,

$$G_e(q) = 4\pi \frac{A \cos \theta_0}{\lambda^2} \quad (2.12)$$

with A the physical aperture size of the element, θ_0 the scanning angle and λ the wavelength. Thus, equation 2.10 becomes:

$$G_a = 10 \log_{10}(N) + 4\pi \frac{A \cos \theta_0}{\lambda^2} \text{ [dBi]} \quad (2.13)$$

Equation 2.11 illustrates that the total number of elements, determines the array factor gain. Therefore, a total number of at least 502 elements are necessary to reach the gain of 27 dBi in the example. This is a minimum when the antenna achieves a 7 dBi element gain. Equation 2.12 shows the embedded element gain depends on the scanning angle and the physical aperture size. This can be improved by increasing the bandwidth of the element, discussed in chapter 1.3.1, or by changing the topology, discussed in chapter 2.8.

Furthermore, the accuracy of the antenna at 6000 m is 50m. This gives an accuracy of $\arctan(50/6000) = 0.47^\circ$. As Robin Radar Systems uses a processing technique to detect an object with a half power beamwidth (HPBW) as a rule of thumb 10 times the accuracy, the HPBW becomes 4.7° . If a square array topology is used, the half power beamwidth in the azimuth plane can be approximated by using the equation for the 3 dB beamwidth of a linear array $\theta_{3\text{dB}}$ [3]:

$$\theta_{3\text{dB}} \sim 0.866\lambda/Nd \sin \theta_0 \quad (2.14)$$

with N the number of elements, d the interelement distance and θ_0 the scanning angle from broadside. For an -3 dB angle of 4.7° at a scanning angle of 30° ($\theta_0 = 60^\circ$), with an interelement distance of $2\lambda/3$, equation 2.14 gives a square array of at least 19×19 elements. This is in total 361 elements without losses. This doesn't meet the number of antennas used in the example and is even 141 elements short. Furthermore, a total loss of 10% is a rule of thumb. This means that a total number of 552 elements are necessitate in the example. This is achieved by a planar array of 24×24 elements, giving a total of 576 elements. Such an example array would meet the requirements regarding gain and accuracy, as a linear array of 24 elements gives a HPBW of 3.66 degrees.

2.7. Amplitude tapering

Antenna arrays without a uniform amplitude distribution have a sidelobe level of -13.6 dB [3]. Sidelobe level (SLL) requires to be minimized, in order to reduce desensitisation of the main beam due to sidelobe emission or deflection directions. One approach to reduce the SLL to a maximum level is amplitude tapering of the antenna array excitation [46]. The amplitude of the elements in the array are multiplied with a distribution called tapering. Often, a Taylor line source or Dolph-Chebyshev distribution is used. Both distributions have their advantages and disadvantages, but for larger arrays Taylor line source

distribution is the favorable [46]. This is due to the fundamental trade-off between maximizing directivity and decreasing the sidelobe level. Dolph-Chebyshev maximizes all the sidelobes to a certain level, but widens the beam, reducing gain and accuracy. Taylor's Distribution ensures the first sidelobe is at a maximum, and subsequently, decreases the sidelobe level for further sidelobes. This keeps the beam more narrow while decreasing the sidelobe level compared to the Dolph-Chebyshev distribution.

2.8. Topology

Another degree of freedom is the topology of the array. As explained in section 2.5, for an element spacing of $2\lambda/3$ the element distribution is still quite dense. Meaning, mutual coupling might affect the radiation pattern of the array in a rectangular grid. Therefore, the interelement spacing may have to be enlarged, which will cause grating lobes. An approach to eliminate these grating lobes is by changing the grid to a triangular or diamond topology [46]. In an array, linear arrays are displaced alternately $d_x/2$ (or $d_y/2$). Therefore, the interelement spacing increases from d_x and d_y to $\sqrt{d_x^2/4 + d_y^2}$. This is shown in figure 2.2.

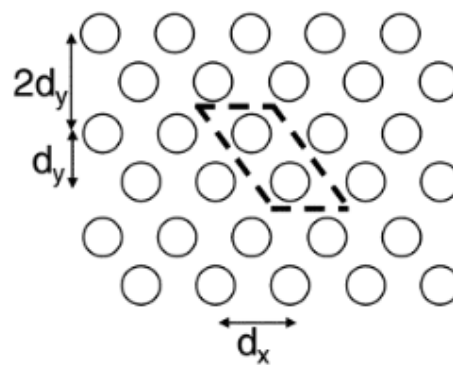


Figure 2.2: A triangular topology for the antenna array [46].

Normally, this would induce grating lobes. However, due to the displacement, the zeros of the cosine pattern align with the grating lobes indices $m + n = \pm(1, 3, 5\dots)$, and therefore, remove the additional lobes. Also, a triangular grid has the same scan limits as the rectangular grid.

Another approach, would be to use a sparse or thinned array [46]. Some applications require only a narrow beam, but not a requirement on grating lobes. The beamwidth is determined by the largest dimension of the aperture. Therefore, lots of elements can be removed, while the array size is not decreased. This will decrease the gain with approximate proportion to the fraction of elements removed, while the beamwidth stays significantly narrow. By removing elements, the interelement spacing effectively increases and grating lobes will occur. For radar purposes, optimal sidelobe level and scanning capabilities are needed, so thinned is not an option and rectangular or triangular are preferred.

2.9. Array feeding structures

One of the constraints is that the antenna is designed on a single PCB. I.e., the radiating part and the electronics will be on opposite sides and feeding structures of the PCB need to be designed and controlled. For a phased array, the antennas need to be excited separately with a different phase and amplitude. The basic layout of a phased array feeding structure has the following form: An up-converted RF signal comes into the system. This is split into a network. Each string of this network has a phase-shifter, and a variable gain amplifier (VGA), to give the desired complex excitation to the antenna. Each string is connected to a different antenna via its feeding mechanism. This basic layout is shown in figure 2.3.

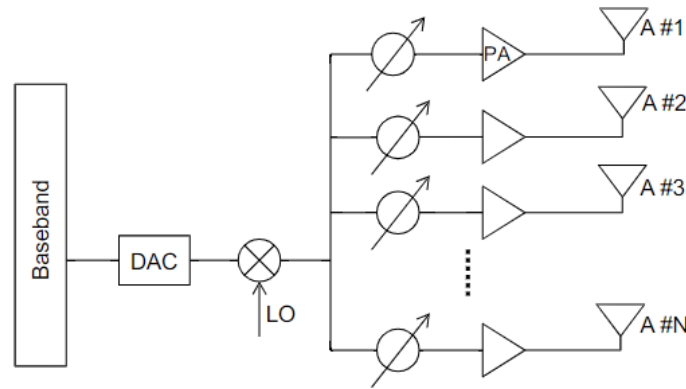


Figure 2.3: The basic layout for an analog beamforming structure [47].

2.10. Cooling structures

The main sources for the dissipated heat are generated by the amplifiers. As power amplifiers have roughly an efficiency of 30% and the the array is quite dense, it can be assumed the cooling structure of the PCB has to be controlled as well. For example when an antenna transmits a power of 50 dBm, about 233 W of heat is generated. As shown in figure 2.4, for an 16x8 array, the temperature is trapped in the center and can't escape as the outer layers warm up as well [48]. This is not exactly the setup, studied in this thesis, but it might be comparable.

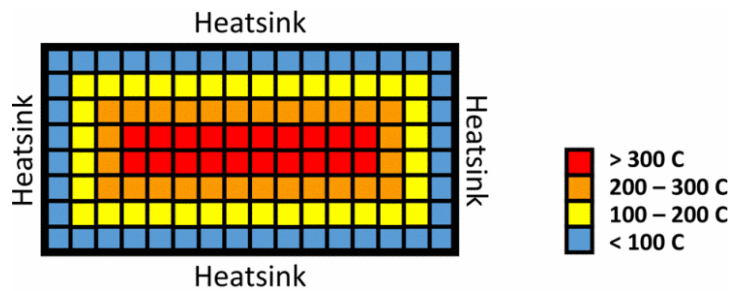


Figure 2.4: The temperature increase across an 16x8 antenna from [48].

In figure 2.4, mostly the heat in the center of a dense array needs to be transferred out of the PCB. The PCB can be cooled, by transferring the generated heat from the antenna to a heat exchanger, either by heat-spreader or heatpipes. Subsequently in the study by Aslan et al. [49], it is shown that increasing the interelement spacing achieves additional cooling. This is another advantage of using a triangular topology, explained in section 2.8. Additionally, another approach is presented by exploiting heat spreaders located in the middle of the patches. This creates a conduction path between all the elements of the antenna and provides cooling without affecting the radiating performance. Finally, the glass transition temperature T_g of the substrate needs to be big enough to withstand the created heat. For example, Rogers RO4350B has a $T_g > 280^\circ\text{C}$ [50], while FR4 has a glass transition temperature of 130°C .

2.11. Summary

All in all, most of the properties regarding a phased antenna array are discussed. A substrate with a low permittivity is desirable, such as RT/Duroid 5880. RT/Duroid6035HTC and RO4350B are also options. The equations to calculate the size of the element are given and a comparison is made between different feeding methods.

Furthermore, an interelement spacing of $2\lambda/3$ is desired, as this gives no grating lobes at a scanning angle of 30° . It is shown that the number of elements, influences the gain requirement and the accuracy of the antenna array. An example has been given to demonstrate the influence. Additionally, to suppress side lobe levels, a Taylor line source distribution over the amplitude distribution is favourable.

Subsequently, by putting the elements into a triangular topology, they are placed further apart from each other. In this way, it keeps the same scanning capabilities, dissipates heat better and reduces mutual coupling in the array.

Finally, feeding and cooling structures are mentioned. A basic layout is given for feeding structures. Regarding cooling structures, it has been shown that especially in the center, a dense array needs to be cooled with heat pipes or something similar, as the heat gets trapped there.

3

Comparative Study on Wideband Patch Antennas

In this chapter, a comparative study on possible wideband antenna element types is made. Each antenna element is simulated in an infinite array, by setting the boundary conditions in the x- and y-plane to be periodic. First, the radiation requirements are specified. The antenna elements will be compared on these requirements. Then, different designs are presented. The antennas are simulated on broadside and on the maximum scanning angle in the azimuth and elevation plane. A trade-off between the antenna elements is made, and finally, it is concluded which antenna element is the best candidate to implement in the antenna array.

3.1. Radiation requirements

The radiation requirements need to fulfill the requirements from chapter 1.2.1, considering the challenges from chapter 1.4 and the goals set in chapter 1.2. In this section, the requirements are presented using a basic patch antenna element. Utilising the properties of this model, the ideal performance of an antenna element is discussed. The following properties are discussed:

- Return Loss (3.1.2)
- Radiation Pattern - Gain (3.1.3)
- Radiation Pattern - Polarimetric properties (3.1.4)
- Manufacturability (3.1.7)
- Signal Fidelity (3.1.5)
- Group Delay (3.1.6)

Each element is simulated in an infinite array as most requirements depend on mutual coupling.

3.1.1. Test patch antenna model

In the design of a static antenna for radar applications, patch antennas have the preference. Therefore, the radar can be made on one PCB, where the radiating elements are on one side and the electronics on the opposite side, connected with vias. The geometry of the vias can be used as tuning. The performance of the patch antenna is computed, thus, the radiating side is only needed for the simulation. In this model, the antenna is excited via a coaxial probe as a substitute for the electronics. External equipment can be used to excite the antenna. As the transmitted power is quite high, Robin Radar Systems requires that the isolation for the coaxial probe is polyether ether ketone (PEEK) [51]. This material has a high temperature resistant thermoplastic, and therefore, is good for soldering in a PCB environment. The electrical properties of PEEK has a dielectric permittivity of 3.1 and a dissipation factor of 0.003. PEEK is also a good option to use in the radar to isolate the vias from the ground plane.

A coaxial fed patch antenna model is used to illustrate the ideal radiation properties. The example model is a patch antenna on a Rogers RT-Duroid5880@substrate. A coaxial probe is placed in the x-direction from the center to the edge of the antenna, such that a horizontal linear polarised wave is excited. The model is shown in figure 3.1 and its parameters are shown in table 3.1. The model is shown in perspective and in side view. Both views are also displayed with and without the substrates to give a clear view where the antenna is situated in the model.

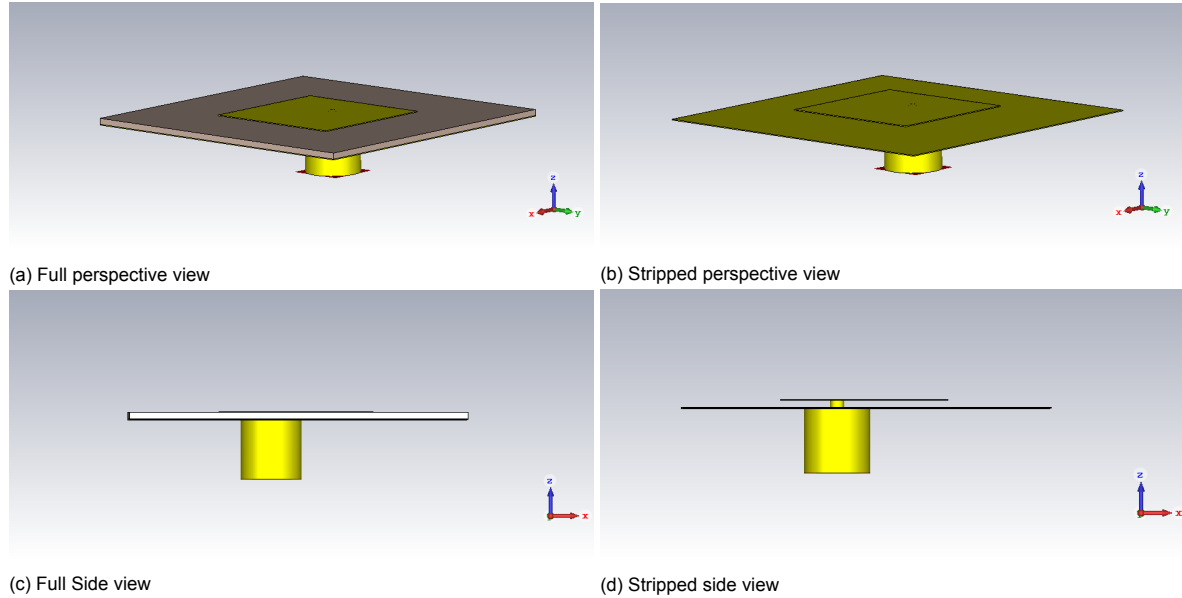


Figure 3.1: The coaxial test model to explain the ideal performance of an antenna with (3.1a/3.1c) and without (3.1b/3.1d) substrates.

Table 3.1: The parameters for the coaxial test antenna model

Parameter	Value	Parameter	Value
Length ground plane	13.0 mm	Height substrate	0.254 mm
Width ground plane	13.0 mm	Radius pin	0.25 mm
Thickness copper	0.035 mm	Radius isolation pin	1.15 mm
Length patch antenna	5.89 mm	Shift pin from edge	2.0 mm
Width patch antenna	6.0 mm		

As the thickness of the copper cladding is equal in all models, it will not be given in the parameters the compared models.

3.1.2. Return loss

The antenna reflection coefficient determines how the antenna is matching with its transmission line. I.e., how much energy is transferred to the antenna and how much energy is reflected back in the transmission line. Ideal antennas radiate without any losses and transmit everything. But in reality, a part of the energy is reflected to the transmission line. The fraction of the energy that is reflected is described by the reflection coefficient Γ in equation 3.1 [3],

$$\Gamma = \frac{Z_A - Z_0}{Z_A + Z_0} \quad (3.1)$$

where Z_A is the complex impedance of the antenna and Z_0 is the characteristic impedance of the transmission line. Ideally, the real part of Z_A is equal to Z_0 and the imaginary part to 0. The reflection Γ is then close to zero. The return loss is expressed by equation 3.2 and is also called S1,1 after the four-port model.

$$RL = -20 \log(|\Gamma|) \quad (3.2)$$

The return loss of smaller than -10 dB is generally assumed as a limit over impedance bandwidth of the antenna. I.e. the frequency range for which an antenna radiates efficiently. The center or resonant frequency is the value, where the return loss is the smallest. For a patch antenna, the center frequency is determined by the length of the patch antenna and the thickness of the substrate, as discussed in section 2.3.

An important characteristic is that an antenna's reflection coefficient changes while scanning. Therefore, the return loss is simulated at broadside, as well at the maximum scanning angles in azimuth and elevation. For simplicity, the comparison on bandwidth is made at broadside ($\theta = 0^\circ$), 30° scanning angle in azimuth ($\theta = 30^\circ, \phi = 0^\circ$) and 15° scanning angle in elevation ($\theta = 15^\circ, \phi = 90^\circ$)

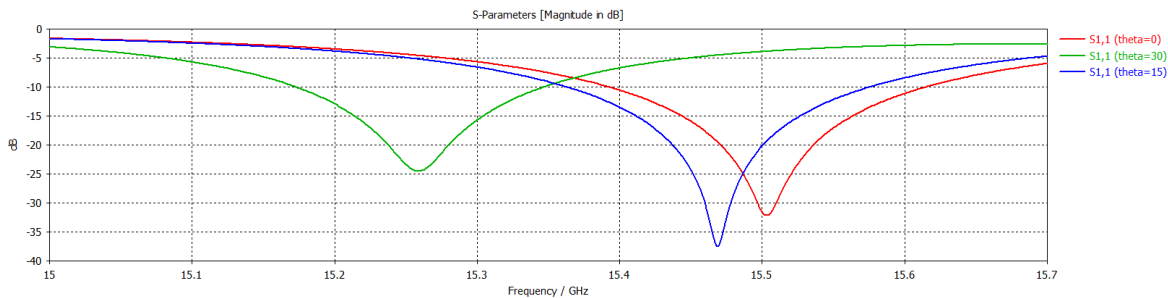


Figure 3.2: The return loss of the coaxial probe patch model while scanning towards three directions: broadside (red), 30° azimuth (green), 15° elevation (blue).

In figure 3.2, the return loss is plotted for the example model at different scanning angles. The impedance bandwidth and center frequency are given for each scanning angle in table 3.2. At broadside (red line), the center frequency at broadside is 15.54 GHz. This changes slightly for a scanning angle of ± 15 degrees in elevation (blue line). But, for a scanning angle of $\pm 30^\circ$ (green line), the center frequency changes to 15.26 GHz.

Furthermore, at broadside the -10 dB limits range from 15.39 till 15.61 GHz and creates an impedance bandwidth of 220 MHz, while at $\theta = 30^\circ$ the limits range from 15.17 till 15.35 GHz and the impedance bandwidth is equal to 280 MHz. However, these bandwidths don't overlap at all, and therefore, there is no useful bandwidth. The bandwidth in the elevation plane is comparable to the bandwidth at broadside. The results are shown in table 3.2.

Table 3.2: Scanning angles for the different return losses of figure 3.2. Also, the center frequency and impedance bandwidth are given.

Scanning angle	Line	Center frequency [GHz]	Impedance bandwidth [GHz]
Broadside	Red	15.50	15.39 - 15.61 = 0.22
30° azimuth	Green	15.26	15.17 - 15.35 = 0.28
15° elevation	Blue	15.47	15.36 - 15.58 = 0.22

Ideally, the center frequency is between 15.4 and 15.7 GHz. As these frequencies are in the impedance bandwidth, it is not bound by that requirement. However, the impedance bandwidth must be at least 1 GHz.

All in all, the return loss changes most while scanning in the azimuth plane. The difference in return loss while scanning in the elevation plane is comparable while scanning towards broadside. A comparison will be made on all three scanning angles, where ideally the impedance bandwidth of each scanning angle overlap each other and is at least 1.5 GHz wide.

3.1.3. Radiation pattern - gain

As explained in chapter 2.6, the scanning capabilities of the full array are limited by the scanning capabilities of a single element. As a directive antenna loses gain on scanning angles, its radiation pattern should be wide enough to have minimum loss. The array factor gain also loses some energy while scanning. On the other hand, this is solved by using an inverse amplitude tapering. This ensures the array factor at broadside decreases, and becomes equal to the array factor gain at a scanning angle.

Robin Radar Systems requires that the loss at the maximum scanning angles is minimal. There is chosen for a maximum loss of 1 dB. I.e., the gain may decrease 1 dB at angles θ from -30 till 30 degrees at angle $\phi = 90^\circ$ and from -15 till 15 degrees at angle $\phi = 0^\circ$. Using the farfield radiation pattern, it is determined if antennas satisfy these requirements. The radiation patterns are displayed as the realized gain, as this takes the mismatch of the antenna to its transmission line into account.

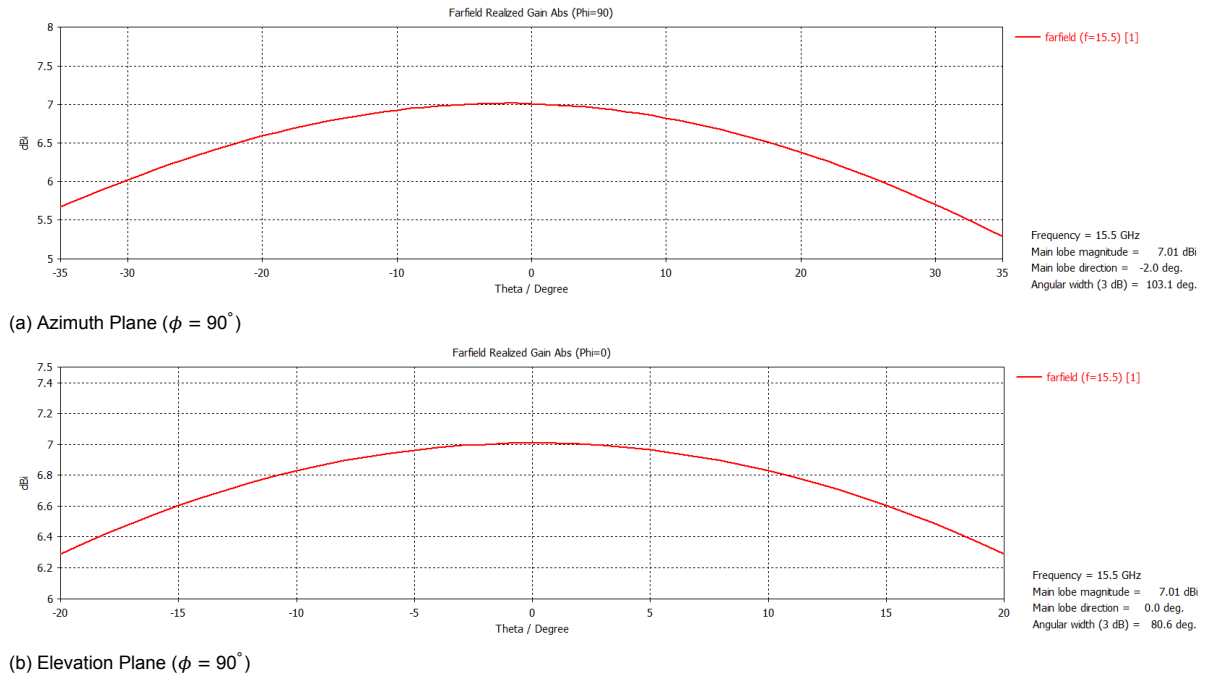


Figure 3.3: The radiation pattern of the coaxial test model at different angles of ϕ .

In figure 3.3a, the realized gain is shown for the test model at $\phi = 90^\circ$. A 1 dB reduction ranges from -30.0 till 26.0 degrees for angle θ , and thus, does not satisfy the requirement. At $\phi = 0^\circ$, displayed in figure 3.3b, the 1 dB reduction ranges from -23.62 till 23.64 degrees and satisfies the requirement.

In the end, each antenna will be compared on level of the realized gain and angular width in the azimuth and elevation plane. Ideally, the gain will only have a loss of 1 dB on the scanning limits, but if none exceeds the 1 dB, the closest will be the favorable. In the azimuth plane, the gain will be plotted from -35 till 35 degrees. And in the elevation plane, the gain will be plotted from -20 till 20 degrees.

3.1.4. Radiation pattern - polarimetric properties

Another relevant aspect of the radiation pattern are the polarimetric properties. The antenna is required to have a linear horizontal polarisation, for this antenna the co-polarisation. The cross polarisation is the polarisation of the wave which stands perpendicular on the required one. In this case, the cross polarisation is vertical oriented. If the cross polarisation level is high, energy is wasted and reducing the detection range. Also, any deviation from a horizontal polarisation, reduces the reflection of the target (drone propeller).

To prevent this, the antenna array is desired to satisfy a cross polarisation level of -25 dB, compared to the main beam, as defined in section 1.2.1. In figure 3.3, the realized gain of the example antenna is a bit over 7 dBi. Therefore, the cross polarisation level is limited to -18 dBi, ideally. But, -20 dB compared to the beam is also acceptable. In figure 3.4, the cross polarisation is plotted for the test model. It is discernible that the patch antenna has a high cross polarisation to the edges of the patch antenna, and therefore, the highest level is measured at an angle ϕ close to 45 or 135 degrees. The high cross polarisation level occur at these specific directions, as it is caused by the corners of the patch antenna.

In figure 3.5, the cross polarisation is displayed at $\phi = 135^\circ$. The cross polarisation, is below -18 dB for an angle θ from -41.0 till 52.4 degrees. Thus, the requirement is satisfied in the radiated direction. However, it should be noted that a high cross polarisation outside the scanning range, should be suf-

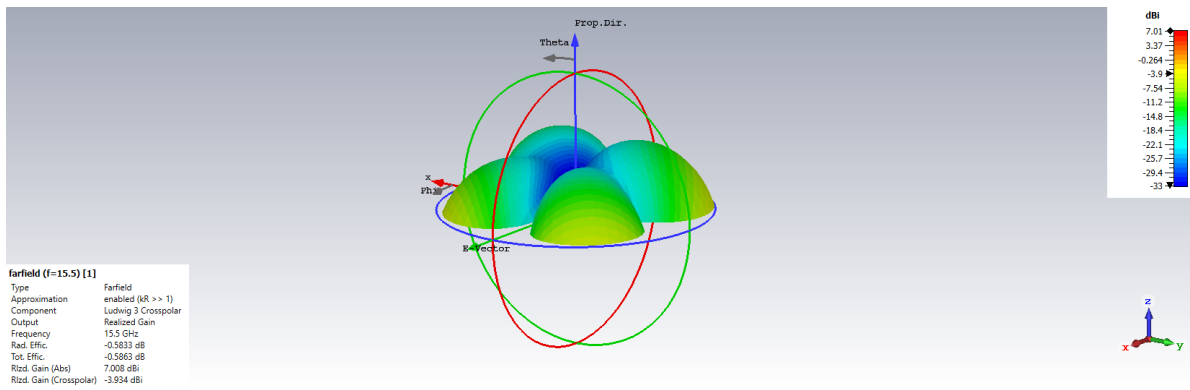


Figure 3.4: The cross polarisation level for the coaxial patch antenna model in 3D.

ficiently low, as this will increase side lobe level. The highest level of the cross polarisation is -3.934 dBi. This is in the direction of one of the corners from the origin. This level is -10.94 dB below the main beam, but much bigger than the desired -25 dBi. On the other hand, the cross polarisation level will decrease in a finite array. As the gain of the array will increase due to the array factor, while the cross polarisation level remains equal.

Finally, the cross polarisation level on one side is higher than the opposite side due to the location of the excitation of the patch. If the coaxial pin moves closer to the center of the patch, the radiated cross polarisation level will even out.

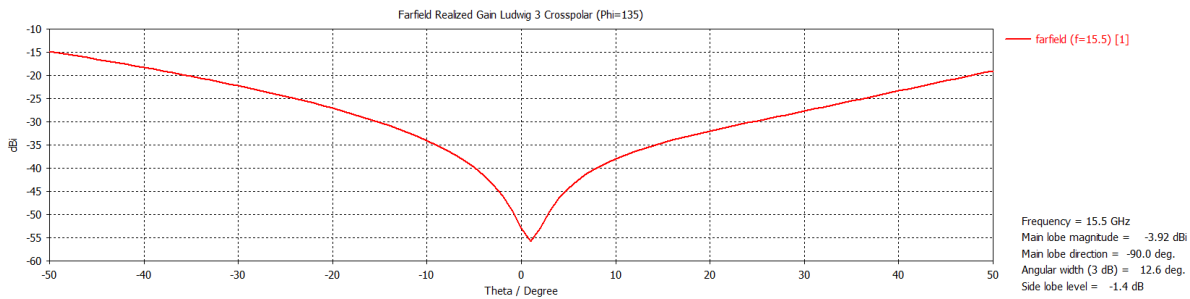


Figure 3.5: The cross polarisation level for the coaxial patch antenna model at $\phi = 135^\circ$.

In the comparison of the simulations probably no antennas will achieve the desire of -25 dB cross polarisation level in the full simulation range. On the other hand, the antenna might achieve this in the radiation direction, such as figure 3.5. Therefore, the comparison looks on irregularities in the cross polarised radiation pattern and if the antenna achieves a -25 dB cross polarisation level at $\phi = 135^\circ$ in the range of $\pm 20^\circ$. The cross polarisation outside the radiated range will be reviewed after a proper candidate is chosen.

3.1.5. Signal fidelity

As wideband antennas radiate over a large frequency band, it is important to know how the signal looks like over space, time and frequency [52]. A parameter that takes this into account is the signal fidelity. This is simulated in CST by using a farfield probe, which is located at a distance of 3λ at broadside. The simulation setup is shown in figure 3.6. Using this probe, it is measurable how the electric farfield behaves over frequency at a certain position. This can be done for horizontal, and vertical polarisation. But, as horizontal polarisation is of interest, as described in chapter 1.2.1. The horizontally polarised field probe is only analysed.

In figure 3.7, the probe values are displayed for the test coaxial patch antenna. The probe values are only shown for the frequencies which are in the region of interest, which are where the antenna radiates properly. The figure illustrates that the electric field in the region of the bandwidth at broadside is within 1 dB difference from each other.

As the requirement for the gain, losses over frequency should be minimized. In figure 3.7, the losses

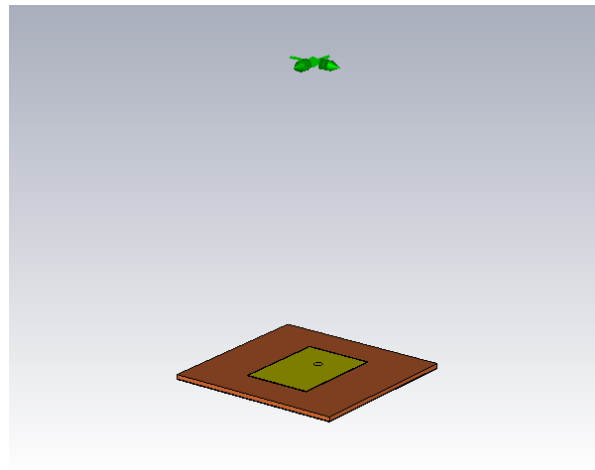


Figure 3.6: The simulation setup for the coaxial test patch antenna measured by a probe at a distance of 3λ .

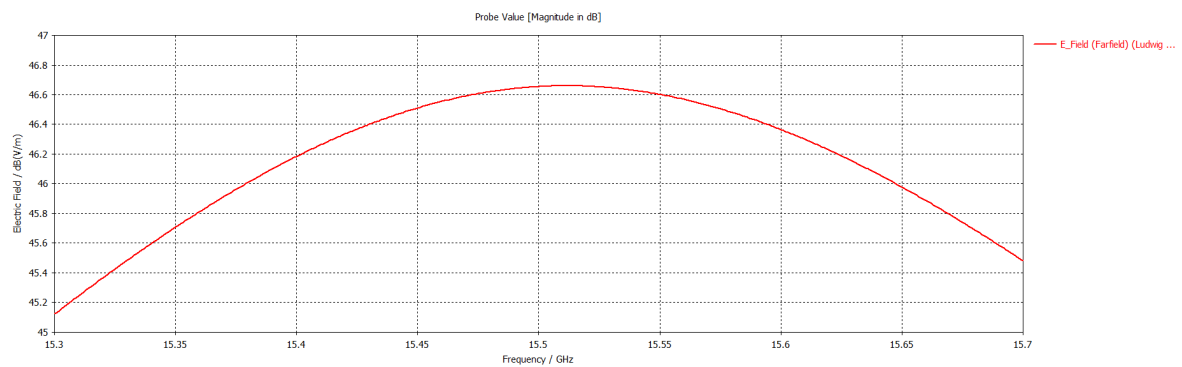


Figure 3.7: The probe value of the test model at a broadside distance 3λ with horizontal polarisation.

are minimal in the region of the bandwidth at broadside. But, if the antennas has a more wideband characteristic, the losses may diverge more. The antennas are compared on the maximum difference in their probes value in the entire frequency band of the impedance bandwidth.

3.1.6. Group delay

Phase non-linearities in communication systems are often undesired as they produce signal distortion. These phase non-linearities are measured in a 2-port system. As small phase ripples on the linearity of the phase can't be measured, the derivative of the phase response over frequency is taken. This is the group delay t_g and shown in equation 3.3 [53].

$$t_g = \frac{-1}{360} \frac{d\phi}{df} \quad (3.3)$$

where ϕ is the phase of $S_{2,1}$ in degrees and f is the frequency in Hz. Group delay is a useful measure to measure phase distortion, as the derivative produces a constant group delay which indicates the transit time t_0 , and a deviation from this average delay indicates distortion. Ideally, there is no distortion. But in reality, there is always a small distortion. This distortion has effect on the range resolution of the antenna. For example, if the group delay is 1 ns, the distortion on the range resolution is 15 cm. This is calculated as the distance travelled by an EM is the speed of light multiplied by the time travelled. For a radar, the wave has to travel forth and back. Thus, the distortion is 15 cm. Graphically, the phase response and group delay are shown in figure 3.8.

To measure this in CST, a 2-port system is created. This setup is shown in figure 3.9. One antenna radiates and the other one is mirrored at a distance of 10λ and receives. From this, the phase of the transmitted energy is simulated. This is plotted in figure 3.10. It is apparent that small phase ripples

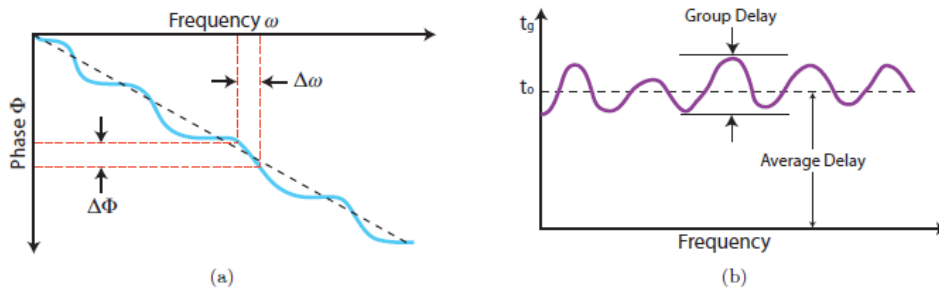


Figure 3.8: What is group delay? (a) Phase response S2,1, (b) Group delay [53]

are hard to determine. The group delay is calculated by CST using the group delay template in CST and is displayed in figure 3.11 over the entire frequency range of 15 till 16 GHz.

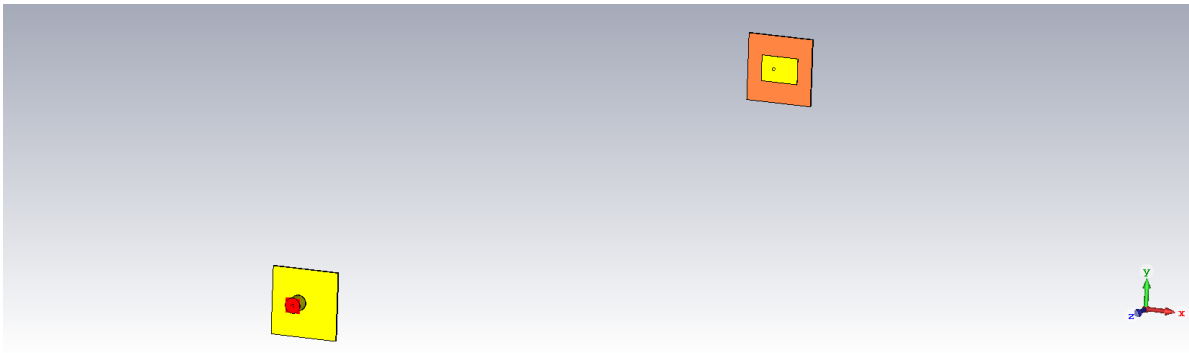


Figure 3.9: The simulation setup for the S2,1 parameters for the coaxial test patch antenna.

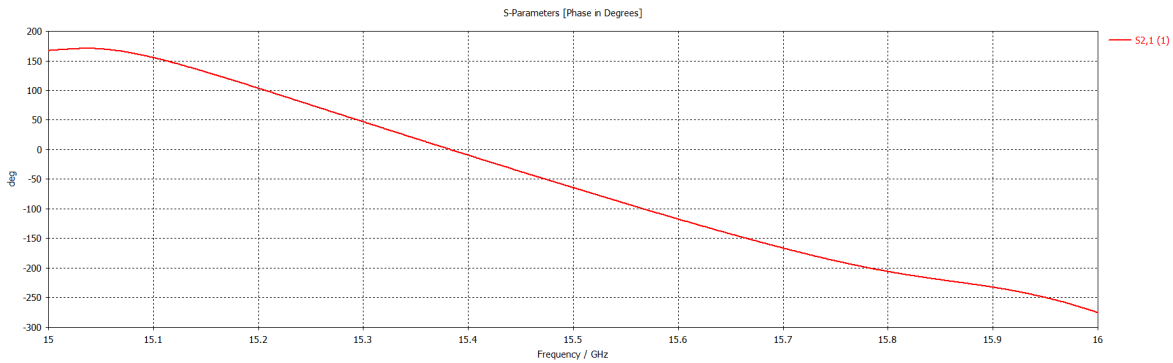


Figure 3.10: The S2,1 phase over frequency for the coaxial test patch antenna.

$$S_r = \frac{c}{2B} \tag{3.4}$$

Figure 3.11 is easier to interpret. The maximum deviation in the broadside impedance bandwidth is equal to 0.28 ns. If this value is acceptable depends on how large the range resolution S_r should be. The range resolution is given by equation 3.4 [3]. c corresponds with the speed of light and B is the bandwidth used in the transmit antenna. If the range resolution is 1 m, the group delay deviation would be insignificant. But, if the range resolution is 15 cm (this corresponds with a bandwidth sweep B of 1 GHz). Two close targets in range are harder to detect with certainty as 0.28 ns corresponds to 4.2 cm. For the comparison a range resolution of 0.5 m will be set. For simplicity, a maximal deviation of 15 cm will be allowed, so a 1 ns difference.

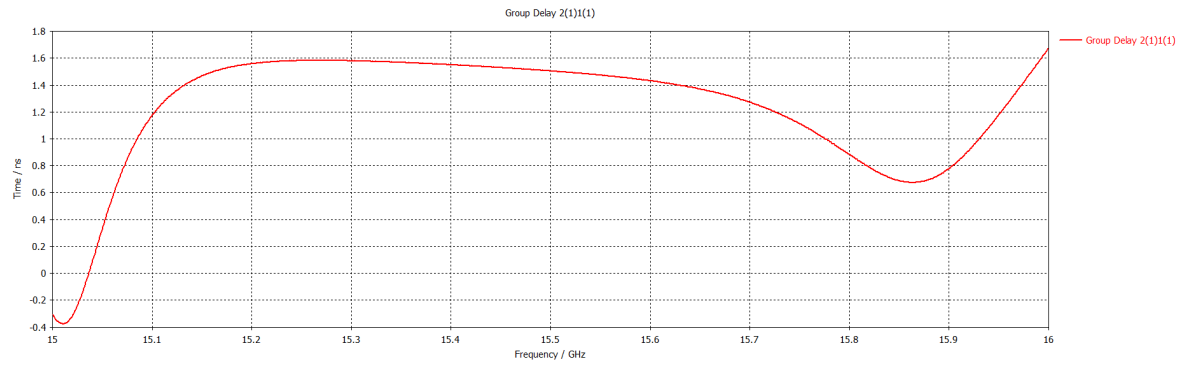


Figure 3.11: The group delay of the coaxial test patch antenna.

3.1.7. Manufacturability

The final property which is compared on is the manufacturability. As the antenna is designed for a radar system, it has to be manufacturable. Otherwise, an antenna can't be produced. The comparison of manufacturability takes every aspect of the design into account. For example if layers, have certain tolerances, or are have vias that can't be made.

As manufacturability is a concept which can't really be compared on hard numbers, such as the other properties. A scale of 5 values is introduced. Each design is discussed shortly, how complex the design is and rated on that scale. The lowest value is double negative – and is barely impossible to manufacture. The highest value is double positive ++ and can be manufactured with common methods. The scale is shown in table 3.3.

Table 3.3: The scale on which manufacturability is rated.

Lowest value				Highest Value
--	-	+/-	+	++

Ideally, the model gets a ++ on manufacturability, such as the test model. The model can be created out of a single substrate, where the patch is edged out of a copper layer. And using a via the pin is connected with a SMP connector. Both substrate thicknesses and printed geometries have tight tolerances.

3.2. Design considerations

In this section, the designs that are considered are discussed and analysed. The designs are attempts to create a new wideband patch antenna. Using the literature study on wideband patch antenna from chapter 1.3, it came forward that three techniques are interesting to have another look at: thick/multi-layer structures, stacked patches and wideband feeding techniques. From the literature study also came forward, that the requirements are difficult to achieve using a single technique, but are only achieved by a combination of them. Therefore, the following patch antenna designs are considered:

- Probe fed stacked patch antenna with a multi-layer substrate
- Proximity fed patch antenna with a multi-layer substrate
- Probe fed double stacked patch antenna with a multi-layer substrate
- Probe fed patch antenna within a multi-layer substrate

3.2.1. Probe fed stacked patch with multi-layer substrate

The first design combines two wideband approaches to widen the bandwidth: a multi-layer substrate, comparable to the model studied by Aslan & Yarovoy [6], is combined with a stacked patch.

The antenna has four substrates, which vary in dielectric permittivity. The bottom layer is Rogers TC600. This substrate has a dielectric permittivity of 6.15. Atop of this lies a Rogers RO3010™ substrate. The first antenna lies atop of this substrate. This antenna is excited by a probe through the bottom two substrates. The following layer of the patch antenna, is a foam layer ($\epsilon_r = 1.06$, $\tan \delta = 0.001$ [54]) of 1mm thick to fill the air cavity [54]. The foam layer has a tolerance in thickness of ± 0.2 mm. The top layer is a Rogers RO3010™ with the patch antenna etched on it. The dielectric properties of the substrates are summarized in table 3.4.

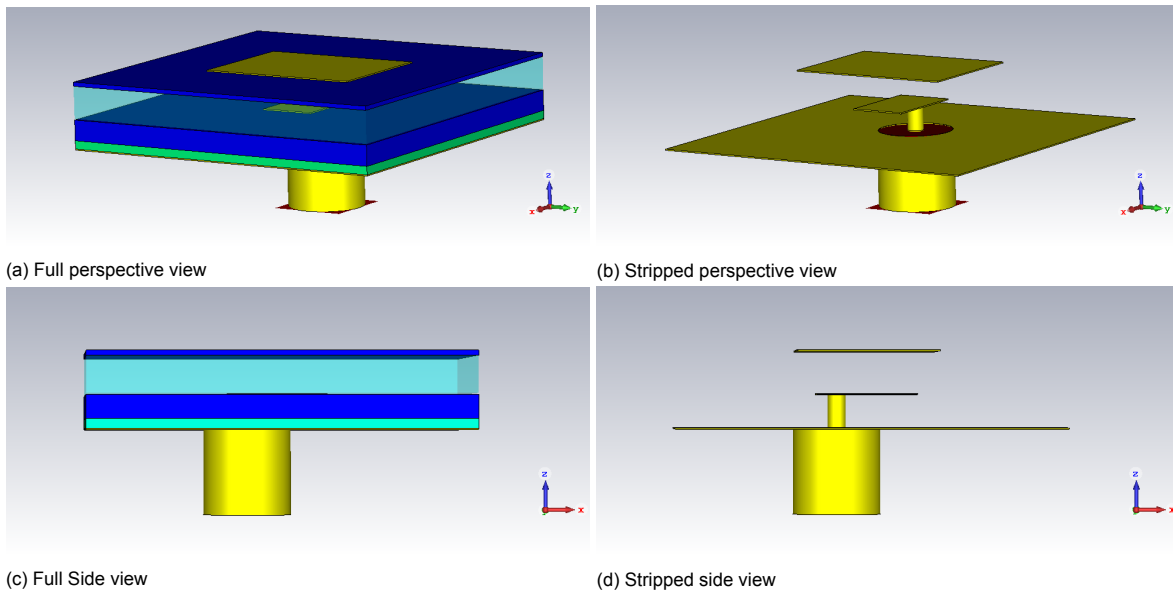


Figure 3.12: Model 1: Probe fed stacked patch in a multi-layer structure from different viewing points. A legend of the used materials as substrate layers is given in table 3.4. The dimensions of the antenna are given in table 3.5.

Graphically, the design is shown in figure 3.12. The top figures show the design from a perspective view, while the bottom figures show the design from the side. Both views show the design with and without the substrates. The parameter values can be found in table 3.5.

Table 3.4: Materials and properties of the substrate layers of the multi-layer substrate described in chapter 3.2.1 [45, 54]. Layer 1 is the bottom layer and layer 4 is the top layer.

Layer	Material	Dielectric permittivity ϵ_r	Loss tangent $\tan \delta$
1	Rogers TC600	6.15	0.0020
2	Rogers RO3010™	10.2	0.0022
3	Foam	1.06	0.0001
4	Rogers RO3010™	10.2	0.0022

Table 3.5: The parameters from the probe fed stacked patch in a multi-layer structure.

Parameter	Value	Parameter	Value
Length ground plane	10.37 mm	Length bottom patch antenna	2.7 mm
Width ground plane	10.37 mm	Width bottom patch antenna	1.7 mm
Height substrate 1	0.254 mm	Length top patch antenna	3.8 mm
Height substrate 2	0.635 mm	Width top patch antenna	5 mm
Height substrate 3	1.0 mm	Radius pin	0.25 mm
Height substrate 4	0.127 mm	Radius isolation pin	1.15 mm
Shift pin from bottom patch edge	0.55 mm	Shift bottom patch on top patch edge	0.55 mm

The return loss of this design is displayed in figure 3.13. The red line represents the return loss at broadside, and the green and blue lines represent the return loss of the antenna while scanning to 30° in azimuth and 15° in elevation, respectively. The antenna has a large bandwidth of 2.61 GHz at with a center frequency of 15.17 GHz. When the antenna scans to 30 degrees in the azimuth plane, the center frequency shifts to 14.67 GHz. Also, the bandwidth decreases a little to 2.09 GHz. The center frequency and bandwidth while scanning to 15 degrees in elevation is comparable to these at broadside. The frequency range of 15.4-15.7 GHz lie in all the impedance bandwidths.

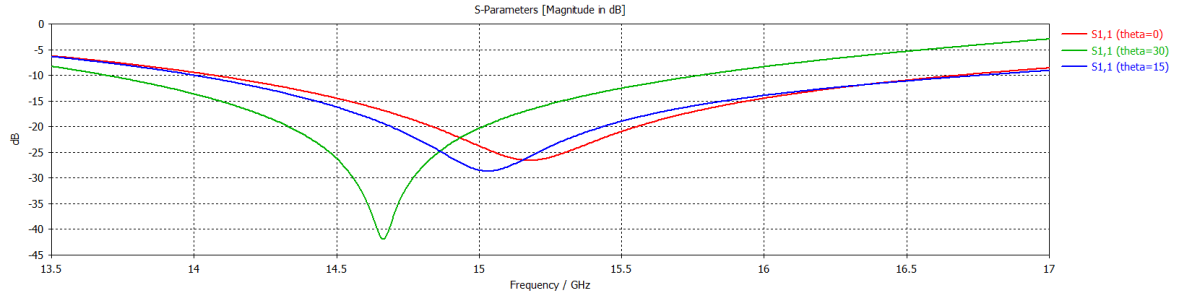
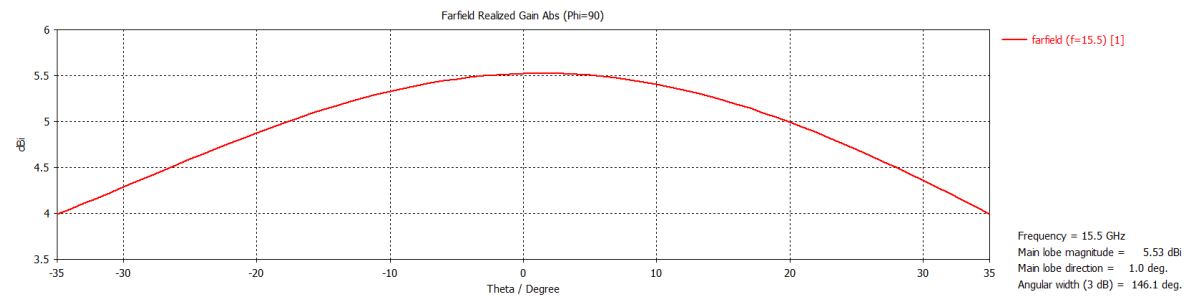
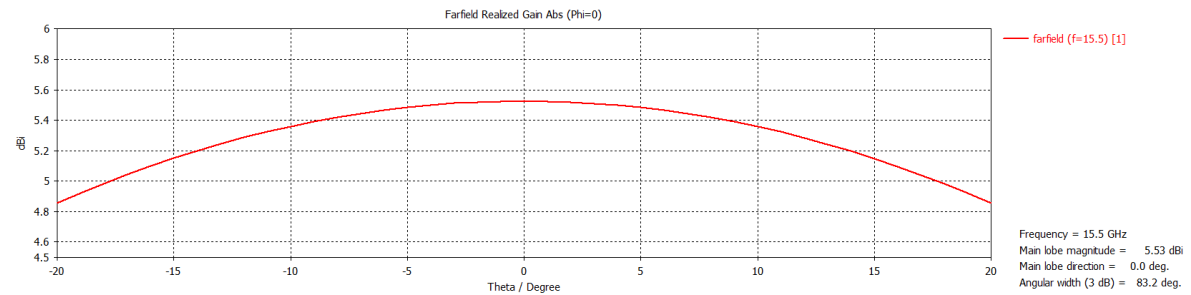


Figure 3.13: The return loss for the probe fed stacked patch in a multi-layer structure. The red line represents the return loss at broadside, the green line at a scanning angle of 30° in azimuth and blue line at a scanning angle of 15° in elevation.

The radiation patterns of the stacked patch antenna are displayed in figure 3.14. The realized gain at $\phi = 90^\circ$ is shown in figure 3.14a. The 1 dB angular width in the azimuth plane is not reached, as the antenna scans from -25.03 till 27.38 degrees. In the elevation plane the antenna reaches to comparable angles, namely -24.33 till 24.28 . This is shown in figure 3.14b and satisfies the requirement.



(a) $\phi = 90^\circ$, azimuth plane



(b) $\phi = 0^\circ$, elevation plane

Figure 3.14: The radiation pattern of the probe fed stacked patch in a multi-layer structure at different angles of ϕ .

The cross polarisation level of the farfield is displayed in figure 3.15. Like the coaxial test antenna, the cross polarisation level has the highest value at all the corners of the patch antenna. This is shown in 3D view in figure 3.15a. Nevertheless, within the required scanning range of the antenna, the cross polarisation level is almost everywhere -25 dB. The highest level of the cross polarisation occurs at $\phi = 135^\circ$. The cut is shown in figure 3.15b. The cross polarisation is below the required -25 dB, while scanning towards a positive angle. But, while scanning to a negative angle of θ , that level is not reached. The cross polarisation level of -25 dB is achieved from an angle of theta from -19.0 till 34.10

degrees. The increasing cross polarisation level in the negative θ direction is due to the coaxial pin, that feeds the lower patch. The pin is much closer to that side of the lower patch, and therefore, the electric field as well as the cross polarisation in those corners is larger than the corners on the other side of the patch antenna.

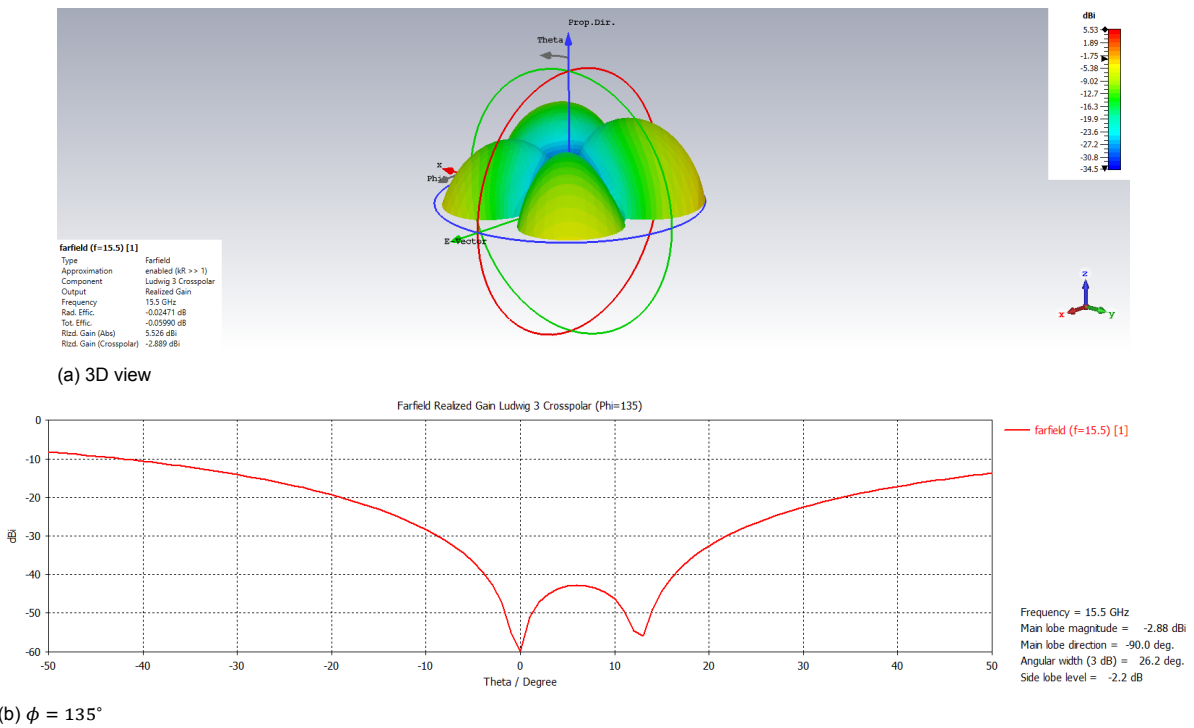


Figure 3.15: The cross polarisation of the radiation pattern of the probe fed stacked patch antenna in a multi-layer structure.

Furthermore, the design is simulated with a farfield probe on broadside. The electric field measured by the probe is displayed in figure 3.16. There is no random distortion within the design. Within the range of the impedance bandwidth at broadside (14.07-16.68 GHz), the electric field differs 1.47 dBV/m. The difference in probe value is even smaller, if there is only looked at the section 15-16.5 GHz. The difference equals then 0.46 dBV/m.

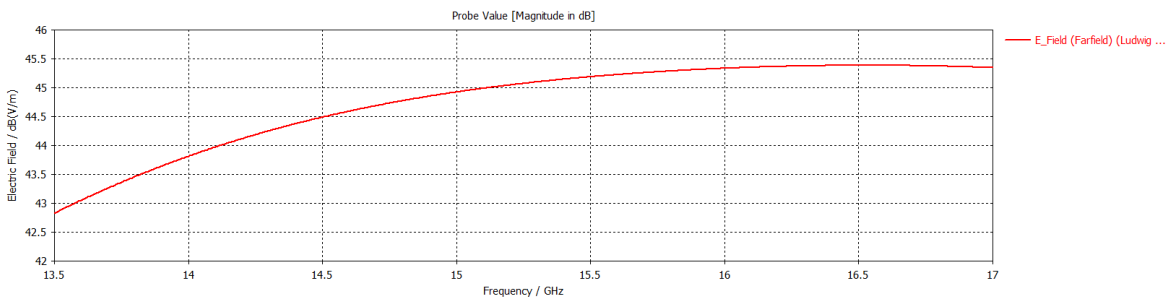


Figure 3.16: The electric field radiated by the probe fed stacked patch antenna in a multi-layer structure measured by a farfield probe at distance 3λ from the antenna.

Subsequently, the group delay is plotted in figure 3.17. Over the entire frequency range from 14.07 till 16.68 the minimum and maximum transit time is 0.769 and 0.867 ns, respectively. This is a maximum deviation of 0.098 ns, and thus, 10 times a small as required.

Finally, the antenna is good to manufacture, but has three drawbacks. The tolerance of the third substrate is 20%. Therefore, the height of the substrate is between 0.8 and 1.2 mm, which is a large deviation. The effects this tolerance have been simulated (and not shown) and are for now neglected. The second downside is that the bottom two substrates need to be glued together and the effect of the glue on the dielectric permittivity and the coupling between the substrates is unknown. The third

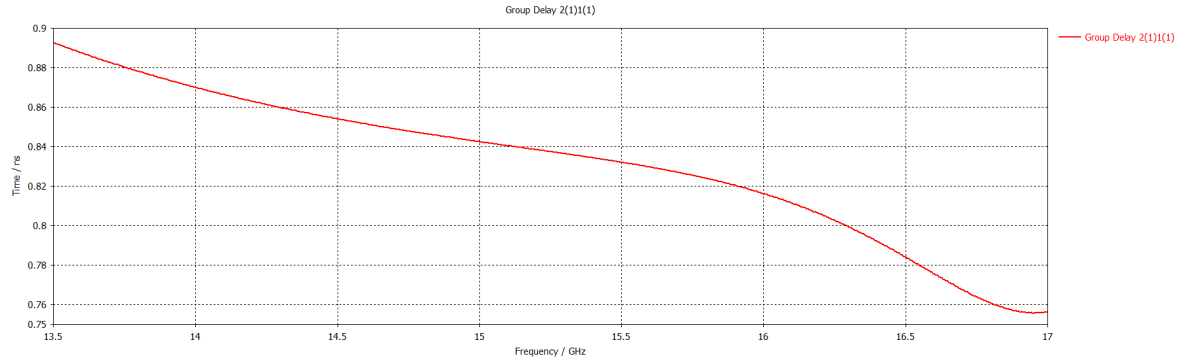


Figure 3.17: The group delay over frequency of the probe fed stacked patch antenna in a multi-layer substrate.

disadvantage is that the top and bottom antennas are up to 0.5 mm displaced from each other. This is as both substrates with the printed antennas are manufactured separately; during assembly, a displacement might occur. Nonetheless, the antenna is still manufacturable, and therefore, this model gets an +/- on manufacturability.

Overall, the design of the probe fed stacked patch antenna satisfies most of the specified requirements. A summary of all the properties for this model is given in table 3.6. It has a large bandwidth of over 2.0 GHz while scanning and at broadside. The scanning angles fall within the -1 dB angular width of the radiation pattern in the elevation plane, and come close in azimuth. Furthermore, the level of signal distortion is satisfactory as well and the group delay is very small. The cross polarisation is only on one side of the patch antenna quite high.

Table 3.6: The summarized properties for the stacked patch in a multi-layer structure model.

Parameter	Value
Center frequency broadside	15.17 GHz
Impedance bandwidth broadside	14.07 - 16.68 = 2.61 GHz
Center frequency 30° azimuth	14.67 GHz
Impedance bandwidth 30° azimuth	13.69 - 15.78 = 2.09 GHz
Center frequency 15° elevation	15.03 GHz
Impedance bandwidth 15° elevation	14.00 - 16.76 = 2.67 GHz
Realized gain	5.53 dBi
1 dB angular width azimuth	-25.03° - 27.38°
1 dB angular width elevation	-24.33° - 24.28°
Cross polarisation level	-8.419 dB
Cross polarisation level ang. width -20 dB	-19.0° - 34.10°
Signal fidelity	1.46 dBV/m
Group delay	0.098 ns
Manufacturability	+/-

3.2.2. Proximity fed patch with a multi-layer substrate

The second design is similar to the antenna design of section 3.2.1. However, the lower radiating patch antenna is comparable to the 'lamppost' feeding strip [33]. The feeding strip is used as a proximity feeding to excite the patch on the top layer. The materials of the multi-layer structure are shown in table 3.7. The first 2 layers have high dielectric permittivities of 6.15 and 10.2. Through these layers the feeding strip is excited with a coaxial pin. Atop lies a foam layer, followed by a layer of RT/Duroid 5880 with the radiating patch antenna on the top layer.

The layout is displayed in figure 3.18. In figure 3.18a and 3.18b, the perspective view of the antenna is shown, and in figure 3.18c and 3.18d the side view. Both views are shown with and without the dielectric substrate layers. The dimensions of this design are given in table 3.8.

The return loss is displayed in figure 3.19. The center frequency is 14.97 GHz at broadside. The impedance bandwidth ranges from 12.97 till 16.71 GHz, and equals 3.74 GHz. When the antenna

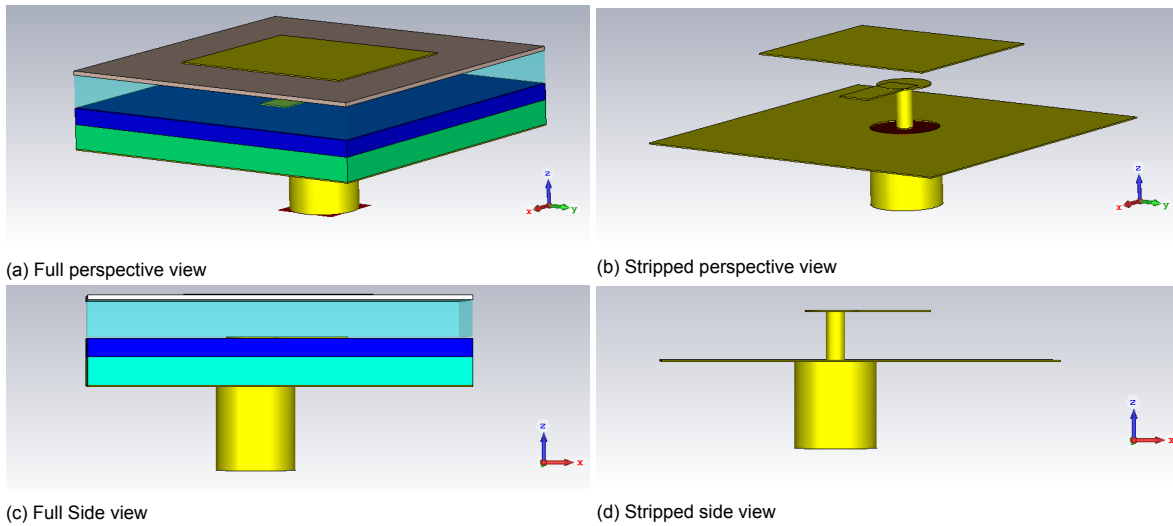


Figure 3.18: Model 2: A proximity fed patch in a multi-layer structure from different viewing points. A legend of the used materials as substrate layers is given in table 3.7. The dimensions of the antenna are given in table 3.8.

Table 3.7: Materials and properties of the substrate layers of the multi-layer substrate described in chapter 3.2.2 [45, 54]. Layer 1 is the bottom layer and layer 4 is the top layer.

Layer	Material	Dielectric permittivity ϵ_r	Loss tangent $\tan \delta$
1	Rogers TC600	6.15	0.0020
2	Rogers RO3010 TM	10.2	0.0022
3	Foam	1.06	0.0001
4	Rogers RT/Duroid5880	2.2	0.0009

Table 3.8: The parameters from the proximity fed patch in a multi-layer structure.

Parameter	Value	Parameter	Value
Length ground plane	10.37 mm	Length feeding strip	2.5 mm
Width ground plane	10.37 mm	Width feeding strip	1.02 mm
Height substrate 1	0.762 mm	Length patch antenna	5.12 mm
Height substrate 2	0.508 mm	Width patch antenna	6.02 mm
Height substrate 3	1.0 mm	Radius pin	0.25 mm
Height substrate 4	0.127 mm	Radius isolation pin	1.05 mm
Radius matching ring	0.81 mm	Shift strip on patch edge	2.0 mm

scans to 30° in the azimuth plane, the center frequency decreases to 14.26 GHz and the impedance bandwidth is 2.95 GHz, namely, from 12.48 till 15.43 GHz. While scanning to 15° in elevation plane, the center frequency is more or less equal to that at broadside. However, the impedance bandwidth increases with another gigahertz to 4.70 GHz due to another small resonance at 17.2 GHz.

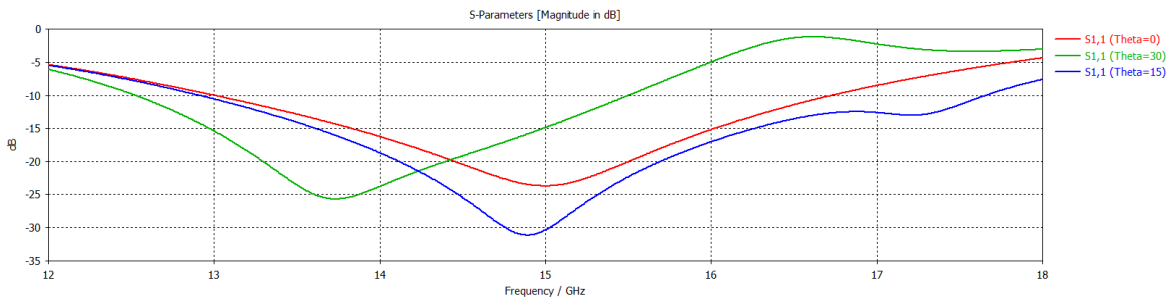
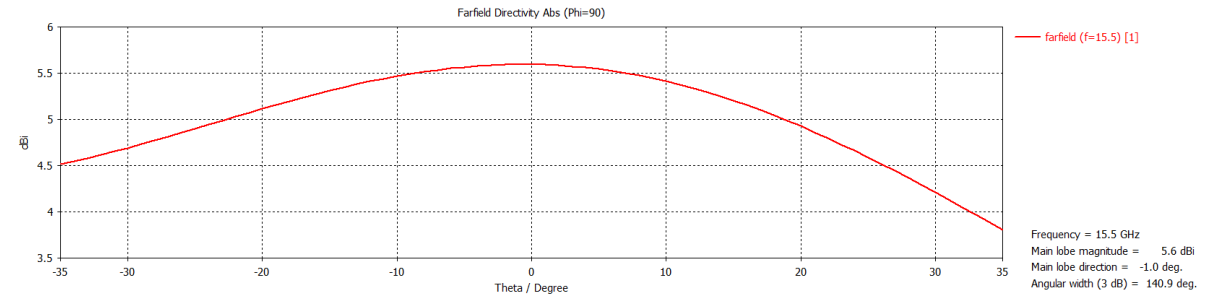
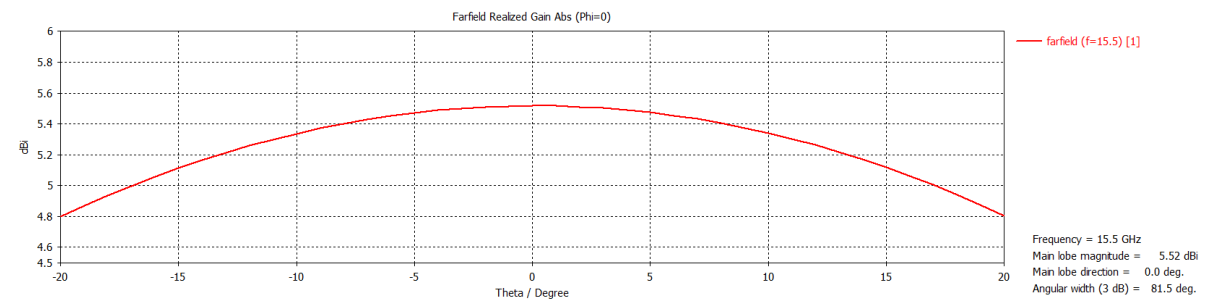


Figure 3.19: The return loss for the proximity fed patch in a multi-layer structure. The red line represent the return loss at broadside, the green line at a scanning angle of 30° in azimuth and the blue line at 15° in elevation.

The radiation patterns in the azimuth and elevation plane for the proximity fed patch antenna are plotted in figure 3.20. The antenna has a realized gain of 5.57 dB, and the 1 dB angular width at a 15 degrees scanning angle is only achieved, namely from -23.55 till 23.55 degrees. In figure 3.20a, the 1 dB angular width in azimuth ranges from -31.64 till 25.08 degrees. Thus, in the azimuth plane the requirement is achieved on one side.

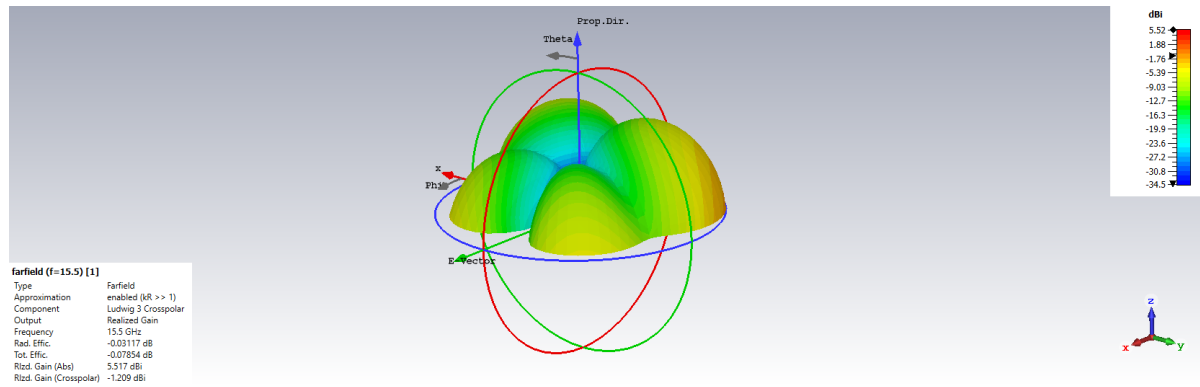


(a) $\phi = 90^\circ$, azimuth plane

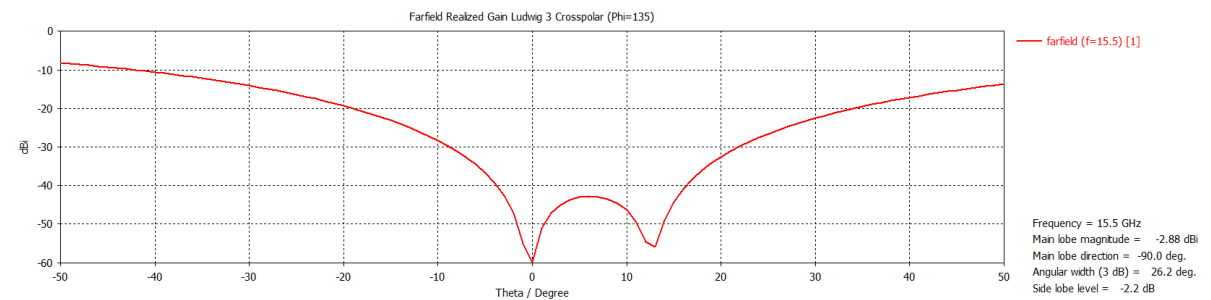


(b) $\phi = 0^\circ$, elevation plane

Figure 3.20: The radiation pattern of the proximity fed patch in a multi-layer structure at different angles of ϕ .



(a) 3D view



(b) $\phi = 135^\circ$

Figure 3.21: The cross polarisation of the radiation pattern of the proximity fed patch in a multi-layer structure.

The cross polarisation of the farfield is plotted in figure 3.21. In one direction the antenna radiates perfectly below 25 dB cross polarisation. However, towards the negative direction a -25 dB level is reached at -15.13 degrees. This is verified at an angle of $\phi = 135^\circ$. The high cross polarisation level to this side of the antenna is due to the excitement of the feeding strip. As the strip is fed via a coaxial pin on 1 side, that side radiates more cross polarisation. The highest cross polarisation level that is measured is -6.742 dB.

The signal distortion is plotted in figure 3.22. As the previous design from section 3.2.1, there is no random signal distortion and the antenna radiates the most, where the return loss is smallest. Within the impedance bandwidth, the electric field strength lies within the range of 43.08 - 45.33 dBV/m. That is a difference of 2.25 dBV/m. This is due to gain loss at the lower frequencies, where the antenna has a directivity of 5+ dBi at 14.5 and 15.5 GHz, at 12 GHz this is 3.5 dBi. However, from 14 till 16.7 GHz, the difference in probe value is just more than 1 dBV/m.

The group delay is plotted in figure 3.23. From 12.97 till 16.71 GHz the average transit is 0.836 ns and deviates 0.0045 ns to both sides. The group delay is thus 0.009 ns. This is over a 100 times smaller than required.

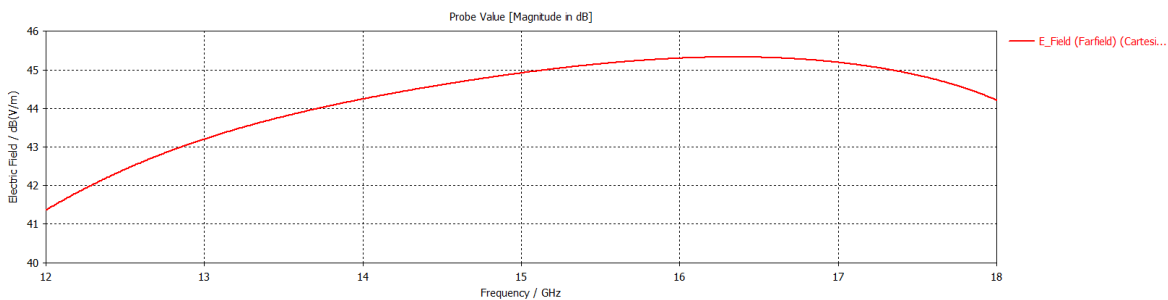


Figure 3.22: The signal fidelity at a distance of 3λ at broadside of the proximity fed patch in a multi-layer structure.

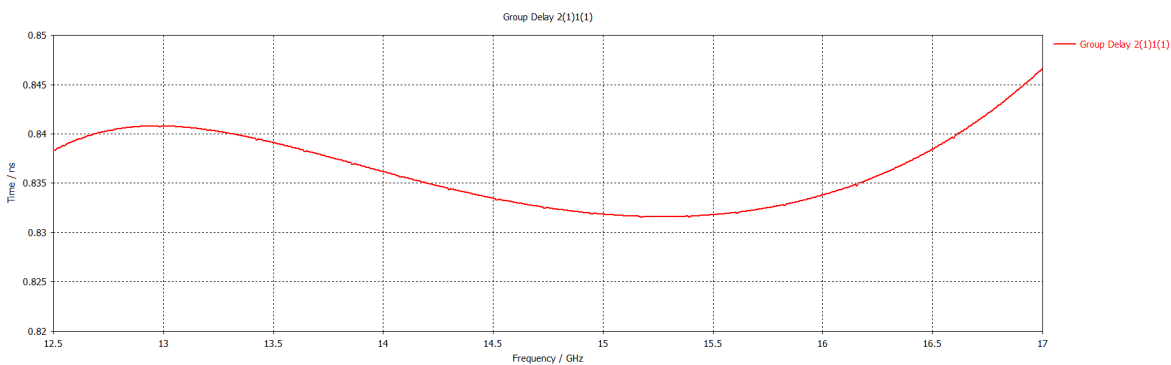


Figure 3.23: The group delay of the proximity fed patch in a multi-layer structure.

Finally, the antenna is quite good to manufacture, but has the same drawbacks as the design of chapter 3.2.1. Therefore, this model gets an +/- on manufacturability, as well.

All in all, the proximity fed patch antenna satisfies most of the specified requirements. All its properties are summarized in table 3.9. The center frequencies are for all three simulations lower than required, but the frequency of 15.4 GHz is in all of the impedance bandwidths. Each impedance bandwidth is almost 3 GHz in all simulations. The scanning angles are within the -1 dB angular width of the radiation pattern in the elevation plane, and on one side in azimuth. Furthermore, the difference in signal fidelity is quite large, but from 14 till 16.7 GHz it is acceptable. The cross polarisation radiation pattern is only too high in the negative x-direction. This is, however, achieved if the limit is -20 dB.

Table 3.9: The summarized properties for the proximity fed patch in a multi-layer structure model.

Parameter	Value
Center frequency broadside	14.97 GHz
Impedance bandwidth broadside	12.97 - 16.71 = 3.74 GHz
Center frequency 30° azimuth	14.26 GHz
Impedance bandwidth 30° azimuth	12.48 - 15.43 = 2.95 GHz
Center frequency 15° elevation	14.89 GHz
Impedance bandwidth 15° elevation	12.91 - 17.66 = 4.75 GHz
Realized gain	5.57 dBi
1 dB angular width azimuth	-31.64° - 25.08°
1 dB angular width elevation	-23.55° - 23.55°
Cross polarisation level	-6.742 dB
Cross polarisation level ang. width -20 dB	-15.13° - 32.51°
Signal fidelity	2.25 dBV/m
Group delay	0.009 ns
Manufacturability	+/-

3.2.3. Probe fed double stacked patch in a multi-layer substrate

The third design has the same setup as the first design except for a few changes. While the first design has one patch on the substrate, and this design has a patch antenna on both sides of the top substrate. This is to create an extra resonance. The used substrate layers are shown in table 3.10. As the antenna was not radiating properly with the existing Rogers Corporation substrates due to their exact thickness and permittivities [45], the antenna is optimized till it had the widest achievable bandwidth. Therefore, the 4th layer substrate is simulated as a optimizable thickness and permittivity, and a substrate with thickness of 0.489 mm and a dielectric permittivity of 5.58 was designed.

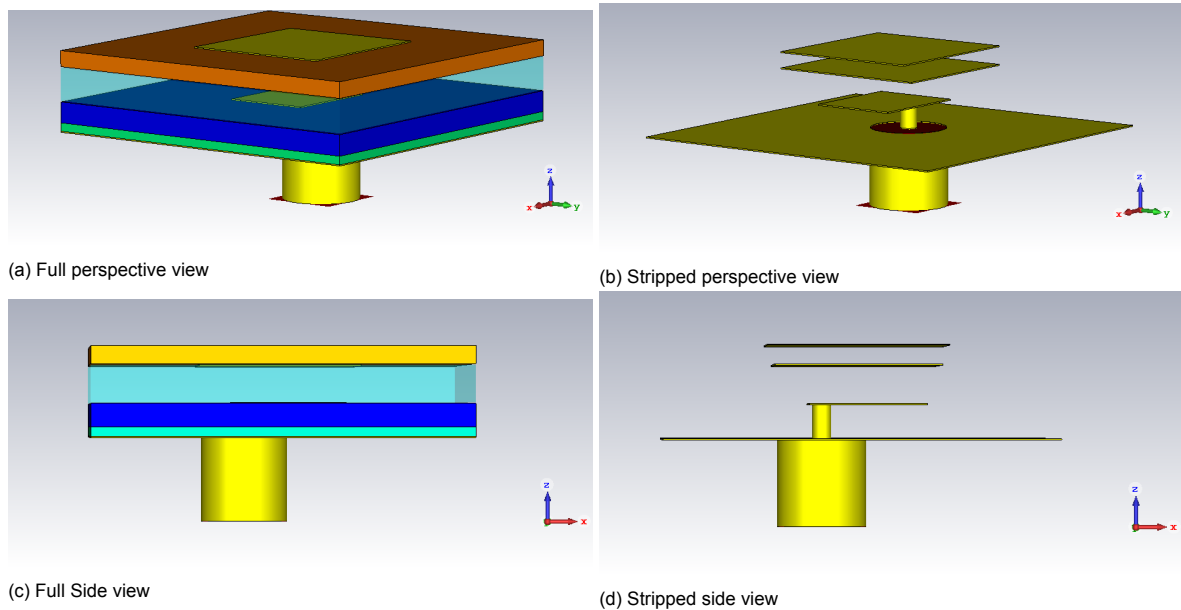


Figure 3.24: Model 3: Probe fed double stacked patch in a multi-layer structure from different viewing points. A legend of the used materials as substrate layers is given in table 3.10. The dimensions of the antenna are given in table 3.11.

The layout of the design is displayed in figure 3.24. Both perspective and side view are shown, as well as the view with and without substrates. Figure 3.24d illustrates that the patch antennas on the top layer are quite close to each other due to the thin substrate of 0.489 mm. The exact dimensions of the model are given in table 3.11. The second patch antenna on the top substrates is a bit larger in length, but a bit smaller in width.

Table 3.10: Materials and properties of the substrate layers of the multi-layer substrate described in chapter 3.2.3 [45, 54]. Layer 1 is the bottom layer and layer 4 is the top layer.

Layer	Material	Dielectric permittivity ϵ_r	Loss tangent $\tan \delta$
1	Rogers TC600	6.15	0.0020
2	Rogers RO3010™	10.2	0.0022
3	Foam	1.06	0.0001
4	Test Material	5.57	n.a.

Table 3.11: The parameters from the proximity fed patch in a multi-layer structure.

Parameter	Value	Parameter	Value
Length ground plane	10.37 mm	Length feeding patch	3.13 mm
Width ground plane	10.37 mm	Width feeding patch	2.59 mm
Height substrate 1	0.254 mm	Length Patch antenna bottom	4.42 mm
Height substrate 2	0.635 mm	Width patch antenna bottom	4.82 mm
Height substrate 3	1.0 mm	Length patch antenna top	4.81 mm
Height substrate 4	0.489 mm	Width patch antenna top	4.53 mm
Radius pin	0.25 mm	Radius Isolation pin	1.15 mm
Shift feeding on bottom patch edge	0.939 mm	Shift pin on feeding patch edge	0.655 mm

The return loss of this model is shown in figure 3.25. The figures illustrates that the antenna still has one resonance, this is probably due to the top patches which are too close to each other. Therefore, there is one strong resonance. The center frequency is at 15.44 GHz, with an impedance bandwidth from 14.43 till 16.32 GHz. At a 30 degree scanning angle in azimuth, the impedance bandwidth ranges from 14.51 till 15.47 GHz, and is almost 1 GHz wide. At 15 degrees in elevation, the resonance frequency is 15.60 GHz with an impedance bandwidth more or less equal to the bandwidth at broadside.

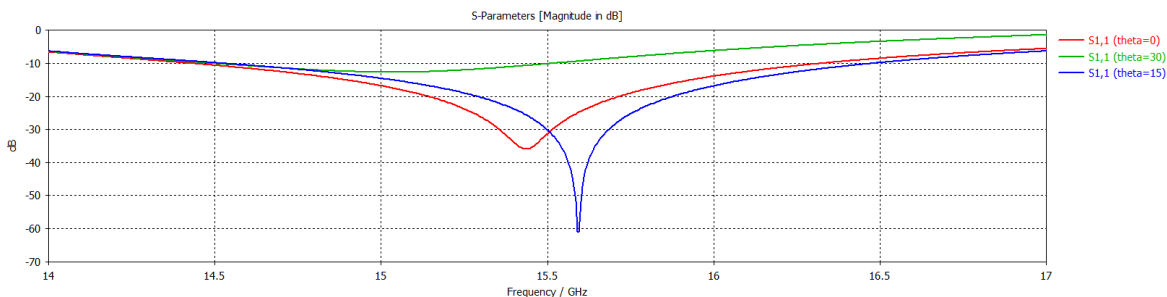
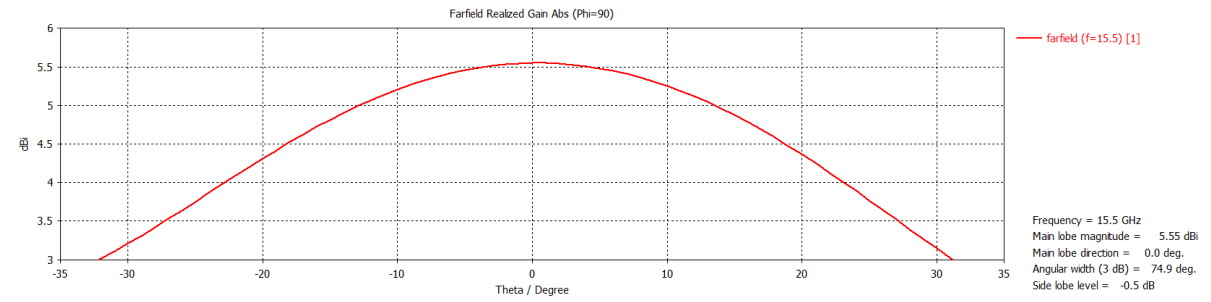


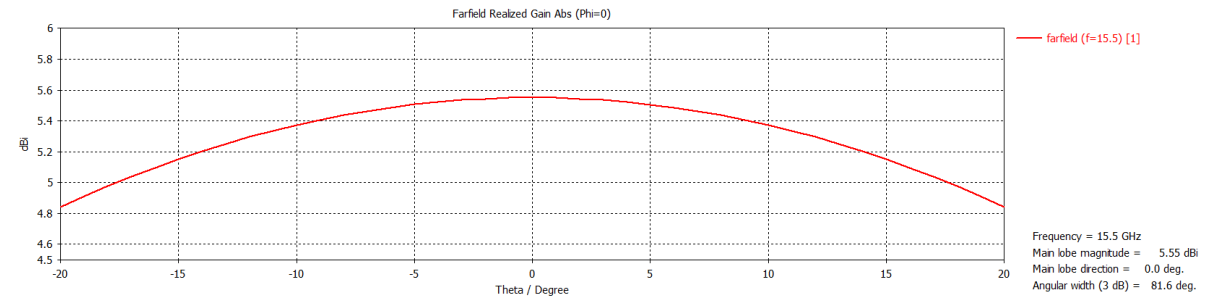
Figure 3.25: The return loss of the double stacked patch antenna in a multi-layer structure. The red line represent the return loss at broadside, the green line at a scanning angle of 30° in azimuth and the blue line at a scanning angle of 15° in elevation line.

The radiation pattern of the double stacked patch antenna is shown in figure 3.26. The realized gain is 5.58 dB at a center frequency of 15.5 GHz. The 1 dB angular width ranges from -17.73° - 18.27° in the azimuth plane, shown in figure 3.26a. In the elevation plane, the angular width reaches an angular width of -23.68 till 23.71 degrees. This is shown in figure 3.26b. Both 1 dB angular widths are small. Probably due to the second patch, influencing the radiation pattern of the lower parasitic patch, too much.

The cross polarisation level of the radiation pattern for this model is shown in figure 3.27. Again, cross polarisation level is the highest at the edges of the antenna, as shown in figure 3.27a. On the other hand, the cross polarisation is in all 4 directions quite comparable. The -25 dB cross polarisation level is satisfied for an angle θ from -14.33 till 22.97 degrees at an angle $\phi = 135^\circ$. This is shown in figure 3.27b. The highest realized gain of the cross polar radiation is -6.408 dB.

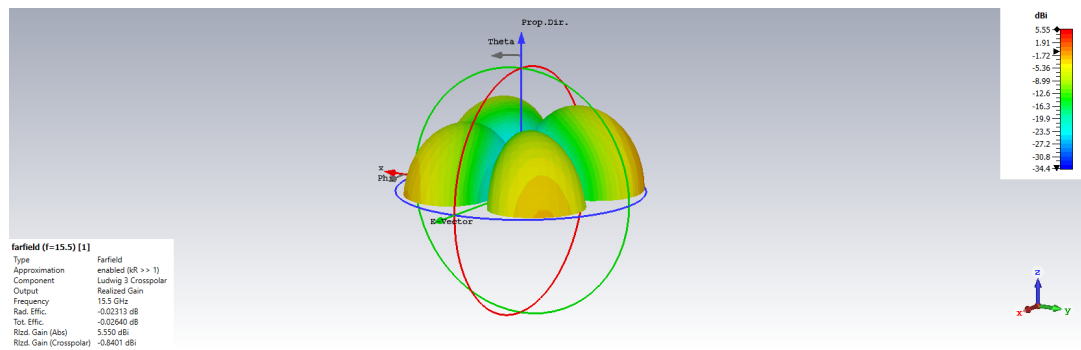


(a) $\phi = 90^\circ$, azimuth plane

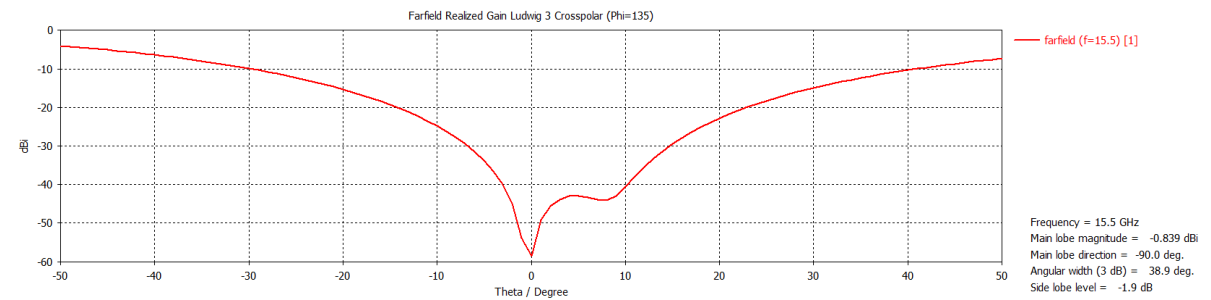


(b) $\phi = 0^\circ$, elevation plane

Figure 3.26: The radiation pattern of the double stacked patch in a multi-layer structure at different angles of ϕ .



(a) 3D view



(b) $\phi = 135^\circ$

Figure 3.27: The cross polarisation of the radiation pattern of the probe fed double stacked patch in a multi-layer structure.

The electric field measured by the far field probe is displayed in figure 3.28. The electric field ranges from 44.07 till 45.10 dBV/m in the region of the impedance bandwidth. This is a difference of 1.03 dBV/m.

The group delay of the design is shown in figure 3.29. The maximum group delay is 0.061 ns, which is quite small. However, there are lots of variations over this frequency band. This means that the effect range resolution will also deviate a lot and will not be stable.

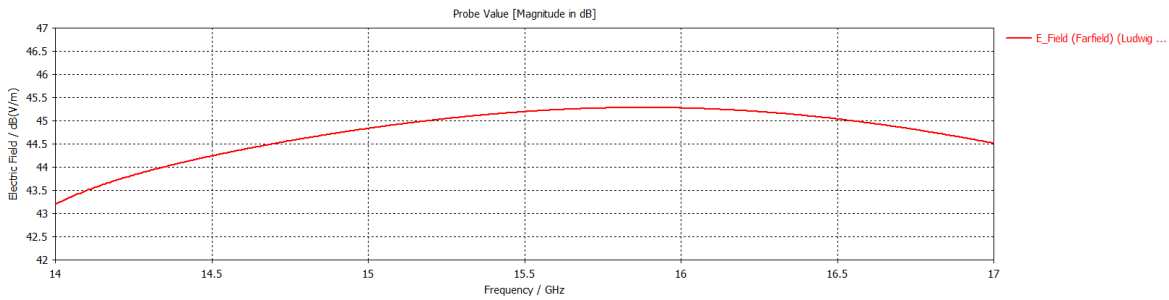


Figure 3.28: The signal fidelity at a distance of 3λ at broadside of the double stacked patch in a multi-layer structure.

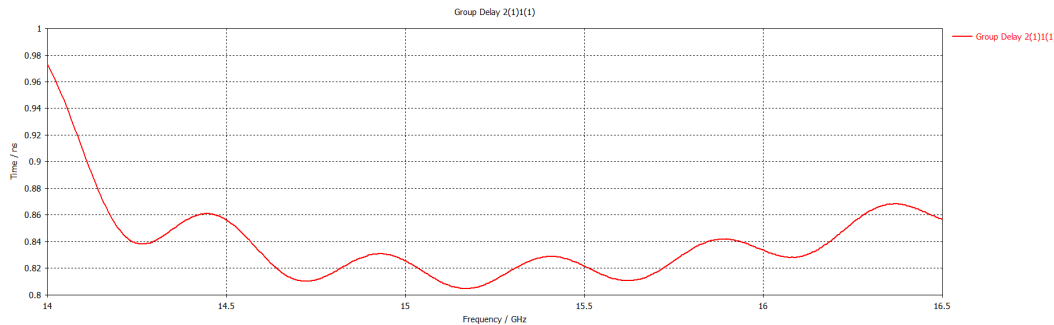


Figure 3.29: The group delay of the double stacked patch antenna in a multi-layer structure.

This model has the same disadvantages regarding manufacturability as the model from chapters 3.2.1 and 3.2.2. However, this model also has a top substrate with an non-existing thickness and dielectric permittivity, and therefore, this model gets also – on manufacturability. As this model is not manufacturable.

Table 3.12: The summarized properties for the double stacked patch in a multi-layer structure model.

Parameter	Value
Center frequency broadside	15.44 GHz
Impedance bandwidth broadside	14.43 - 16.32 = 1.89 GHz
Center frequency 30° azimuth	15.02 GHz
Impedance bandwidth 30° azimuth	14.51 - 15.49 = 0.98 GHz
Center frequency 15° elevation	15.60 GHz
Impedance bandwidth 15° elevation	14.52 - 16.48 = 1.96 GHz
Realized gain	5.58 dBi
1 dB angular width azimuth	-17.73° - 18.27°
1 dB angular width elevation	-23.68° - 23.71°
Cross polarisation level	-6.408 dB
Cross polarisation level ang. width -20 dB	-14.33° - 22.97°
Signal fidelity	1.03 dBV/m
Group delay	0.061 ns
Manufacturability	+/-

To summarize, the double stacked patch satisfies some requirements, but not the most important ones. The properties of this design are summarized in table 3.12. The impedance bandwidth at broadside and 15 degrees elevation satisfy the 1 GHz requirement, but in azimuth this isn't satisfied. Regarding scanning capabilities in azimuth, this model under performs and just reaches half of the required 1 dB angular width. The cross polarisation level is also too high in the radiation pattern. The antenna is also not manufacturable. In the end, the antenna performs well on signal fidelity, but this does not outweigh the disadvantages regarding the radiation pattern, impedance bandwidth and manufacturability

3.2.4. Probe fed patch in a multi-layer substrate

The fourth design uses a comparable design of a multi-layer substrate. The four different substrate layers are shown in table 3.13. In this design, there is only a radiating patch on substrate layer 2. I.e., the patch antenna has a 2-layer substrate, with a 2-layer superstrate.

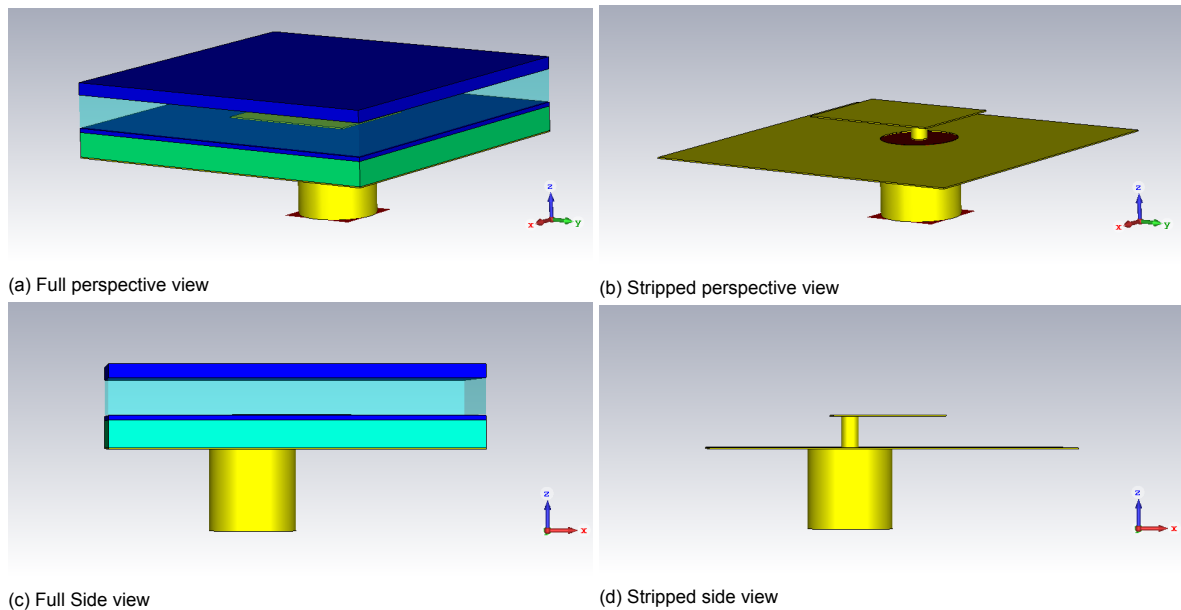


Figure 3.30: Model 4: Probe fed patch antenna within a multi-layer structure from different viewing points. A legend of the used materials as substrate layers is given in table 3.13. The dimensions of the antenna are given in table 3.14.

Graphically, this is shown in figure 3.30. The superstrate is matched to the antenna. This design might show any irregularities, what influence the stacked patches from chapter 3.2.1 and 3.2.3 as well. The materials used as sub- and superstrates are found in table 3.13. Furthermore, the exact thicknesses and other values for the parameters can be found in table 3.14. The antenna's size 3.21 by 4.19 mm, which is small. However, the theory from chapter 2.3 explained that as substrates have a high permittivity and are together quite thick, the element size decreases.

Table 3.13: Materials and properties of the substrate layers of the multi-layer substrate described in chapter 3.2.4 [45, 54]. Layer 1 is the bottom layer and layer 4 is the top layer.

Layer	Material	Dielectric permittivity ϵ_r	Loss tangent $\tan \delta$
1	Rogers TC600	6.15	0.0020
2	Rogers RO3010 TM	10.2	0.0022
3	Foam	1.06	0.0001
4	Rogers RO3010 TM	10.2	0.0022

Table 3.14: The parameters from the probe fed patch within a multi-layer structure.

Parameter	Value	Parameter	Value
Length ground plane	10.37 mm	Length patch antenna	3.21 mm
Width ground plane	10.37 mm	Width patch antenna	4.19 mm
Height substrate 1	0.762 mm	Radius pin	0.25 mm
Height substrate 2	0.127 mm	Radius isolation pin	1.18 mm
Height substrate 3	1.0 mm	Shift pin on patch edge	0.53 mm
Height substrate 4	0.381 mm		

The return loss of the patch antenna within a multi-layer structure is shown in figure 3.31. At broadside, the impedance bandwidth ranges from 14.52 till 16.01 GHz with a center frequency of 15.34 GHz. While scanning in the azimuth plane, the impedance bandwidth is at a slightly smaller; from 14.06 till 15.38

GHz with a center frequency of 14.84 GHz. The return loss, while scanning in the elevation plane, is comparable with the return loss at broadside. The center frequency is 15.23 GHz and the bandwidth ranges from 14.39 - 15.96 GHz.

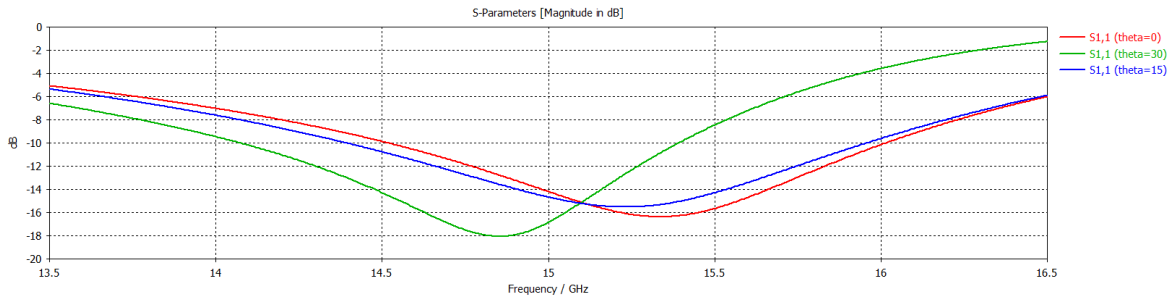
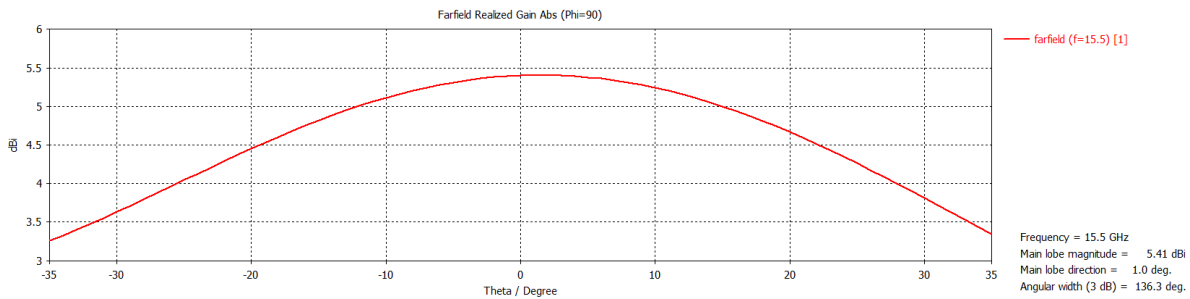
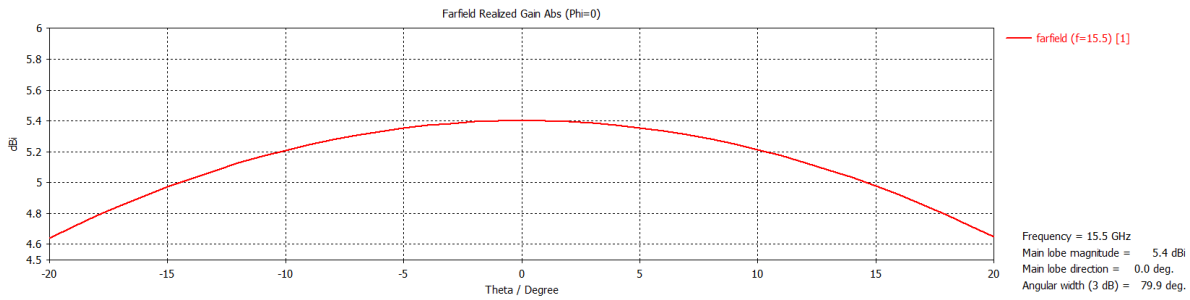


Figure 3.31: The return loss for the probe fed patch within a multi-layer structure. The red line represent the return loss at broadside, the green line at a scanning angle of 30° in azimuth and the blue line at 15° in elevation.

The farfield radiation patterns in azimuth and elevation are displayed in figure 3.32. On the one hand, the antenna does not have a wide radiation pattern in the azimuth plane. The 1 dB angular width ranges from -20.60 till 23.32 degrees. This is illustrated in figure 3.32a. On the other hand, figure 3.32b shows that in elevation the antenna can scan from -22.90 till 23.00 which satisfies the 1 dB angular width.



(a) $\phi = 90^\circ$, azimuth plane



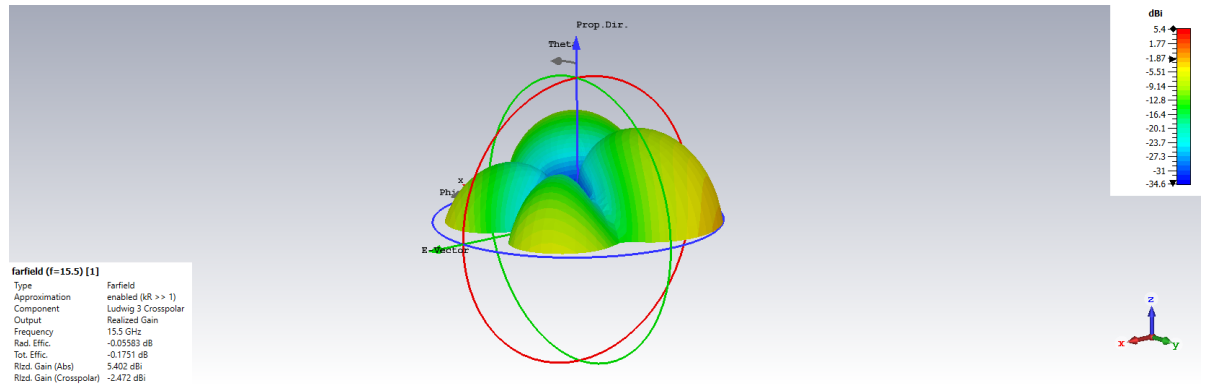
(b) $\phi = 0^\circ$, elevation plane

Figure 3.32: The radiation pattern of the probe fed patch antenna within a multi-layer structure at different angles of ϕ .

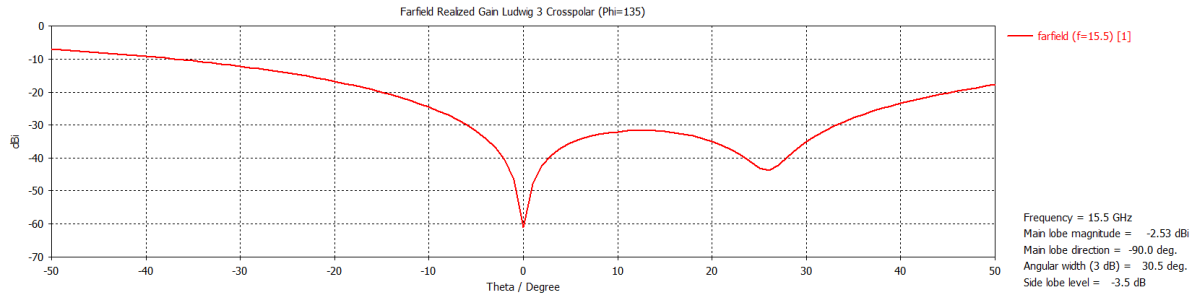
The cross polarisation level of the radiation pattern is shown in figure 3.33. The polarisation changes from horizontal to vertical, especially, at the corners of the patch antenna. This is illustrated in figure 3.33a. The level of the cross polarisation is shown in the $\phi = 135^\circ$ cut in figure 3.33b. It ranges under the -25 dB in the scanning range from -14.85 till 45.15 degrees. The highest magnitude of the cross polarisation is -2.296 dBi, which is -7.696 dB under the maximum realized gain.

Subsequently, the signal fidelity of the design is shown in figure 3.34. The probe at broadside measures no distortions. The received electric field is very stable as in the frequency range of the bandwidth the probe value range from 44.15 - 45.09 dBV/m and the difference is 0.94 dBV/m.

The group delay is plotted in figure 3.35. While the double stacked patch antenna had a small group delay and lots of small variations, this design has an average transit time of 0.853 ns over the full range



(a) 3D view



(b) $\phi = 135^\circ$

Figure 3.33: The cross polarisation of the radiation pattern of the probe fed patch antenna within a multi-layer structure.

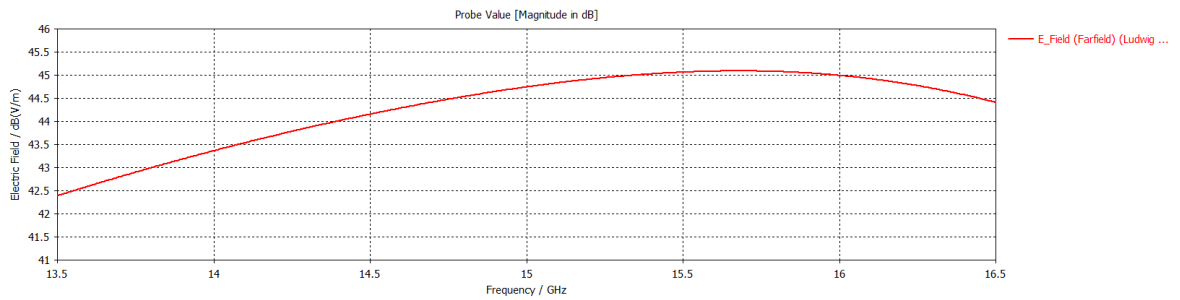


Figure 3.34: The signal fidelity at a distance of 3λ at broadside of the patch within a multi-layer structure.

of the plot. In the range of scanning on broadside (14.5-16.01 GHz), the group delay is 0.012 ns, which is comparable to the proximity fed patch antenna.

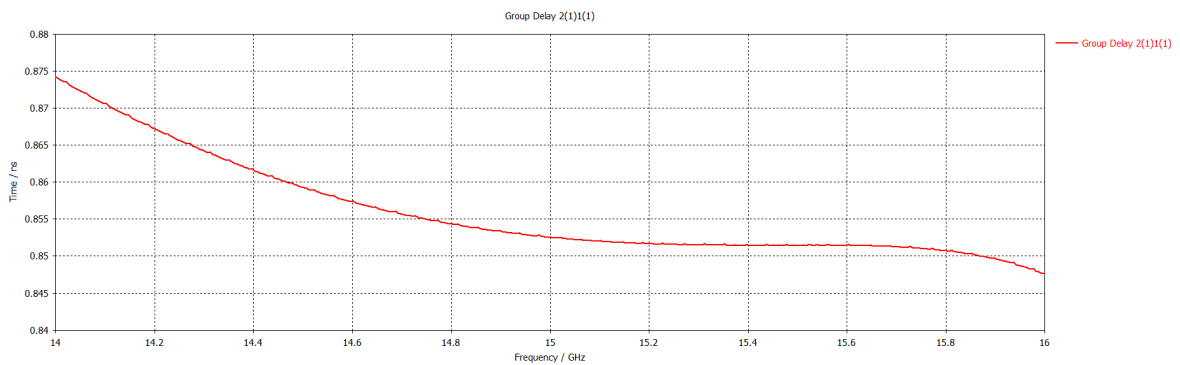


Figure 3.35: The group delay of the patch in a multi-layer structure.

Regarding manufacturability, the model only has two disadvantages. The two substrates need to be glued together, the effect of this is unknown. The other disadvantage is that the foam layer has a tolerance of 20%. Thus, this antenna is better manufacturable as it has less uncertainties than the other models, and therefore, has a + on manufacturability.

All in all, the fourth and final model performs less than other models, but still has some good properties. A summary of this model's performance is found in table 3.15. At first, it has less uncertainties and is thus easier to manufacture. It achieves the 1 dB angular width in elevation. Also, the difference in signal fidelity is only 0.94 dBV/m. However, none of the reflection coefficients achieve the desired bandwidth, the scanning capability in azimuth does not reach the 1 dB limit and the cross polarisation level in the scanning area is -20 dB instead of -25 dB.

Table 3.15: The summarized properties for the probe fed patch within a multi-layer structure model.

Parameter	Value
Center frequency broadside	15.34 GHz
Impedance bandwidth broadside	14.52 - 16.01 = 1.49 GHz
Center frequency 30° azimuth	14.84 GHz
Impedance bandwidth 30° azimuth	14.06 - 15.38 = 1.32 GHz
Center frequency 15° elevation	15.23 GHz
Impedance bandwidth 15° elevation	14.39 - 15.96 = 1.57 GHz
Realized gain	5.4 dBi
1 dB angular width azimuth	-20.60° - 23.32°
1 dB angular width elevation	-22.90° - 23.00°
Cross polarisation level	-7.696 dB
Cross polarisation level ang. width -20 dB	-14.85° - 45.15°
Signal fidelity	0.94 dBV/m
Group delay	0.012 ns
Manufacturability	+

3.3. Trade-off

All proposed antennas have an adequate radiation performance. None of them meet all the requirements of the ideal antenna, but some perform better than others. To compare each of them, a pass-fail table is made. This is shown in table 3.16. If the antenna meets the requirement, a + is given. And a - is given if the antenna does not meet the requirement. If the antenna's performance is debatable, a +/- is the proper mark. Comparing out of the blue is impossible, therefore, there has to be an order of importance for the properties.

The most important property is the scanning capability of the antenna. The requirement is that the scanning loss is minimal, and therefore, a loss of 1 dB is preferred. In elevation, all antennas have more or less equal scanning capabilities. However, in azimuth two antennas outperform the other two. These are the stacked antenna and proximity fed antenna, where the proximity fed has the best capabilities. It should be noted that this antenna still does not achieve the 1 dB angular width on both sides, but towards the negative azimuth direction.

After the scanning capabilities, impedance bandwidth is the most important property. The requirement is to have at least a impedance bandwidth of 1 GHz at all scanning angles. The superstrate antenna does not achieve this number, while the double stacked antenna only achieves this at broadside and 15 degrees elevation. Both the stacked and proximity fed patch achieve the requirement. At broadside they achieve a bandwidth of 2.87, and respectively, 3.74 GHz. At the scanning angle in azimuth this is a bit less. Therefore, the proximity fed is the best antenna regarding return loss, followed by the stacked patch antenna.

The following property is the manufacturability. All the models have the same disadvantages, except for the superstrate which has one disadvantage less. Therefore, the preferred antenna regarding manufacturability is the superstrate antenna. Followed by each of the other three.

All antennas achieve the required group delay. The smallest group delay is 0.009 ns of the proximity fed patch. This is 100x smaller than required. The largest group delay is achieved by the stacked patch antenna. But, the antenna's group delay is still 10x smaller than required. The only drawback in

the group delays of the proposed antennas is the amount of fluctuations in the double stacked patch antenna. This has a lot of influence on the range resolution over frequency. Conclusively, all antennas perform good on group delay, except for the double stacked antenna due to the large amount of fluctuations.

And the last two properties are signal fidelity and cross polarisation level. On signal fidelity, the superstrate and double stacked antenna perform best, while the proximity fed performs worst. But, the impedance bandwidth of the proximity fed is twice as large, and thus, the signal fidelity is measured over twice as much frequency range. Otherwise, the proximity fed is quite comparable to the other two, just like the stacked antenna. Regarding cross polarisation level the stacked patch antenna performs best, followed by the proximity fed patch antenna. However, the cross polarisation level is a desire and not a requirement. For a limit of -20 dB, all antennas suffice.

All in all, both the stacked patch antenna and the proximity fed antenna mostly outperform the other two antennas. However, on scanning capabilities and bandwidth the proximity fed patch antenna performs better. Therefore, the proximity fed patch is chosen as preferred antenna element. A 4x4 antenna array is designed in chapter 4 using this model.

Table 3.16: The pass/fail comparison of the different designs on all the requirements specified in section 3.1. in order of importance.

Model	Stacked	Proximity fed	Double stacked	Superstrate
Angular width (1 dB), azimuth	-	+/-	-	-
Angular width (1 dB), elevation	+	+	+	+
Imp. bandwidth broadside	+	+	+	+/-
Imp. bandwidth 30° azimuth	+	+	-	-
Imp. bandwidth 15° elevation	+	+	+	+
Manufacturability	+/-	+/-	-	+
Center frequency broadside	-	-	+	+/-
Center frequency 30° azimuth	-	-	-	-
Center frequency 15° elevation	-	-	+	+/-
Group delay	+	+	+	+
Signal fidelity	+/-	-	+	+
Cross polarisation level	+	+	+	+

3.4. Conclusion

To summarize, in this chapter a comparative study between different wideband patch antennas has been made, simulated in an infinite array. First, all the properties, and the relation the requirements, are explained. The ideal parameters are also discussed. Then, four designs are simulated and elaborated upon. These are compared and finally, the proximity fed patch in a multi-layer substrate, described in chapter 3.2.2, has been chosen as the best option. This patch antenna has the best scanning capabilities and the widest impedance bandwidth of 3.74 GHz at broadside, and with these, the best overall performance.

4

Patch Antenna Array

This chapter presents the results of the simulation of a 4x4 antenna array using the embedded element from the selected in chapter 3. It is simulated in broadside direction, and to the limits, while scanning in both planes simultaneously. Furthermore, the antenna's performance is tested on impedance bandwidth, scanning capabilities at multiple frequencies and cross-polarisation level. First, this chapter describes how the array is designed from the infinite array model. Then, the results of the array are presented. Finally, the results will be compared with the infinite array model.

4.1. The Model

This section gives a detailed explanation of the proposed antenna array. At first, the chosen solution from chapter 3 was simulated in a 4x4 array. But, the far field results showed a significant loss in the realized gain of 2.3 dBi, while scanning towards one of the limits in the negative x-direction This is as the antenna has a stronger coupled electric field in the positive x-direction. The maximum electric field is displayed in appendix B.2. A loss of 2.3 dBi is too much and therefore, optimization of the design is necessary. Nonetheless, the idea of a proximity fed patch in a multi-layer environment still has the potential of a wideband patch antenna and after some small alterations in the model, the model in figure 4.1 is proposed.

Table 4.1: Comparison of the parameters of the new proposed array and the chosen infinite array model from chapter 3.

Parameter	New value [mm]	Previous model value [mm]
Height substrate 1	0.762	0.762
Height substrate 2	0.508	0.508
Height substrate 3	1.000	1.000
Height substrate 4	0.254	0.127
Total length ground plane	41.49	10.37
Total width ground plane	51.61	10.37
Length patch antenna	6.0	5.12
Width patch antenna	6.2	6.02
Distance x between antennas	10.37	10.37
Distance y between antennas	12.90	10.37
Length feeding strip	2.3	2.5
Width feeding strip	0.9	1.02
Radius matching ring strip	0.7	0.81
Translation strip on pin from edge	1.8	2.0
Radius pin	0.25	0.25
Radius insulator pin	1.15	1.05

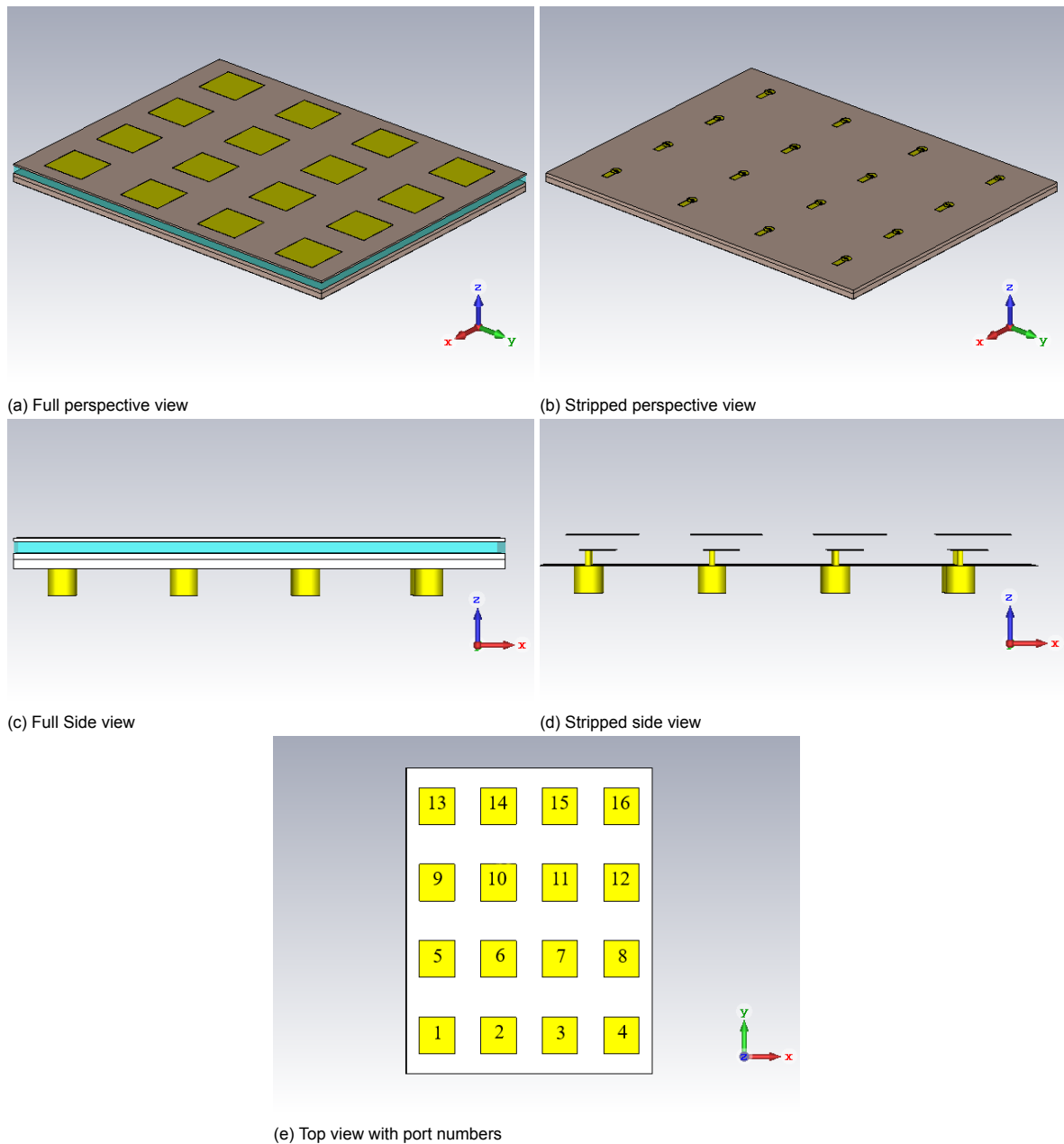


Figure 4.1: The array model from different views.

In the proposed model, the top substrate is twice as thick; the separations between elements in the y-direction have become larger, as the scanning requirements in this direction are smaller. This has more advantages: there is less coupling between elements in this direction and heat density is lower.

Furthermore, the length of the patch antenna has become larger, namely 6.0 mm. Theoretically, the length of the patch antenna on the top substrate is 6.356 mm. Therefore, the resonance frequency of the top patch is around 15.5 GHz. The length of the feeding strip is 2.5 mm. While for a resonance frequency of 15.5 GHz, the calculated length would be 2.754 mm, if the average dielectric permittivity is taken for the bottom substrates. In the new model, the dimensions of the feeding strip have decreased from 2.5 till 2.3 mm. All the parameters and those of the previous infinite array model are shown in table 4.1. Nonetheless, all the used materials, and their respective thicknesses, remain equal, as shown in table 4.2.

Table 4.2: The materials used in the design of the array and the chosen patch antenna from chapter 3.

Parameter	Material	Dielectric constant ϵ_r	Dissipation factor $\tan \delta$
Substrate 1	Rogers TC600	6.15	0.002
Substrate 2	Rogers RO3010	11.2	0.0022
Substrate 3	Foam	1.06	0.0001
Substrate 4	Rogers RT5880	2.2	0.0009
Insulator	PEEK	3.1	0.003

4.2. Simulation Results

Subsequently, the array is simulated using the transient solver in CST. The ports are normalized to a fixed impedance of 50Ω and the simulation is done with an accuracy of -40 dB . The simulation is done in the frequency range from 11 till 19 GHz. This is a wide simulation frequency range. However, at some simulations the return loss is smaller than -10 dB at those frequencies.

The model is tested at 5 different angles: at broadside and its four maximum scanning limits (azimuth = $\pm 30^\circ$ & elevation = $\pm 15^\circ$). The corresponding angles with the scanning limit were shown in table 2.1. Using these angles, the phase of each element is calculated using the equations from chapter 2.5 and the exact phase shift of each element is given in table B.1 in appendix B.1.

4.2.1. Return Loss

As the antenna is designed for radar, and is likely to become big. The return loss of the center four patch antennas in the 4×4 array are only of interest. These are antenna 6, 7, 10 and 11 in figure 4.1e. These antennas are influenced by antennas from all directions, while antennas in the outer ring are not. Also, a 6×6 array is simulated. The center 4×4 elements are only excited, as these are only of interest. The 6×6 array model should coincide more with the infinite array model.

In figure 4.2, the active s-parameters for the center four patch antennas are plotted of the proposed 4×4 array at broadside. The s-parameters for antennas 6 and 10 and for antennas 7 and 11 are equal at broadside. The resonance frequencies are 15.25 and 16.89 GHz for element 6 and 10 and are 15.38 and 16.80 GHz for element 7 and 11. These resonances lie around the required 15.4–15.7 GHz band. The bandwidth for each element can be found in table 4.3. All four elements have a large bandwidth of 3.64 and 2.96 GHz, respectively.

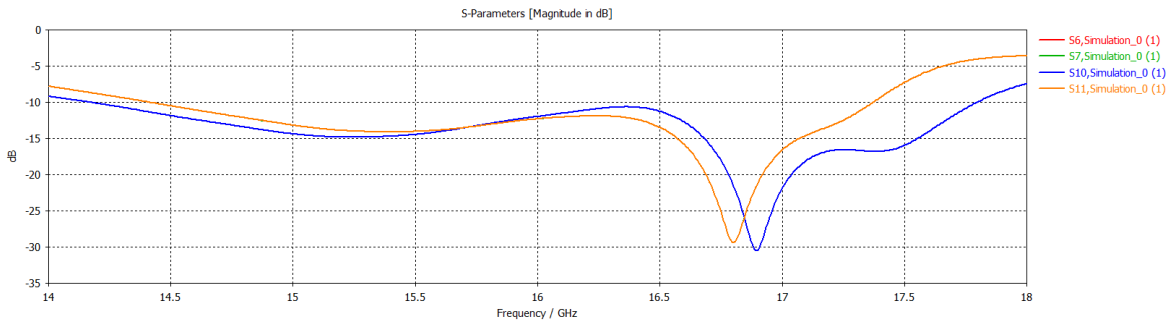


Figure 4.2: The return loss for patch number 6 and 10 (blue) and for patch number 7 and 11 (orange) at broadside.

Element No.	-10 dB frequency low [GHz]	-10 dB frequency high [GHz]	Impedance bandwidth [GHz]
6	14.16	17.80	3.64
7	14.41	17.37	2.96
10	14.16	17.80	3.64
11	14.41	17.37	2.96

Table 4.3: The impedance bandwidth for each of the four elements at broadside.

The active s-parameters are also plotted at the maximum scanning angles of the array. The S-parameters for these simulations are shown in figure 4.3. The return loss is only plotted for a positive elevation angle, as the return loss at a negative elevation is a mirrored version of the return loss at a positive elevation. Nonetheless, the return loss at a negative angle is shown in appendix C.1.1. The impedance bandwidth of these simulations for a positive elevation are summarized in table 4.4.

Almost all the active s-parameters of the center elements are in the proximity of the -10 dB limit over the frequency range. Most of the elements have a large impedance bandwidth, but some have multiple regions it radiates properly. This is due to the difference in phase excitation, and therefore, the mutual coupling is different. For example, in figure 4.3a, the antenna array scans towards element number 11. Element 6, 7 and 10 have a large impedance bandwidth. However, due to the phase difference in the other elements, this return loss is much more distorted. On the other hand, everywhere there are multiple resonances, the antenna's return loss is still close to the -10 dB limit, and thus, is the antenna still properly matched.

Table 4.4: The impedance bandwidth for element 6, 7, 10 and 11, while scanning to different maxima in azimuth and elevation.

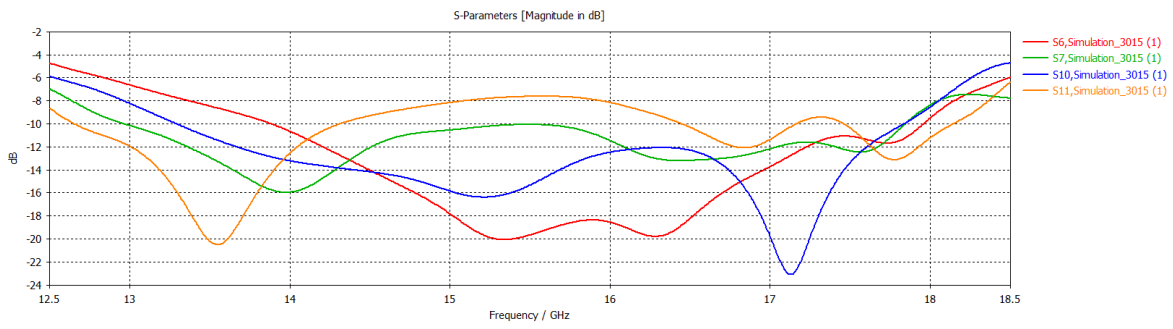
Azimuth	Elevation	Element number	Frequency low [GHz]	Frequency high [GHz]	Impedance bandwidth [GHz]
30°	15°	6	13.88	17.96	4.08
30°	15°	7	12.96	17.84	4.88
30°	15°	10	13.29	17.83	4.53
30°	15°	11	12.65/16.45/17.46	14.31/17.16/18.24	1.66/0.71/0.78
-30°	15°	6	12.82/15.47	14.79/17.29	1.97/1.82
-30°	15°	7	13.46/16.33	15.68/16.96	2.22/0.63
-30°	15°	10	12.54/16.03	14.29/17.74	1.75/1.71
-30°	15°	11	13.04/17.92	15.45/18.22	2.41/0.30

Table 4.5: The impedance bandwidth of the active s-parameters from 8 of the 16 center elements in the 6x6 array.

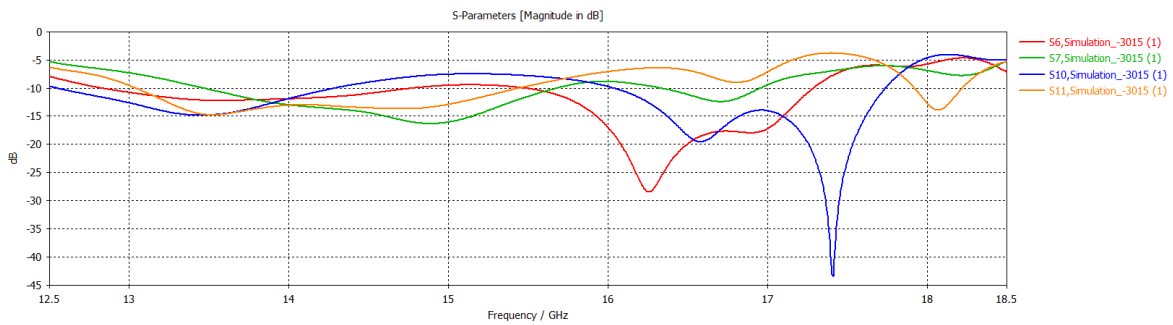
Element number	Frequency low [GHz]	Frequency high [GHz]	Impedance bandwidth [GHz]
1	14.61	16.90	2.29
2	14.58	17.04	2.46
3	14.50	17.09	2.59
4	14.68	16.94	2.26
5	14.47	17.03	2.56
6	14.34	16.02	1.68
7	14.34	17.90	3.56
8	14.48	17.09	2.61

In figure 4.4, the return loss of 8 of the 16 elements in a 6x6 array are plotted. This will create an array which will come close to the infinite array model, and therefore, close to a larger array. As the antenna array is symmetrical, the return loss for element 1 till 8 is equal to element 9 till 16. Therefore, the return loss of element 9 till 16 is plotted in appendix C.1.2. The impedance bandwidth for the eight elements is shown in table 4.5. Almost each element's impedance bandwidth ranges from 14.3-14.6 GHz till approximately 17.0 GHz. This gives an impedance bandwidth of 2.4-2.6 GHz on average.

However, the 4 center elements are more influenced by mutual coupling and have a different impedance bandwidth. For element 7 and 11, the impedance bandwidth ranges from 14.34 till 17.90 GHz, which gives a bandwidth of 3.56 GHz. On the other hand, the bandwidth of element 6 and 10 range from 14.34 till 16.02 GHz. This gives a smaller impedance bandwidth of 1.68 GHz than on average. But, these two elements have another bandwidth region that ranges from 16.60 GHz till at 18.50+ GHz. Also, the region from 16.02 till 16.60 GHz, that is above the -10 dB limit, reaches only a maximum of -9.13 dB. The active s-parameters react in this way due to mutual coupling. As the electrical field is much stronger in the x-direction than the y-direction, shown in appendix B.2 the mutual coupling is much stronger in the x-direction and the center antennas are much more influenced by the antennas in the x-direction.

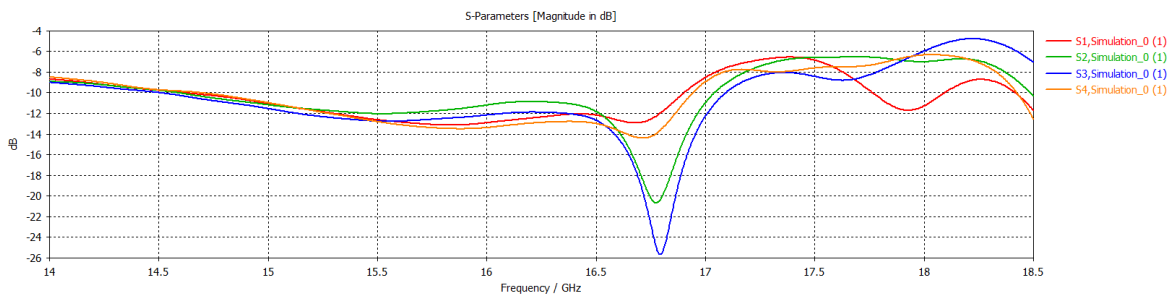


(a) Azimuth = 30° and elevation = 15°.

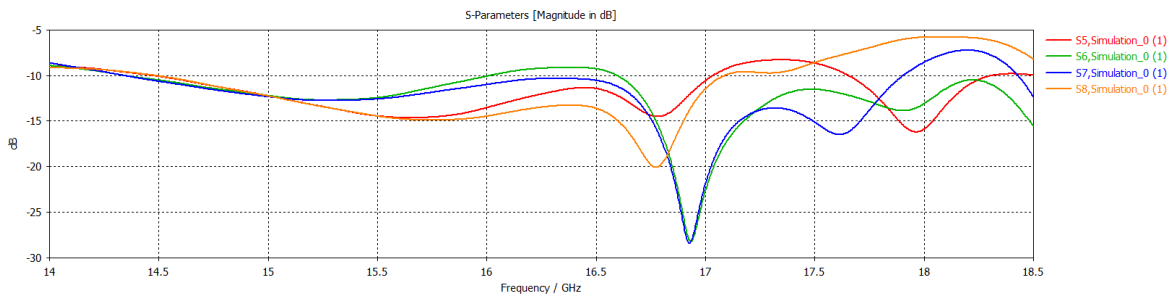


(b) Azimuth = -30° and elevation = 15°.

Figure 4.3: The active s-parameters for the center four patches at the different scanning limits for a positive elevation.



(a) Element 1 till 4.



(b) Element 5 till 8.

Figure 4.4: The active s-parameters for the left half of the center 16 patches in the 6x6 array.

Overall, the antenna array has a good performance regarding return loss. In the 4x4 array, the center patches exhibit a wide impedance bandwidth of almost 3 GHz. While scanning into the positive azimuth direction the antennas create an even larger bandwidth, and the antenna is matched, properly. But, scanning to the negative azimuth direction, the antenna has two regions of bandwidth where the antenna array is matched to its transmission line. The antenna, however, still performs well in the 15 GHz region. In the 6x6 array simulation, the center 16 elements are excited, such that its performance is closer to the infinite array solution. On average, the impedance bandwidth of each element is 2.50 GHz. This is 15.92% of relative impedance bandwidth at a center frequency of 15.7 GHz. This becomes even larger, when more elements will perform equally as antenna element 7 and 11. Then, the impedance bandwidth is equal to 3.56 GHz.

4.2.2. Radiation Pattern

Another important property is the radiation pattern of the antenna array. It determines if the antenna radiates properly, if the polarisation of the antenna is horizontal and how much the sidelobe level is. Therefore, there is looked at multiple frequencies at the radiation pattern, namely, 14.5, 15.5 and 16.5 GHz. As the antenna is wideband, the radiation pattern has to be quite equal at all frequencies. The polarisation of the antenna is simulated, and thus, the cross-polarisation level is also taken into account at these different frequencies.

Figures 4.5-4.7 illustrate the farfield simulations. The farfield is plotted as realized gain as this takes all the losses due reflection into account. The broadside simulation is plotted from front and top view. All the other simulations are shown from top view. The maximum amplitude of all the main lobes at broadside and all the scanning angles are shown in table 4.6. At broadside, the main lobe have a realized gain amplitude of 17.20, 18.06 and 17.12 dBi, at respectively, 14.5, 15.5 and 16.5 GHz.

Table 4.6: The maximum realized gain of the main lobe and its cross-polarisation level compared to the main lobe for each simulation with different frequencies and scanning angles.

Frequency [GHz]	Scanning angles (azimuth/elevation)	Main lobe [dBi]	Cross-polarisation level [dBi]
14.5	0° / 0°	17.20	-19.131
14.5	30° / 15°	16.07	-17.705
14.5	-30° / 15°	16.28	-15.356
14.5	-30° / -15°	16.28	-15.356
14.5	30° / -15°	16.07	-17.704
15.5	0° / 0°	18.06	-22.588
15.5	30° / 15°	16.59	-16.621
15.5	-30° / 15°	16.45	-13.518
15.5	-30° / -15°	16.45	13.518
15.5	30° / -15°	16.59	-16.621
16.5	0° / 0°	17.12	-9.814
16.5	30° / 15°	16.53	-15.988
16.5	-30° / 15°	14.04	-7.925
16.5	-30° / -15°	14.04	-7.925
16.5	30° / -15°	16.53	-15.988

While scanning the losses at 14.5 GHz are the smallest, namely 1.08 dB. The maximum loss at 15.5 GHz is 1.61 dB and at 16.5 GHz 2.98 dB. The losses at 16.5 are almost twice as large as at 16.5. However, these high losses are only in the negative azimuth direction, as the positive azimuth direction only has a loss 0.59 dB. In figures 4.7c and 4.7e, it is observable that the antennas have high side lobes or grating lobes at this frequency. This is probably due to the higher electric field in the patch, therefore, the array has a stronger coupling between the elements, which influence the main lobe magnitude.

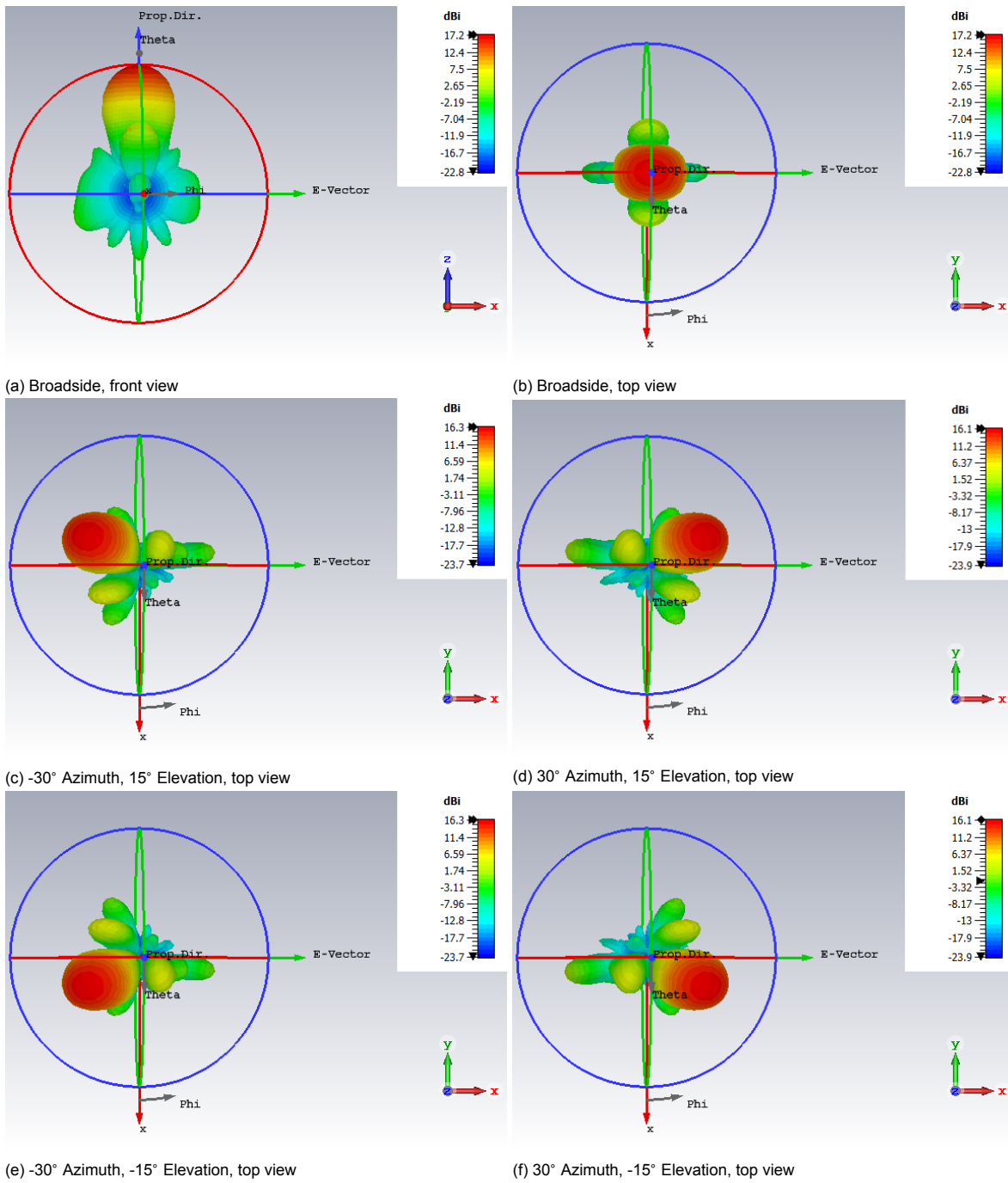


Figure 4.5: The far field radiation pattern of the array (expressed in realized gain) at a frequency of 14.5 GHz at different scanning angles.

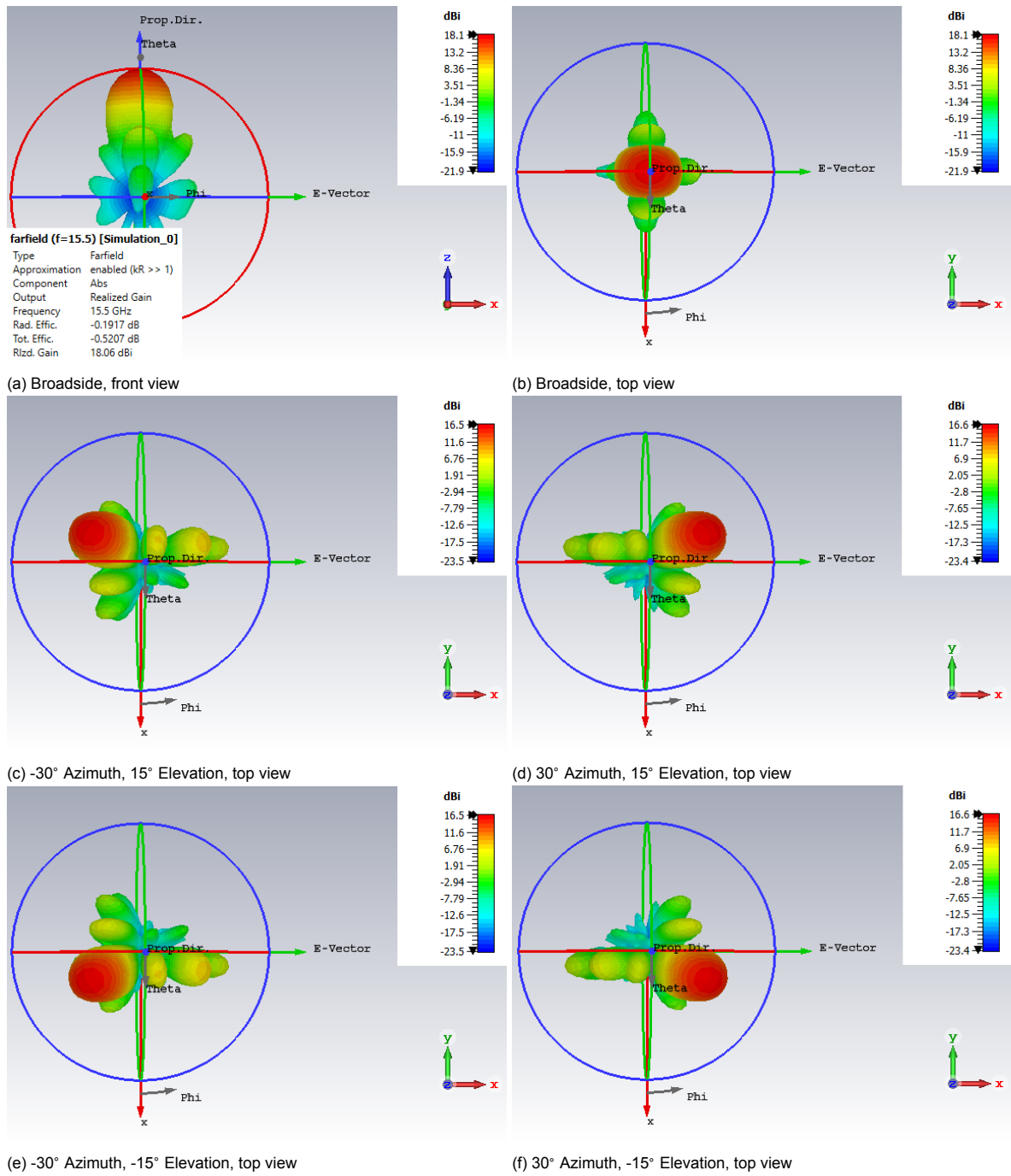


Figure 4.6: The far field radiation pattern of the array (expressed in realized gain) at a frequency of 15.5 GHz at different scanning angles.

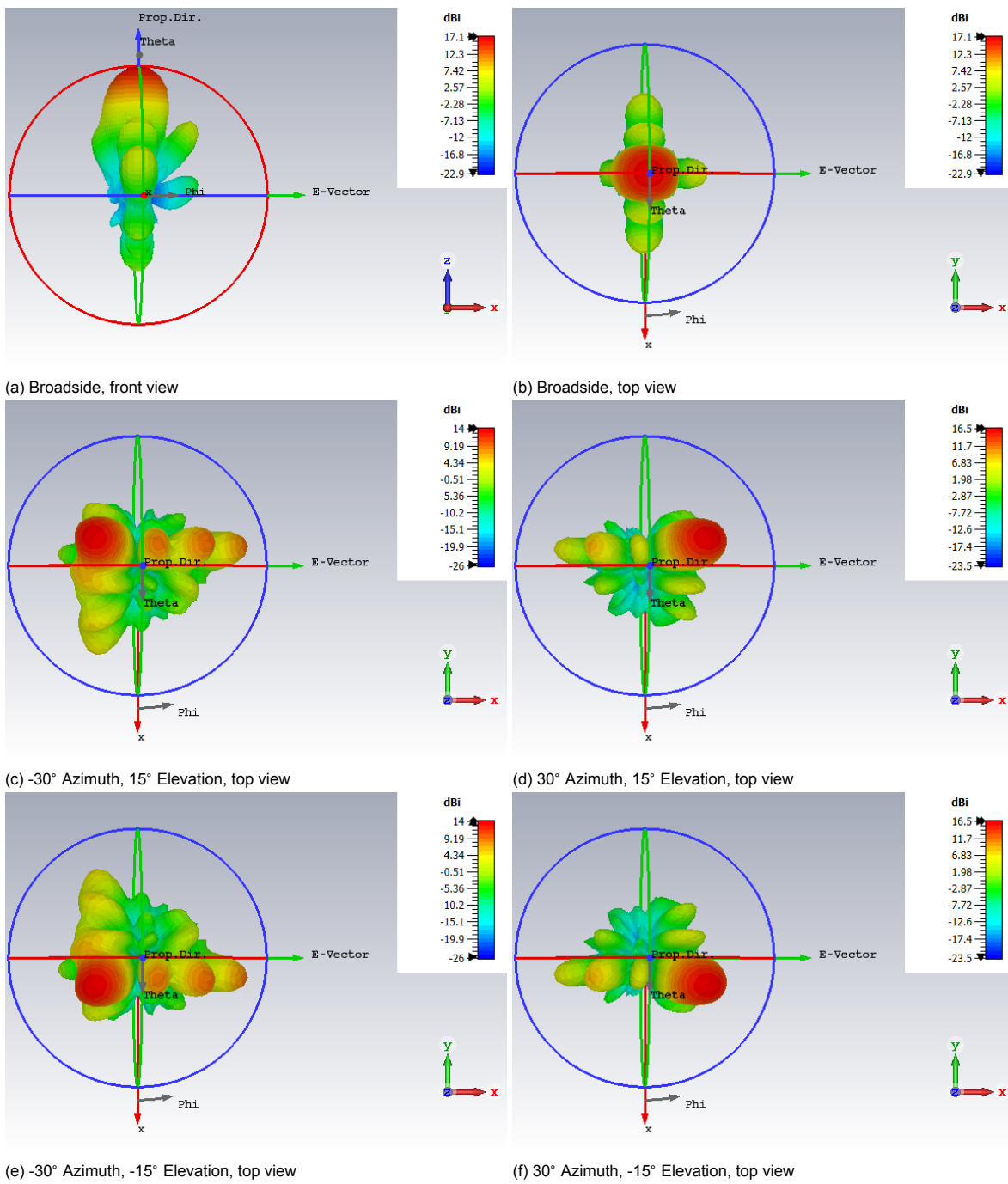


Figure 4.7: The far field radiation pattern of the array (expressed in realized gain) at a frequency of 16.5 GHz at different scanning angles.

The cross-polarisation level is shown in figures 4.8-4.10. These are also plotted from the top view (except for the broadside pattern), as well as at the 3 different frequencies. The maximum magnitude for each plot is shown in table 4.6. This shows that the cross-polarisation level at 14.5 GHz is between 15 and 19.1 dB smaller than the main lobe. At 15.5 GHz, the difference with the main lobe is between -13.52 and -22.58 dB. The difference is especially larger at broadside. Furthermore, at 16.5 GHz the cross-polarisation level is between 7.9 and 16.01 dB smaller than the main lobe.

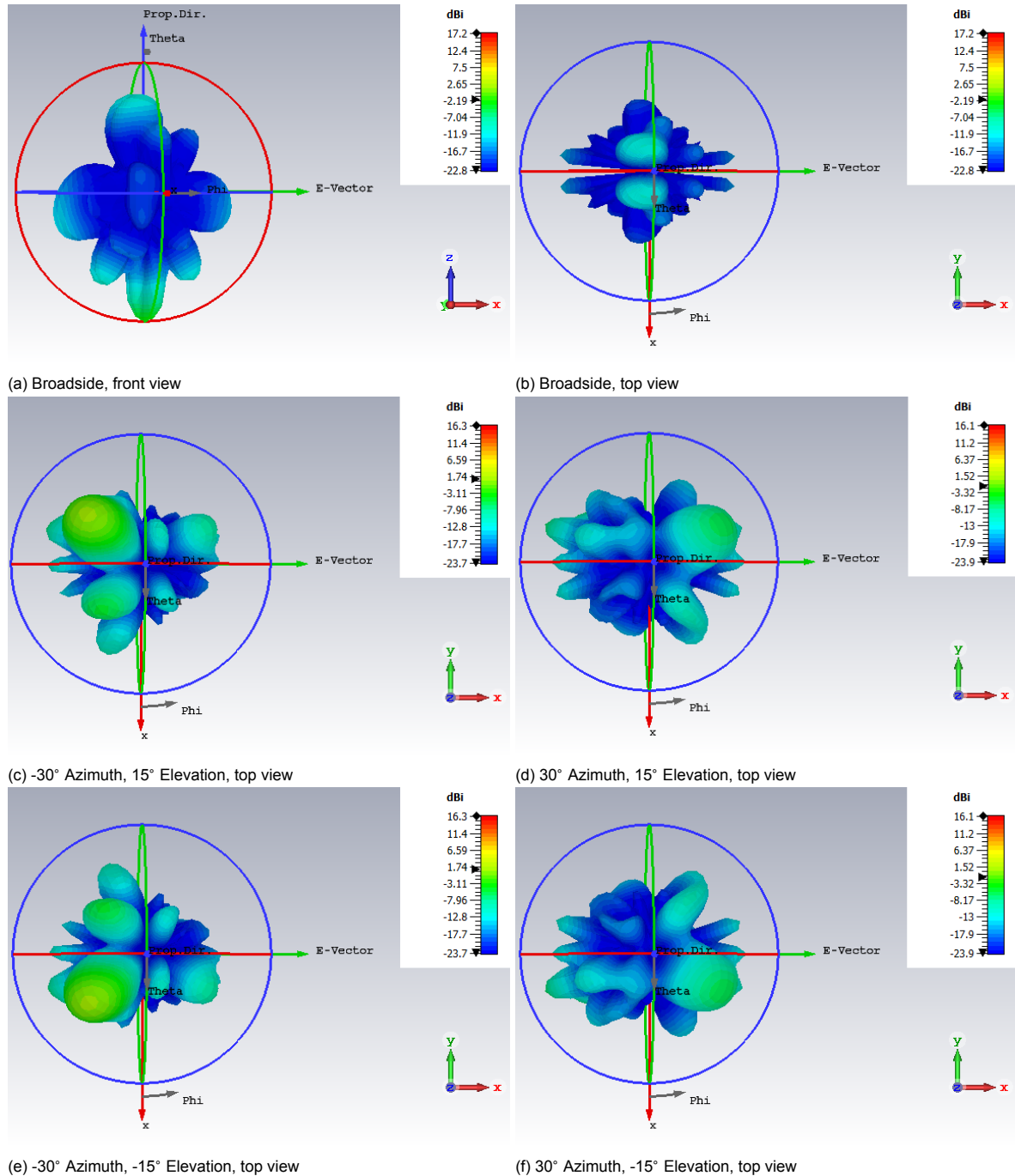


Figure 4.8: The cross-polarisation pattern of the array (expressed in realized gain) at a frequency of 14.5 GHz at different scanning angles.

Especially at 14.5 and 15.5 GHz, the highest cross-polarisation level is in the same direction as the scanning direction. For example, while scanning towards -30° azimuth and 15° elevation, the highest magnitude is in that same direction. This is shown in figures 4.8c and 4.9c. It is expected that the cross-polarisation at these frequencies will decrease compared to the main lobe at an even larger array and will therefore, fulfill the requirement of the cross-polarisation level.

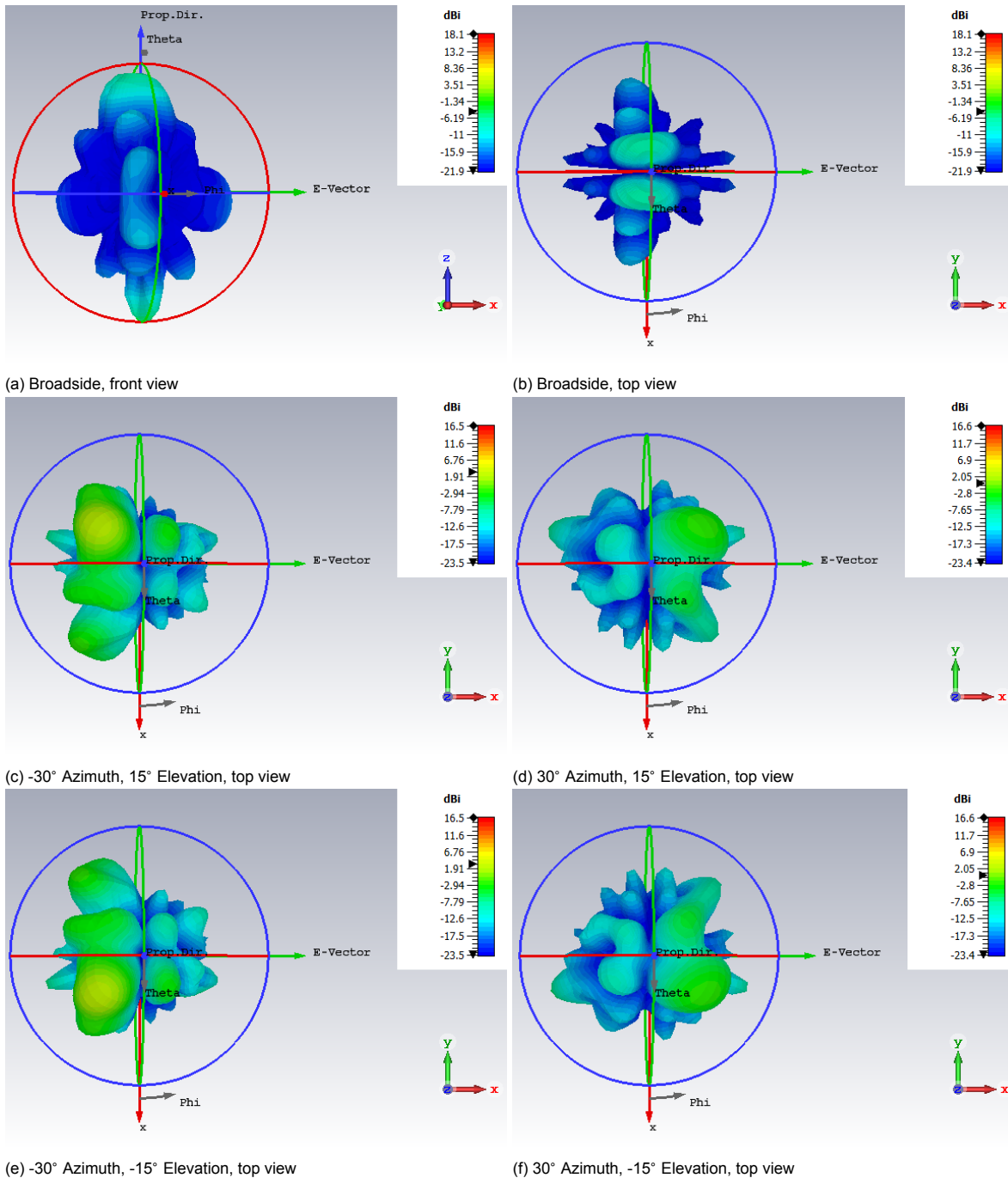


Figure 4.9: The cross-polarisation pattern of the array (expressed in realized gain) at a frequency of 15.5 GHz at different scanning angles.

However at 16.5 GHz, the cross-polarisation level is much larger than at the lower frequencies. This is due to the stronger electric field generated in the patch antenna. This creates much more surface waves, and therefore, the cross-polarisation level is much higher.

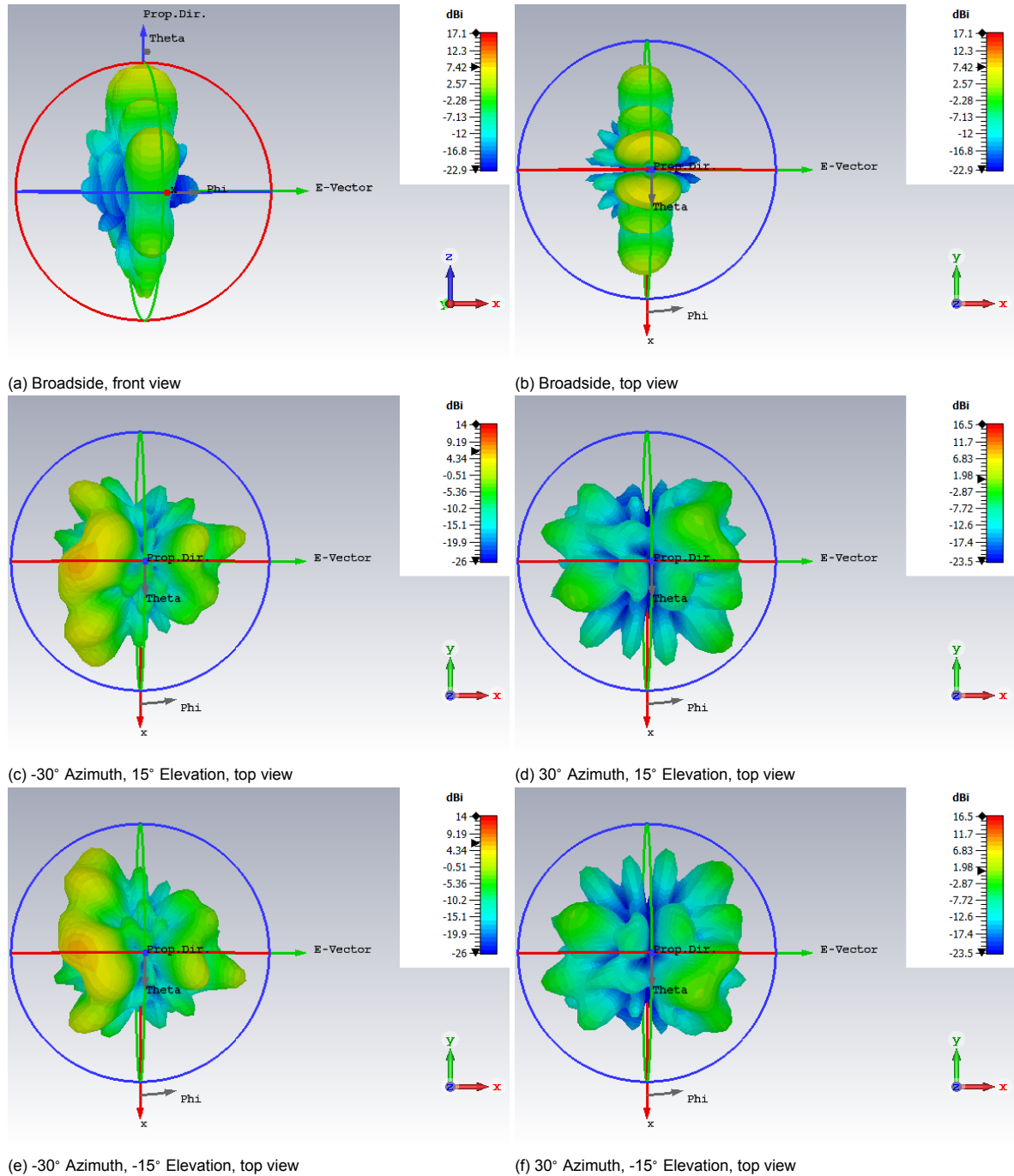


Figure 4.10: The cross-polarisation pattern of the array (expressed in realized gain) at a frequency of 14.5 GHz at different scanning angles.

All in all, the antenna radiates properly at the frequencies of 14.5 and 15.5 GHz. It has only maximum losses of 1.08 and 1.61 dB at these frequencies while scanning. On the other hand, at 16.5 GHz there are much more losses which are caused by the cross polarisation level.

4.2.3. Signal Fidelity

A probe is located at a distance of 3λ from the array at broadside to observe its signal fidelity. The probe values for the horizontal and vertical polarisation are shown in figure 4.11. In the region from 14 till 16.3 GHz, the probe value is stable while slightly increasing. It is in the range of 68.26 till 69.69 dBV/m. However, when the frequency becomes larger than 16.3 GHz, the probe value decreases with approximately 3 dB. This might become a problem as the resonances of the center four patch antennas are at frequency of 16.8 GHz. The decrease can be explained by the increased cross polarisation level into other directions at that frequency. This explains also the decrease in the main lobe in figure 4.7.

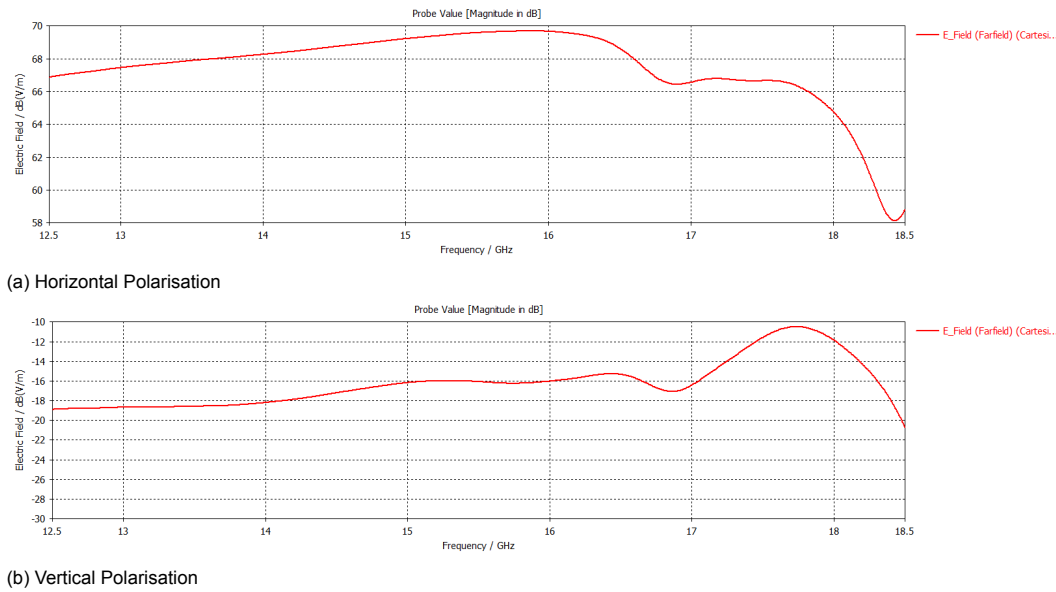


Figure 4.11: The signal fidelity of the proposed array for different polarisations at a broadside distance of 3λ

4.2.4. Manufacturability

As described in section 1.2, the antenna array is designed to be on a single PCB. The antenna array on the radiating side and on the opposite side electronics, such as amplifiers and phase-shifters. In general, this patch has three problems regarding its manufacturability for the radar: The shift of the top substrate and the lower two substrates, the tolerance of the third substrate and connection of the bottom two substrates.

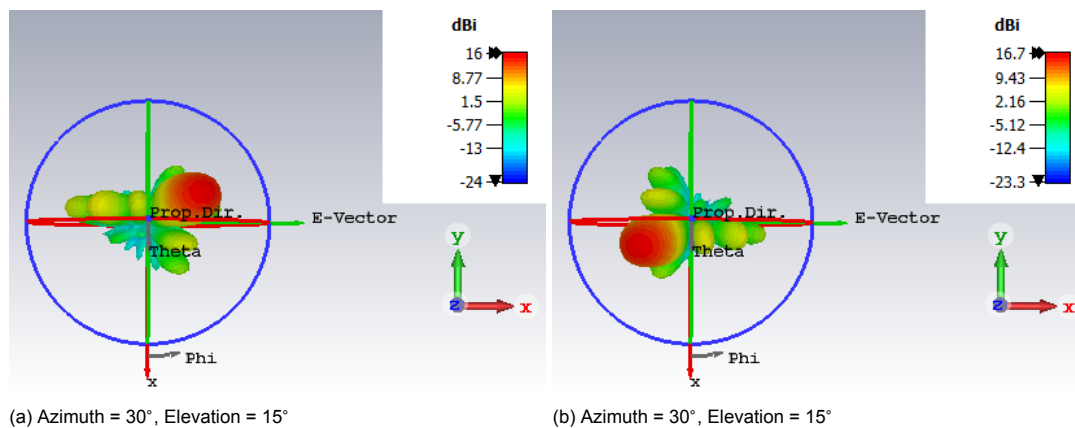


Figure 4.12: Comparison of two radiation patterns with different scanning angles when the feeding is shifted 0.5 mm towards the the positive x-direction at 15.5 GHz.

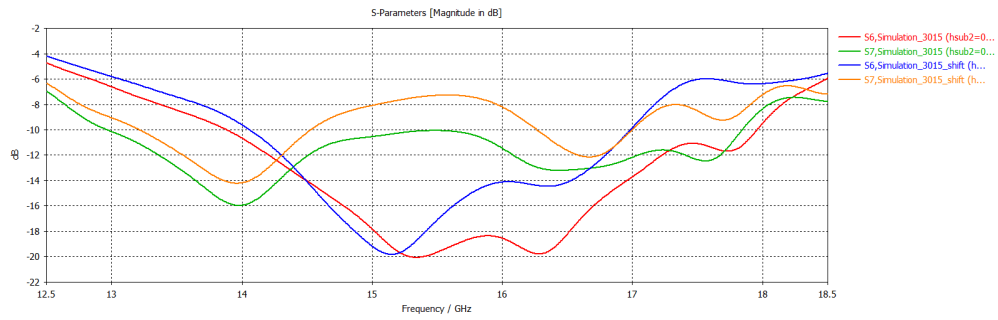
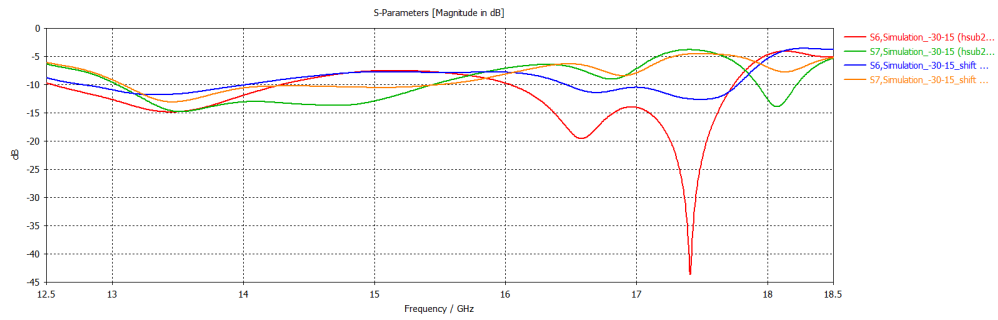
(a) Azimuth = 30° & elevation = 15° to broadside(b) Azimuth = -30° & elevation = -15° to broadside

Figure 4.13: Comparison of the active s-parameters of the patch antennas 6 and 7 with different scanning angles when the feeding is shifted 0.5 mm towards the the positive x-direction. The red and green line are the return of element 6 and 7 at broadside, while the blue and yellow line are the return loss for element 10 and 11 at the scanning limit, respectively.

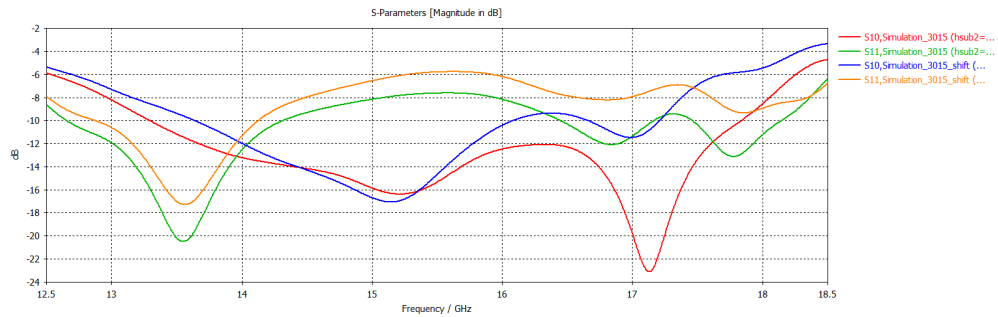
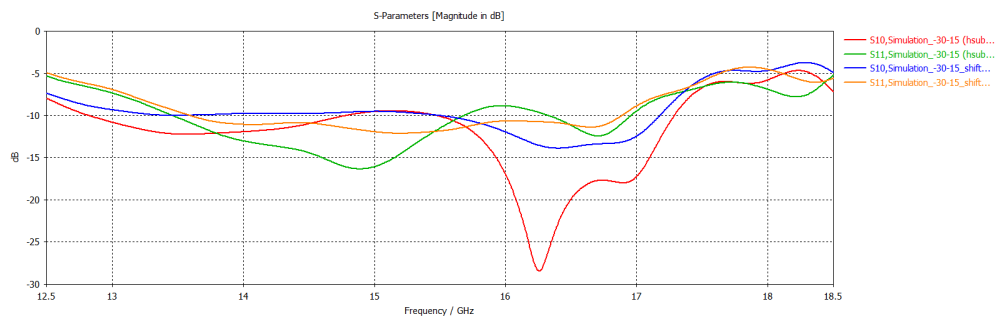
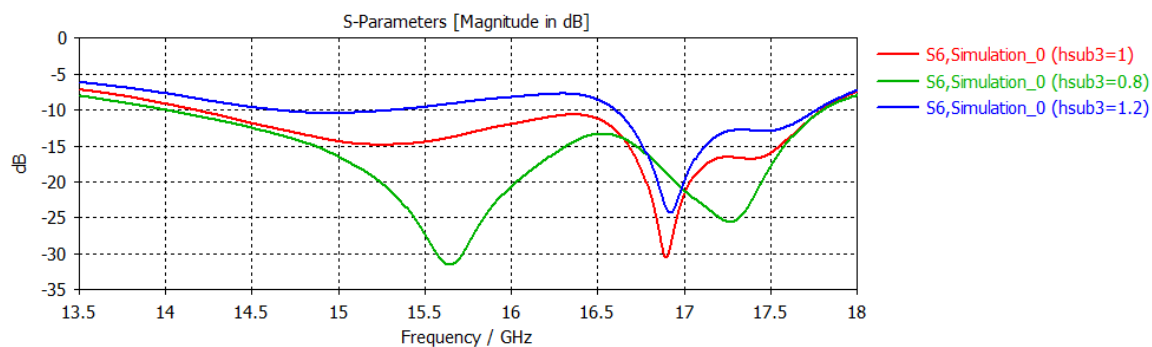
(a) Azimuth = 30° & elevation = 15° to broadside(b) Azimuth = -30° & elevation = -15° to broadside

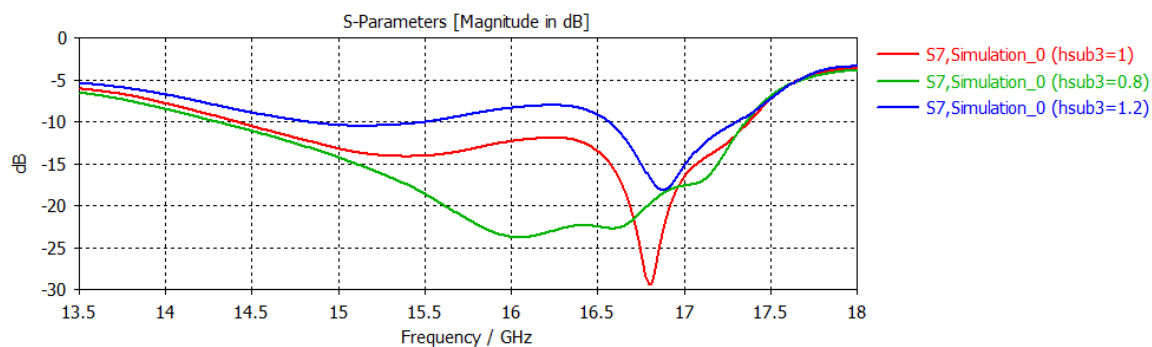
Figure 4.14: Comparison of the active s-parameters of the patch antennas 10 and 11 with different scanning angles when the feeding is shifted 0.5 mm towards the the positive x-direction. The red and green line are the return of element 6 and 7 at broadside, while the blue and yellow line are the return loss for element 10 and 11 at the scanning limit, respectively.

The first problem influences mostly the radiation pattern and also the return loss of the antenna. The maximum shift has been determined to be 0.5 mm. This influences the patch antenna array's radiation pattern as the top layer is not perfectly matched anymore with the bottom layer, due to its displacement. Also, the shift will cause a stronger scan away from the shift as each element's radiation pattern tends to radiate in the direction from the center point of the feeding to the center point of the top patch. For example, if the top layer is shifted 0.5 mm in the positive x-direction, scanning in the negative azimuth direction will radiate stronger than scanning in the positive azimuth direction. This is shown in figure 4.12. The magnitudes of the main lobes at 15.5 GHz is 16.0 and 16.7 dBi while scanning, if the feeding is shifted 0.5 mm forward. This was 16.59 and 16.45 at the original position. Also, the active s-parameters change, shown in figures 4.13 and 4.14. Overall, the antennas keep the same resonances. But, the coupling between the antenna and the feeding strips becomes weaker, and therefore, the reflection coefficient is less matched properly.

The second problem is tolerance of the third layer substrate. The thickness of the foam layer is irregular as it is somewhere between 0.8 and 1.2 mm thick. A tolerance of 20% is quite a lot. This will influence mostly the return loss. If the foam layer is thinner than the coupling between the feeding strips and antennas will be stronger, and vice versa. This is shown in figure 4.15. The active s-parameters are plotted for elements 6, 7, 10 and 11. As the substrate becomes thinner, the active s-parameters are stronger and have a better return loss. While the main lobe of the array barely changes, shown in figure 4.16. Furthermore, the datasheet of the foam [54] does not mention if the tolerance is either over the whole plate, or partly. In other words, if one part of the foam is 0.8 mm and 5 cm further the thickness is 1.2 mm or the foam is even. Also, the foam is simulated as a homogeneous layer with a constant dielectric permittivity. This is as the density of the foam in the datasheet is only valid for a minimum thickness of 10 mm, while the proposed model uses a thickness of 1 mm.



(a) Element 6 & 10



(b) Element 7 & 11

Figure 4.15: Comparison of the active s-parameters of the center four patches at broadside when the foam layer is different heights.

Subsequently, the third issue is that the lower 2 substrates need to be glued together without a copper layer between this. However, using the Multilayer Adhesive System [55], the substrates can be put together without too much influence on RF signals. So, this is not considered a serious problem.

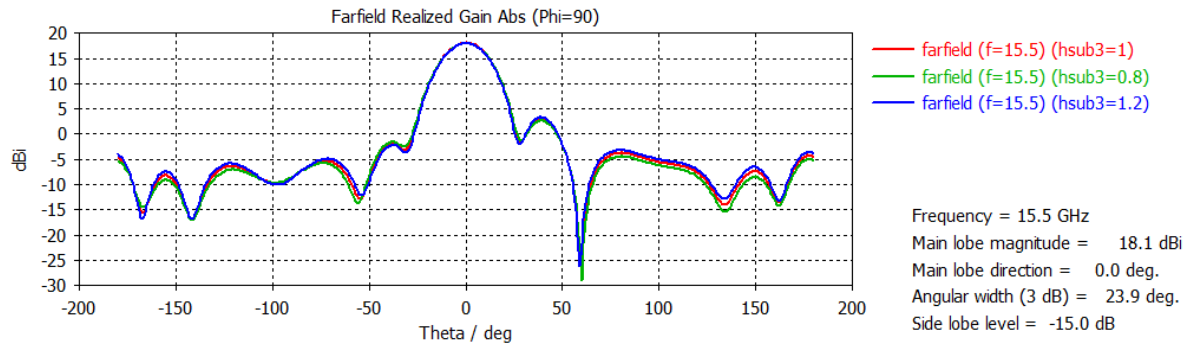


Figure 4.16: Comparison of the radiation pattern of the array at broadside when the foam layer is different heights at 15.5 GHz.

Also, the feed of the antenna is replaced by a via and a SMP connector. The simulation has been adopted as follows to represent this. The via has a radius of 0.25 mm and the SMP connector has a pin with 0.25 mm and a dielectric insulator PEEK with a radius of 1.15 mm.

All in all, the antenna array is dependent on some critical factors (most critical are given first and should be paid attention to): The foam layer between substrate 2 and 4 has a tolerance of 20%. This influence the return loss a lot. Then, the top substrate should placed carefully, such that the antenna radiates in the right direction. A shift has influences on the radiation pattern and the return loss of the antenna array. The third problem was the assembly of substrate 1 with substrate 2. However, the multilayer adhesive system is a solution to put substrates together without additional RF influences.

4.3. Comparison with the infinite array

In this section a comparison will be made between the antenna array and its infinite array. The performance is compared on return loss, scanning performance and signal fidelity.

In figure 4.17, the return loss is plotted for the patch element in an infinite array at broadside and the 4 different scanning limits. At broadside the impedance bandwidth ranges from 14.94 till 16.72 GHz with a resonance frequency at 15.84 GHz. Comparing this to the return loss of the 4x4 array, this is much smaller. The lower frequency of the impedance bandwidth is at 14.94 GHz, while in the 4x4 array these are 14.16 and 14.41 GHz. While the higher frequency band, is much smaller, namely 16.72 GHz over 17.37 and 17.80 GHz.

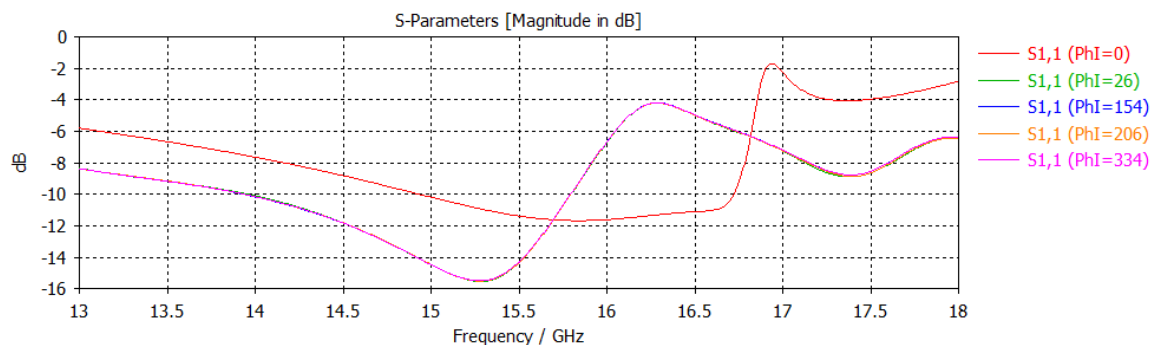


Figure 4.17: The return loss of the comparable patch antenna in an infinite array simulation.

On the other hand, when the simulation at broadside is compared to the 16 center elements of the 6x6 array, the return loss starts shows similarities. The average of the lower frequency of the bandwidth is at 14.50 GHz and the average of the higher frequency of the bandwidth is at 17.00 GHz. These are already much closer to the infinite array model.

Furthermore, the return loss is compared, while scanning to the required limits in azimuth and elevation. The return loss at each scanning limit has an equal return loss, with a resonance frequency at 15.28 GHz and a impedance bandwidth from 13.93 till 15.79 GHz, Comparing this to the 4x4 array, gives almost no similarities, except for, if the array scans to the negative azimuth direction. In that

Table 4.7: The realized gain of the radiation patterns from figure 4.18 at different scanning angles at 15.5 GHz.

Angle Azimuth	Angle elevation	Realized gain [dBi]
0°	0°	6.827
30°	15°	5.107
-30°	15°	3.89
-30°	-15°	3.928
30°	-15°	5.122

case, the return loss for the 4 center antennas create a comparable return loss to the infinite array simulation. Where figure 4.17 creates one impedance bandwidth but a second is almost achieved around 17.3 GHz. The 4x4 array while scanning towards the negative azimuth direction has these two bandwidths, and therefore, shows similarities.

Subsequently, the farfield radiation pattern is compared to the loss in its infinite array solution at broadside. For this, the gain at 15.5 GHz is compared. The gain of the 4x4 array at broadside is 18.06 dBi. Using equations 2.10 and 2.11, the realized gain of a single element is calculated, namely 6.02 dBi, as $10 \log 16 = 12.04 \text{dB}$. Now, most of the losses should come due to the loss in the radiation pattern of the element and not due to the array factor. In figure 4.18, the far field radiation patterns are shown for the angles $\phi = \pm 26^\circ$ from the positive x-axis for all angles of θ in the range from -40 till 40 degrees. Thus, -26° corresponds to azimuth and elevation of 30 degrees and -15 degrees. But also, -30 degrees and 15 degrees, and vice versa.

In table 4.7, the realized gain at the scanning limits are given from the farfield plots of figure 4.18. The gain losses in the infinite array simulation are much bigger while scanning. This ranges between losses of 2.937 and 1.75 dB, while the maximum loss in the 4x4 array was 1.61 dB. This loss could be smaller as the 4x4 array is influenced by less antennas than the elements in the infinite array.

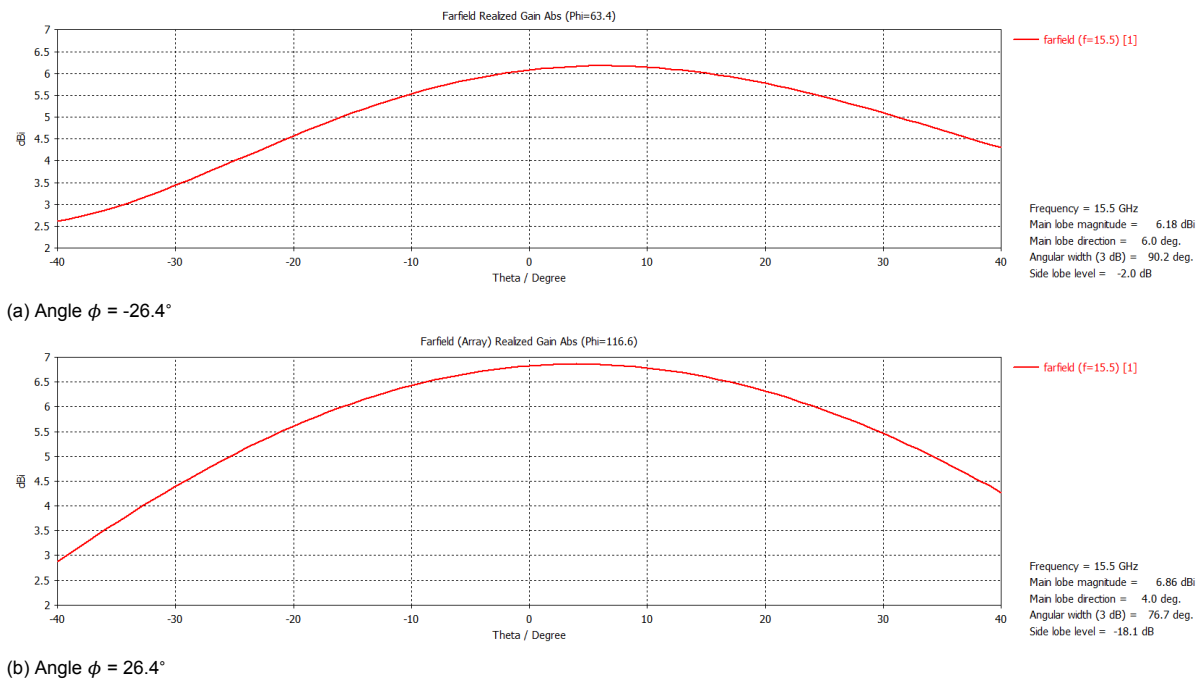


Figure 4.18: The radiation pattern of the comparable patch antenna in an infinite array simulation at different angles of phi from the positive x-axis at 15.5 GHz.

Finally, the array is compared on signal fidelity. In figure 4.19 the fidelity is plotted for the patch antenna in the infinite array. The probe value is stable and ranges around 45 dBV/m, until the frequencies of 16.8 till 17.0 GHz, there the measured probe value drops almost 20 dB. Something comparable happens in the signal fidelity of the array in figure 4.11. The simulated probe value is quite stable, until 16.6-16.7 GHz, then it drops by 2 or 3 dB.

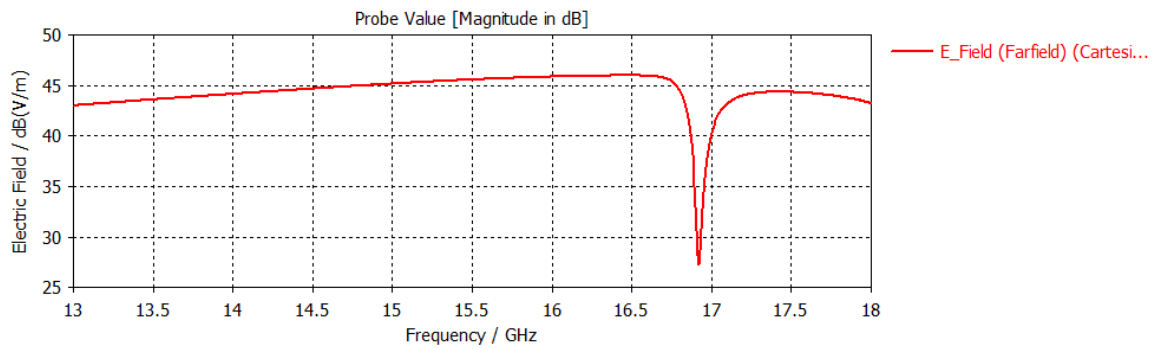


Figure 4.19: The signal fidelity of the comparable patch antenna in an infinite array simulation.

4.4. Conclusion

A newly proposed patch antenna array is presented, based on the chosen design of chapter 3. The array is created from the antenna element, which is slightly optimized. The performance of the antenna array is simulated. The 4x4 array exhibits a wide impedance bandwidth of at least 2.96 GHz. In the 6x6 array, the average impedance bandwidth is 2.50 GHz.

In the 4x4 array the maximum scanning loss is 1.13 dB at 14.5 GHz, 1.61 dB at 15.5 GHz and 3.08 dB at 16.5 GHz. And the cross-polarisation level is between -15 and -22.58 dB at 14.5 and 15.5 GHz. According to the signal fidelity, the antenna array radiates good from 14 till 16.3 GHz. Despite, some critical factors, the array is manufacturable.

Subsequently, the array is compared to its patch in the infinite array simulation. Large differences between the 4x4 model and the infinite array model have been observed. The 6x6 model tends to converge to the infinite case however, giving confidence in the results.

5

Results and Verification

This chapter presents the results acquired from testing the prototype of the designed array from chapter 4. The prototype is tested and its performance is compared to its simulation results. First, the design of the prototype is explained. The differences with the simulation and other assumptions are presented, too. Then, the measurements are explained. Followed by, the results of the measurements. The measurements are compared to the results of the simulated antenna array from chapter 4 for verification. Finally, a verdict is given if the prototype is comparable to the created antenna.

5.1. The Prototype

As described in section 1.2, the antenna array is to be designed on a single PCB. The array on the radiating side with on the opposite side electronics, such as amplifiers and phase-shifters. The radius of connecting vias can be of any size, as long as enough power is radiated through the antennas. In this design, the radius is simulated to be 0.25 mm. As the radiating side is only of interest, the pin is ended with a modeled SMA connector. The connector exists out of a pin with 0.25 mm and the dielectric insulator PEEK of 1.15 mm. However, a SMA or SMP connector with an inner radius of 0.25 mm is not available at stock. Thus, a SMP of 0.4 mm radius from Rosenberger is used instead [56]. This connector has Liquid-crystal polymer (LCP) as a dielectric and has a 50Ω impedance.

This creates a mismatch in the resistance of the port, exciting the antenna. This mismatch is due to the different thicknesses of the feeding pin, from 0.4 mm radius in the connector to 0.25 mm in the via. As the feeding pin becomes smaller, the resistance of the pin becomes larger and the current that can flow through the pin becomes smaller as well. I.e., the feeding strip isn't matched to 50Ω and the antenna won't radiate properly.

The prototype arrived and has been assembled at Robin Radar Systems. The substrate layer 1 & 2 and 4 are shown in figure 5.1a. The substrates are shown from their top and bottom view. Furthermore, their is used a frame to hold substrate layer number 3. This is shown in figure 5.1b. In this figure, also the foam layer is presented. The prototype is assembled, and the result is shown on the cover page of this thesis. What should be noted is that the top substrate with the patch antennas is very thin. In the assembly of the array, the 4 corners of the top substrate are a bit too tight, and therefore, the top substrate is bulging.

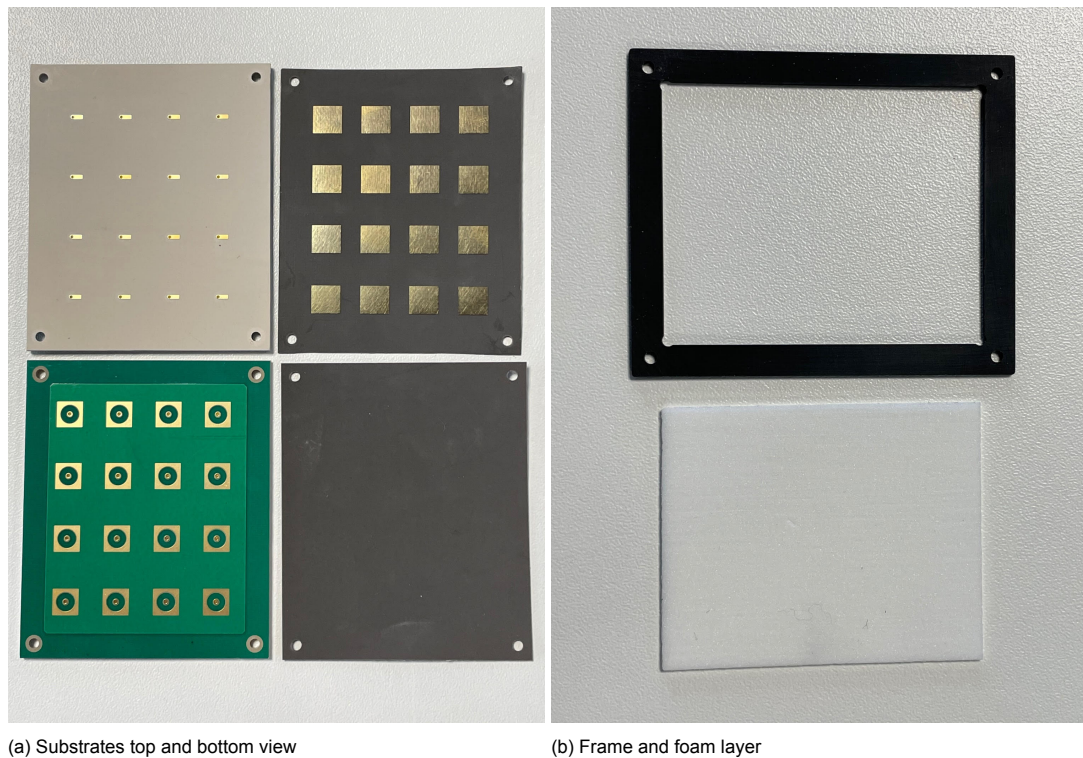


Figure 5.1: All the substrate layers manufactured for the prototype. In figure 5.1a is the top and bottom view of the feeding strips, followed by the top and bottom view of substrate layer 4. In figure 5.1b is the foam layer and the frame to hold it.

5.2. Measurement Setup

This section describes measurement equipment and setup. The goals of this project are to create a wideband antenna with certain scanning capabilities. Therefore, a comparison on return loss and radiation pattern are conducted at least.

The reflection coefficient of the antenna elements themselves as well as the coupling between the elements are measured. These measurements give the passive S-parameters. Via the Matlab scripts in appendix A, the active S-parameters are calculated. These are then compared to the active S-parameters simulated in CST.

For the radiation pattern, four measurements are conducted:

- Co-polarisation pattern of element 6
- Cross polarisation pattern of element 6
- Co-polarisation pattern of element 6, 7, 10 and 11
- Cross polarisation pattern of element 6, 7, 10 and 11

The radiation pattern of element number 6 is measured, while the other ports are terminated with 50Ω . The cross polarisation pattern is measured by rotating the PCB 90 degrees. These two measurements are also conducted, while the four center patch antennas are excited simultaneously. These measurements give the radiation pattern at broadside. The measured radiation patterns are compared with the simulated ones on the frequencies of 13.5, 14.5, 15.5 and 16.5 GHz.

The measurements are conducted in the lab and anechoic chamber at Robin Radar Systems. The anechoic chamber is visible in figure 5.2a. First, the S-parameters for each individual element are measured by the vector network analyzer (VNA) KEYSIGHT E5063A. This is done by first calibrating the VNA on the frequency range from 12.5 till 17 GHz using the KEYSIGHT ECal Module N7554A. Whereafter, each individual element is measured and the coupling between each individual element is measured. The VNA is first calibrated to remove all effects frequency range from the transmission line.

Therefore, the offset on the VNA is set to 0 dB and the passive S-parameters can be measured correctly. The measurement setup for the S-parameters is displayed in figure 5.2b. The measured S-parameters are exported to Matlab and plotted using the Matlab codes in appendix A.1 and A.2.

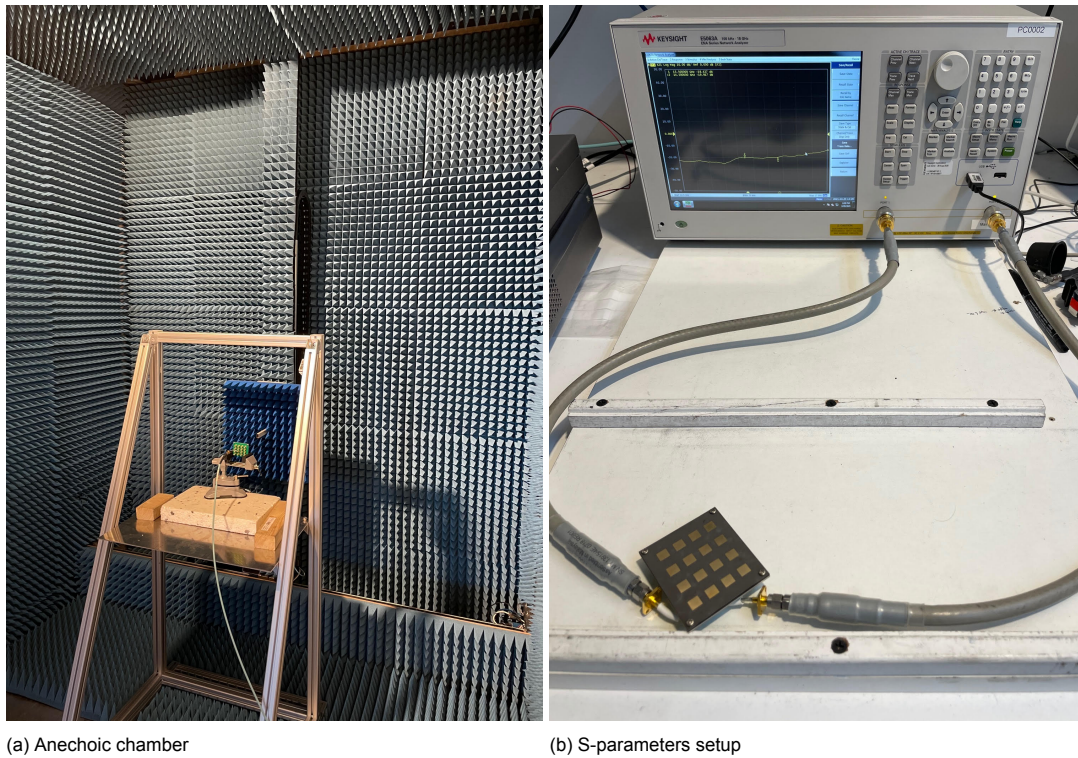


Figure 5.2: The measurement setup for the phased patch antenna array. The anechoic chamber is used to measure the radiation pattern of the antennas. The S-parameters are measured using a VNA.

Subsequently, the radiation pattern of a single element number 6 and the 2x2 center patch antennas is measured. The measurement is done in the near field of the antenna array using a planar scan with a waveguide probe. The antenna array is placed at 40 cm distance of the waveguide probe. The element is excited using the VNA. The planar scan moves in a grid of 40 by 40 cm, where the origin of the grid is the patch antenna. The planar takes steps of 0.5 till 0.7 mm. These are approximately steps of $\lambda/4$ till $\lambda/3$ big. These steps can't be too big. Otherwise, information of the radiation pattern is missed.

First the single element is measured with a horizontal and vertical polarisation. This is done by a single cable. However, for the excitation of the four elements a 4 way power splitter is used. The cables coming out of each channel from the splitter are of equal length. Thus, each element is excited with equal amplitude and phase. All elements which aren't excited are terminated with 50Ω . After these measurements software from Robin Radar Systems is used to convert the near field to farfield. These plots are extracted to Matlab to plot the farfield radiation pattern at the different frequencies using the Matlab code from appendix A.3.

Ultimately, all the measuring equipment is displayed in table 5.1. Each measurement is displayed in a different column.

Table 5.1: The measuring equipment used for each of the three measurements: Return Loss, near field radiation pattern, farfield gain measurement.

Return Loss measurement	Near field radiation pattern
VNA KEYSIGHT E5063	VNA KEYSIGHT E5063
Calibrator KEYSIGHT ECal Module N7554A	Calibrator KEYSIGHT ECal Module N7554A
2 SMA cables	Mini-Circuits ZN4PD1-183W-S+ Power splitter
2 SMA to SMP converters	2 SMA cables
	4 SMA to SMP converters

5.3. Measurements & Verification

This section will present the results for the measurements. After the assembly, first the return loss of the antenna has been measured, followed by the radiation pattern. These measurements are done using the measurement setup explained before.

5.3.1. Return Loss

The passive S-parameters of the prototype are measured with the VNA. These are exported to Matlab and the active S-parameters at broadside were calculated. The active S-parameters for the center four elements are given in figures 5.3 and 5.4. These are of interest as these patch antenna are most influenced by mutual coupling of the other elements. The active S-parameters at broadside of the other elements are given in appendix C.2.1. In all the figures, the simulated active S-parameters are given by the dashed line and the measured active S-parameters are given by the solid line.

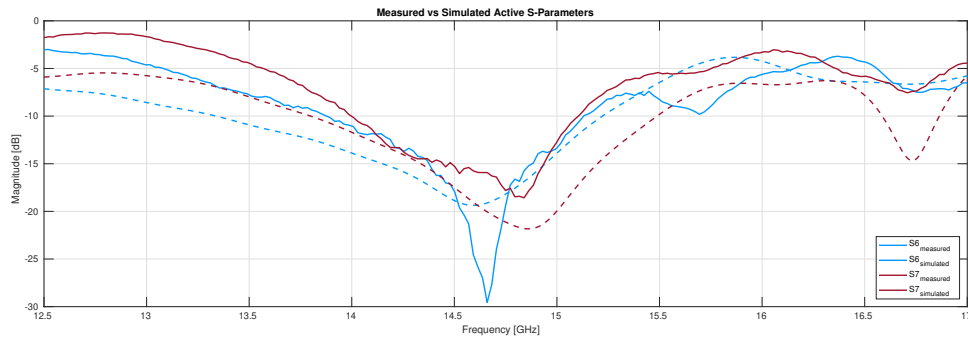


Figure 5.3: The active S-parameters of elements 6 and 7 of the prototype compared to its simulation for antenna element 6 and 7 of the array. The dashed lines are the simulated S-parameters and the solid lines are the measured S-parameters.

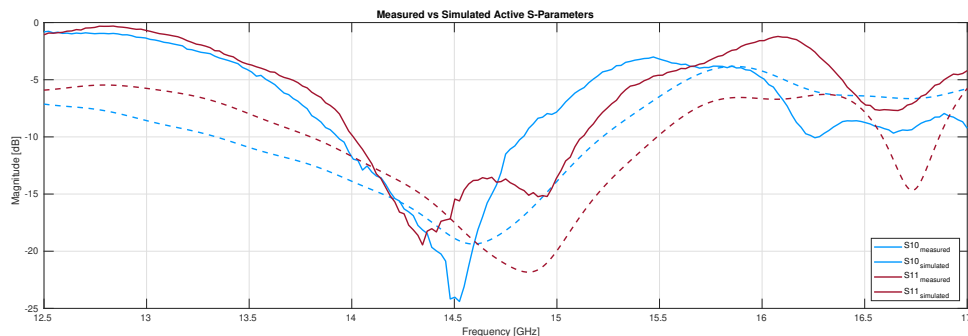


Figure 5.4: The active S-parameters of elements 10 and 11 of the prototype compared to its simulation for antenna element 10 and 11 of the array. The dashed lines are the simulated S-parameters and the solid lines are the measured S-parameters.

Comparing the simulations with the measurements in figure 5.3, the measured resonance frequencies of the antenna elements both match the simulated one. The resonances and impedance bandwidth of the antenna elements are displayed in table 5.2. All the four elements match almost in their resonance frequency, except for element 11. But, this element has two resonances close together, and only the strongest one was taken. The other resonance which is in the same impedance bandwidth is 15.95 GHz, and therefore, almost equal to the resonance of the simulated element. It is also observable that element 7 and 11 have another resonance around 16.7 GHz. Both of the measured antenna elements have also a resonance at that frequency, except that they are not below -10 dB. Furthermore, the measured impedance bandwidth of the antenna elements vary between 0.90 and 1.23 GHz. While, the simulated bandwidth is either 1.69 or 1.88 GHz.

The main differences in the active S-parameters are due to the different phase-responses measured by the antenna. As described, the antenna's top substrate is bulging, and therefore, a phase difference as the gap between the feeding strip and the antenna is increased further. This was already observed

for the reflection coefficient with due to tolerance of the substrate thickness in figure 4.15. As the active S-parameters depend on the passive S-parameters magnitude and phase, this is of influence on the reflection coefficient. This yields also for the active S-parameters shown in appendix C.2.1.

The S-parameters are not simulated at a scanning angle, but this phase difference will especially influence the return loss at scanning angles, as the phase is used as well. This could be prevented by, for example widening the assembly holes, but this creates the problem that the antenna elements are not straight on their feeding strips. Another solution could be to glue the center of the top substrate, but the influences by the glue are also unknown on the performance.

Table 5.2: The resonance frequencies f_c and impedance bandwidth B of the active S-parameters at broadside of the center four elements measurements and simulations.

Element no.	Measured f_c [GHz]	Simulated f_c [GHz]	Measured B [GHz]	Simulated B [GHz]
6	14.66	14.59	13.88-15.11 = 1.23	13.34-15.22 = 1.88
7	14.84	14.86	14.00-15.10 = 1.10	13.80-15.49 = 1.69
10	14.52	14.59	13.93-14.83 = 0.90	13.34-15.22 = 1.88
11	14.35	14.86	14.01-15.12 = 1.11	13.80-15.49 = 1.69

5.3.2. Radiation Pattern

The radiation pattern has been measured in the anechoic chamber at Robin Radar Systems for element 6 and the four center elements. The measurements are done in the near field and converted to the far field using software from Robin Radar Systems. The files are exported to Matlab and using Matlab, the far field radiation pattern is plotted for the co- and cross polarisation. This is done at the frequencies of 13.5, 14.5, 15.5 and 16.5 GHz. Unfortunately, the data is normalised during the conversion from near field to farfield; thus, the difference between the co-polarisation level and cross-polarisation level can't be extracted from these measurements. Also, the extracted data has a domain issue, as the magnitude of the data is in spherical coordinates, while the axes are still in Cartesian coordinates. This makes it hard to compare it directly to the simulated data from CST. However, the most clear views are chosen to compare the results. Therefore, the extracted data is plotted from the top view and a 3D perspective view. And, the simulated data extracted from CST, is plotted from the top view of the 3D simulation and in perspective view from the 3D simulation.

A comparison is made for the frequencies of 14.5 and 16.5 GHz. The frequency of 14.5 GHz is compared, as the resonance frequency of the antenna is at this frequency. While the frequency of 16.5 GHz is compared as the radiation pattern has some irregularities. The other measurements and simulations of the other two frequencies are displayed in appendix C.2.2. First the co-polarisation radiation pattern of the single element is compared to the simulations at the different frequencies. Then, the cross-polarisation radiation pattern of the single element. Followed by both polarisation radiation patterns of the center four patches.

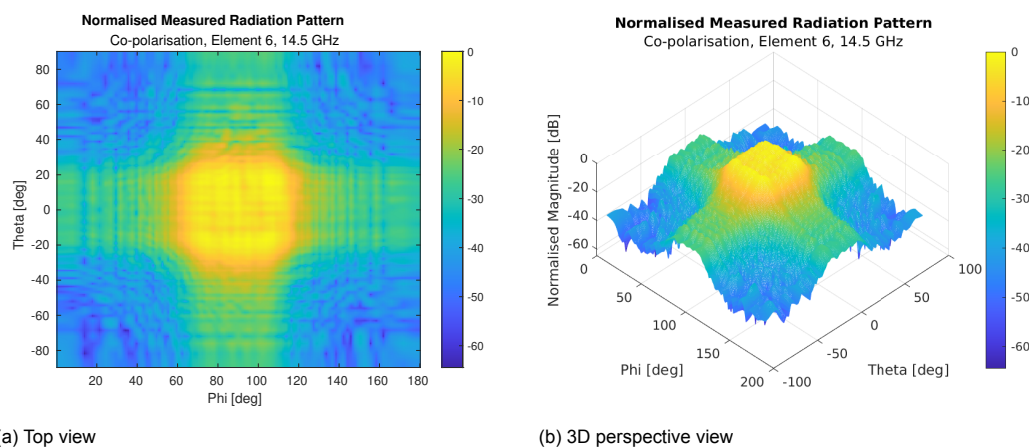


Figure 5.5: The measured co-polarisation radiation pattern of element number 6 from different viewing points. The pattern is normalised and is measured at a frequency of 14.5 GHz.

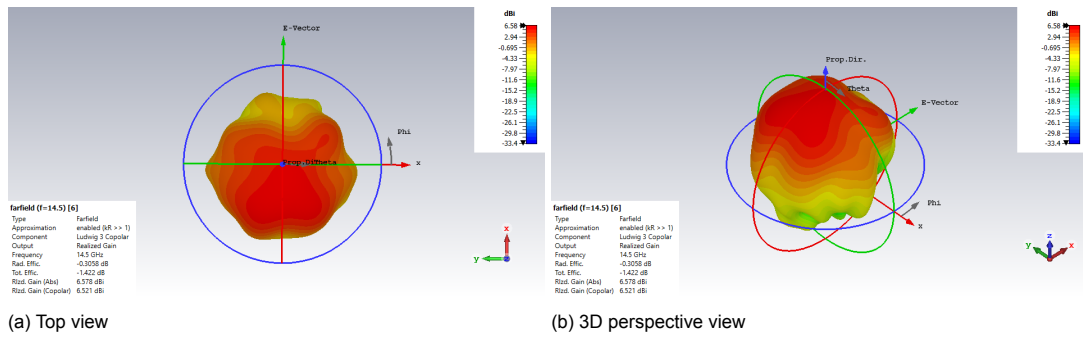


Figure 5.6: The simulated co-polarisation radiation pattern of element number 6 from different viewing points. The pattern is normalised and is simulated at a frequency of 14.5 GHz.

The measured radiation pattern of antenna 6 at 14.5 GHz is shown in figure 5.5. The co-polarisation of the radiation pattern is displayed. Comparing this, to the simulated radiation pattern in figure 5.6. The radiation pattern looks quite similar to each other, as well as to the radiation pattern of a patch antenna. The simulated antenna has some influences of mutual coupling from the other elements in the positive x-direction. This is observable in the top view in figure 5.6a.

The simulations at 16.5 GHz for the single element are harder to compare. The simulated results are shown in figure 5.8. The pattern is wide in the y-direction and has a side lobe in the negative x-direction. In the measured results, this is observed as well. This is shown in figure 5.7a. Around theta is -10 degrees, there is a gap in the radiation pattern, which indicates there is a sidelobe present as well. In top view of the simulation in figure 5.8a, there is also a sidelobe in the positive x-direction. This is slightly visible in the measured data in the top view, as there are some parts of higher measured magnitude around theta is 40 degrees in figure 5.7a.

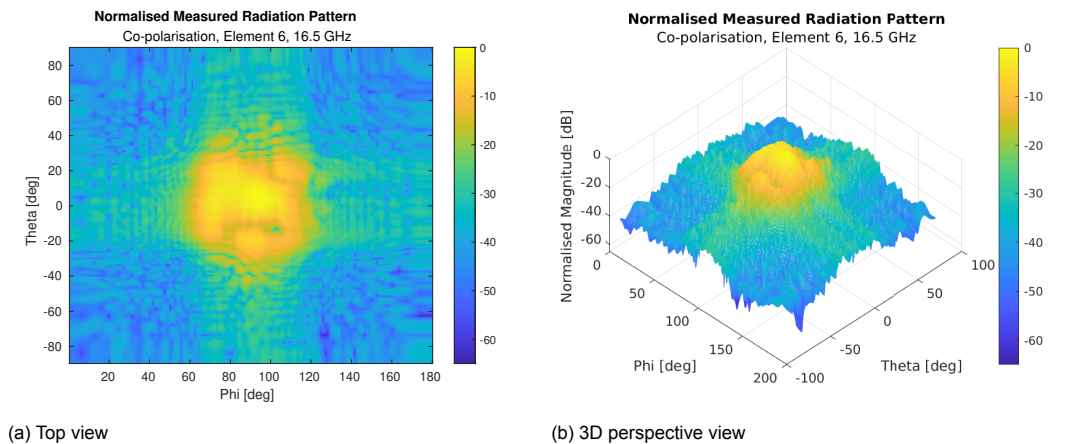


Figure 5.7: The measured co-polarisation radiation pattern of element number 6 from different viewing points. The pattern is normalised and is measured at a frequency of 16.5 GHz.

The measured and simulated cross polarisation level of the element at 14.5 GHz is displayed in figures 5.9 and 5.10, respectively. This is much harder to compare than the co-polarisation pattern as it is much weaker and radiates in more directions. But, from what is shown in the top view from both figures, a similarity is discernible. In the simulated pattern, there is a main pattern at the origin which forms the shape of an 'n'. This is also observed in the measured data. As the data is centered around negative theta, and there is a small gap at phi is 90 degrees. Furthermore, there are two side lobes in the positive x-direction in the simulation. These could be compared to the side lobes at theta is equal to 45/50 degrees in figure 5.9a.

The simulated cross polarisation level at 16.5 GHz is much stronger than at 14.5 GHz. This is shown in figure 5.12. It is observed that the cross polarisation level has two strong lobes towards the positive x-axis and 2 long shaped lobes in the negative direction. In these long shaped lobes the magnitude is decreased in the center. These characteristics of the cross polarisation pattern are observed in the

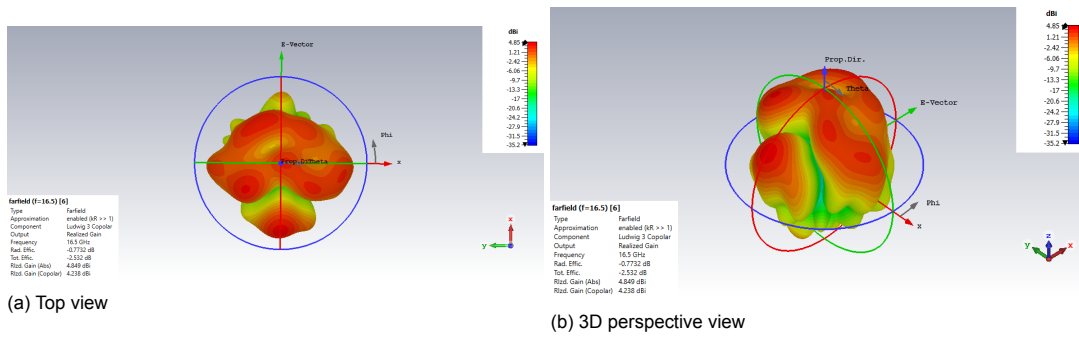


Figure 5.8: The simulated co-polarisation radiation pattern of element number 6 from different viewing points. The pattern is normalised and is simulated at a frequency of 16.5 GHz.

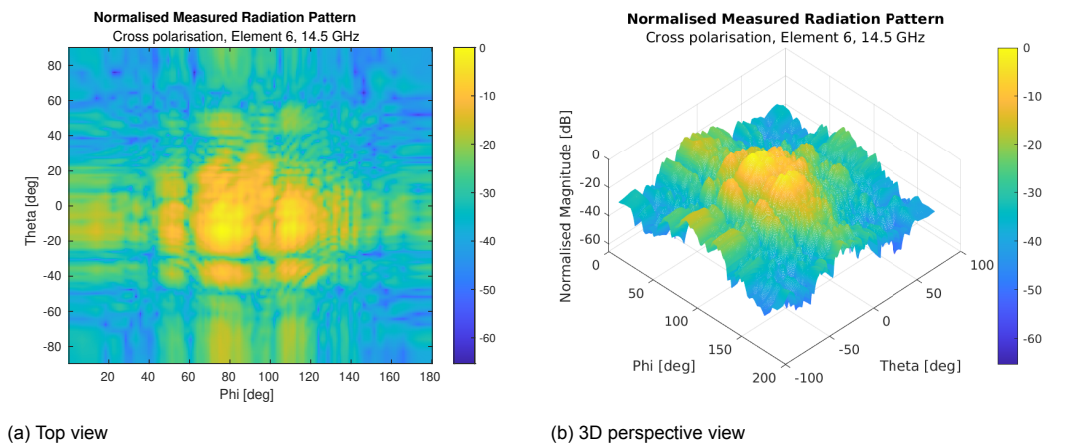


Figure 5.9: The measured cross polarisation radiation pattern of element number 6 from different viewing points. The pattern is normalised and is measured at a frequency of 14.5 GHz.

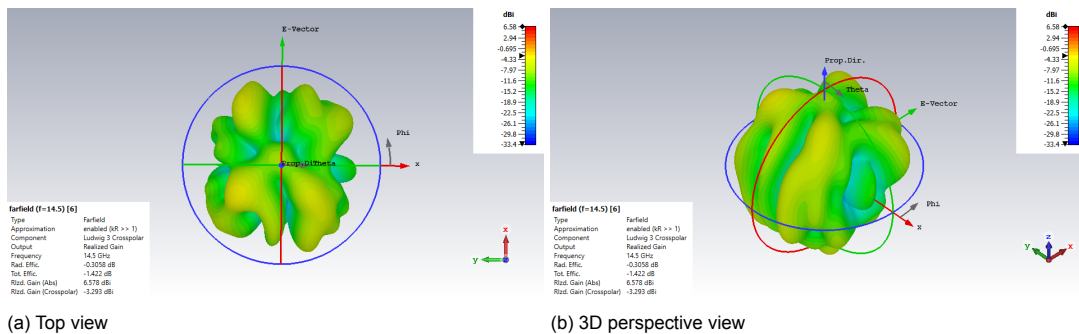


Figure 5.10: The simulated cross polarisation radiation pattern of element number 6 from different viewing points. The pattern is normalised and is simulated at a frequency of 14.5 GHz.

measured data as well. The pattern is displayed in figure 5.11. The two lobes in the positive x-direction are observed at theta equal to 20 degrees. While there are 4 lobes in the negative x-direction, a strong one at theta from 0 till -20 degrees and a weaker one theta equal to -40 degrees. Also, it is clear that in both simulated and measured data the cross-polarisation is low at phi is 90 degrees. At last, in the measured data there is observed a decrease of -20 till -30 dB in gain, while the gain in the simulated data decreases from -1.529 dBi till -17 dB or even lower in some parts. This is also a decrease of almost -20 dB, and thus, comparable.

The center four elements are excited simultaneously and the measured radiation pattern at 14.5 GHz is displayed in figure 5.13. This is very comparable to the simulated radiation pattern at 14.5 GHz, shown in figure 5.14. As there is one main lobe at broadside in both plots. There are some sidelobes in the simulated radiation pattern, but these are at an angle theta of 90 degrees. This can't be measured

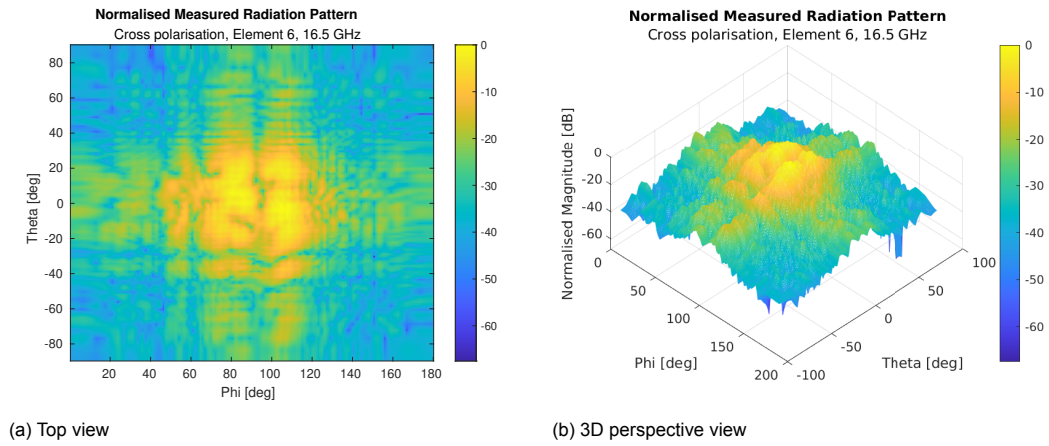


Figure 5.11: The measured cross polarisation radiation pattern of element number 6 from different viewing points. The pattern is normalised and is measured at a frequency of 16.5 GHz.

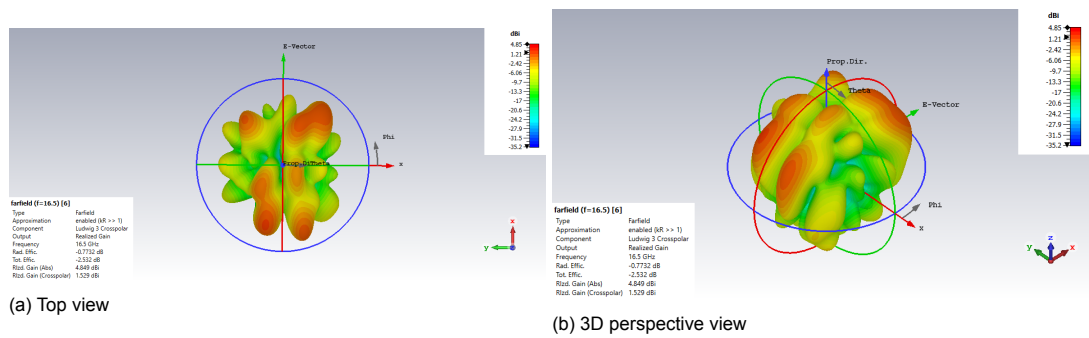


Figure 5.12: The simulated cross polarisation radiation pattern of element number 6 from different viewing points. The pattern is normalised and is simulated at a frequency of 16.5 GHz.

by a planar scan, when the antenna is just radiating towards broadside.

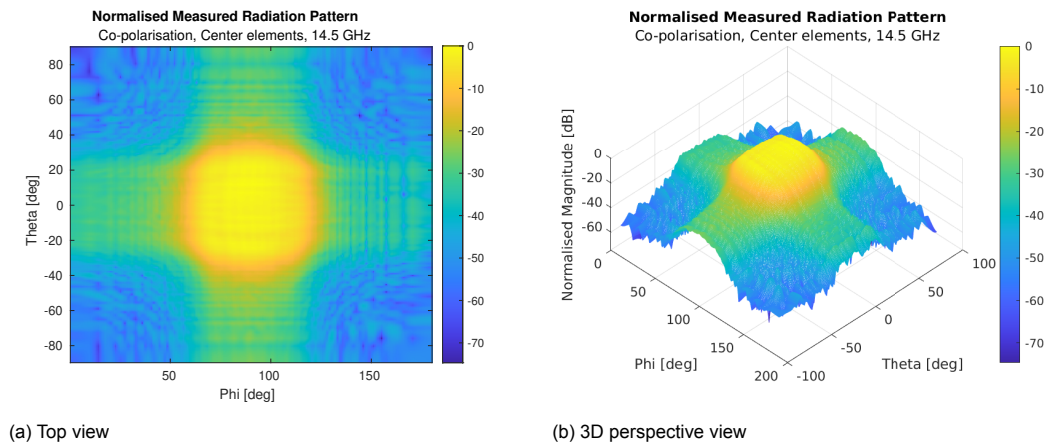


Figure 5.13: The measured co-polarisation radiation pattern of the 4 center elements from different viewing points. The pattern is normalised and is measured at a frequency of 14.5 GHz.

More interesting is the co-polarisation radiation pattern at 16.5 GHz. The coupling between the elements in the x-direction is much stronger in this direction. Therefore, there is a kind of gap in both the measured and the simulated data. The measured radiation pattern at 16.5 GHz is displayed in figure 5.15 and the simulated pattern is displayed in figure 5.16. Both plots show the gap in the main lobe in the positive x-direction. The sidelobes in the simulated radiation pattern can also be observed in the top view of the measured data in figure 5.15a. These sidelobes are expressed as a kind of waves

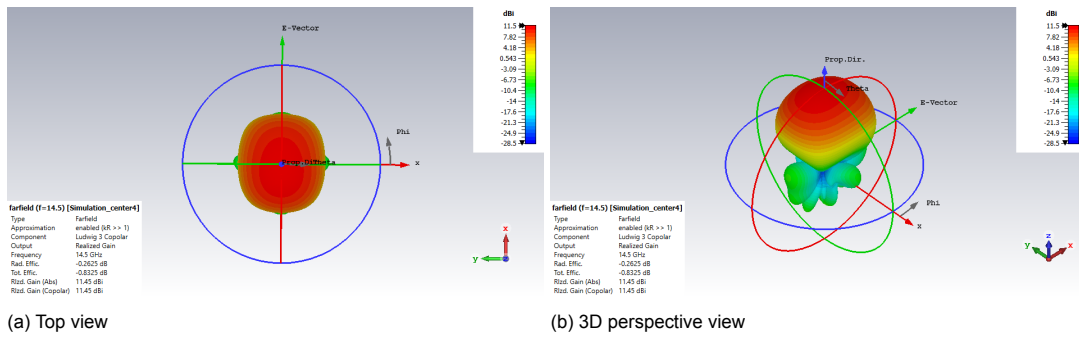


Figure 5.14: The simulated co-polarisation radiation pattern of the 4 center elements from different viewing points. The pattern is normalised and is simulated at a frequency of 14.5 GHz.

around theta is ± 40 degrees.

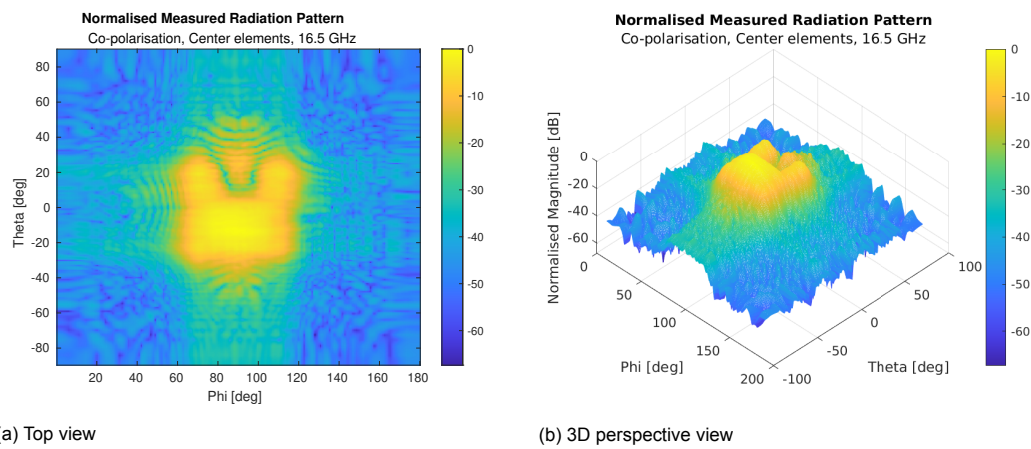


Figure 5.15: The measured co-polarisation radiation pattern of the 4 center elements from different viewing points. The pattern is normalised and is measured at a frequency of 16.5 GHz.

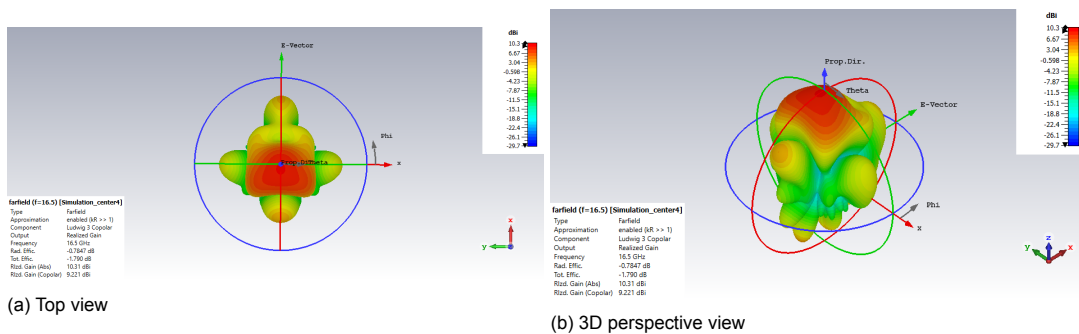


Figure 5.16: The simulated co-polarisation radiation pattern of the 4 center elements from different viewing points. The pattern is normalised and is simulated at a frequency of 16.5 GHz.

Finally, the cross polarisation level of the center four patch antennas are compared at both frequencies. The measured cross polarisation pattern of the center antennas at 14.5 GHz are displayed in figure 5.17. The simulated radiation pattern is shown in figure 5.18. It is observed that the patterns compare easy as there are only two main lobes for a positive z, which is seen in both figures.

The cross polarisation pattern at 16.5 GHz is comparable to the pattern at 14.5 GHz, except that the pattern has much more sidelobes in every direction. It is clear where the sidelobes are in the simulated pattern in figure 5.20. It is also observed that there are two large main lobes, which are weaker in magnitude in the center of lobes. The measured cross polarisation radiation pattern is shown in figure

5.19. It seems that there are some sidelobes in the x- and y-direction, displayed by the waves in the top view of the pattern, shown in figure 5.19a. However, the measured main lobes of the cross polarisation are not weakened in the center, while the simulated pattern is weakened. Therefore, the cross-polarisation for multiple elements is comparable at different frequencies, except for the sidelobe levels at the higher frequency.

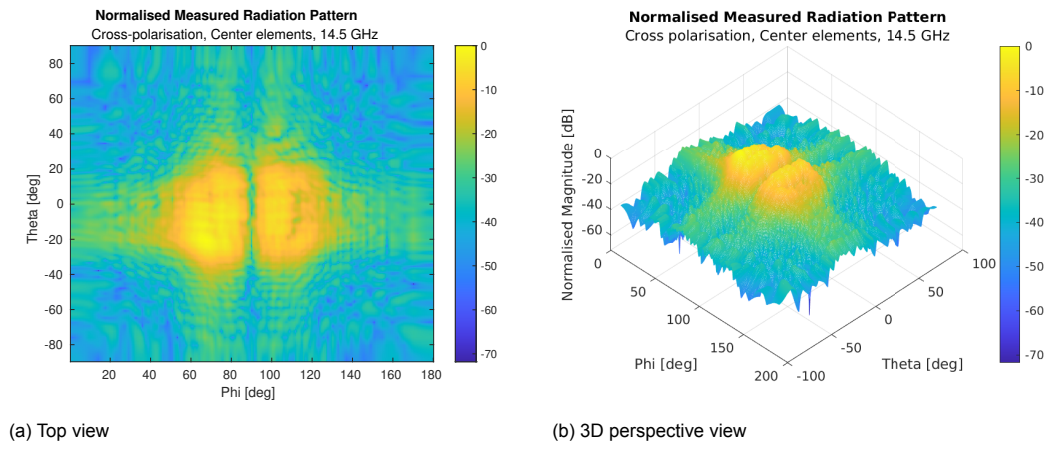


Figure 5.17: The measured cross polarisation radiation pattern of the 4 center elements from different viewing points. The pattern is normalised and is measured at a frequency of 14.5 GHz.

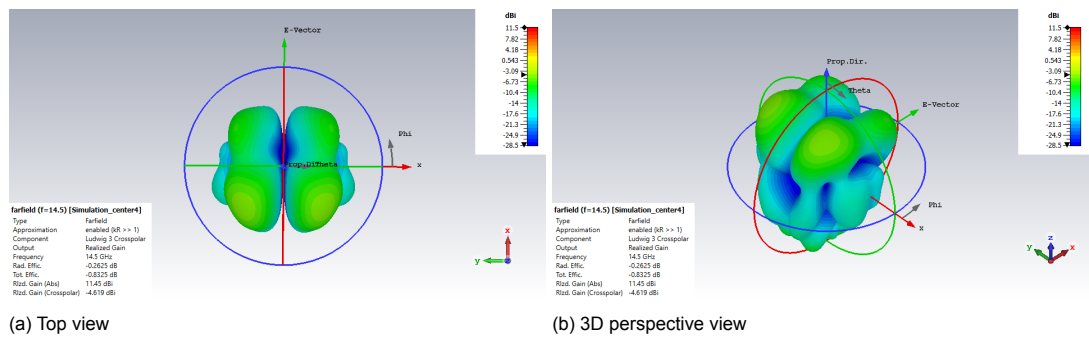


Figure 5.18: The simulated cross polarisation radiation pattern of the 4 center elements from different viewing points. The pattern is normalised and is simulated at a frequency of 14.5 GHz.

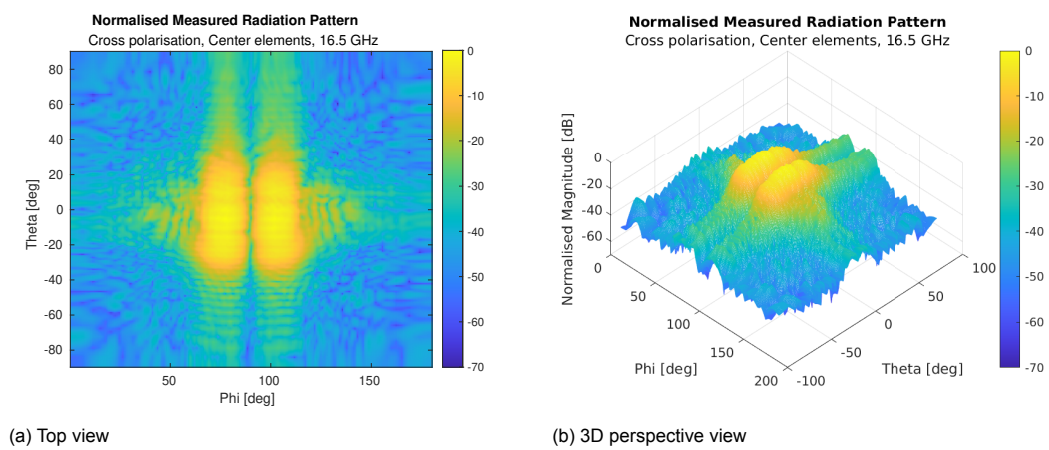


Figure 5.19: The measured cross polarisation radiation pattern of the 4 center elements from different viewing points. The pattern is normalised and is measured at a frequency of 16.5 GHz.

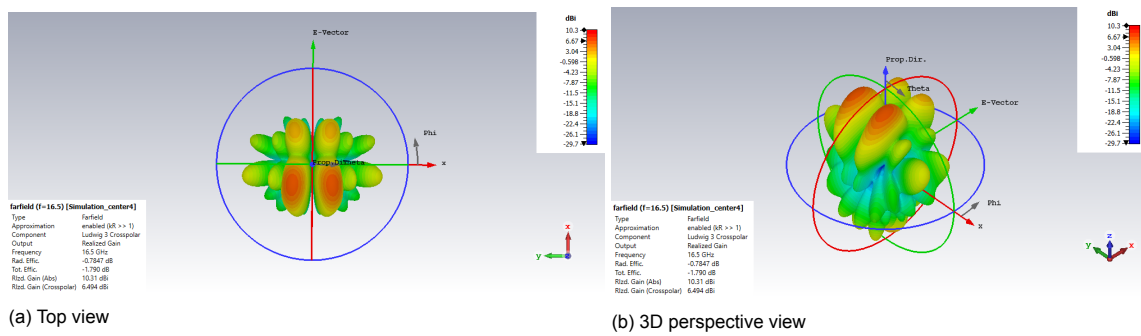


Figure 5.20: The simulated cross polarisation radiation pattern of the 4 center elements from different viewing points. The pattern is normalised and is simulated at a frequency of 16.5 GHz.

All in all, the measured radiation pattern at broadside is comparable to the simulated pattern for the single element, as well as, the center four elements. Unfortunately, the gain couldn't be extracted out of the measured data, and thus, could not be compared. The bulging of the top substrate doesn't have influence on the radiation pattern on broadside. However, as this has influence on the phase distribution of the elements, the radiation patterns at scanning angle will probably be influenced by this. More measurements with phase shifters are necessary in order to draw conclusions about this.

5.4. Conclusion

To conclude, the design of the prototype has been explained. The measurements and their setups are presented. Whereafter, the measurements were performed and the results have been presented. These have been compared to the simulated results from CST. The active S-parameters of the center four elements are comparable to the simulated ones except that the measured return loss is much weaker. The radiation patterns at broadside are comparable to the simulations. This is for the co-polarisation as well as the cross polarisation patterns. Nonetheless, the antenna array radiates comparable to the simulated antenna array and the concept of a proximity fed antenna in a multi-layer substrate has been proven.

6

AMC Ground Plane

As described in chapter 1, an artificial magnetic conducting ground plane can be a useful addition to existing antennas to increase their current performance. Therefore, a literary study has been conducted if the proposed antenna array from chapter 4 could be enhanced, to improve performance. This chapter describes the literary study and how an AMC element is chosen. Then, a comparison is made between multiple artificial magnetic conducting ground unit cells. These unit cells are added to the model of a single patch in an infinite array model study improvements. The enhancements are summarized using the infinite array model and a suggestion is made whether or not the antenna from chapter 4 could be enhanced.

6.1. AMC element selection

Studying the existing literature in chapter 1, there are plenty of AMC unit cells that improve either the impedance bandwidth or its radiation performance. Most ideally, the side- and backlobes of the patch antenna due to surface waves are reduced, while the impedance bandwidth is kept equal. Also, the antenna's polarisation must be maintained. From the literature review, it is discernible that each unit cell's size is around $\lambda/10$ to $\lambda/6$. In comparison to the proximity fed antenna, this is quite small, as the antenna's is approximately $\lambda/3$.

The selection of an adequate unit cell is done by comparing multiple candidates. They are compared using the unit cell simulation in CST. This is a simulation for periodic structures. A Floquet port is used for the simulation, which is a port to simulate a plane wave radiating onto the unit cell. This plane wave have a propagation direction that is set by frequency, phasing, and geometry of the AMC unit cell [57]. The unit cells are tested on their reflection coefficient, which should be close to zero as the backward radiated wave by the antenna, is supposed to be reflected into the radiating direction of the antenna. If the unit cell reflects almost perfectly in the required frequency range, the unit cell is implemented in the infinite array antenna model from chapter 3. These results are compared and a proper candidate is chosen to improve the performance of an antenna array.

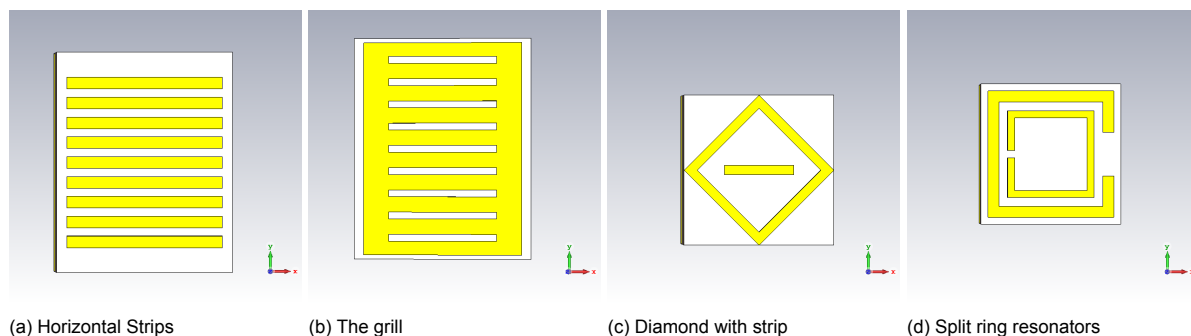


Figure 6.1: The candidate unit cells that will be simulated in an infinite array simulation.

The simulated unit cells are shown in figure 6.1. These unit cells all have a reflection coefficient close to zero, and are implemented as a ground plane on the infinite array model. Also, the polarisation of the unit cells is designed to be horizontally polarised. The following unit cells are considered:

- Horizontal strips (chapter 6.1.1)
- A horizontally polarised grill (chapter 6.1.2)
- A diamond with a horizontal strip (chapter 6.1.3)
- Two split ring resonators (chapter 6.1.4)

All of the above are simulated in two varieties: as a full AMC ground plane and as a kind of stripped version around the feeding pin and patch antenna. This simulation is done as the field below the antenna is stronger coupled than next to the antennas. Therefore, a reflector, such as an AMC ground plane, to the weaker sides of an antenna might be a solution to improve the performance. In the models, a comparison is conducted between the S-parameters, the farfield radiation pattern and its cross-polarisation pattern. These properties will determine if the antenna's performance can be enhanced by an AMC ground plane.

6.1.1. Horizontal strips

The horizontal strips is a unit cell, where a single strip in the x-direction, recurs multiple times. The two varieties are shown in figure 6.2. The first model is displayed in figure 6.2a. The AMC ground plane is full of strips, symmetrically below the patch. The second model is a stripped version, and shifted due to the feeding pin. This model is displayed in figure 6.2b. The main difference between these two models is that the strips are also smaller.

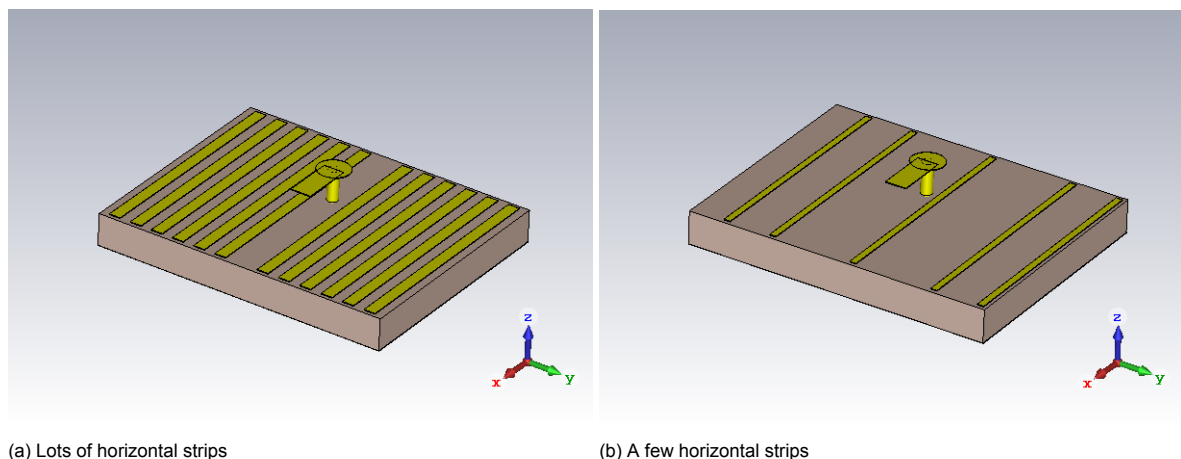
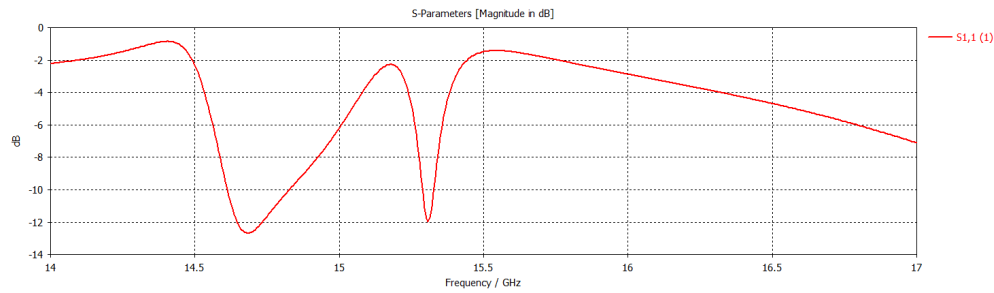


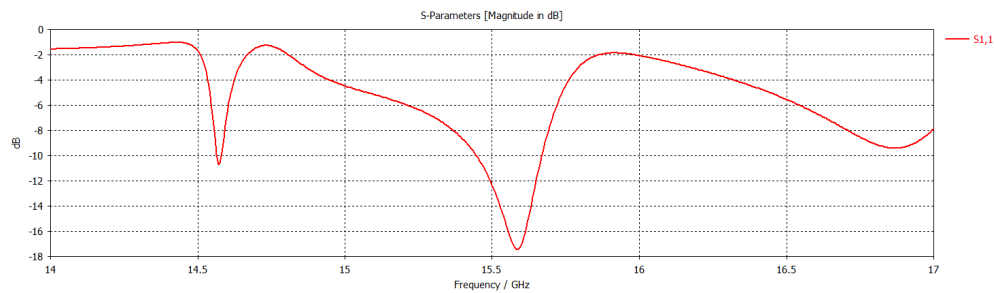
Figure 6.2: The horizontal strips unit cells implemented on the antenna in perspective view without the top substrates and the patch antenna. The feeding strip is shown to show the unit cells in perspective.

The S-parameters of these models are shown in figure 6.3. It is clear that for both simulations the reflection coefficient has become worse. The impedance bandwidth has decreased in both cases to a maximum of approximately 250 MHz. Both antennas have two resonances. But, these are really small in amplitude and narrow band. Also, it seems that there is a third resonance in both antennas towards 17 GHz.

The absolute value of the radiation pattern for both antennas is shown in figure 6.4. The strips disorientate the focus of the radiation pattern into the positive z-direction. For the unit cell of the lots of strips, the antenna does not even radiate in the broadside direction anymore. This is due to the high cross polarisation level, displayed in figure 6.5a. Using fewer strips as a unit cell, the radiation pattern also exhibits a larger cross polarisation level, shown in figure 6.5b. However, the antenna still has a wide radiation pattern towards the main direction.

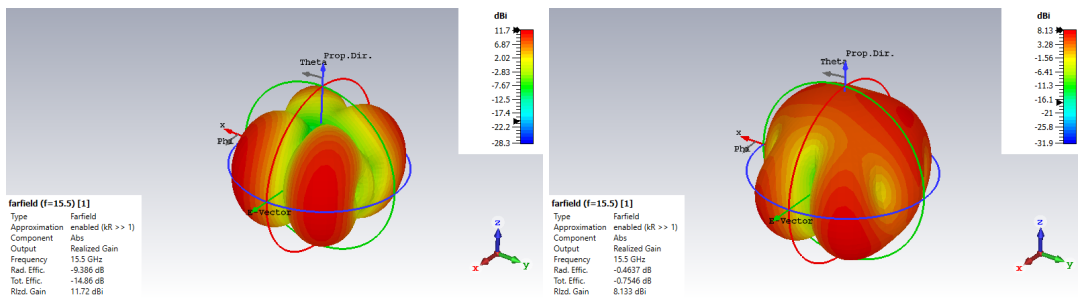


(a) Lots of horizontal strips



(b) A few horizontal strips

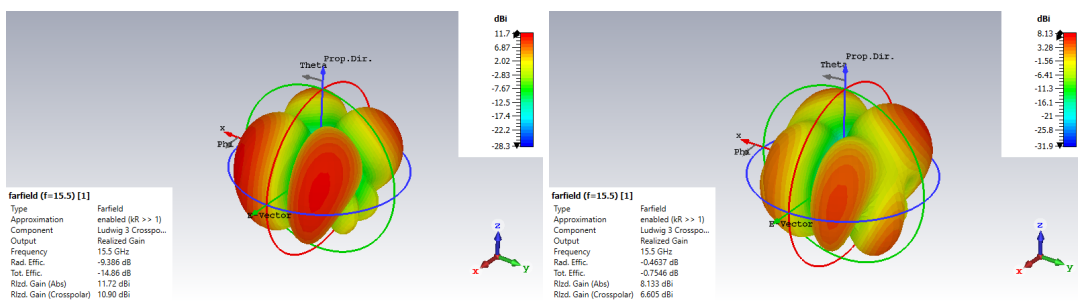
Figure 6.3: The reflection coefficient of the two antenna models with the two different strips AMC structures simulated in an infinite array.



(a) Lots of horizontal strips

(b) A few horizontal strips

Figure 6.4: The 3D radiation patterns of the two antenna models with the different strips AMC structures simulated in an infinite array. The model is simulated at a frequency of 15.5 GHz and the absolute value of the pattern is displayed.



(a) Lots of horizontal strips

(b) A few horizontal strips

Figure 6.5: The 3D radiation patterns of the two antenna models with the different strips AMC structures simulated in an infinite array. The model is simulated at a frequency of 15.5 GHz and the cross polarisation radiation pattern is displayed.

To conclude, adding strips as an AMC ground plane is not beneficial. Both unit cells don't improve the performance of the antenna. The impedance bandwidth decreases a lot and the radiation pattern exhibits a large cross polarisation level. The antenna with a lot of strips as an AMC ground plane doesn't even radiate to broadside anymore.

6.1.2. Horizontally polarised grill

This unit cell is similar to the unit cell from chapter 6.1.1. This unit cell, however, has a connection at both ends of the strips to the other strips. Implementation in the antenna is shown in figure 6.6a. The variety is shown in figure 6.6b, where the grill has been divided into two small ones on both sides of the patch antenna.

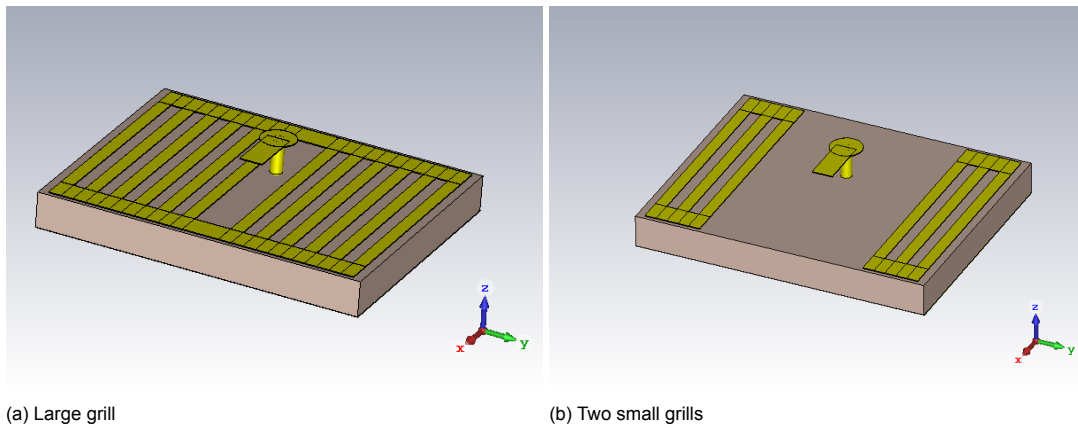


Figure 6.6: The grill unit cells implemented on the antenna in perspective view without the top substrates and the patch antenna. The feeding strip is shown to show the unit cells in perspective.

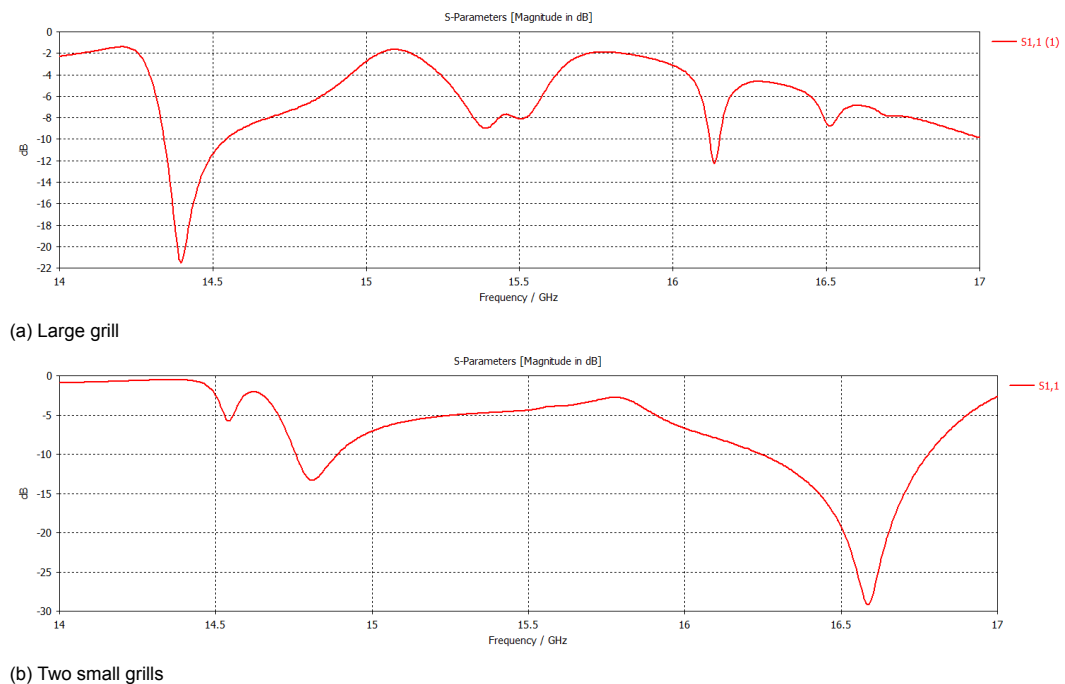


Figure 6.7: The reflection coefficient of the two antenna models with the two different grill AMC structures simulated in an infinite array.

The reflection coefficient of the antennas with the grill AMC unit cell is displayed in figure 6.7. It is observable that the large grill below the feeding strips creates up to five resonances in the frequency band of 14 to 17 GHz. These resonances are all narrow band and exist due to the different lengths in the grill. The smaller grills only have three resonances, from which only two are below -10 dB. There is a strong resonance around 16.6 GHz which has an impedance bandwidth of approximately 0.5 GHz. There are fewer resonances due to the stronger coupling between the antenna and its feeding strip as this is the resonance excited by the antenna. Nonetheless, it was much wider in the infinite array simulation of just the antenna.

The radiation patterns of both antenna designs are shown in figure 6.8. Both antennas are displayed with their absolute value. It is discernible in figure 6.8a, that the antenna element with the large grill radiates stronger in other directions than broadside. This is partly due to the large cross polarisation level, which is shown in figure 6.9a. However, the co polarisation level is also large, especially, in the corners of the grill in the negative z-direction. The radiation pattern of the two smaller grills, is comparable to an omnidirectional pattern of a regular patch antenna. This is displayed in figure 6.8b. The cross polarisation level is also less than the larger grill. This is shown in figure 6.9b. But, radiates to the same directions, due to the same horizontal oriented currents that run through the grill and are bent into vertically radiated waves by the corners of the grill.

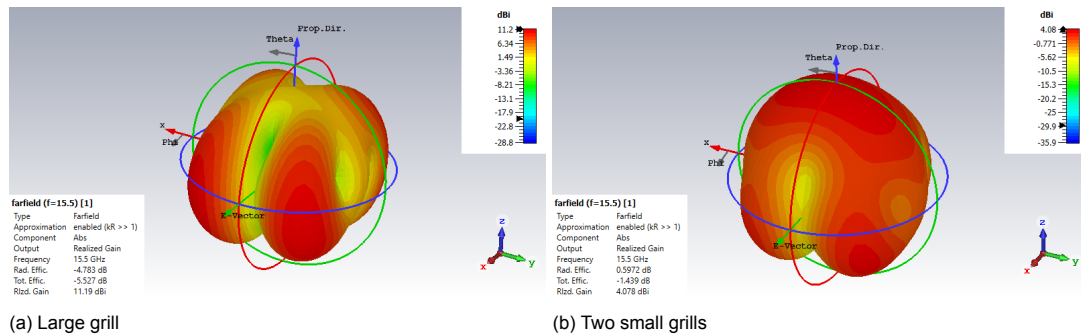


Figure 6.8: The 3D radiation patterns of the two antenna models with the different grill AMC structures simulated in an infinite array. The model is simulated at a frequency of 15.5 GHz and the absolute value of the pattern is displayed.

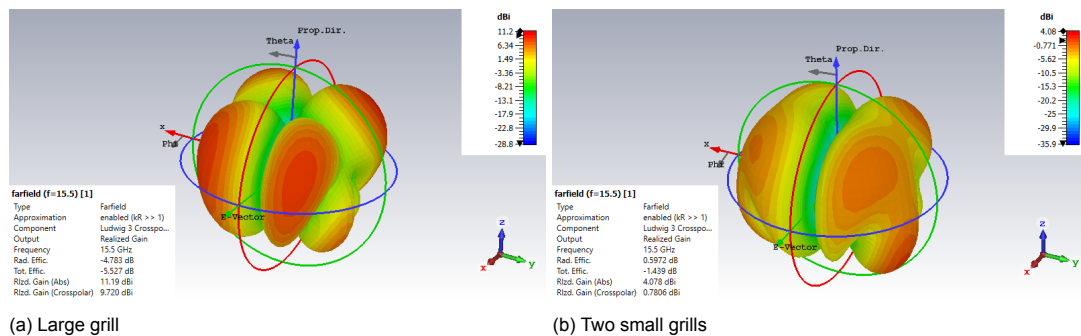


Figure 6.9: The 3D radiation patterns of the two antenna models with the different grill AMC structures simulated in an infinite array. The model is simulated at a frequency of 15.5 GHz and the cross polarisation radiation pattern is displayed.

To summarize, different types of grills have been discussed to implement as AMC unit cells. The gain of the antenna increases till a maximum of 11.9 dB for a full grill below the antenna. However, the return loss of the antenna is distorted, the antenna does not radiate to broadside and the antenna has a large cross-polarisation level due to this addition. More interesting might be to add, the two small grills at the sides of the substrate. The radiation pattern is still omnidirectional and the antenna still has the same resonance as the original antenna. But, the impedance bandwidth is smaller and the cross-polarisation level is somewhat larger.

6.1.3. Diamond with a horizontal strip

The third candidate as an AMC unit cell is a diamond with a horizontal strip. The strip is added to create an extra resonance with a horizontal reflection. The candidate has been implemented twice: an antenna with lots of unit cells and one with much less unit cells. This is shown in figure 6.10. For the antenna with less unit cells, the inner rows of unit cells are removed, as well as the center patch of the middle rows. This is to create a larger gap between the feeding strip and the unit cells below the strip.

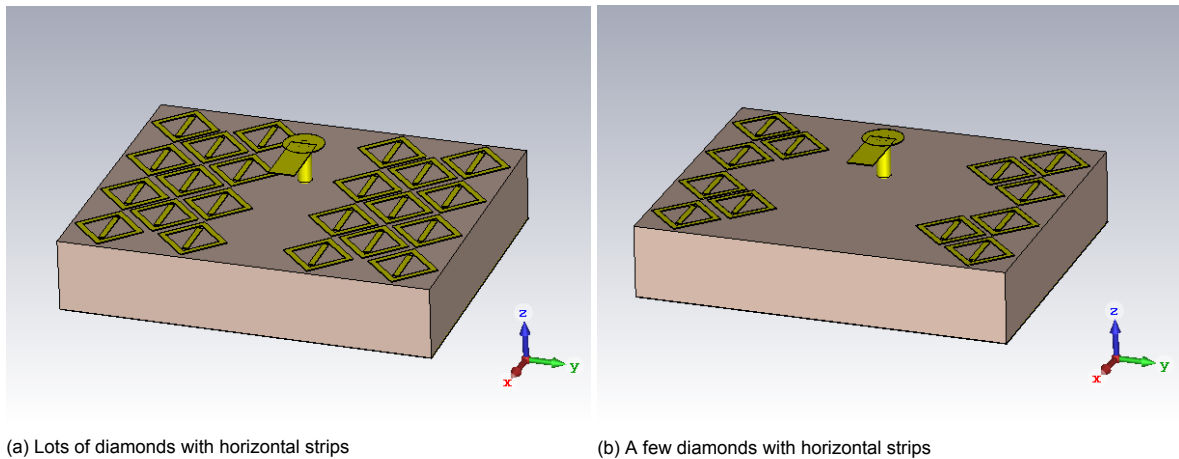


Figure 6.10: The diamond unit cells implemented on the antenna. The unit cell has a horizontal strip to create a larger reflection in the horizontal polarisation. The models are shown in perspective view without the top substrates and the patch antenna. The feeding strip is shown to show the unit cells in perspective.

It is discernible in figure 6.11, that both antennas have three resonances. Both antennas have the resonance from the antenna around 16.6 GHz and another resonance around 16 GHz, due to the AMC unit cell. They also have a third resonance at different frequencies. The resonance with lots of unit cells is at 15.5 GHz. This is observable in figure 6.11a. However, two of three resonances from that antenna are not below -10 dB and don't radiate properly. The antenna with the fewer unit cells has an extra resonance around 14.1 GHz. This is displayed in figure 6.11b. This antenna has two resonances that radiate below -10 dB. But, both antennas' resonances are still weak and narrow band.

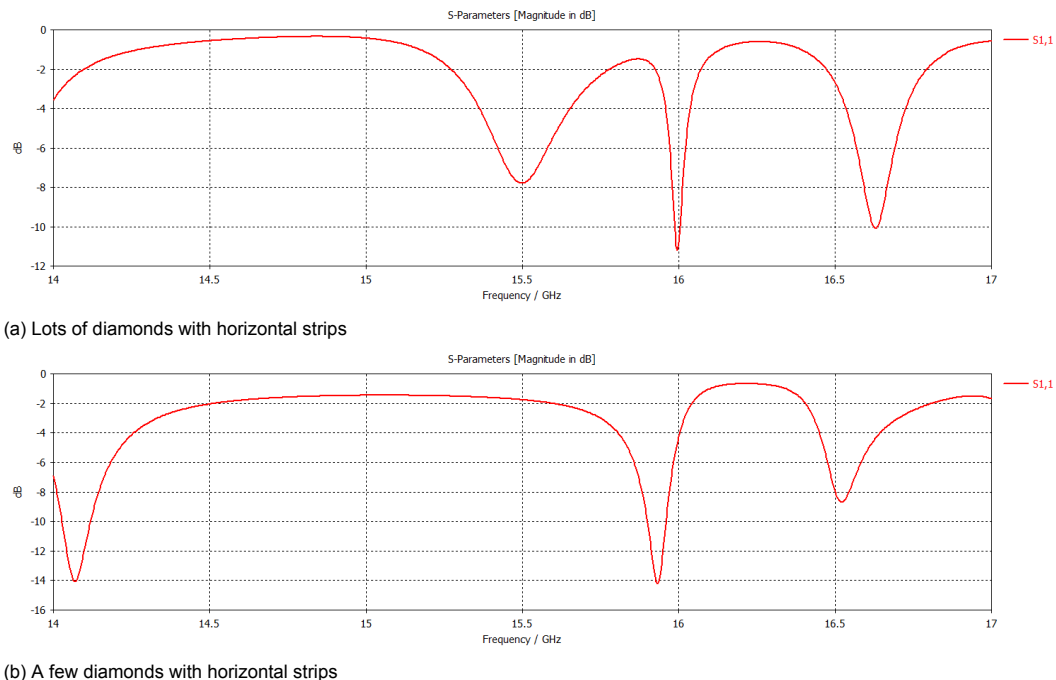


Figure 6.11: The reflection coefficient of the two antenna models with the two different diamond AMC structures simulated in an infinite array.

The absolute value of the radiation pattern of these antennas is displayed in figure 6.12. The antenna with lots of unit cells radiates strongly in the positive and negative x-direction. This is shown in figure 6.12a. But, the antenna doesn't radiate properly towards broadside. The radiation pattern is strong due to the coupling between the antenna and the unit cells. The cross-polarisation level, how-

ever, is much weaker than the co polarisation pattern. But, the antenna still has some currents running in the vertical direction, and therefore, some vertical polarised waves are excited. The antenna with fewer unit cells has a more omnidirectional radiation pattern. This is displayed in figure 6.12b. But, this antenna has a much stronger cross polarisation level compared to the absolute value than the antenna with lots of unit cells. This is shown in figure 6.13b. The antenna, however, has an asymmetrical radiation pattern towards broadside and is strong coupled towards the positive x-direction than the y-direction. This is due to the currents flowing in the feeding strip towards this direction and the antenna which is strong coupled around these directions.

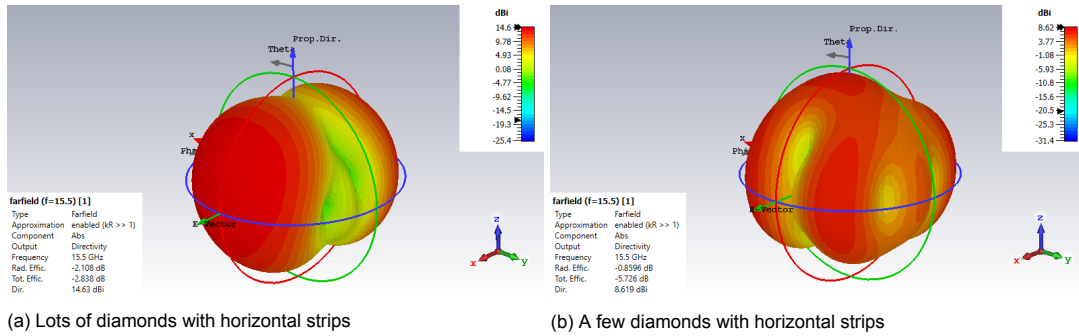


Figure 6.12: The 3D radiation patterns of the two antenna models with the different diamond AMC structures simulated in an infinite array. The model is simulated at a frequency of 15.5 GHz and the absolute value of the pattern is displayed.

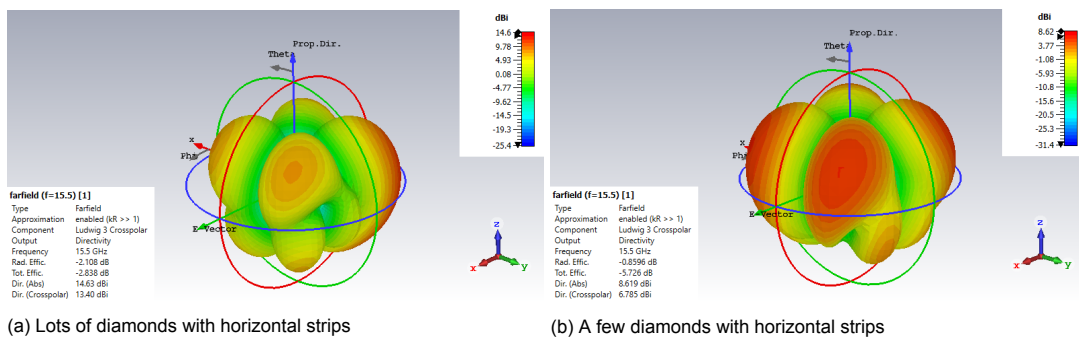


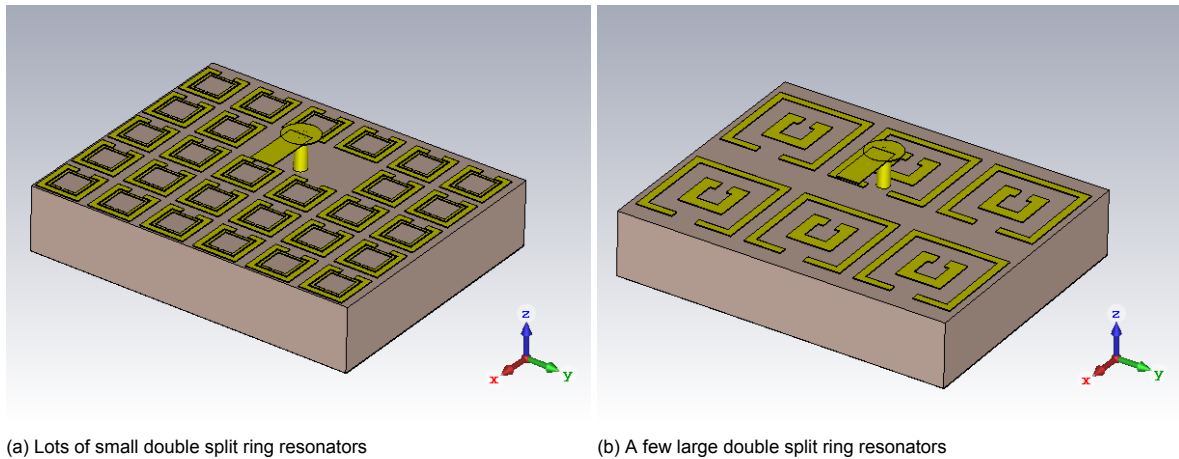
Figure 6.13: The 3D radiation patterns of the two antenna models with the different diamond AMC structures simulated in an infinite array. The model is simulated at a frequency of 15.5 GHz and the cross polarisation radiation pattern is displayed.

All in all, the diamond unit cell doesn't improve the antenna. The radiation pattern is strongly influenced by the unit cell, such that the antenna (almost) does not radiate towards broadside direction. The unit cells create extra resonances, but these are weak and narrow band. Also, the unit cells create large side lobe levels, which is undesirable.

6.1.4. Two split ring resonators

The final candidate as a unit cell is two split ring resonators. These have proven to be a good candidate as AMC ground plane in literature and are easy to implement. The split ring resonators implemented on the antenna are shown in perspective view in figure 6.14. The antenna's feeding strip is only shown as this brings the AMC ground plane good into perspective. In figure 6.14a, 28 unit cells of size $\lambda/10$ are implemented. And in figure 6.14b, 6 unit cells of size approximately $\lambda/6$ is displayed. In the ground plane with the smaller unit cells, two unit cells are removed to free space for the pin, while the pin in the other antenna is implemented within a split ring resonator.

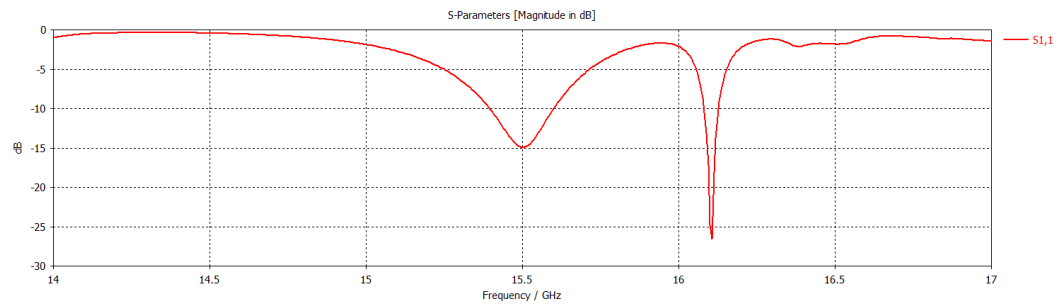
The reflection coefficient for the implemented split ring resonators are plotted in figure 6.15. The s-parameters for the $\lambda/10$ sized unit cell are displayed in figure 6.15a and for the larger unit cell in figure 6.15b, respectively. Both antennas have the same resonances at 15.5 and 16.1 GHz.



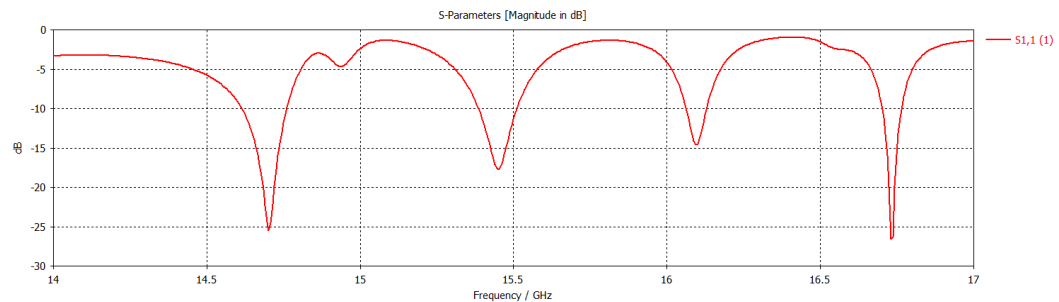
(a) Lots of small double split ring resonators

(b) A few large double split ring resonators

Figure 6.14: The double split ring resonator unit cells implemented on the antenna in perspective view without the top substrates and the patch antenna. The feeding strip is shown to show the unit cells in perspective.



(a) Lots of small double split ring resonators



(b) A few large double split ring resonators

Figure 6.15: The reflection coefficient of the two antenna models with the two different split ring resonator AMC structures simulated in an infinite array.

The radiation pattern of the antenna models with the different SRR structures are displayed in figure 6.16. It is apparent that the antenna with lots of AMC unit cells has a strong radiation pattern in the positive and negative x-direction. This is due to the AMC. Also, the absolute radiation pattern of the antenna with less SRR is distorted. It is observable that the antenna radiates strongly towards the positive x-direction. This is as the feeding pin is somewhat placed inside the AMC unit cell, and therefore, has a strong reflector towards the negative axis. The cross polarisation radiation pattern of both antennas with an SRR AMC ground plane is shown in figure 6.17. It is observed that the cross polarisation level is mostly towards the ground plane as there are all the edges which convert the pattern into a cross polarised pattern.

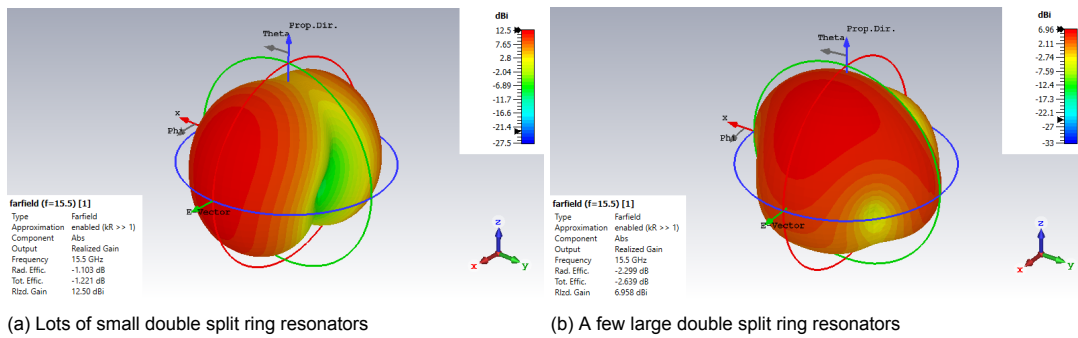


Figure 6.16: The 3D radiation patterns of the two antenna models with the different split ring resonator AMC structures simulated in an infinite array. The model is simulated at a frequency of 15.5 GHz and the absolute value of the pattern is displayed.

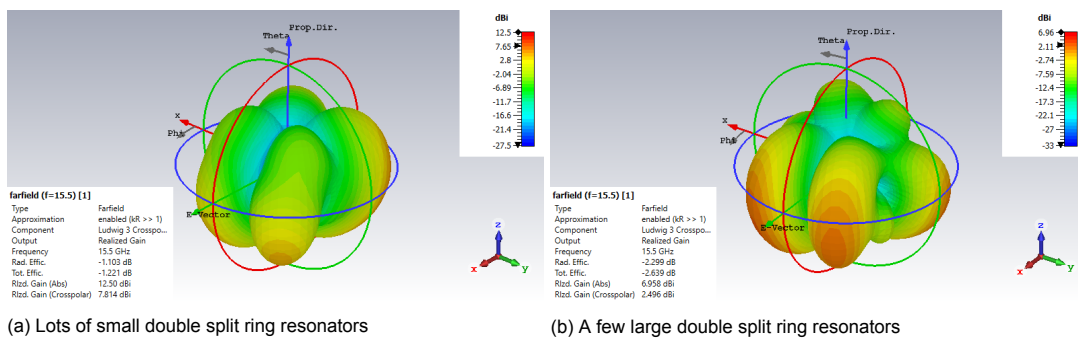


Figure 6.17: The 3D radiation patterns of the two antenna models with the different split ring resonator AMC structures simulated in an infinite array. The model is simulated at a frequency of 15.5 GHz and the cross polarisation radiation pattern is displayed.

6.1.5. Summary

All in all, none of the above described unit cells implemented as AMC ground planes improve the antenna's performance on all three radiation properties. The gain of the antennas is increased by some of the antennas, especially the ones with a large AMC ground plane. However, the radiation pattern in all cases is distorted a lot and the antenna does not radiate towards broadside anymore. Also, all unit cells distort the s-parameters and create a large cross polarisation radiation pattern. Both are undesirable, as a wideband antenna with a horizontally linear polarisation is required. As none of the antennas radiate properly with the AMC unit cells as a ground plane, the effect of the location of the unit cells on the antenna's performance is investigated in the following section.

6.2. Location of ground plane

All the proposed AMC ground planes from chapter 6.1, were situated below the patch antenna with a substrate thickness comparable to the total thickness of the whole antenna. As all elements did not increase the performance of the antenna in an infinite array, the unit cell of chapter 6.1.3 is simulated with a different substrate thickness and on other locations in order to enhance the antenna's performance. Also, the amount of unit cells is investigated. The following locations are investigated with multiple amounts of unit cells:

- Below substrate 1 with a thinner substrate (chapter 6.2.1)
- Atop substrate 2 next to the feeding strip (chapter 6.2.2)
- Between substrate 1 and 2 next to the feeding strip (chapter 6.2.3)

All the antenna elements combined with the different AMC structures are compared on S-parameters, broadside radiation pattern and cross polarisation radiation pattern.

6.2.1. Regular location with a thinner substrate

In this model, the AMC ground plane is located below substrate 1. Despite the model from chapter 6.1.3 has a really thick substrate, which is almost comparable to the thickness of the whole antenna, this model has a thinner substrate. This is to compare how much the thickness of the substrate below the AMC ground plane influences the radiation properties. The model is shown in figure 6.18.

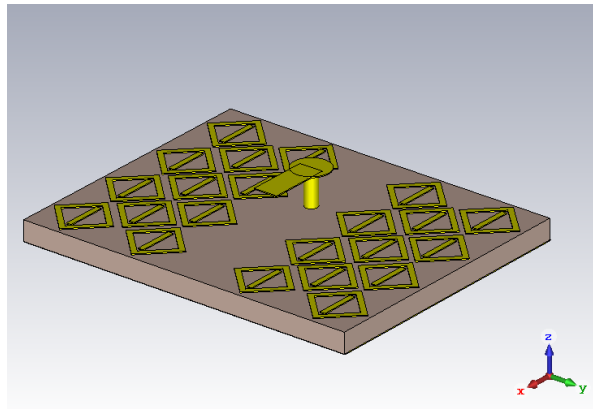


Figure 6.18: The same antenna as from chapter 6.1.3, but with a thinner substrate for the AMC unit cells.

The S-parameters are displayed in figure 6.19. It is discernible that there are two resonances at the frequencies of approximately 14.7 and 15.2 GHz, both with a small bandwidth. However, the resonance from the antenna, which was observable in chapter 6.1.3, is gone. As the resonances change with substrate thickness, the thinner substrate is probably not reflecting the frequency of approximately 16.7 GHz anymore, and therefore, the original resonance has been removed.

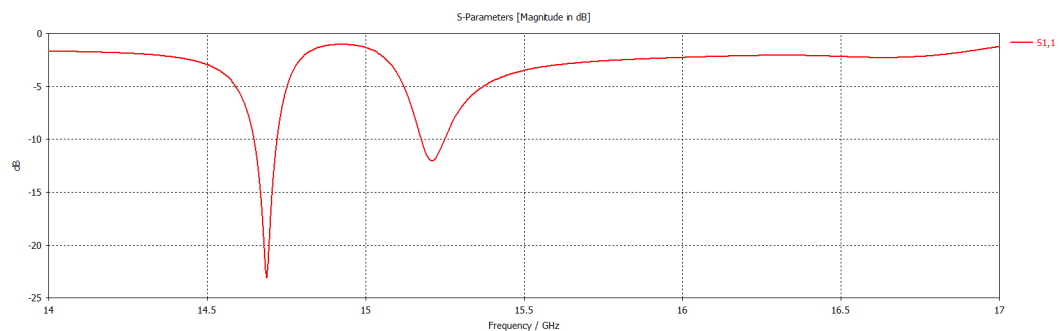


Figure 6.19: The reflection coefficient of the the antenna model in an infinite array simulation. There is an AMC ground plane added of diamond shaped unit cells with a horizontal strip, where the AMC ground plane is thinner than usual.

The radiation pattern of the antenna is shown in figure 6.20. The absolute value of the antenna as well as the cross polarisation level has been displayed. The antenna is strongly radiating towards the sides of the antenna instead of broadside, due to the high cross polarisation level. Also, the antenna itself radiates more strongly towards the corners of the AMC ground plane instead of the antenna.

To summarize, decrease the substrate thickness of the AMC ground plane does not solve the issue of chapter 6.1.3 to improve the performance of the antenna. The antenna radiates with a higher gain, but in the wrong direction and with high cross polarisation level.

6.2.2. Atop substrate 2 next to the feeding strip

Another approach is to place the AMC unit cells next to the feeding strip on substrate layer 2. This removes the extra substrate layer, created for the AMC ground plane and this could strengthen the coupling between the feeding strip and the antenna. The design is simulated with two amounts of AMC unit cells. The simulations setups are displayed in figure 6.21. In figure 6.21b, there are only located two rows of unit cells along the edges of the substrate to improve the performance. It has also

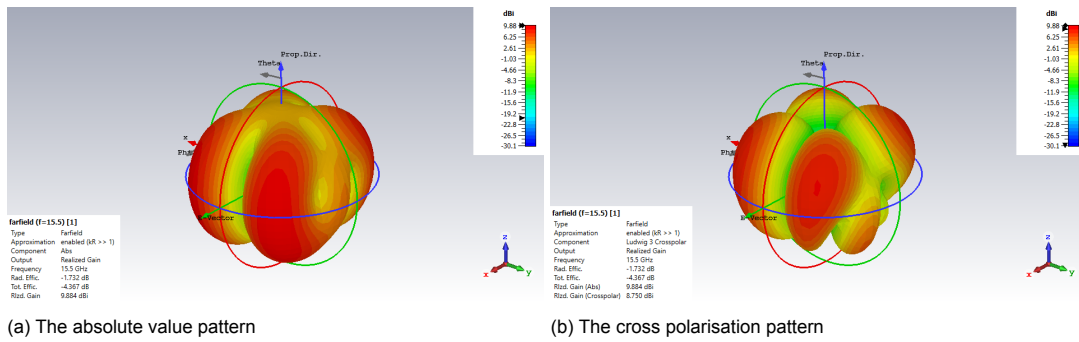


Figure 6.20: The 3D radiation patterns of the antenna model in an infinite array simulation. There is an AMC ground plane added of diamond shaped unit cells with a horizontal strip. The substrate of the ground plane is smaller than usual. The model is simulated at a frequency of 15.5 GHz and the absolute value and cross polarisation radiation patterns are given.

been simulated how the performance of the antenna is adjusted, if there are 4 unit cells added. This is displayed in figure 6.21a.

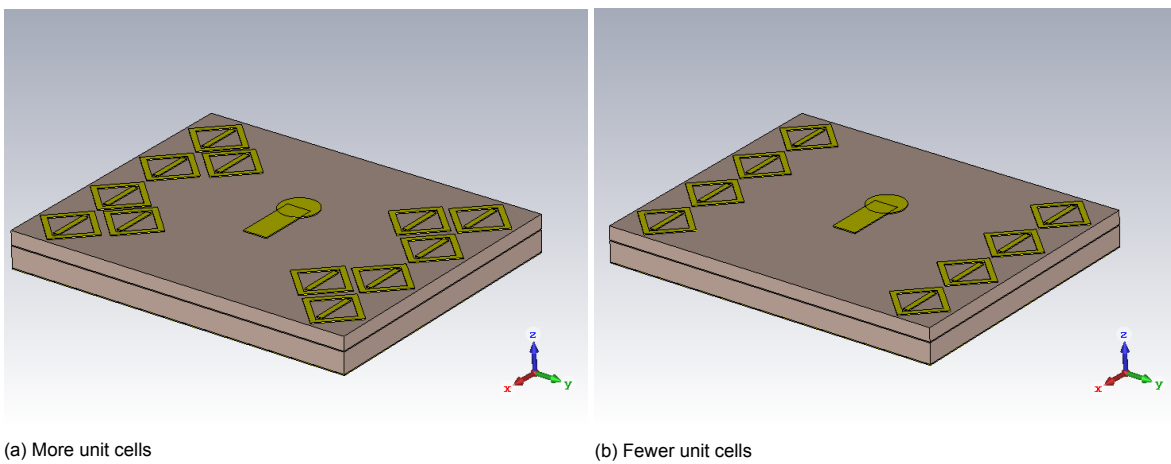


Figure 6.21: The diamond unit cells implemented on the antenna. The unit cell has a horizontal strip to create a larger reflection in the horizontal polarisation. The unit cells are implemented atop substrate 2 next to the feeding strip of the antenna. The models are shown in perspective view without the top substrates and the patch antenna. The feeding strip is shown to show the unit cells in perspective.

The return loss of the antennas are displayed in figure 6.22. The resonance of the antenna itself has been kept in both situations, but is shifted a little into opposite directions. For the extra added unit cells, there has been created an extra resonance around 15.5 GHz and the resonance of the antenna has slightly decreased to below 16.5 GHz. This is displayed in figure 6.22a. While the resonance of the antenna with fewer unit cells has been shifted towards 16.8 GHz. Also, an extra resonance has been added. However, by adding fewer unit cells the reflection coefficient is barely below -10 dB.

The radiation pattern of the unit cells located atop of substrate 2 is displayed in figure 6.23. The absolute value is shown, and it is observable that both antennas don't radiate properly anymore. The antenna with more unit cells radiates in the x-direction, while the antenna with fewer unit cells radiates more towards the y-direction instead of broadside. The antenna with fewer unit cells radiates in this direction as the surface currents from the feeding strips radiates strongly towards the unit cells; this is stronger than the coupling between the strip and the antenna, and therefore, the antenna radiates towards the y-direction. Also, the cross-polarisation level of the antenna with fewer unit cells is radiating in the y-plane. This is displayed in figure 6.24b. The cross polarisation level of the antenna with more unit cells is radiating towards the negative z-direction and is 4 dB weaker than the antenna's maximum value. This is shown in figure 6.24a.

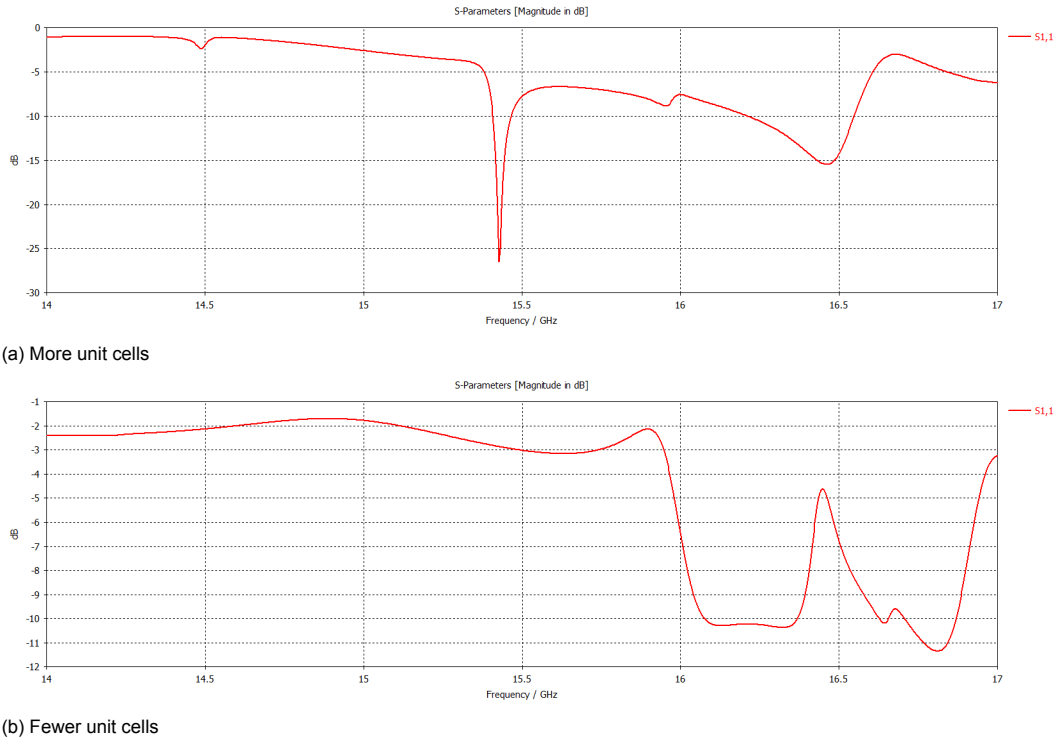


Figure 6.22: The reflection coefficient of the antenna model in an infinite array simulation. There AMC unit cells diamond shaped unit cells with a horizontal strip, which are located next to the feeding strip on the same substrate.

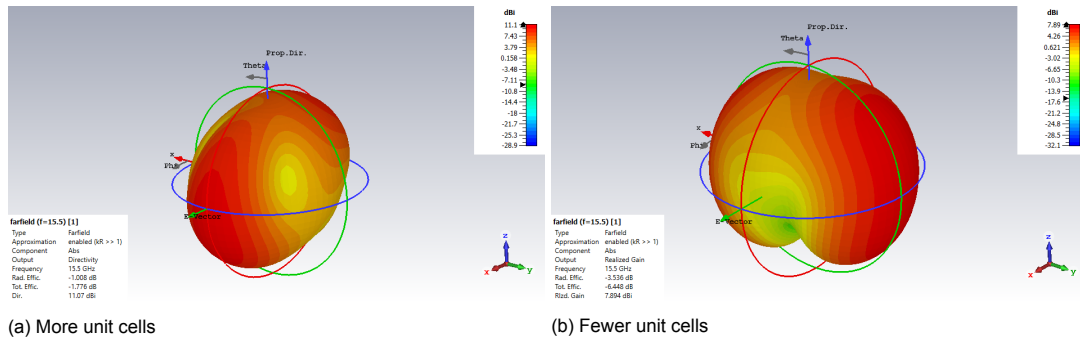


Figure 6.23: The 3D radiation patterns of the antenna model in an infinite array simulation. The AMC unit cells are diamond shaped with a horizontal strip and are added around the feeding strip of the antenna on the same substrate. The model is simulated at a frequency of 15.5 GHz and the absolute value of the radiation pattern of the same antenna with different amounts of unit cells is given.

All in all, by placing the unit cells next to the antenna on the same substrate, the radiation performance of the antenna is not improved. By implementing the unit cells, the antenna radiates to different directions than it is supposed to, as the coupling between the feeding strip and the antenna is weaker than the coupling between the feeding strip and the unit cells. Also, the antenna with fewer unit cells has a high cross polarisation level towards the same direction as the absolute value of the radiation pattern. Therefore, placing unit cells next to the feeding strip is not recommended.

6.2.3. Between substrate 1 and 2 next to the feeding strip

The final approach that is investigated is to put the AMC unit cells between substrate layer 1 and substrate layer 2 in the antenna. By placing the unit cells between the substrate, the feeding strip is still electromagnetically coupled with the patch antenna with no direct interference from the unit cells. This is displayed in figure 6.25. In figure 6.25a, the antenna has 4 more unit cells that are closing to the feeding strip and will influence the antenna more. The other model has only 8 unit cells along the

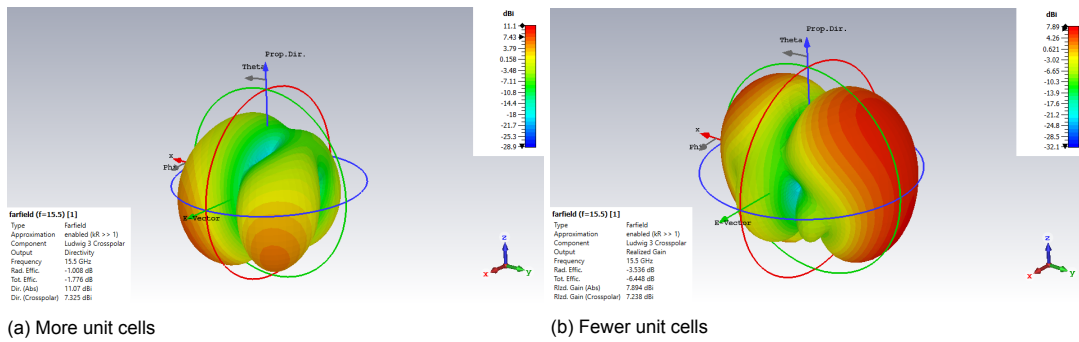


Figure 6.24: The 3D radiation patterns of the antenna model in an infinite array simulation. The AMC unit cells are diamond shaped with a horizontal strip and are added around the feeding strip of the antenna on the same substrate. The model is simulated at a frequency of 15.5 GHz and the cross polarisation radiation pattern of the same antenna with different amounts of unit cells is given.

boundaries of the ground plane.

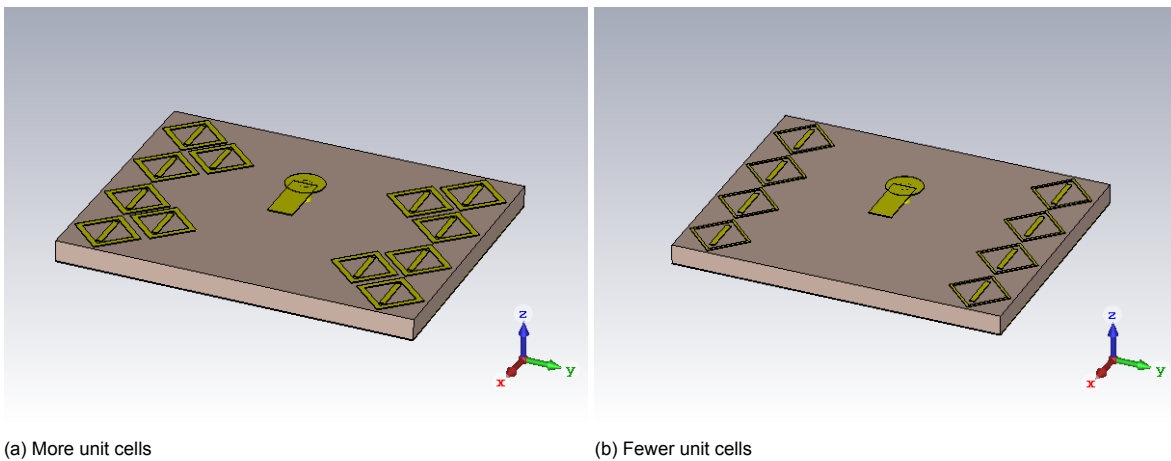
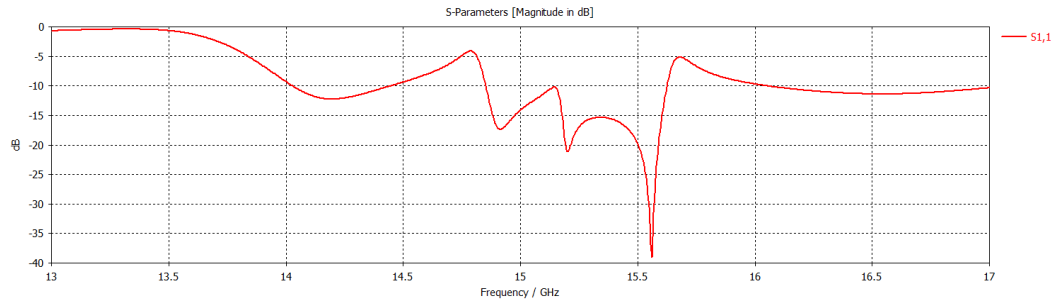


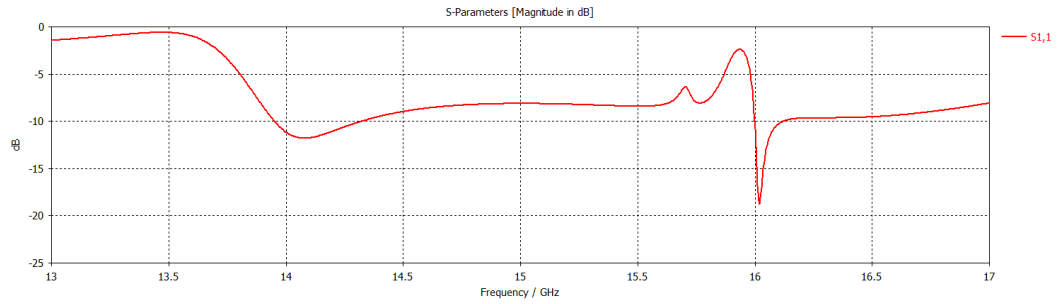
Figure 6.25: The diamond unit cells implemented on the antenna. The unit cell has a horizontal strip to create a larger reflection in the horizontal polarisation. The unit cells are implemented between substrate 1 & 2 of the antenna. The models are shown in perspective view without the top substrates and the patch antenna. The feeding strip is shown to show the unit cells in perspective.

The reflection coefficient of both antennas are shown in figure 6.26. The reflection coefficient comes already closer to a wideband antenna than the unit cells at the other locations. In figure 6.26a the antenna has 5 resonances, where 3 of them are close together and create an impedance bandwidth of approximately 800 MHz. There are also to other resonances which have also a large impedance bandwidth of 500 MHz and 1 GHz, respectively. These other resonances are really weak and just below the -10 dB. Removing the center unit cells from the antenna, gives the reflection coefficient in figure 6.26b. The antenna only has two resonances below -10 dB. But, it is notable that the antenna's reflection coefficient almost creates a wideband character in the frequency range of 14 - 17 GHz as the reflection coefficient is around the -10 dB.

The radiation patterns of the antennas are shown in figure 6.27, for the absolute value, and in figure 6.28, for the cross polarisation level. Locating the unit cells between the lower two substrates increases the gain slightly. For the antenna with fewer unit cells, the antenna still has a broadside radiation pattern, however the 1 dB angular width decreases. Also, the cross polarisation level is still quite small in this antenna, but still radiates towards the four corners of the patch antenna. It seems that the fewer unit cells on the side, the radiation pattern is affected less. As the antenna with more unit cells between the substrates, radiates as well towards to positive x direction. Also, the cross polarisation radiation pattern radiates towards all four corners, just as a regular patch antenna.

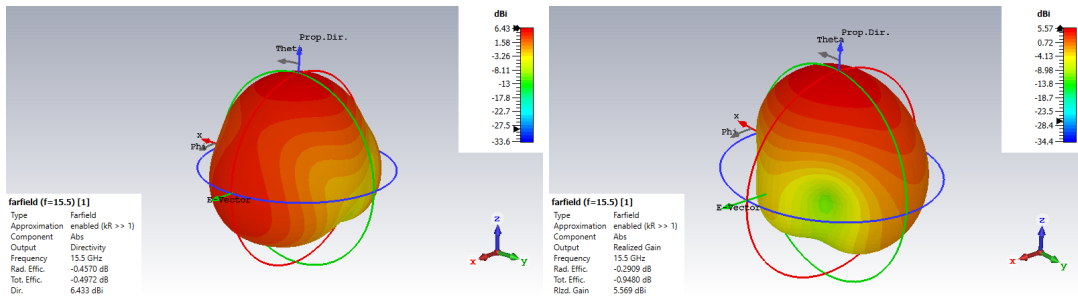


(a) More unit cells



(b) Fewer unit cells

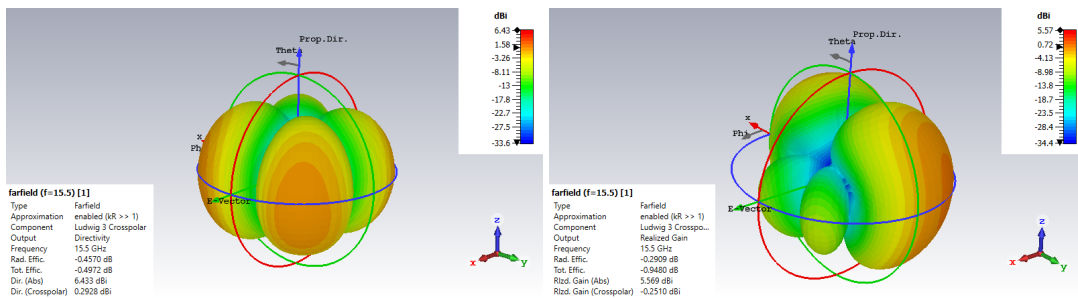
Figure 6.26: The reflection coefficient of the antenna model in an infinite array simulation. There AMC unit cells diamond shaped unit cells with a horizontal strip, which are located next to the feeding strip between substrate 1 & 2 of the antenna.



(a) More unit cells

(b) Fewer unit cells

Figure 6.27: The 3D radiation patterns of the antenna model in an infinite array simulation. The AMC unit cells are diamond shaped with a horizontal strip and are added around the feeding strip of the antenna between the bottom two substrates below the feeding strip. The model is simulated at a frequency of 15.5 GHz and the absolute value of the radiation pattern of the same antenna with different amounts of unit cells is given.



(a) More unit cells

(b) Fewer unit cells

Figure 6.28: The 3D radiation patterns of the antenna model in an infinite array simulation. The AMC unit cells are diamond shaped with a horizontal strip and are added around the feeding strip of the antenna between the bottom two substrates below the feeding strip. The model is simulated at a frequency of 15.5 GHz and the cross polarisation radiation pattern of the same antenna with different amounts of unit cells is given.

To summarize, the location of the AMC unit cell between the substrates does not improve the performance of the antenna directly. But, the simulations have shown that they might. Therefore, further research on the location of the AMC unit cell has to be conducted in order to be certain about improving the performance of an antenna.

6.2.4. Summary

In this section, the antenna has been simulated with AMC unit cells on different locations. The locations were as a ground plane, but with a thinner substrate. Next to the feeding strip on the same substrate, as well as next to the feeding strip between substrate 1 & 2. The first two locations did not improve the antenna's performance. But, by placing the AMC unit cells between the antennas, the performance of the antenna might be improved. At the moment, the antenna's performance has not been improved. However, the return loss of the antenna is around -10 dB in the frequency band of 14 till 17 GHz. Also, the gain of the element has increased slightly, while the cross polarisation level remain small. On the other hand, the increased gain reduced the antenna's 1 dB angular width regarding scanning. All in all, the location of the AMC unit cells between the substrates might increase the radiation performance of the antenna, but needs some further research.

6.3. Conclusion

Literature has proven that AMC ground planes might be a valuable addition to patch antennas to improve their performance. In this chapter, the process of an AMC unit cell selection has been described. Multiple unit cells have been implemented and their performance have been simulated with the proximity fed patch antenna in a multi-layer substrate. None of these improved the performance of the antenna. Also, the effect of the location of the unit cell on the antenna has been studied. It is shown that the location of the AMC unit cells between the substrates, might increase the antenna's radiation performance. But, this needs further research. Nonetheless, the antenna's performance has not been improved by using an artificial magnetic ground plane.



Conclusions and Recommendations

The goal of this project is to design a wideband antenna array using printed antennas. The antenna has to fulfill the requirement of an impedance bandwidth of at least 1 GHz. Furthermore, the array should be able to scan $\pm 30^\circ$ in azimuth and $\pm 15^\circ$ in elevation with minimal losses. The antenna should excite a horizontally polarized wave, where it is desired to have a maximum cross polarisation of -25 dB. Also, the side lobe level should not exceed -25 dB. The complete set of design requirements are described in chapter 1.

The antenna array design has been performed in the following phases: generic array design assuming uncoupled antenna elements with omnidirectional radiation patterns, comparative study of possible antenna element types and selection of the best candidate, array design with embedded antenna elements, and array verification using a created prototype. Also, A study on an additional enhancement using meta-materials is done in an attempt to improve the antenna's performance.

A generic analysis of patch antenna and antenna arrays is presented in chapter 2. The study shows how a patch antenna array is designed and what trade-offs should be considered to satisfy the requirements.

In chapter 3, a feasibility study is presented on creating a wideband antenna element. In this study, a comparison is made on different patch elements simulated in an infinite array. The final chosen design is a proximity fed patch antenna in a multi-layer substrate with a bandwidth of 3.74 GHz at broadside which possesses the best steering capabilities.

The best candidate from the comparative study in chapter 3 has been used to perform full-wave analysis of a 4 by 4 antenna array in chapter 4. It was investigated that the antenna could be optimized to minimize scan losses. The array achieves a bandwidth of 2.96 GHz at broadside and has a maximum realized gain loss of 1.6 dB while scanning to its required limits. The side lobe level is -14.7 dB at 15.5 GHz. This could be reduced by using an amplitude taper. Also, at this frequency a cross polarisation level of -20 dB is achieved. However, at 16.5 GHz the cross polarisation level is only -7.76 dB, which is undesired. The finite array is also compared to the infinite array solution, and it is illustrated that the solutions have comparable parameters and achieve the set goals.

Furthermore, the array design is implemented in a PCB design environment, and a prototype of the model has been manufactured. This is presented in chapter 5. The performance of the created prototype shows lots of similarities compared to the simulated performance. The single element's radiation patterns and the center four elements are comparable at broadside. Also, the active S-parameters coincide with each other. The results show a verified active impedance bandwidth at broadside of minimal 0.9 GHz.

Finally, a feasibility study was made on improving the array performance by using an artificial magnetic ground plane. This study was a subgoal of this project and described in chapter 6. The study shows that an AMC ground plane is a valuable addition to many antennas. With the proposed AMC unit cells as a ground plane, our antenna is negatively influenced, however, and the design requirements are not reached anymore. The performance of the array for different locations of the AMC unit cells has also been investigated. All the locations, however, influence the antenna array's performance negatively. Nevertheless, the model still achieves the goals without the artificial magnetic ground plane.

Several novel elements have been used in the array design. In particular, implementing this specific multi-layer structure with the different antenna elements creates a wideband antenna element. Also, the design of an AMC ground plane was attempted to implement into a proximity fed antenna in a multi-layer structure. Usage of AMC's combined with a stacked or proximity fed antenna has barely been found in the literature.

7.1. Recommendations

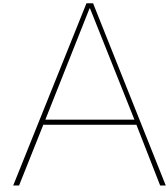
The current study has revealed a number of questions and a follow up study on these questions is recommended. These are:

This thesis is focused on antenna array radiation, while the appropriate feeding structure was outside of the scope of the thesis. Therefore, the feeding pin of the antenna had a mismatch. Impedance matching is dependent on the feeding geometry, and optimization for the final design is advised.

Also, heat protection has largely been out of scope, but might be required on the structure as a larger antenna array will dissipate more heat. Therefore, additional research in heat dissipation of this antenna is adjured.

Furthermore, the tolerance of the third substrate, the foam layer, is large. With that difference the antenna's radiation performance is distorted. Searching for a reduction in tolerance is advised.

Finally in literature, it was discernible that AMC ground planes are a good enhance for antennas. This thesis couldn't find an improvement in performance using an AMC ground plane. But, in literature other examples are discovered that could improve this antenna. As this antenna is strongly electromagnetic coupled between its substrates, a metamaterial radome or superstrate might be an alternative to investigate.



Matlab scripts

A.1. Code to plot the active S-parameters

Listing A.1: Matlab code to read the data and calculate the active S-parameters and plot them. The readdata and readdatasim functions are functions to read the data from csv files

```
1 %% Matlab script to calculate all the active S-parameters from the passive
2 % Created by J.P. Bout
3
4 clear all;
5 [S1,S2,S3,S4,S5,S6,S7,S8,S9,S10,S11,S12,S13,S14,S15,S16, P1,P2,P3,P4,P5,P6,P7,P8,P9,P10,P11,P12,P13,P14,
6   P15,P16,freq] = readdata();
7 [S_sim_act,P_sim_act,freq_sim] = readdatasim();
8
9 %%
10 theta = 0;
11 phi = 0;
12 dx = 12.9e-3;
13 dy = 10.3e-3;
14
15 %%
16 [S_act_mag1,S_act_ph1] = calc_s_par_act(S1,P1,theta,phi,freq,dx,dy);
17 [S_act_mag2,S_act_ph2] = calc_s_par_act(S2,P2,theta,phi,freq,dx,dy);
18 [S_act_mag3,S_act_ph3] = calc_s_par_act(S3,P3,theta,phi,freq,dx,dy);
19 [S_act_mag4,S_act_ph4] = calc_s_par_act(S4,P4,theta,phi,freq,dx,dy);
20 [S_act_mag5,S_act_ph5] = calc_s_par_act(S5,P5,theta,phi,freq,dx,dy);
21 [S_act_mag6,S_act_ph6] = calc_s_par_act(S6,P6,theta,phi,freq,dx,dy);
22 [S_act_mag7,S_act_ph7] = calc_s_par_act(S7,P7,theta,phi,freq,dx,dy);
23 [S_act_mag8,S_act_ph8] = calc_s_par_act(S8,P8,theta,phi,freq,dx,dy);
24 [S_act_mag9,S_act_ph9] = calc_s_par_act(S9,P9,theta,phi,freq,dx,dy);
25 [S_act_mag10,S_act_ph10] = calc_s_par_act(S10,P10,theta,phi,freq,dx,dy);
26 [S_act_mag11,S_act_ph11] = calc_s_par_act(S11,P11,theta,phi,freq,dx,dy);
27 [S_act_mag12,S_act_ph12] = calc_s_par_act(S12,P12,theta,phi,freq,dx,dy);
28 [S_act_mag13,S_act_ph13] = calc_s_par_act(S13,P13,theta,phi,freq,dx,dy);
29 [S_act_mag14,S_act_ph14] = calc_s_par_act(S14,P14,theta,phi,freq,dx,dy);
30 [S_act_mag15,S_act_ph15] = calc_s_par_act(S15,P15,theta,phi,freq,dx,dy);
31 [S_act_mag16,S_act_ph16] = calc_s_par_act(S16,P16,theta,phi,freq,dx,dy);
32
33 %%
34 figure;
35 plot(freq*1e-9,S_act_mag1,'linewidth',1.5)
36 set(gcf,'position',[10 50, 1500, 500])
37 grid on;
38 hold on;
39 plot(freq*1e-9,S_act_mag2,'linewidth',1.5)
40 plot(freq*1e-9,S_act_mag3,'linewidth',1.5)
41 plot(freq*1e-9,S_act_mag4,'linewidth',1.5)
42 hold off;
43 legend(['S01_{active}';'S02_{active}';'S03_{active}';'S04_{active}']);
44 xlabel('Frequency [GHz]')
45 ylabel('Magnitude [dB]')
46 title('Measured S-Parameters')
47
48 figure;
49 plot(freq*1e-9,S_act_mag5,'linewidth',1.5)
50 set(gcf,'position',[10 50, 1500, 500])
51 grid on;
52 hold on;
```

```

53 plot(freq*1e-9,S_act_mag6,'linewidth',1.5)
54 plot(freq*1e-9,S_act_mag7,'linewidth',1.5)
55 plot(freq*1e-9,S_act_mag8,'linewidth',1.5)
56 hold off;
57 legend(['S05_{active}';'S06_{active}';'S07_{active}';'S08_{active}']);
58 xlabel('Frequency [GHz]')
59 ylabel('Magnitude [dB]')
60 title('Measured S-Parameters')
61
62 figure;
63 plot(freq*1e-9,S_act_mag9,'linewidth',1.5)
64 set(gcf,'position',[10 50, 1500, 500])
65 grid on;
66 hold on;
67 plot(freq*1e-9,S_act_mag10,'linewidth',1.5)
68 plot(freq*1e-9,S_act_mag11,'linewidth',1.5)
69 plot(freq*1e-9,S_act_mag12,'linewidth',1.5)
70 hold off;
71 legend(['S09_{active}';'S10_{active}';'S11_{active}';'S12_{active}']);
72 xlabel('Frequency [GHz]')
73 ylabel('Magnitude [dB]')
74 title('Measured S-Parameters')
75
76 figure;
77 plot(freq*1e-9,S_act_mag13,'linewidth',1.5)
78 set(gcf,'position',[10 50, 1500, 500])
79 grid on;
80 hold on;
81 plot(freq*1e-9,S_act_mag14,'linewidth',1.5)
82 plot(freq*1e-9,S_act_mag15,'linewidth',1.5)
83 plot(freq*1e-9,S_act_mag16,'linewidth',1.5)
84 hold off;
85 legend(['S13_{active}';'S14_{active}';'S15_{active}';'S16_{active}']);
86 xlabel('Frequency [GHz]')
87 ylabel('Magnitude [dB]')
88 title('Measured S-Parameters')
89
90 % figure;
91 % plot(freq*1e-9,S_act_ph)
92 % set(gcf,'position',[10 50, 1500, 500])
93 % grid on;
94
95 %%
96 figure;
97 newcolors = {'#0099FF','0099FF','#A2142F','#A2142F'};
98 colororder(newcolors)
99 plot(freq*1e-9,S_act_mag6,'linewidth',1.5)
100 set(gcf,'position',[10 50, 1700, 500])
101 grid on;
102 hold on;
103 plot(freq_sim,S_sim_act(:,6),'--','linewidth',1.5)
104 plot(freq*1e-9,S_act_mag7,'linewidth',1.5)
105 plot(freq_sim,S_sim_act(:,7),'--','linewidth',1.5)
106 hold off;
107 legend(['S6_{measured}';'S6_{simulated}';'S7_{measured}';'S7_{simulated}'],'location','southeast');
108 xlabel('Frequency [GHz]')
109 ylabel('Magnitude [dB]')
110 title('Measured vs Simulated Active S-Parameters')
111 xlim([12.5 17])
112
113 figure;
114 newcolors = {'#0099FF','0099FF','#A2142F','#A2142F'};
115 colororder(newcolors)
116 plot(freq*1e-9,S_act_mag10,'linewidth',1.5)
117 set(gcf,'position',[10 50, 1700, 500])
118 grid on;
119 hold on;
120 plot(freq_sim,S_sim_act(:,10),'--','linewidth',1.5)
121 plot(freq*1e-9,S_act_mag11,'linewidth',1.5)
122 plot(freq_sim,S_sim_act(:,11),'--','linewidth',1.5)
123 hold off;
124 legend(['S10_{measured}';'S10_{simulated}';'S11_{measured}';'S11_{simulated}'],'location','southeast');
125 xlabel('Frequency [GHz]')
126 ylabel('Magnitude [dB]')
127 title('Measured vs Simulated Active S-Parameters')
128 xlim([12.5 17])
129
130
131 %%
132 figure;
133 newcolors = {'#0099FF','0099FF','#A2142F','#A2142F'};
134 colororder(newcolors)
135 plot(freq*1e-9,S_act_mag1,'linewidth',1.5)
136 set(gcf,'position',[10 50, 1700, 500])

```

```

137 grid on;
138 hold on;
139 plot(freq_sim, S_sim_act(:,1), '--', 'linewidth', 1.5)
140 plot(freq*1e-9, S_act_mag2, 'linewidth', 1.5)
141 plot(freq_sim, S_sim_act(:,2), '--', 'linewidth', 1.5)
142 hold off;
143 legend(['S1_{measured}'; 'S1_{simulated}'; 'S2_{measured}'; 'S2_{simulated}'], 'location', 'southeast');
144 xlabel('Frequency [GHz]')
145 ylabel('Magnitude [dB]')
146 title('Measured vs Simulated Active S-Parameters')
147 xlim([12.5 17])
148
149 figure;
150 newcolors = {'#0099FF', '#0099FF', '#A2142F', '#A2142F'};
151 colororder(newcolors)
152 plot(freq*1e-9, S_act_mag3, 'linewidth', 1.5)
153 set(gcf, 'position', [10 50, 1700, 500])
154 grid on;
155 hold on;
156 plot(freq_sim, S_sim_act(:,3), '--', 'linewidth', 1.5)
157 plot(freq*1e-9, S_act_mag4, 'linewidth', 1.5)
158 plot(freq_sim, S_sim_act(:,4), '--', 'linewidth', 1.5)
159 hold off;
160 legend(['S3_{measured}'; 'S3_{simulated}'; 'S4_{measured}'; 'S4_{simulated}'], 'location', 'southeast');
161 xlabel('Frequency [GHz]')
162 ylabel('Magnitude [dB]')
163 title('Measured vs Simulated Active S-Parameters')
164 xlim([12.5 17])
165
166 figure;
167 newcolors = {'#0099FF', '#0099FF', '#A2142F', '#A2142F'};
168 colororder(newcolors)
169 plot(freq*1e-9, S_act_mag5, 'linewidth', 1.5)
170 set(gcf, 'position', [10 50, 1700, 500])
171 grid on;
172 hold on;
173 plot(freq_sim, S_sim_act(:,5), '--', 'linewidth', 1.5)
174 plot(freq*1e-9, S_act_mag8, 'linewidth', 1.5)
175 plot(freq_sim, S_sim_act(:,8), '--', 'linewidth', 1.5)
176 hold off;
177 legend(['S5_{measured}'; 'S5_{simulated}'; 'S8_{measured}'; 'S8_{simulated}'], 'location', 'southeast');
178 xlabel('Frequency [GHz]')
179 ylabel('Magnitude [dB]')
180 title('Measured vs Simulated Active S-Parameters')
181 xlim([12.5 17])
182
183 figure;
184 newcolors = {'#0099FF', '#0099FF', '#A2142F', '#A2142F'};
185 colororder(newcolors)
186 plot(freq*1e-9, S_act_mag9, 'linewidth', 1.5)
187 set(gcf, 'position', [10 50, 1700, 500])
188 grid on;
189 hold on;
190 plot(freq_sim, S_sim_act(:,9), '--', 'linewidth', 1.5)
191 plot(freq*1e-9, S_act_mag12, 'linewidth', 1.5)
192 plot(freq_sim, S_sim_act(:,12), '--', 'linewidth', 1.5)
193 hold off;
194 legend(['S9_{measured}'; 'S9_{simulated}'; 'S12_{measured}'; 'S12_{simulated}'], 'location', 'southeast');
195 xlabel('Frequency [GHz]')
196 ylabel('Magnitude [dB]')
197 title('Measured vs Simulated Active S-Parameters')
198 xlim([12.5 17])
199
200 figure;
201 newcolors = {'#0099FF', '#0099FF', '#A2142F', '#A2142F'};
202 colororder(newcolors)
203 plot(freq*1e-9, S_act_mag13, 'linewidth', 1.5)
204 set(gcf, 'position', [10 50, 1700, 500])
205 grid on;
206 hold on;
207 plot(freq_sim, S_sim_act(:,13), '--', 'linewidth', 1.5)
208 plot(freq*1e-9, S_act_mag14, 'linewidth', 1.5)
209 plot(freq_sim, S_sim_act(:,14), '--', 'linewidth', 1.5)
210 hold off;
211 legend(['S13_{measured}'; 'S13_{simulated}'; 'S14_{measured}'; 'S14_{simulated}'], 'location', 'southeast');
212 xlabel('Frequency [GHz]')
213 ylabel('Magnitude [dB]')
214 title('Measured vs Simulated Active S-Parameters')
215 xlim([12.5 17])
216
217 figure;
218 newcolors = {'#0099FF', '#0099FF', '#A2142F', '#A2142F'};
219 colororder(newcolors)
220 plot(freq*1e-9, S_act_mag15, 'linewidth', 1.5)

```

```

221 set(gcf, 'position', [10 50, 1700, 500])
222 grid on;
223 hold on;
224 plot(freq_sim, S_sim_act(:,15), '--', 'linewidth', 1.5)
225 plot(freq*1e-9, S_act_mag16, 'linewidth', 1.5)
226 plot(freq_sim, S_sim_act(:,16), '--', 'linewidth', 1.5)
227 hold off;
228 legend(['S15_{measured}'; 'S15_{simulated}'; 'S16_{measured}'; 'S16_{simulated}'], 'location', 'southeast');
229 xlabel('Frequency [GHz]')
230 ylabel('Magnitude [dB]')
231 title('Measured vs Simulated Active S-Parameters')
232 xlim([12.5 17])

```

A.2. Function to calculate the active S-parameters

Listing A.2: Function to calculate the active S-parameters.

```

1 %% Function to calculate the active S-parameters
2 % Made by J.P. Bout
3
4
5 function [S_act_mag, S_act_ph] = calc_s_par_act(S,P, theta , phi , f , dx , dy)
6
7 S_act = 0;
8 S_check = S.*(cosd(P)+1j*sind(P));
9 lambda = 3e8/f;
10 k = 2*pi./lambda;
11
12
13 for m = 1:1:4
14     for n = 1:1:4
15         if m == 1
16             S_act = S_act + S_check(:,n).*exp(1j*k.*(n*dx*sind(theta)*cosd(phi)+m*dy*sind(theta)*sind(phi)));
17         elseif m == 2
18             S_act = S_act + S_check(:,(n+4)).*exp(1j*k.*(n*dx*sind(theta)*cosd(phi)+m*dy*sind(theta)*sind(phi)
19             ));
20         elseif m == 3
21             S_act = S_act + S_check(:,(n+8)).*exp(1j*k.*(n*dx*sind(theta)*cosd(phi)+m*dy*sind(theta)*sind(phi)
22             ));
23         elseif m == 4
24             S_act = S_act + S_check(:,(n+12)).*exp(1j*k.*(n*dx*sind(theta)*cosd(phi)+m*dy*sind(theta)*sind(phi)
25             ));
26         else
27             return;
28         end
29     end
30 end
31
32 S_act_mag = 20*log10(abs(S_act));
33 S_act_ph = angle(S_act)/pi*180;
34
35 end

```

A.3. Code to plot the measured radiation pattern

Listing A.3: Code to read the measured FF data and plot the data in 3D and from top view.

```

1 %% Matlab code to plot the gain pattern of the measured data
2 % Made by J.P. Bout
3
4 clear all;
5 close all;
6 clc;
7
8 %T1 = readtable('ciara_Jelle_enkel_co_pol_logmag13_5ghz', ...
9 %             'ReadVariableNames', false);
10 %T1 = readtable('ciara_Jelle_enkel_x_pol_logmag13_5ghz', ...
11 %             'ReadVariableNames', false);
12 %T1 = readtable('ciara_Jelle_verticaal_logmag16_5ghz', ...
13 %             'ReadVariableNames', false);
14 T1 = readtable('ciara_Jelle_x_pol_logmag14_5ghz', ...
15 %             'ReadVariableNames', false);
16
17 %extract data out of table and convert to array
18 Phi = table2array(T1(:,1));
19 Theta = table2array(T1(:,2));
20 Mag = table2array(T1(:,3));
21
22 %determine number of elements
23 no_elem = length(Mag)^(0.5);
24
25 %Reshape data to plot 3D figures

```

```
26 Phi2 = reshape(Phi,[no_elem,no_elem]);
27 Theta2 = reshape(Theta,[no_elem,no_elem]);
28 %dMag = reshape(Mag,[no_elem,no_elem]); %co-pol
29 Mag = reshape(Mag,[no_elem,no_elem]); %cross-pol -> rotation
30
31 %Plot figure 3D
32 figure;
33 mesh(Phi2+90,Theta2,(Mag));
34 set(gca,'YDir','Normal');
35 colorbar;
36 xlabel('Phi [deg]')
37 ylabel('Theta [deg]')
38 zlabel('Normalised Magnitude [dB]')
39 view(45,60)
40 [t1,s1] = title('Normalised Measured Radiation Pattern', ...
41               'Co-polarisation, Center elements, 13.5 GHz');
42
43 %Plot figure top view
44 figure;
45 imagesc(Phi+90,Theta,Mag);
46 set(gca,'YDir','Normal');
47 colorbar;
48
49 xlabel('Phi [deg]')
50 ylabel('Theta [deg]')
51 zlabel('Normalised Magnitude [dB]')
52 [t2,s2] = title('Normalised Measured Radiation Pattern', ...
53               'Cross polarisation, Element 6, 13.5 GHz');
```


B

Extra array material

B.1. Phase excitation

Table B.1: The phase distribution of the array for scanning to different angles.

Element Number	Azimuth/Elevation = 30°/15°	Azimuth/Elevation = -30°/15°	Azimuth/Elevation = -30°/-15°	Azimuth/Elevation = 30°/-15°
1	227.77°	-55.75°	-227.77°	55.75°
2	133.26°	38.76°	-133.26°	-38.76°
3	38.76°	133.26°	-38.76°	-133.26°
4	-55.75°	227.77°	55.75°	-227.77°
5	170.43°	-113.09°	-170.43°	113.09°
6	75.92°	-18.58°	-75.92°	18.58°
7	-18.58°	75.92°	18.58°	-75.92°
8	-113.09°	170.43°	113.09°	-170.43°
9	113.09°	-170.43°	-113.09°	170.43°
10	18.58°	-75.92°	-18.58°	75.92°
11	-75.92°	18.58°	75.92°	-18.58°
12	-170.43°	113.09°	170.43°	-113.09°
13	55.75°	-227.77°	-55.75°	227.77°
14	-38.76°	-133.26°	38.76°	133.26°
15	-133.26°	-38.76°	133.26°	38.76°
16	-227.77°	55.75°	227.77°	-55.75°

B.2. Electric field antenna array

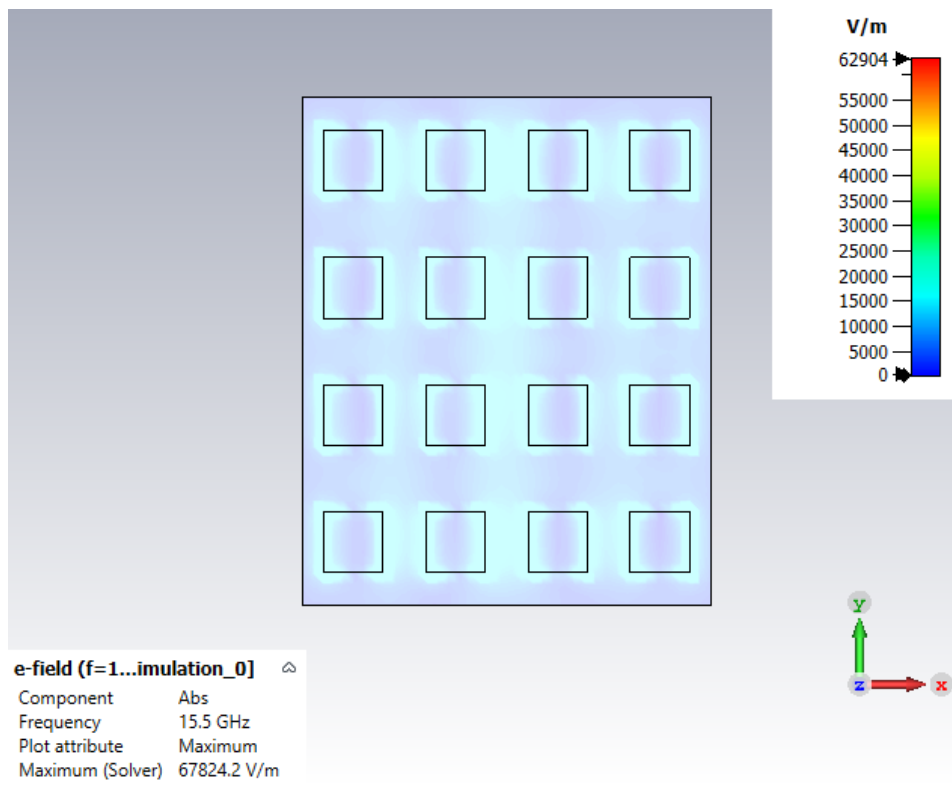
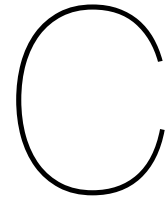
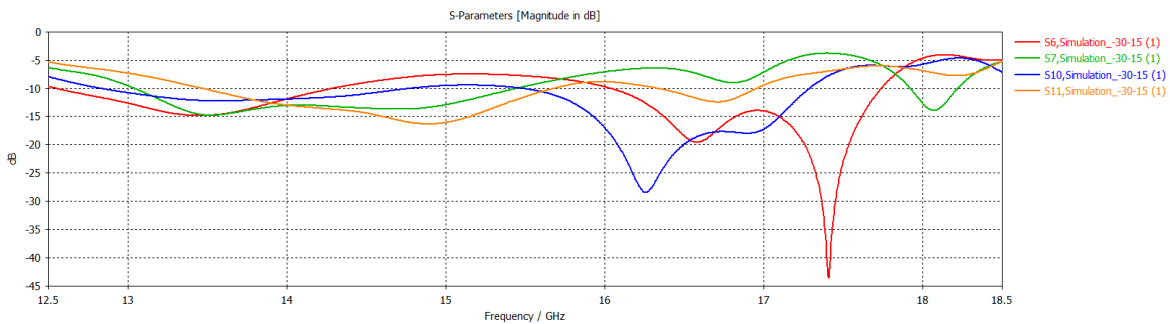


Figure B.1: The maximum electric field on the antenna array.

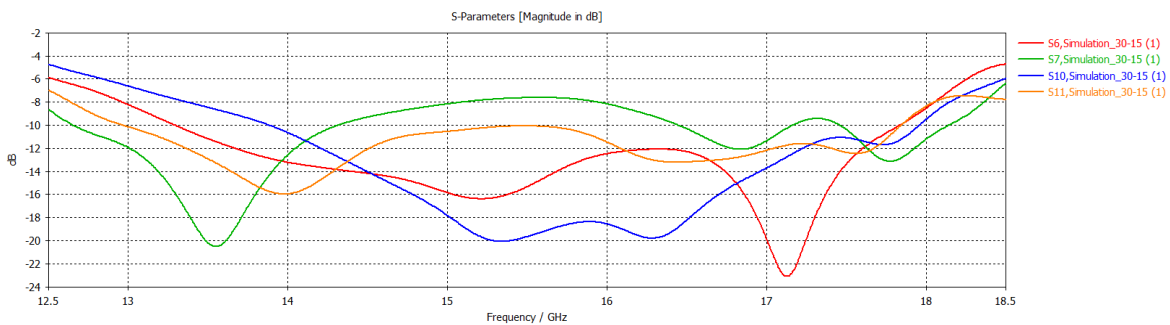


Extra results material

C.1. Antenna Array Simulations C.1.1. Return loss at negative elevation



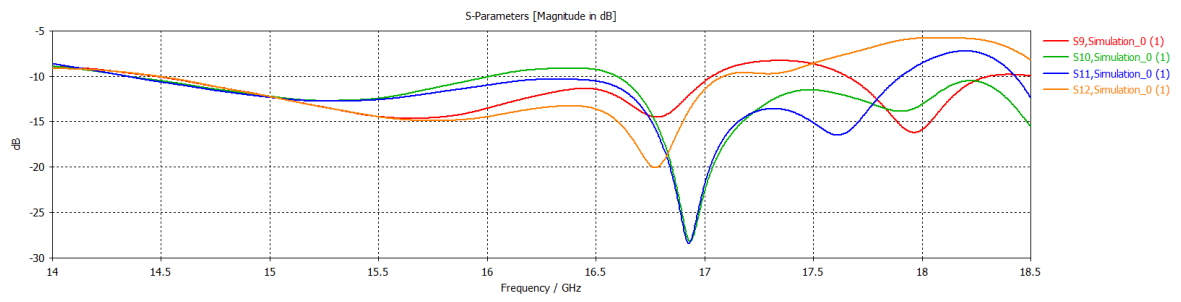
(a) Azimuth = -30° and elevation = -15° .



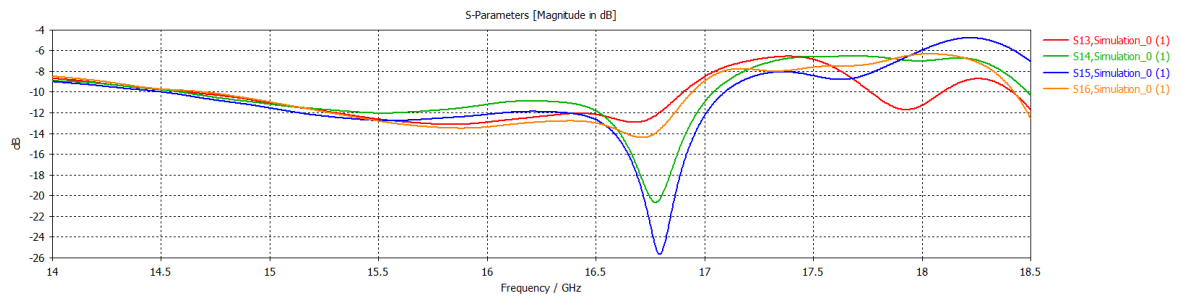
(b) Azimuth = 30° and elevation = -15° .

Figure C.1: The active s-parameters for the center four patches at the different scanning limits for only negative elevation.

C.1.2. 6x6 array



(a) Element 9 till 12.



(b) Element 13 till 16.

Figure C.2: The active s-parameters for the right half of the 16 patches in the 6x6 array.

C.2. Verification results

C.2.1. Active S-parameters

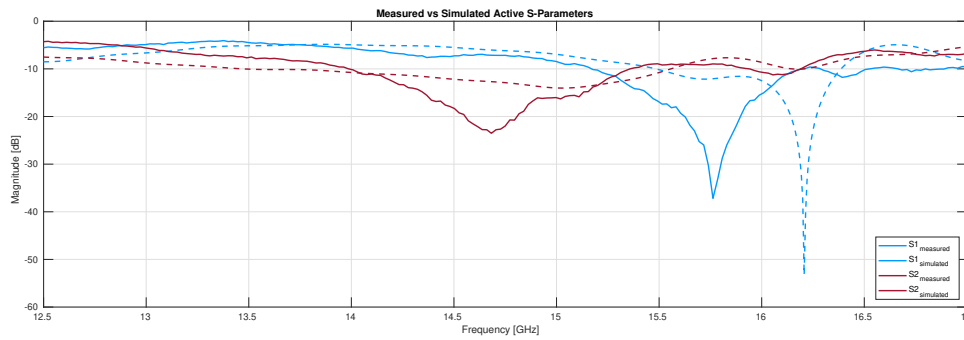


Figure C.3: The active S-parameters of elements 1 and 2 of the prototype compared to its simulation for antenna element 10 and 11 of the array. The dashed lines are the simulated S-parameters and the solid lines are the measured S-parameters.

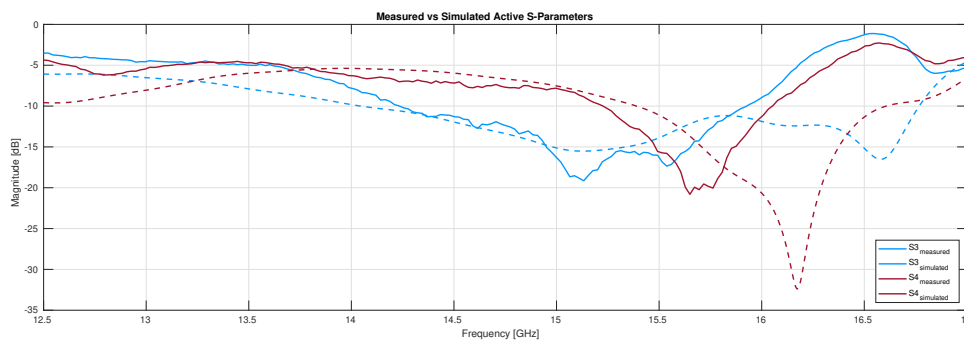


Figure C.4: The active S-parameters of elements 3 and 4 of the prototype compared to its simulation for antenna element 10 and 11 of the array. The dashed lines are the simulated S-parameters and the solid lines are the measured S-parameters.

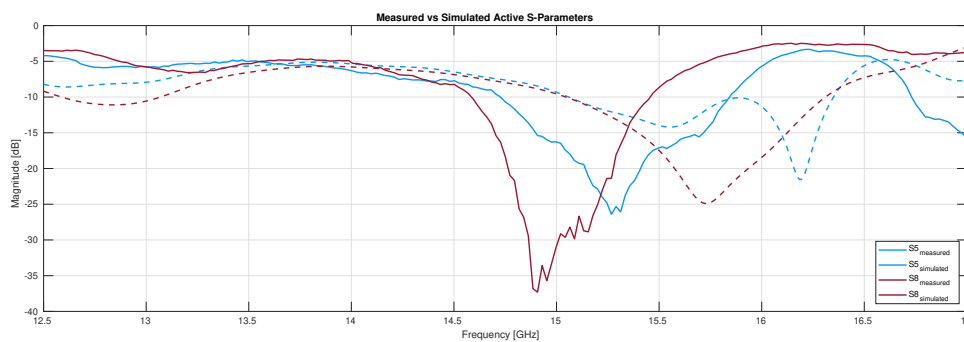


Figure C.5: The active S-parameters of elements 5 and 8 of the prototype compared to its simulation for antenna element 10 and 11 of the array. The dashed lines are the simulated S-parameters and the solid lines are the measured S-parameters.

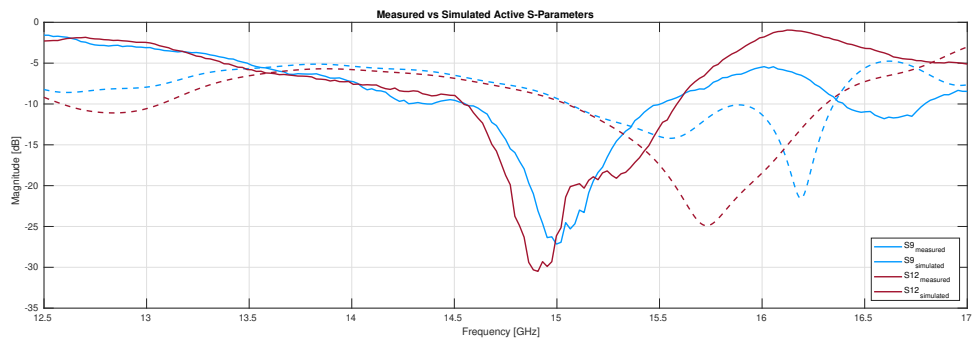


Figure C.6: The active S-parameters of elements 9 and 12 of the prototype compared to its simulation for antenna element 10 and 11 of the array. The dashed lines are the simulated S-parameters and the solid lines are the measured S-parameters.

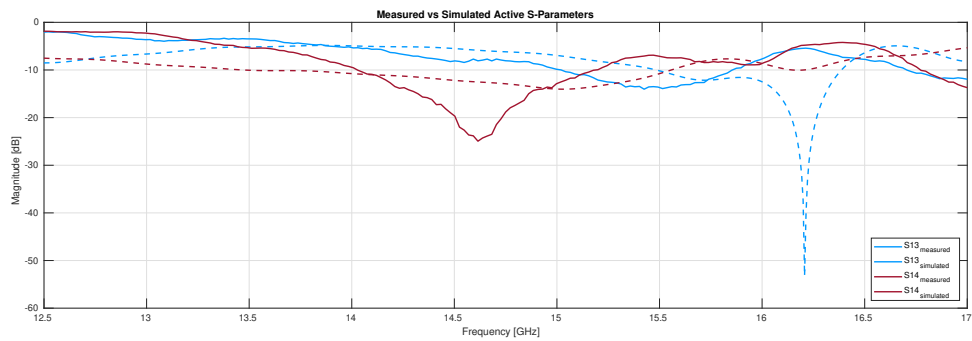


Figure C.7: The active S-parameters of elements 13 and 14 of the prototype compared to its simulation for antenna element 10 and 11 of the array. The dashed lines are the simulated S-parameters and the solid lines are the measured S-parameters.

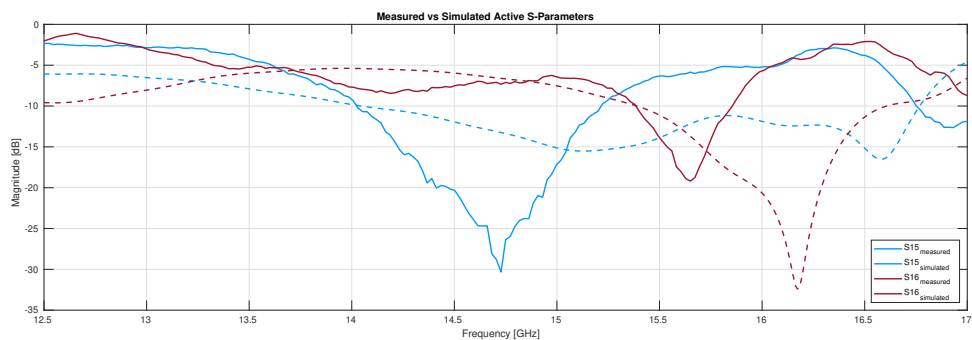


Figure C.8: The active S-parameters of elements 15 and 16 of the prototype compared to its simulation for antenna element 10 and 11 of the array. The dashed lines are the simulated S-parameters and the solid lines are the measured S-parameters.

C.2.2. Radiation Patterns

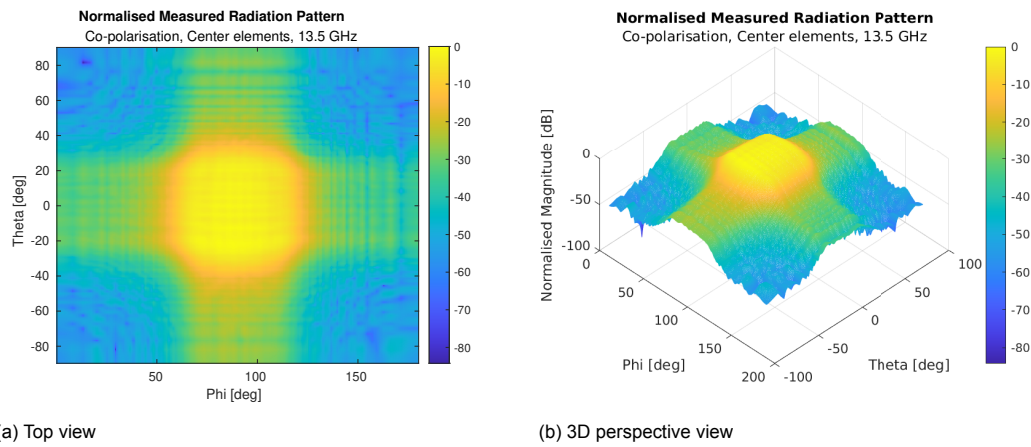


Figure C.9: The measured co-polarisation radiation pattern of the 4 center elements from different viewing points. The pattern is normalised and is measured at a frequency of 13.5 GHz.

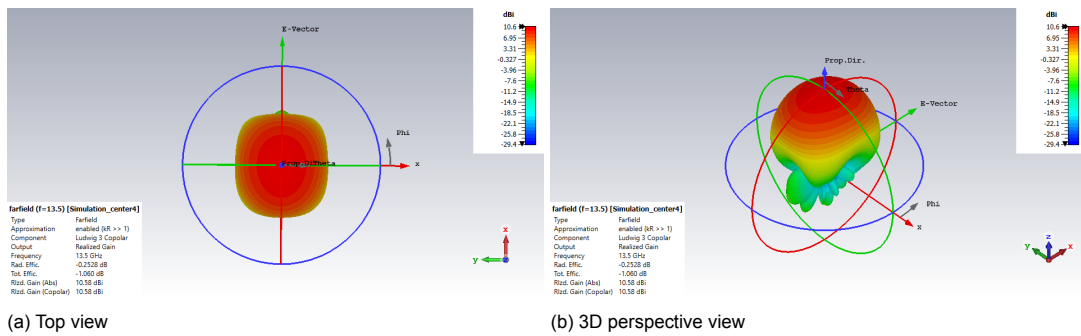


Figure C.10: The simulated co-polarisation radiation pattern of the 4 center elements from different viewing points. The pattern is normalised and is simulated at a frequency of 13.5 GHz.

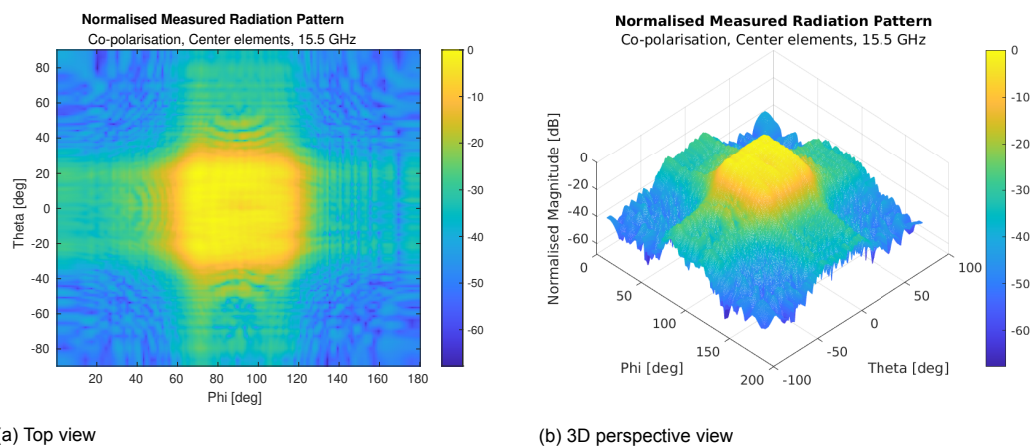


Figure C.11: The measured co-polarisation radiation pattern of the 4 center elements from different viewing points. The pattern is normalised and is measured at a frequency of 15.5 GHz.

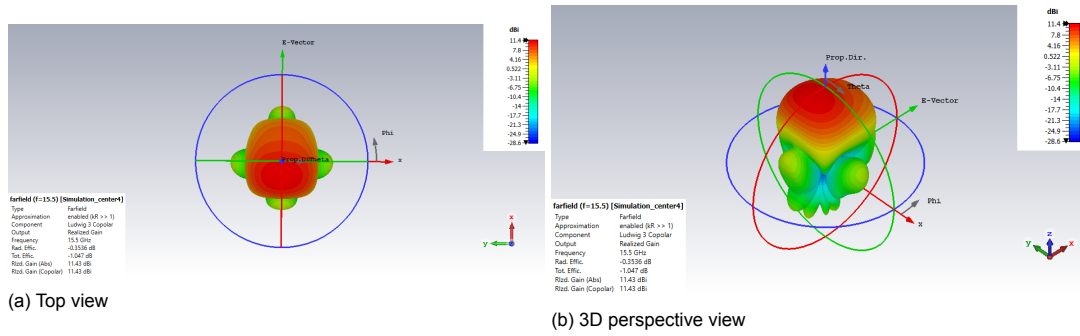


Figure C.12: The simulated co-polarisation radiation pattern of the 4 center elements from different viewing points. The pattern is normalised and is simulated at a frequency of 15.5 GHz.

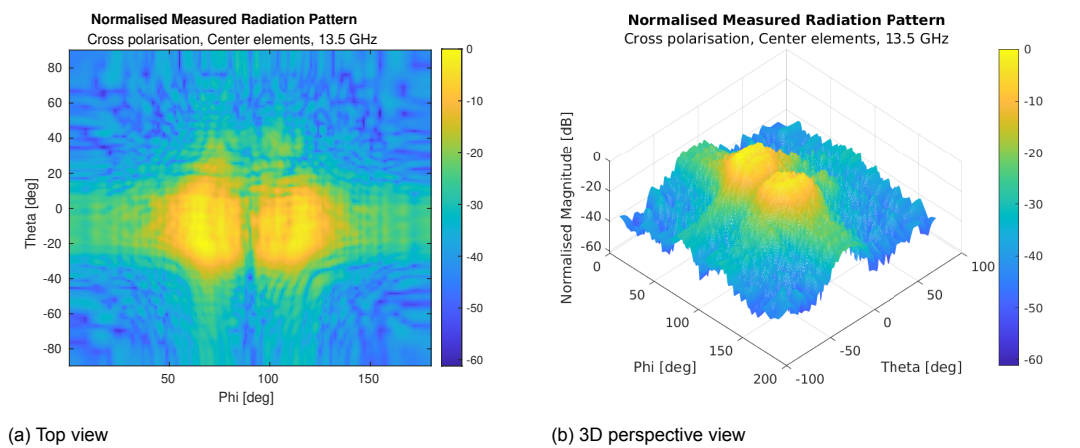


Figure C.13: The measured cross-polarisation radiation pattern of the 4 center elements from different viewing points. The pattern is normalised and is measured at a frequency of 13.5 GHz.

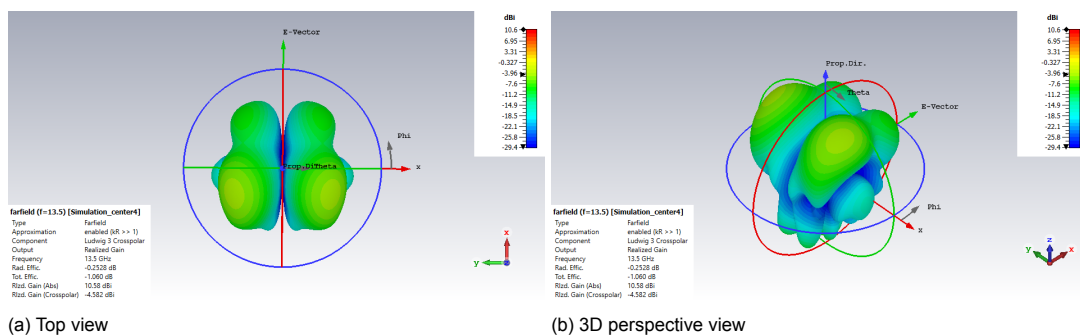


Figure C.14: The simulated cross polarisation radiation pattern of the 4 center elements from different viewing points. The pattern is normalised and is simulated at a frequency of 13.5 GHz.

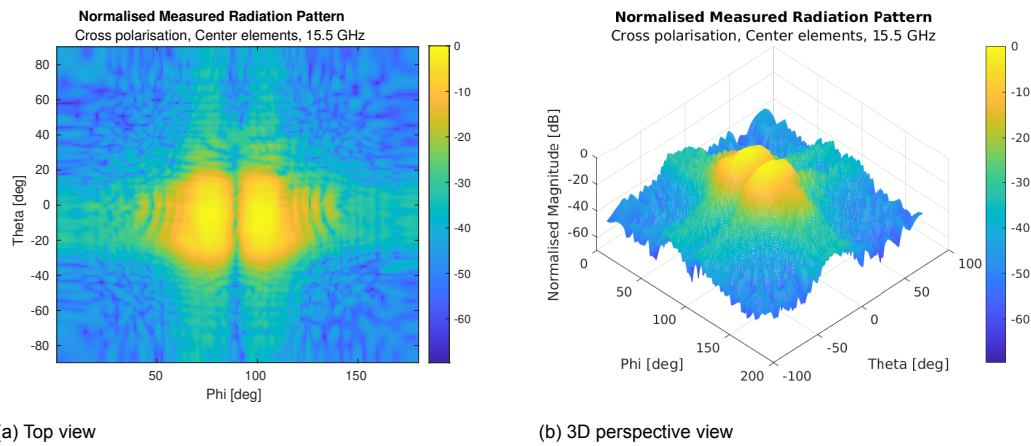


Figure C.15: The measured cross-polarisation radiation pattern of the 4 center elements from different viewing points. The pattern is normalised and is measured at a frequency of 15.5 GHz.

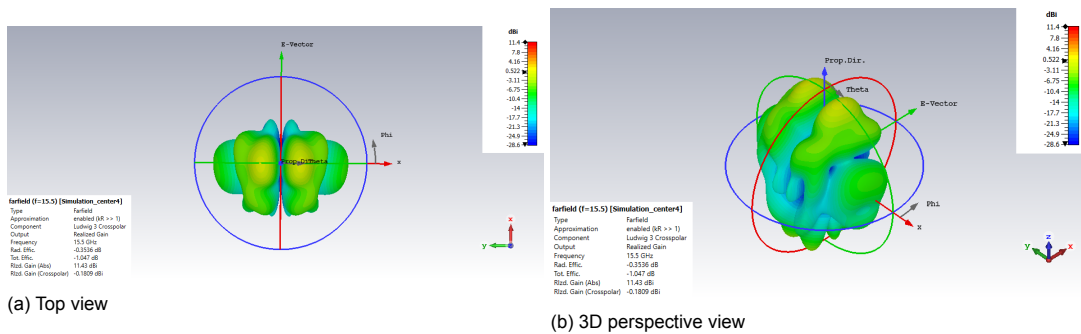


Figure C.16: The simulated cross polarisation radiation pattern of the 4 center elements from different viewing points. The pattern is normalised and is simulated at a frequency of 15.5 GHz.

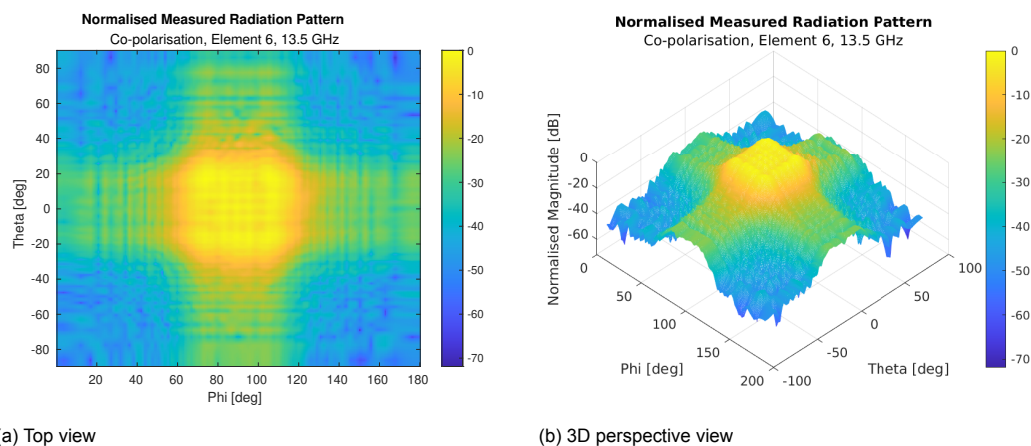


Figure C.17: The measured co-polarisation radiation pattern of element number 6 from different viewing points. The pattern is normalised and is measured at a frequency of 13.5 GHz.

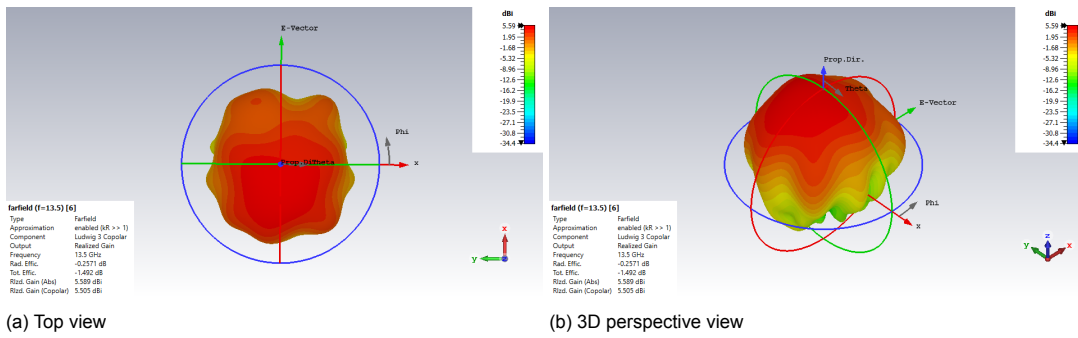


Figure C.18: The simulated co-polarisation radiation pattern of element number 6 from different viewing points. The pattern is normalised and is simulated at a frequency of 13.5 GHz.

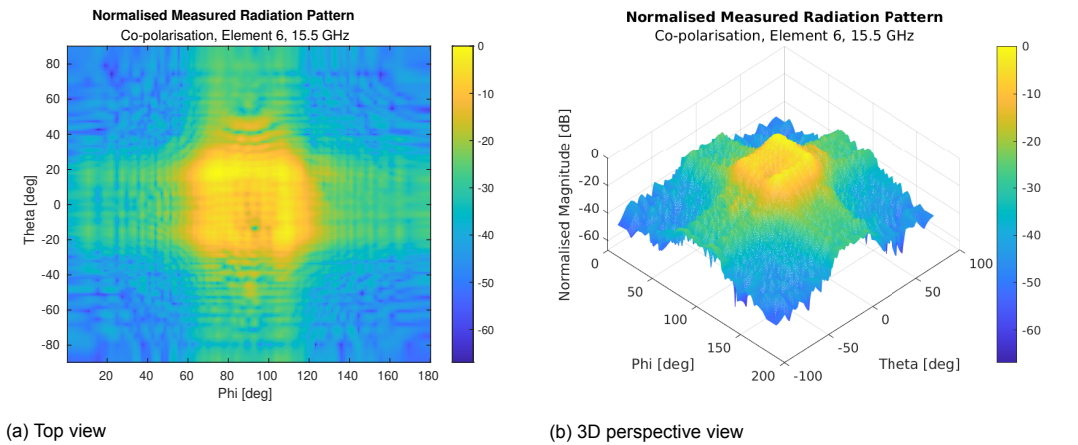


Figure C.19: The measured co-polarisation radiation pattern of element number 6 from different viewing points. The pattern is normalised and is measured at a frequency of 15.5 GHz.

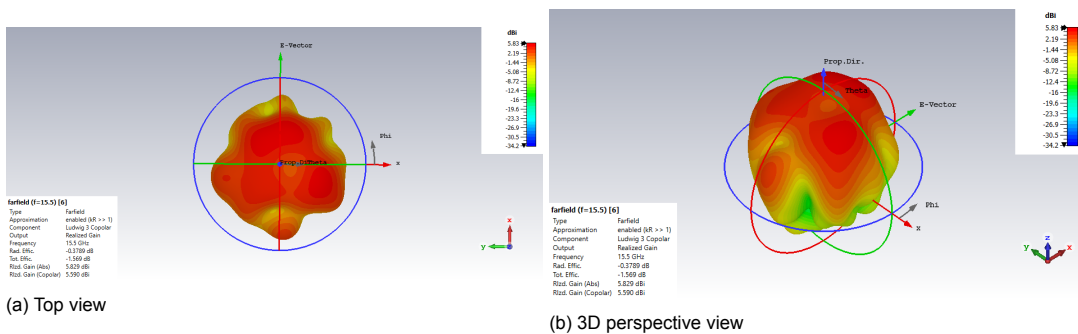


Figure C.20: The simulated co-polarisation radiation pattern of element number 6 from different viewing points. The pattern is normalised and is simulated at a frequency of 15.5 GHz.

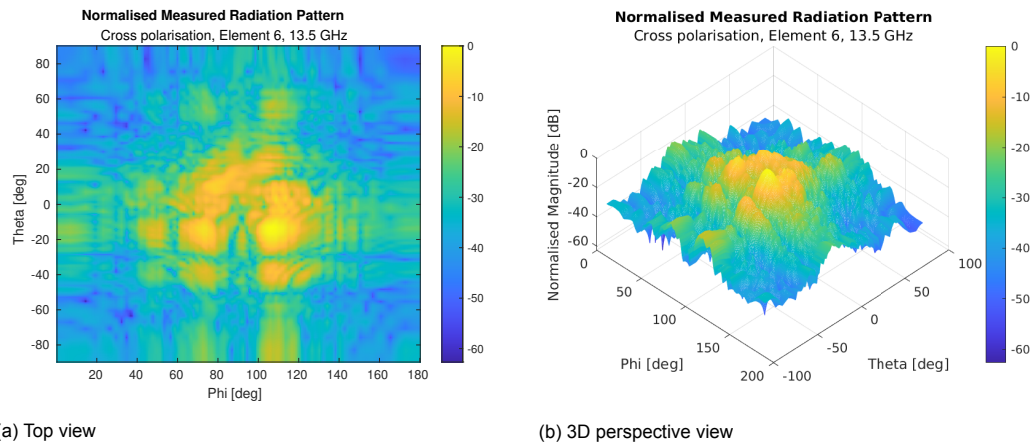


Figure C.21: The measured cross-polarisation radiation pattern of element number 6 from different viewing points. The pattern is normalised and is measured at a frequency of 13.5 GHz.

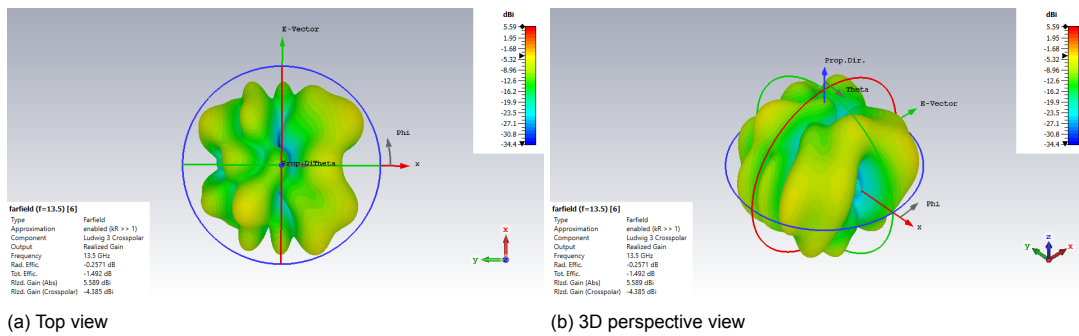


Figure C.22: The simulated cross polarisation radiation pattern of element number 6 from different viewing points. The pattern is normalised and is simulated at a frequency of 13.5 GHz.

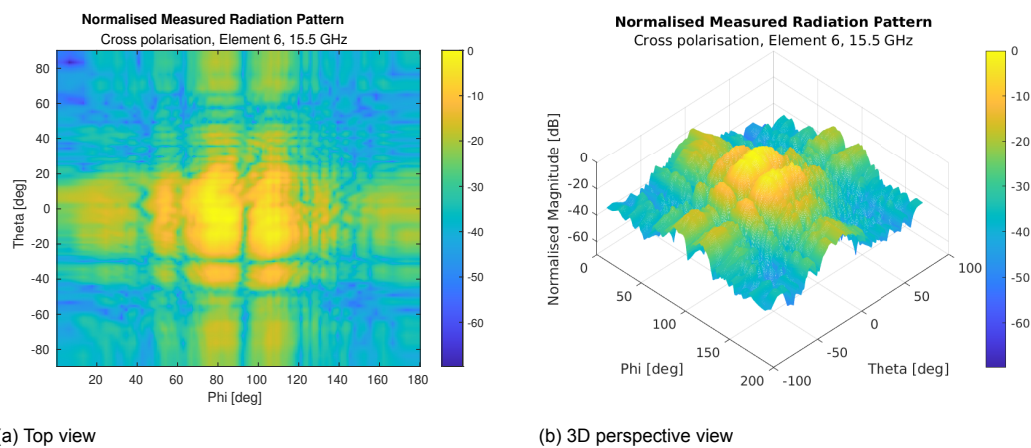


Figure C.23: The measured cross-polarisation radiation pattern of element number 6 from different viewing points. The pattern is normalised and is measured at a frequency of 15.5 GHz.

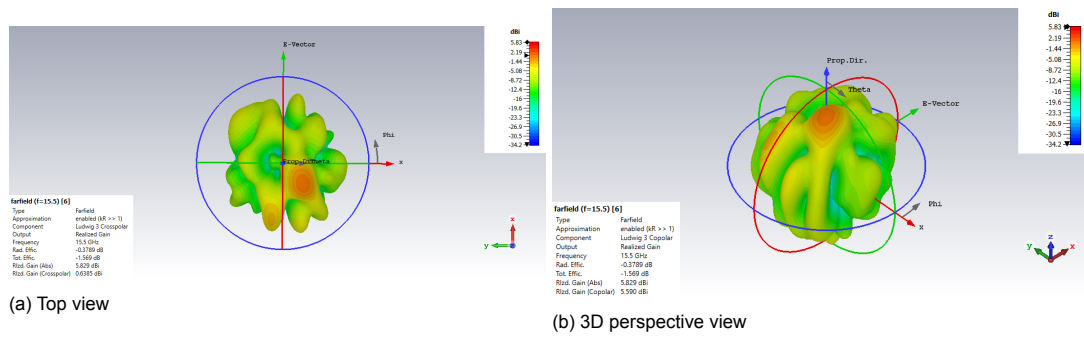


Figure C.24: The simulated cross polarisation radiation pattern of element number 6 from different viewing points. The pattern is normalised and is simulated at a frequency of 15.5 GHz.

Bibliography

- [1] D. D. Grieg and H. F. Engelmann, "Microstrip-a new transmission technique for the kilomegacycle range," *Proceedings of the IRE*, vol. 40, no. 12, pp. 1644–1650, 1952.
- [2] C. Peixeiro, "Microstrip patch antennas: An historical perspective of the development," in *2011 SBMO/IEEE MTT-S International Microwave and Optoelectronics Conference (IMOC 2011)*, 2011, pp. 684–688.
- [3] C. A. Balanis, *Antenna Theory: Analysis and Design*. USA: Wiley-Interscience, 2005.
- [4] A. K. Verma and Nasimuddin, "Analysis of circular microstrip patch antenna as an equivalent rectangular microstrip patch antenna on iso/anisotropic thick substrate," *IEE Proceedings - Microwaves, Antennas and Propagation*, vol. 150, no. 4, pp. 223–229, 2003.
- [5] I. H. Hasan, M. N. Hamidon, A. Ismail, I. Ismail, A. S. Mekki, M. A. Mohd Kusaimi, S. Azhari, and R. Osman, "YIG thick film as substrate overlay for bandwidth enhancement of microstrip patch antenna," *IEEE Access*, vol. 6, pp. 32 601–32 611, 2018.
- [6] Y. Aslan and A. Yarovoy, "Reduction of mutual coupling between closely spaced patch antennas using dielectric stratification technique," in *2017 47th European Microwave Conference (EuMC)*, 2017, pp. 248–251.
- [7] S. Bhardwaj and Y. Rahmat-Samii, "C-shaped, e-shaped and u-slotted patch antennas: Size, bandwidth and cross-polarization characterizations," in *2012 6th European Conference on Antennas and Propagation (EUCAP)*, 2012, pp. 1674–1677.
- [8] M. Abbaspour and H. R. Hassani, "Wideband planar patch antenna array on cylindrical surface," *IEEE Antennas and Wireless Propagation Letters*, vol. 8, pp. 394–397, 2009.
- [9] R. Dalvi and A. Dessai, "Effects of different substrates on staircase shaped microstrip patch antenna for Ku band," in *2018 IEEE International Conference on Computational Intelligence and Computing Research (ICIC)*, 2018, pp. 1–6.
- [10] J. Guo, Y. Zou, and C. Liu, "Compact broadband crescent moon-shape patch-pair antenna," *IEEE Antennas and Wireless Propagation Letters*, vol. 10, pp. 435–437, 2011.
- [11] J. Chatterjee, A. Mohan, and V. Dixit, "Broadband circularly polarized h-shaped patch antenna using reactive impedance surface," *IEEE Antennas and Wireless Propagation Letters*, vol. 17, no. 4, pp. 625–628, 2018.
- [12] Y. Shi and J. Liu, "A circularly polarized octagon-star-shaped microstrip patch antenna with conical radiation pattern," *IEEE Transactions on Antennas and Propagation*, vol. 66, no. 4, pp. 2073–2078, 2018.
- [13] C. Deng, Y. Li, Z. Zhang, and Z. Feng, "A wideband sequential-phase fed circularly polarized patch array," *IEEE Transactions on Antennas and Propagation*, vol. 62, no. 7, pp. 3890–3893, 2014.
- [14] S. E. Valavan and P. Knott, "Improving bandwidth of planar microstrip patch array antennas," in *2015 German Microwave Conference*, 2015, pp. 371–373.
- [15] N. Yoon and C. Seo, "A 28-ghz wideband 2 x 2 u-slot patch array antenna," *Journal of electromagnetic engineering and science*, vol. 17, no. 3, pp. 133–137, 07 2017.
- [16] J. Saini and S. K. Agarwal, "T and I slotted patch antenna for future mobile and wireless communication," in *2017 8th International Conference on Computing, Communication and Networking Technologies (ICCCNT)*, 2017, pp. 1–5.

- [17] J. Wei, X. Jiang, and L. Peng, "Ultrawideband and high-gain circularly polarized antenna with double-y-shape slot," *IEEE Antennas and Wireless Propagation Letters*, vol. 16, pp. 1508–1511, 2017.
- [18] J. D. Díaz, J. L. Salazar-Cerreno, J. A. Ortiz, N. A. Abooserwal, R. M. Lebrón, C. Fulton, and R. D. Palmer, "A cross-stacked radiating antenna with enhanced scanning performance for digital beamforming multifunction phased-array radars," *IEEE Transactions on Antennas and Propagation*, vol. 66, no. 10, pp. 5258–5267, 2018.
- [19] S. Liu, W. Wu, and D. Fang, "Single-feed dual-layer dual-band e-shaped and u-slot patch antenna for wireless communication application," *IEEE Antennas and Wireless Propagation Letters*, vol. 15, pp. 468–471, 2016.
- [20] S. Costanzo and A. Costanzo, "Compact musa: Modified u-slot patch antennas with reduced cross-polarization," *IEEE Antennas and Propagation Magazine*, vol. 57, no. 3, pp. 71–80, 2015.
- [21] M. El-Sayed, N. Gad, M. El-Aasser, and A. Yahia, "Slotted rectangular microstrip-antenna design for radar and 5 g applications," in *2020 International Conference on Innovative Trends in Communication and Computer Engineering (ITCE)*, 2020, pp. 330–334.
- [22] S. Mishra, P. Wankhade, and A. Sahu, "Design and analysis of t and u shaped slots with truncated corner rectangular microstrip patch antenna for return loss enhancement," in *2016 Symposium on Colossal Data Analysis and Networking (CDAN)*, 2016, pp. 1–7.
- [23] K. Klionovski and A. Shamim, "Physically connected stacked patch antenna design with 100% bandwidth," *IEEE Antennas and Wireless Propagation Letters*, vol. 16, pp. 3208–3211, 2017.
- [24] C. Huang, W. Pan, X. Ma, and X. Luo, "Wideband radar cross-section reduction of a stacked patch array antenna using metasurface," *IEEE Antennas and Wireless Propagation Letters*, vol. 14, pp. 1369–1372, 2015.
- [25] N. Yan, K. Ma, and H. Zhang, "A novel substrate-integrated suspended line stacked-patch antenna array for wlan," *IEEE Transactions on Antennas and Propagation*, vol. 66, no. 7, pp. 3491–3499, 2018.
- [26] N. Yan, K. Ma, and Y. Luo, "An sisl sequentially rotated feeding circularly polarized stacked patch antenna array," *IEEE Transactions on Antennas and Propagation*, vol. 68, no. 3, pp. 2060–2067, 2020.
- [27] A. Bondarik and D. Sjöberg, "Gridded parasitic patch stacked microstrip array antenna for 60 ghz band," *IET Microwaves, Antennas Propagation*, vol. 14, no. 8, pp. 712–717, 2020.
- [28] J. Hu, Z. Hao, and W. Hong, "Design of a wideband quad-polarization reconfigurable patch antenna array using a stacked structure," *IEEE Transactions on Antennas and Propagation*, vol. 65, no. 6, pp. 3014–3023, 2017.
- [29] B. Yang, A. Yarovoy, and S. E. Amaldoss, "Performance analysis of a novel ltcc uwb 60 ghz semi-shielded aperture stacked patch antenna with differential feeding," in *Proceedings of the 5th European Conference on Antennas and Propagation (EUCAP)*, 2011, pp. 1882–1885.
- [30] K. M. Mak, H. W. Lai, and K. M. Luk, "A 5G wideband patch antenna with antisymmetric l-shaped probe feeds," *IEEE Transactions on Antennas and Propagation*, vol. 66, no. 2, pp. 957–961, 2018.
- [31] S. Haider, "Antennas for frequency reconfigurable phased arrays," Ph.D. dissertation, Delft University of Technology, Delft, 2015. [Online]. Available: <https://doi.org/10.4233/uuid:8f0cd1af-dcab-4124-aa42-50f9240c236c>
- [32] H. Wong, Q. W. Lin, H. W. Lai, and X. Y. Zhang, "Substrate integrated meandering probe-fed patch antennas for wideband wireless devices," *IEEE Transactions on Components, Packaging and Manufacturing Technology*, vol. 5, no. 3, pp. 381–388, 2015.

- [33] S. Valavan, "Dual-band planar wide-angle scanning phased arrays," Ph.D. dissertation, Delft University of Technology, Delft, 2014. [Online]. Available: <https://doi.org/10.4233/uuid:0ae6e349-07c4-4ca6-9393-71f1dba14db8>
- [34] R. Dewan, M. Rahim, M. Hamid, M. Yusoff, N. Samsuri, N. Murad, and K. Kamardin, "Artificial magnetic conductor for various antenna applications: An overview," *International Journal of RF and Microwave Computer-Aided Engineering*, vol. 27, no. 6, p. e21105, 2017. [Online]. Available: <https://onlinelibrary.wiley.com/doi/abs/10.1002/mmce.21105>
- [35] D. Sievenpiper, "High-impedance electromagnetic surfaces," Ph.D. dissertation, Dept. Elect. Eng., Univ. California at Los Angeles, Los Angeles, CA, 1999. [Online]. Available: <http://optoelectronics.eecs.berkeley.edu/ThesisDan.pdf>
- [36] A. Ghosh, V. Kumar, G. Sen, and S. Das, "Gain enhancement of triple-band patch antenna by using triple-band artificial magnetic conductor," *IET Microwaves, Antennas Propagation*, vol. 12, no. 8, pp. 1400–1406, 2018.
- [37] Y. Zhong, G. Yang, and L. Zhong, "Gain enhancement of bow-tie antenna using fractal wideband artificial magnetic conductor ground," *Electronics Letters*, vol. 51, no. 4, pp. 315–317, 2015.
- [38] R. Chair, Kwai-Man Luk, and Kai-Fong Lee, "Measurement and analysis of miniature multilayer patch antenna," *IEEE Transactions on Antennas and Propagation*, vol. 50, no. 2, pp. 244–250, 2002.
- [39] M. Ameen and R. K. Chaudhary, "Metamaterial-based wideband circularly polarised antenna with rotated v-shaped metasurface for small satellite applications," *Electronics Letters*, vol. 55, no. 7, pp. 365–366, 2019.
- [40] W. Lin, S. Chen, R. W. Ziolkowski, and Y. J. Guo, "Reconfigurable, wideband, low-profile, circularly polarized antenna and array enabled by an artificial magnetic conductor ground," *IEEE Transactions on Antennas and Propagation*, vol. 66, no. 3, pp. 1564–1569, 2018.
- [41] M. Manoj, M. Remsha, V. A. Shameena, K. Vasudevan, and P. Mohanan, "Artificial magnetic conductor-backed dual band antenna for wireless applications," in *2019 URSI Asia-Pacific Radio Science Conference (AP-RASC)*, 2019, pp. 1–4.
- [42] C. Zhang, J. Gao, X. Cao, L. Xu, and J. Han, "Low scattering microstrip antenna array using coding artificial magnetic conductor ground," *IEEE Antennas and Wireless Propagation Letters*, vol. 17, no. 5, pp. 869–872, 2018.
- [43] Y. Zheng, J. Gao, Y. Zhou, X. Cao, L. Xu, S. Li, and H. Yang, "Metamaterial-based patch antenna with wideband rcs reduction and gain enhancement using improved loading method," *IET Microwaves, Antennas Propagation*, vol. 11, no. 9, pp. 1183–1189, 2017.
- [44] J. Zhu, S. Li, S. Liao, and Q. Xue, "Wideband low-profile highly isolated MIMO antenna with artificial magnetic conductor," *IEEE Antennas and Wireless Propagation Letters*, vol. 17, no. 3, pp. 458–462, 2018.
- [45] *Product Selector Guide*, Rogers Corporation, 5 2020, revision 2.
- [46] R. J. Mailloux, *Phased Array Antenna Handbook (3rd Edition)*. Artech House, 2018. [Online]. Available: <https://app.knovel.com/hotlink/toc/id:kpPAAHE005/phased-array-antenna/phased-array-antenna>
- [47] A. Yarovoy and J. Puskely, "EE4016 - Antenna Systems: L4. Antenna Arrays - Beamforming," 2020.
- [48] E. McCune, "Energy efficiency maxima for wireless communications: 5G, IoT, and massive MIMO," in *2017 IEEE Custom Integrated Circuits Conference (CICC)*, 2017, pp. 1–8.
- [49] Y. Aslan, J. Puskely, J. H. J. Janssen, M. Geurts, A. Roederer, and A. Yarovoy, "Thermal-aware synthesis of 5G base station antenna arrays: An overview and a sparsity-based approach," *IEEE Access*, vol. 6, pp. 58 868–58 882, 2018.

- [50] *RO4000[®] Series*, Rogers Corporation, 4 2018, revised 1376.
- [51] "Peek." [Online]. Available: <https://www.polyfluor.nl/nl/materialen/peek/>
- [52] D. Lamensdorf and L. Susman, "Baseband-pulse-antenna techniques," *IEEE Antennas and Propagation Magazine*, vol. 36, no. 1, pp. 20–30, 1994.
- [53] *Understanding the Fundamental Principles of Vector Network Analysis*, Application note 1287-1 ed., Agilent Technologies, 2005.
- [54] *ROHACELL[®] HF*, ROHACELL, 5 2020.
- [55] *Fabrication Notes: RO3000[®] and RO3200TM Series High Frequency Laminates*, Rogers Corporation, 5 2020, revision 1476.
- [56] *SMP STRAIGHT PLUG PCB LIMITED DETENT*, Rosenberger, 7 2016.
- [57] *Getting Started with HFSSTM: Floquet Ports*, ANSYS, 3 2015.